ROYAUME DU MAROC
Université Mohammed V - RABAT -
جامعة محمد الخامس – الرباط –
Faculté des sciences
كلية العلوم
CENTRE D'ETUDES DOCTORALES - SCIENCES ET TECHNOLOGIES

THESE

En vue de l'obtention du : DOCTORAT

Centre de Recherche : *Sciences des Matériaux*

Structure de Recherche *Laboratoire des matériaux, Nanotechnologies et Environnement (LMNE)*

Discipline : *Chimie-physique*

Spécialité : *Électrochimie-Corrosion-Matériaux*

Présentée et soutenue le 06 /10 /2023

par : Maha EL HAWARY

Evaluation of an experimental and theoretical approach to metal corrosion (Aluminum -Copper - stainless steel 307L) during and after biodiesel production, including an assessment of the effectiveness of coffee grounds extract in inhibiting corrosion.

JURY

Ratiba **BOUSSEN**	*PES, Université Mohammed V, Faculté des Sciences - Rabat*	**Présidente/Rapportrice**
Hassane OUDDA	*PES, Université Ibn Tofail, Faculté des Sciences - Kénitra*	**Examinateur/Rapporteur**
Adnane **EL HAMIDI**	*PH, Université Mohammed V, Faculté des Sciences - Rabat*	**Examinateur/ Rapporteur**
Abdelkader **ZARROUK**	*PH, Université Mohammed V, Faculté des Sciences - Rabat*	**Examinateur**
El mostapha **LOTFI**	*PES, ENSAM_Université Mohammed V à Rabat*	**Examinateur**
Mariam **KHACHANI**	*PH, Université Mohammed V, Faculté des Sciences - Rabat*	**Co-encadrante**
Abdelkbir BELLAOUCHOU	*PES, Université Mohammed V, Faculté des Sciences - Rabat*	**Directeur de Thèse**

Année Universitaire :2022/2023

Dedication

Not all phrases have the ability to express thanks, love, respect, and appreciation. This work is dedicated to:

My treasured parents

Your unwavering support, love, and guidance shaped who I am. Words cannot express my gratitude for all you've done. Your belief in me empowered my pursuit of excellence. I adore and respect you immensely. God bless you.

My Spiritual father''ELHAJ OMAR NEKKACH "

With heartfelt gratitude, I honor his memory because throughout my educational endeavors, my father was my constant cheerleader, motivator during challenging times, and guiding light in moments of doubtHe celebrated my successes with boundless pride and provided a comforting embrace during my failures, reminding me that setbacks are merely stepping stones to more outstanding achievements.

To my nursing mother''RABIA"

I am grateful for the values you have instilled in me, the importance of hard work, perseverance, and dedication. Your relentless pursuit of excellence serves as a constant reminder of the heights I can achieve.

To my sister Khadija

With a big thank you, I dedicate my thesis to my ***kindred spirit Khadija***. You have been an unfailing source of support, inspiration, and motivation throughout my studies. Your confidence in my abilities, combined with your frequent declarations of solidarity, stimulated me afterward in the face of adverse conditions.

To my beloved youngest brother and sister

Thank you for bearing with my sour mood during the preparation phase; I dedicate this work to you as a token of my love and af

Acknowledgment

This work was carried out at the Materials, Nanotechnologies and Environment Laboratory (***LMNE***) of the Mohammed "V " University- Faculty of Science of Rabat, under the direction of ***Mr. Abdelkbir BELLAOUCHOU***.

I would like to begin by expressing my deep appreciation to my thesis supervisor, Professor ***Abdelkbir Bellaouchou.*** He holds the position of Professor of Higher Education at the Faculty of Sciences de Rabat and serves as the Director of the Materials, Nanotechnologies, and Environment Laboratory (LMNE). ***Professor Bellaouchou*** graciously allowed me to work under his expert guidance and as a member of his esteemed team. His invaluable advice and support have been instrumental throughout the course of my study. In addition to his remarkable professional qualities, I have had the privilege of witnessing his exceptional human qualities. I have learned an immense amount from him, and for that, I am truly grateful.

I would like to express my deep gratitude and appreciation to my co-supervisor**, *Pr. Mariam KHACHANI,*** for her invaluable advice, support, and expertise throughout my thesis. Her dedication, patience, and commitment to my academic development have been instrumental to the success of my research. Her constructive comments, meticulous attention to detail, and insightful suggestions have greatly enhanced the quality of my work.

I want to express my gratitude to ***Pr. Ratiba BOUSSEN*** for accepting the role of thesis President/Examiner. I am grateful for her willingness to provide her expertise and time to examine my study. Thank you for your encouragement and dedication to my studies. My work's bounds Her intelligent recommendations, scrupulous attention to detail, and constructive comments have substantially improved the quality of my work.

I would like to warmly thank ***Pr. Hassane OUDDA*** Professor of higher education at the Faculty of Sciences in Kenitra, for the benevolent attention granted to this work and participation in this jury, and for having accepted to be rapporteur and examiner of this manuscript.

I am extremely grateful to my examiner/rapporteur, ***Pr. Adnane EL HAMIDI,*** for his valuable contribution in assessing my Ph.D. thesis. His insight, thorough evaluation, and positive remarks have greatly improved the quality of my research work. I appreciate his commitment, time, and insightful comments, which have greatly enriched my scientific work.

would like to express my infinite gratitude to **Pr.** ***Abdelkader*** **ZARROUK**, Professor at the Faculty of Sciences in Rabat, for his constant assistance throughout my doctoral research, always accompanied by great kindness and availability. I would also like to thank him for agreeing to act as an examiner for this work.

I sincerely appreciate ***Pr. El Mostapha Lotfi,*** Professor at the National School of Arts and Crafts in Rabat, for agreeing to act as examiner of this work. His valuable contribution and constructive criticism of the contents of this thesis are greatly appreciated.

I want to express my gratitude to ***Pr.GUENBOUR Abdellah*** for his continuous support and encouragement throughout my thesis. His unwavering belief in my abilities and his willingness to offer guidance and assistance have been crucial to my accomplishments.

I am filled with gratitude for my greatest comrade, ***Labrag Jihane***, for whom I have shown sincere affection and unwavering friendship. She has been a constant source of comfort in difficult times, shining in my life like a beacon of hope and perseverance.
Finally, I'd like to thank everyone who offered encouragement and support during the process of this assignment, whether in person or from afar. I remember fondly my interactions with colleagues at the Materials, Nanotechnologies, and Environment Laboratory ***(LMNE),*** which resulted in many wonderful times

Abstract

Recent years have seen a significant increase in the use of biodiesel as an alternative to conventional fossil fuels. However, there are serious concerns about the impact of biodiesel on metal corrosion. This is due to the presence of impurities, particularly water, which can create acidic conditions in fuel tanks and ultimately lead to corrosion of metals used for fuel storage and transportation.

This thesis aims to evaluate the corrosion behavior of metals in biodiesel from different feedstocks using homogeneous and heterogeneous catalysts. The study will examine the behavior of metals by electrochemical methods (OCP, EIS, and polarization curves) at room temperature during two hours of production and storage; in addition, spectroscopic techniques (FTIR, GS-MS, UV absorption, and FAAS) were applied to examine changes in the composition of the biodiesel before and after the tests. Subsequently, the metal surface was evaluated by (SEM/EDX), (XRD) and UV-Vis-NIR absorption. In addition, the inhibitory effect of coffee grounds (HECG) on SWCO biodiesel was investigated using weight measurements for 1128 h and various electrochemical techniques previously applied to the metal surface.

Keywords ; corrosion-biodiesel ; 307L stainless steel- Alumimim -Copper ; DFT&MDS ; UV-Vis-NIR ; SEM/EDX, DRX ; corrosion inibition ‘ HECG’ ; FAAS ; FTIR, GS-M

Résumé

Ces dernières années ont vu une augmentation significative de l'utilisation du biodiesel comme alternative aux carburants fossiles conventionnels. Cependant, l'impact du biodiesel sur la corrosion des métaux suscite de vives inquiétudes. Ceci est dû à la présence d'impuretés, en particulier l'eau, qui peut créer des conditions acides dans les réservoirs de carburant et finalement conduire à la corrosion des métaux utilisés pour le stockage et le transport des carburants.

Cette thèse vise à évaluer le comportement à la corrosion des métaux dans le biodiesel provenant de différentes matières premières en utilisant des catalyseurs homogènes et hétérogènes. L'étude examinera le comportement des métaux par des méthodes électrochimiques (OCP, EIS, et courbes de polarisation) à température ambiante pendant deux heures de production et pendant le stockage ; en outre, des techniques spectroscopiques (FTIR, GS-MS, absorption UV et FAAS) ont été appliquées pour examiner les changements dans la composition du biodiesel avant et après les tests. Ensuite, la surface métallique a été évaluée par (SEM/EDX), (XRD) et absorption UV-Vis-NIR. En outre, l'effet inhibiteur du marc de café (HECG) sur le biodiesel SWCO a été étudié en utilisant des mesures de poids pendant 1128 h et diverses techniques électrochimiques précédemment appliquées à la surface métallique.

Mots- clés : corrosion-biodiesel ; L'acier inoxydable 307L -Alumimim -Cuivre ; DFT&MDS ; UV-Vis-NIR ; SEM/EDX, DRX ; corrosion inibition ‘ HECG’ ; FAAS ; FTIR, GS-MS.

Résumé détaillé

Ces dernières années, l'utilisation du biodiesel comme alternative aux combustibles fossiles conventionnels a connu une augmentation significative. Toutefois, l'impact du biodiesel sur le comportement des métaux face à la corrosion suscite de vives inquiétudes. Ceci est dû à la présence d'impuretés, en particulier l'eau, qui peut créer des conditions acides dans les conteneurs de carburant et finalement conduire à la corrosion des métaux utilisés dans le stockage et le transport des carburants. cette thèse vise à évaluer le comportement à la corrosion des métaux dans le biodiesel provenant de différentes matières premières en utilisant des catalyseurs homogènes et hétérogènes. L'étude examinera le comportement des métaux à la fois à température ambiante pendant une période de deux heures et pendant le stockage pendant 264 heures par des méthodes électrochimiques (OCP, EIS, et courbes de polarisation).

Cependant, des techniques spectroscopiques (FTIR, GS-MS, absorption UV et FAAS) ont été employées pour étudier les changements dans la composition de la solution de biodiesel avant et après les essais. La surface métallique a été évaluée par SEM/EDS, (XRD) et absorption UV-Vis-NIR. En outre, l'effet inhibiteur du marc de café (HECG) sur le biodiesel SWCO a été étudié. En outre, les propriétés anticorrosion de l'extrait ont été déterminées en utilisant des mesures de poids pendant 1128 h et diverses techniques électrochimiques précédemment utilisées. De plus, l'approche de corrélation (DFT et simulations de dynamique moléculaire (SMD)) a été appliquée pour soutenir les résultats expérimentaux qui favorisent l'aluminium comme métal de base pour la synthèse du biodiesel en raison de son faible taux de corrosion pendant le processus de production et que le métal a été protégé par la formation d'une barrière Al2 O3 et que les molécules de linoléate de méthyle agissent également comme une couche protectrice. Ceci a été confirmé par le SEM/EDS qui a prouvé que le métal présentait de légères piqûres localisées sur la surface, ce qui a entraîné une faible vitesse de corrosion.

L'acier inoxydable 307L utilisé pour le stockage a été choisi pour étudier la relation entre la dégradation du biodiesel et son comportement à la corrosion dans la solution SWCO en appliquant toutes les techniques mentionnées précédemment. Les résultats de cette étude ont révélé une faible influence de l'ester méthylique sur la dégradation de l'acier inoxydable 307L, montrant un faible taux de corrosion avec des micro-piqûres localisées principalement dues à l'oxydation du biodiesel qui augmente avec le temps de contact avec le métal.
En outre, les techniques d'analyse de surface ont confirmé que la surface de l'acier inoxydable 307L était protégée par un film passif d'oxyde de chrome (Cr2O3) qui améliorait la résistance du métal à

la corrosion et au processus de vieillissement. L'efficacité potentielle du HECG dans l'inhibition de la corrosion de l'acier inoxydable 307L dans le milieu biodiesel SWCO. Les études électrochimiques associées à l'analyse de surface montrent que l'ajout de HECG au milieu conduit à une réduction de la vitesse de corrosion de l'acier inoxydable 307L dans la solution de biodiesel SWCO. D'autres facteurs affectant l'activité inhibitrice sont la température et le temps d'immersion (1128H). L'analyse de la surface (SEM/EDX, DRX, absorption UV-Vis-NIR) montre la présence d'un film dû à l'adsorption de l'HECG sur la surface.

List of Figures

Chapter I

Chapter II

Chater: III

List of Tables

Chapter I

Chapter II

Chapter III

Liste of abbreviations

η_{inh}	*the absolute hardness of the inhibitor*
η_{metal}	*the absolute hardness of the metal used*
η_{pdp}	*inhibitory efficiency of the polarization curves*
R%	*The extraction yield*
A	*Absorbance*
χ	*electronigativity*
Cdl	*double-layer capacitance.*
C_{H2O}	*The concentration of pure water.*
χ_{inh}	*denote the absolute electronegativity value of the used inhibitor*
Cinh:	*The concentration of inhibitor.*
χ_{metal}	*denote the absolute electronegativity value of the used metal*
COMPASS:	*Condensed-phase Optimized Molecular Potentials for Atomistic Simulation Studies.*
ΔGads	*Free Energy of Adsorption*
ΔHa:	*Free Activation Enthalpy*
ΔN	*Electronic transfert*
DRX :	*X-ray Diffraction*
ΔSa:	*Entropy of activation*
$E_{binding}$	*binding energy*
E_{mol}	*energy molecul*
$E_{surface}$	*surface energy*
Ea:	*activation energy.*
E_{corr}	*The corrosion potentiel .*
$E_{intercartion}$	*interaction energy*
EIS:	*Electrochemical Impedance Spectroscopy*
ESP	*Electrostatic potential*
f-	*The Fukui index for the electrophilic attack*
f+	*The Fukui index for the nucleophilic attack*
f°	*The Fukui index for the radical attack*
FMO:	*Molecular Frontier Orbitals*
FTIR	*Fourier-transform infrared spectroscopy*
GC/MS	*Gas chromatography coupled to mass spectroscopy*

GGA:	*Generalized Gradient Approximations.*
η	*the overall hardness*
HF:	*Hartree-Fock*
HOMO:	*Highest occupied molecular orbital*
η_{WL}	*inhibitory efficiency of the weight loss*
IA	*Acidity index*
Icorr	*: Corrosion current density.*
Kads	*adsorbation constant*
LCAO:	*Linear combination of the atomic orbitals.*
LDA:	*Approximation of local density.*
LUMO:	*Lowest unoccupied molecular orbitals.*
μ	*The chemical potential electronic*
m_{coeff}	*mass of the sample taken for test*
MDS:	*Molecular Dynamics Simulations*
MEP:	*Molecular Electrostatic Potential*
m_{ext}	*mass of the extract*
M_{KOH}	*The molar mass of KOH*
m_{oil}	*mass of the oil sample*
qk	*the electronic population of the atom k in the neutral molecule*
qk (N−1)	*the electronic population of the atom k in the cationic molecule*
qk (N+1)	*the electronic population of the atom k in the anionic molecule*
σ	*The softness*
SEM	*Scanning Electron Microscope.*
V_{ads}	*adsorbation rate*
V_{KOH}	*Normilty of the KOH solution*
ω	*Overall Electrophilic Index*
Wcorr	*corrosion rate*

Content

General introduction

The recent worldwide changes in weather and climate conditions have required reflection on exploiting essential resources sustainably. It is intended to be a means of configuring civilization and human activity so that society, its members, and economies can meet its needs and express its most tremendous potential at present while preserving biodiversity and natural ecosystems, planning and acting to achieve pro-efficiency in the maintenance of these indefinite ideals[1]. Therefore, facing this problem considerable attention was directed to the production of biodiesel as new alternative engine fuel, clean, safe, and biodegradable. The benefits of using biofuels are the reduction of hazardous emissions such as carbon monoxide and the improvement of exhaust gas quality[2]. As all the organic carbon in biofuel is photosynthetic, it does not contribute to a net increase in the amount of carbon dioxide (CO_2) in the atmosphere and thereby the greenhouse effect. The substitution of biofuels for resource-limited fossil fuels has many potential benefits. Biofuels are alternative fuels produced from biomass and used in transport. There are two main biofuel sectors: bio-gasoline, produced from sugar-based bioethanol, and biodiesel, produced from edible and non-edible oils[3].

According to previous studies, biodiesel is more corrosive than diesel fuel due to its higher hygroscopicity, higher electrical conductivity, higher polarity, higher solvency, the presence of water and oxygen in biodiesel, which promotes microbial growth, and finally its auto-oxidation, which produces corrosive agents[4]. Therefore, During the production, storage, transport, and use, the corrosive behavior of biodiesel was found to increase. Furthermore, many engine parts are made of metals like aluminum, copper, and alloys that can corrode when exposed to biodiesel[5]. The specificities of biodiesel lead to many operating problems, such as incompatibility of materials, formation of heavy deposits on the engine, clogging of injectors, blockage of filters, delamination of piston rings, etc. It is noted that the situation became more complicated when the contact of biodiesel with different metals and the dissolved oxygen can aggravate the corrosive nature of the biodiesel to different levels[6]. There are various investigations in the literature concerning the corrosion of different metals in biodiesel.

In addition, many engine parts are made of metals such as copper, aluminum, and stainless steel, and their alloys can corrode when in contact with biodiesel solvent[7].

Furthermore, the biodiesel industry requires corrosion- and degradation-resistant materials due to the specific properties of the chemical reactants and catalysts used in the biodiesel production process.

On the other hand, corrosiveness decreases by the existence of free water and fatty acids[8].

The utilization of inexpensive and low-quality feedstocks, such as used waste cooking oil, animal fat, or tall oil, as a substitute for refined vegetable oil will greatly enhance the economic viability of biodiesel. Consequently, using WCO highly available may be typically considered a more cost-efficient and

economical alternative[9]. Moreover, trans-esterification is the most method used to yield fatty acid alkyl esters (biodiesel) and glycerol, based on chemical reactions involving catalysts, vegetable oil, and alcohol. The renewable feedstock used in the production outlines the transesterification processes, whereby the triglycerides are reacted with used alcohol (usually methanol or ethanol) to form alkyl esters, glycerol, and other residues, principally long-chain C16 and C18 alkyl esters, some researchers have noticed that the existence of free fatty acids, oxygen fractions, water content, and impurities remaining after treatment lead to an increase in the corrosivity of biodiesel versus diesel fuel[10].

Biodiesel exhibits weak oxidative stability; therefore, the addition of antioxidants to biodiesel is standard practice in the biodiesel industry to retard its oxidation process and the formation of corrosive compounds. Corrosion experts have the best possibilities to use various types of corrosion inhibitors as additives in biofuels to control/prevent their corrosive nature towards various metallic materials. Therefore, the most effective way to protect metals against corrosion reactions is to use corrosion inhibitors derived from low-cost, renewable sources, which provide high inhibition efficiency while having little or no environmental impact. Further, corrosion inhibitors can adsorb metal surfaces, which helps them block a variety of active sites, which is how they primarily stop corrosion[11]. Generally, synthetic organic compounds are currently applied as corrosion inhibitors in different biofuels for reducing their corrosive character for different metallic materials used in transport engine parts, fuel storage systems, etc.

This research aims to investigate the experimental and theoretical approaches of metals (307L Al-Cu-stainless steel) corrosion during and following biodiesel synthesis, with an evaluation of the corrosion inhibition of 307L stainless steel using coffee grounds extract.

The manuscript is structured into tree chapters which are described below:

***Chapter I*:** Literature Review: Various types of biofuels, including those sourced from renewable origins, are employed for fuel production. Furthermore, different catalysts are utilized in this process, employing diverse techniques for biodiesel fabrication and characterization. This chapter presents a comprehensive overview of these aspects, with a particular focus on corrosion. It provides a general description and reviews the use of corrosion inhibitors for metals in aggressive environments. The research methodology employed in this field involves identifying intermolecular interactions that govern the adsorption mechanism using quantum chemistry methods. Additionally, the chapter describes also modeling approaches for studying molecular structure, specifically emphasizing Density Functional Theory (DFT) calculations based on solving the Schrödinger equation. These approaches are classified into DFT and MDS molecular dynamics simulations, as well as independent gradient models. The software employed in these studies is also mentioned. The combined utilization of experimental and theoretical approaches, along with result comparisons, has

significantly contributed to a better understanding of these intricate phenomena occurring at the interface between metals and solutions.

Chapter II: In this chapter, we will outline the investigation methods and the experimental conditions: including biodiesel production & characterization; also, various electrochemical methods(OCP , EIS , TAFEL) and experimental conditions of all our assays, and both surface analysis(SEM/EDX , DRX, UV-VIS-NIR) and solution analysis techniques(UV-VIS, FAAS).

Chapter III: presents the Results & discussions of this thesis which consists of three parts A.B.C:

Part A: The focus of this part was to investigate the corrosion behavior of copper, aluminum, and stainless steel in biodiesel during production at room temperature and evaluate its impact on the degradation of fuel properties using electrochemical analysis. For a better understanding of the adsorption phenomenon, both quantum chemical calculations (DFT using DMol^3) and molecular dynamics simulations (MDS) were performed.

Part B: In this part, the 307L stainless steel used in section A was chosen to evaluate its corrosion resistance in biodiesel produced from an SWCO using a solid acid catalyst during 11 days of storage, this study was carried out by applying electrochemical methods (OCP, EIS, polarization curves), while changes in the biodiesel composition were examined by FTIR, GS-MS, and UV absorption, and the surface analysis was evaluated SEM/EDS microscopy techniques, X-ray diffraction (XRD) analysis and UV-Vis-NIR absorption.

Part C: This section of the thesis aims to study the inhibitory activity of coffee grounds HECG in SWCO biodiesel. Additionally, the anticorrosion properties of the extract have been thoroughly investigated using the weight measurements for 1128h and various electrochemical techniques.

The highlighting of the adsorption process's importance in explaining the metal-inhibitor interactions. The analysis and characterization of the metal surface treated by scanning electron microscopy (SEM), and X-ray diffraction (XRD), UV-Vis-NIR.

Finally, we end this thesis with a general conclusion that summarizes the main results of this work and specifies our contribution to this field. Some new directions are also proposed.

Chapter I

Literature Review - Problem Statement

I. Overview of Biodiesel

I.1. Introduction

Over the past decade, biofuel production and consumption have increased significantly due to population growth, growth in the transportation and industrial sectors, and other factors. The global oil demand is rising in African nations, which have weak links in the worldwide economic and trade system and rely on oil production for energy. Oil usage contributes to major environmental issues. Indeed, the gases emitted by fuel burning are the primary contributors to air pollution and global warming.

The world is increasingly interested in biofuels, particularly biodiesel from non-edible renewable sources known as second-generation biodiesel and locally produced bioethanol (Brazil and U.S.A). The production of biofuels production from food sources (so-called first-generation biofuels) has resulted in a rise in food costs. This issue, combined with the desire to replace fossil fuels, has focused research on the principal source of production of these biofuels, non-edible biomass. As a result, we chose a source that is extensively distributed in Morocco, has simple access, and has a large amount of non-edible oil, in this instance, the lentisk (pistachio lentiscus).

This chapter will first discuss the state of the art in biofuels, then focus on the energy value of biofuels and present their families and production procedures. Technical progress also has a significant impact on production costs, and new production techniques that are less expensive to make biofuels more competitive are developed, and research continues in this direction. This is why it is vital to describe in full the process of converting biomass into fuel employed in this study, namely transesterification, with an emphasis on the global position of this renewable energy material in general and Morocco in particular.

I.2. The biofuels

Biofuels are fluids made from non-fossil organic materials and obtained from biomass or feedstock, which is the biodegradable portion of agricultural, forestry, and associated sectors' products, wastes, and residues, as well as the biodegradable component of industrial and municipal waste.[12] Biofuel is a general term that refers to a variety of fuels, including bioethanol, biodiesel, bio-oil, biogas, Fischer-tropsch liquids, and biohydrogen.

The most common ones are bioethanol and biodiesel, which are produced from biomass through chemical or biological catalysis. Biofuels are a sustainable energy source that doesn't harm the environment, making them a tool for long-term progress. They contribute to a decrease in

greenhouse gas emissions, which improves air quality[13]. Furthermore, they can replace fossil fuels and provide economic stability by reducing energy dependence.

I.2.1 The biogas

Biogas is a gaseous by-product of various processes used to extract biomass; they are produced by fermentation (microbial digestion in the absence of oxygen) of the organic matter. The main results are the production of methane (a combustible molecule in natural gas), carbon monoxide, and hydrogen.

Biogas can be produced by gasifying (thermal cracking) wood or mechanizing organic waste. Similar to how biogas is produced, several natural processes (such as ruminant digestion and wetlands' natural decomposition) are involved. However, human-generated sources of biogas, such as solid waste from sanitary or technical landfills or sludge from wastewater treatment facilities, are also significant and, rather than being waste, could be used as feedstock to produce energy[14].

I.2.2 The Bioethanol

Bioethanol is a fuel that plays an important role in the preservation of the environment by mitigating global warming and preserving fossil fuels. It is an alcoholic beverage produced by fermenting carbohydrates. Reducing the consumption of crude oil and environmental pollution can be accomplished through the production of bioethanol from biomass or waste***(Figure.I. 1)*** [15].

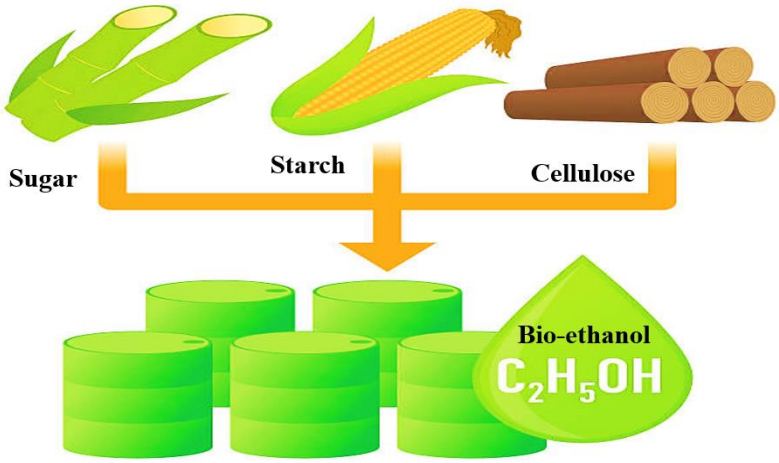

Figure.I. 1:bio-ethanol productions sources

Bioethanol comes from the alcoholic fermentation of simple sugars by yeasts; the simple sugars must be obtained from biomass and the sources of the raw material for bioethanol production are:

- Simple sugars or hydrolysed (degraded) starch from consumable plants (sugarcane, corn, etc.); are agrofuels.
- Plant debris of all kinds (forestry residues, sawmill chips or cellulose (cellulosic ethanol); cellulose can be hydrolysed into fermentable simple sugar.

The ethanol produced by this fermentation is combustible and can be added to conventional fuels. The alcohols can be used as fuel additives and in other instances, they are used as raw material for the manufacture of other fuels; in engines designed for this use. Ethanol content can be as high as 85%, but a lower content of 5-10% is currently being added to car fuels without any engine modifications[16].

I.2.3 The biodiesel

Biodiesel is a biofuel made from lipids (vegetable oils and animal fats) that is designed for use in diesel engines.

The most frequent raw materials used in the production of biodiesel are:

- Vegetable oils, both virgin and used; this is also agrofuel.
- Algae or microalgae-derived oils (algo-fuel).
- Fats from animals (relatively little used).

Biodiesel is fairly comparable to normal diesel and may be utilized without substantial engine changes; it is a promising fuel that emits less pollution. It is now added in variable quantities to ordinary diesel[17].

I.3. Biofuel classification

I.3.1 Definition

Biofuels are liquid or gaseous fuels obtained by the transformation of non-fossil organic materials from plant biomass (wood, wood by-products, beet, wheat, corn, rapeseed, sunflower, potato, etc.) wood, wood by-products, beet, wheat, corn, colza, sunflower, etc.) or animal (manure, fats). From their origin, biofuels are considered renewable energy sources.

Three generations of biofuels have been identified over the years:

I.3.2. The First-generation of Biofuels

First-generation biofuel is an agrofuel made from crops usually used for food, notably the reserve organs of oil and sugar plants. These biofuels are distinguished by their widespread commercialization and relatively easy manufacturing procedures. The most common first-generation biofuel is ethanol, the production of which is mostly dominated by Brazil and the United States. It is produced by yeast fermentation of simple sugars from plants (sugarcane and beet) or starch from grains (corn and wheat). It may be combined directly with gasoline at ratios ranging from 5 to 26%, or even more, for the so-called flexible cars that have been successfully launched in Brazil.[18]

I.3.3 The second generation of biofuels.

The direct correlation between energy and food resources in the manufacture of first-generation biofuels leads early to research for new types of biofuels. Therefore, the technology is currently being developed to exploit biomass rich in cellulosic materials such as wood, leaves, and stems of plants or those from green waste. These materials are known as lignocellulosic biomass because they are derived from carbonaceous or woody components that are not directly used in food production.[19,20]It is specified that the characteristics of this product of availability and non-competition with food compared to the first generation of biofuels. The deployment of this technology at the industrial stage allows the production of second-generation bioethanol, biodiesel, biohydrogen, or biogas.

The principal advantage of second-generation biofuels is that these products limit the uncomfortable duality between the production of food and those biofuels while allowing, it is to be hoped, more efficient use of agricultural land.

I.3.4. The third generation of biofuels

The biofuels known as the third generation, obtained from microbes and microalgae, would offer a solution free of the primary disadvantages of first and second-generation biofuels.

The current approaches have typically proven that types of microorganisms such as yeast, fungi, and microalgae can be effectively used to produce biodiesel, the reason being that these particular organisms can biosynthesize and store significant amounts of fatty acids, similar to those found in vegetable oils.[21]

Algae are considered one of the most ancient forms of life on the planet; they exist in virtually all ecosystems, in a wide variety of forms, and have the highest growth rate of all the plant kingdoms; they adapt to a wide variety of environmental conditions.

Algal cells are miniaturized biochemical factories that absorb CO_2 and produce lipids, proteins, and carbohydrates. In addition, their photosynthetic activity is much higher than that of land plants and consequently more productive.[22]

I.4. biofuel production processes

The production processes of the first-generation biofuels are illustrated in ***Figure. I. 2***. The principal production techniques are as follows:

- **Biodiesel:** is a mixture of fatty acid esters. It is obtained from the reaction process between vegetable oil (rape, sunflower) and alcohol. This process is called "transesterification".
- **Bioethanol:** the manufacturing process is based on the transformation of sugar contained in the plant material into alcohol (ethanol) by fermentation. It is blended with gasoline either directly or in a different chemical form.

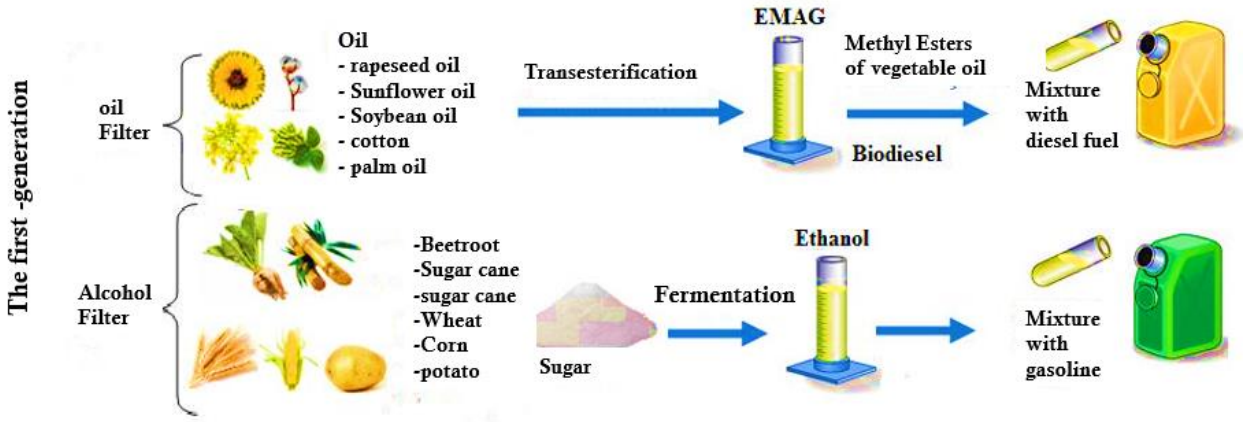

Figure. I. 2: the 1st generation biofuel.

As described i*n* ***Figure. I. 3***, there exist two principal techniques for producing second-generation biofuels:

- **The thermochemical route:** is more related to industrial applications. It involves known processes to produce synthetic fuels from raw materials containing carbon and hydrogen, including coal, biomass or natural gas.

The biomass was converted to synthesis gas (mixture of CO and H_2) under towering conditions of pressure and temperature (1,000 °C and 4 bars). The obtained products (pyrolysis or liquefaction oils, synthesis gas) are consumed directly for steam or electricity production or converted into liquid biofuels.[23]

- **The biochemical route:** is also known as a humid path because it consumes biomass Originating directly from the field or the forest.

Lignocellulosic biomass is essentially composed of cellulose, hemicellulose and lignin. The fundamental difficulties of this procedure concern the separation of these three components by soft chemical processes and the use of microorganisms that transform the fermentable part of the material into ethanol with a satisfactory yield.

The biomass (lignocellulosic type) is converted into sugar by enzymes. Therefore, the sugar produced is then converted into ethanol by a fermentation process.

The result is so-called second-generation ethanol. The ultimate products can be bioethanol, biodiesel, biohydrogen or biogas.[24]

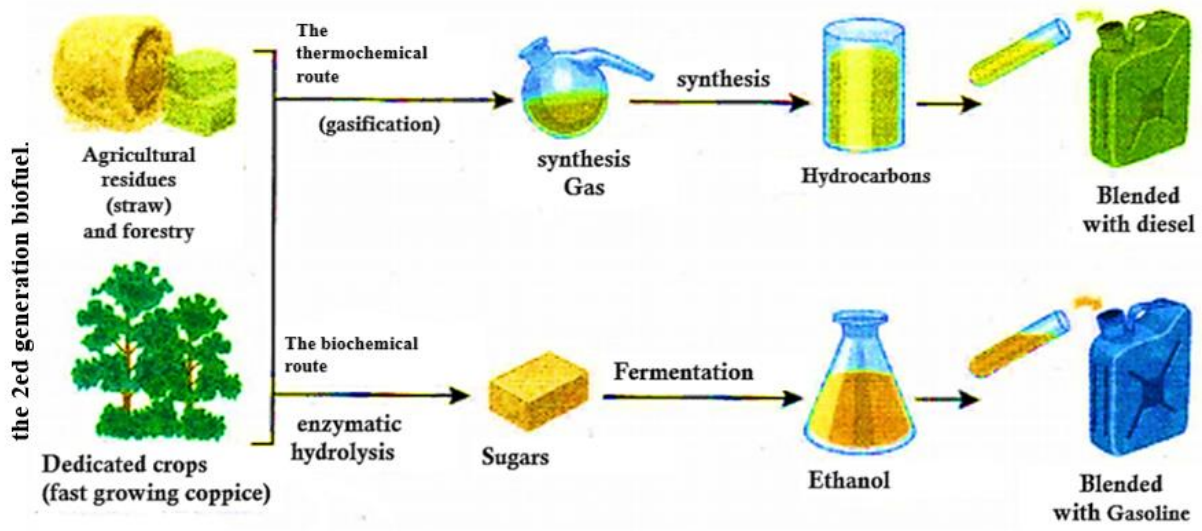

Figure. I. 3: the 2ed generation biofuel.

Besides, the production of 3rd generation biofuel is presented in ***Figure. I.4*** based on the employment of microorganisms via photosynthesis (microalgae) using CO2 and light, or by fermentation (yeast, bacteria, microalgae) using various organic substrates. It is a need to recuperate the triglycerides contained in the algae to convert them into biodiesel.[25]

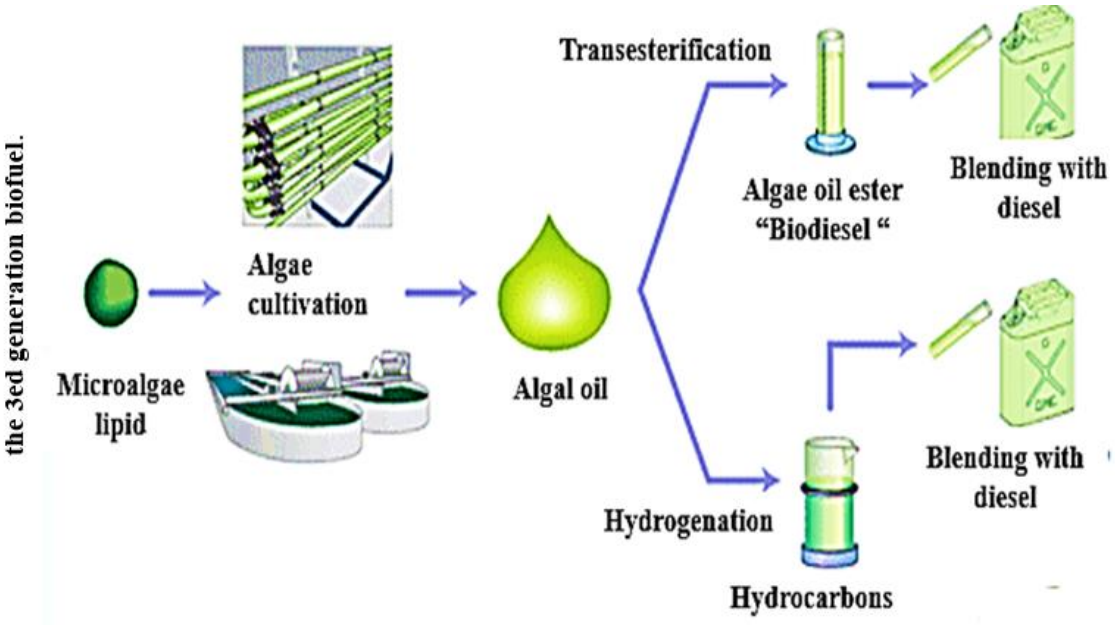

Figure. I.4:the 3rd generation biofuels.

We have previously identified biofuels as an alternative to fossil fuels in transportation. However, it is important to emphasize their use to produce electricity. ***Figure. I. 5*** illustrates the potential of converting biomass into electricity.

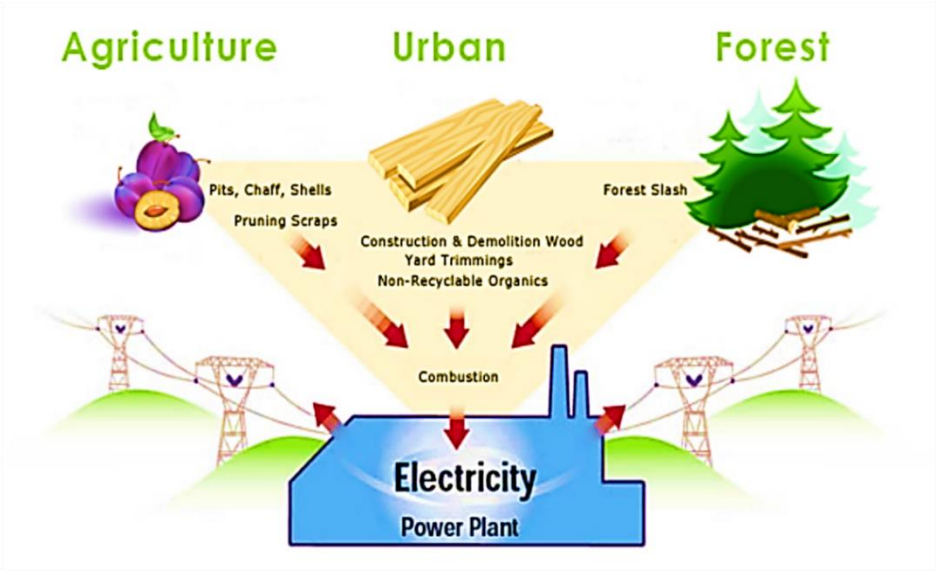

Figure. I. 5:The biomass conversion to electricity.

It remains to mention the use of biomass has no impact on the alimentation. Morocco has over 3,500 km of oceanfront. Biomass production will not present the fundamental obstacle to developing the second-generation biofuel sector. Further, since Morocco is a great fertilizer producer, it typically follows that energy process development from aerial biomass would help provide markets for Moroccan fertilizers. In addition, the initiation of more large-scale projects in Africa is consistent

with the development of environmentally friendly pathways for the production of biofuels for electricity generation.[26]We present below an overview of Morocco's biofuel potential.

I.5. Biofuel potential in Morocco

Morocco has considerable potential for biofuels due to the multiplication of agricultural development projects that will generate massive amounts of waste that can be recycled into first and second-generation biofuels. In addition, Morocco has arid and semi-arid lands that can be used for the cultivation of non-food oilseeds. Its varied climate can provide active investigation for biomass productivity without intentionally harming the food needs of populations. Moreover, Morocco has more than 3500 km of coastline that can constitute a reservoir of biomass for the production of second-generation biofuels and microalgae farms for the production of lipids to replace vegetable oils as raw material for the production of first-generation biodiesel (3rd generation biofuels). The geographical position between Europe and Africa can effectively promote the technology transferred to construct powerful biorefineries to exploit African biomass.

I.6. The viability of biodiesel in Morocco

The generation of renewable energy at a reasonable cost without affecting human nutrition is as great a challenge as reducing the greenhouse gases caused by fossil fuels. In Morocco, like in developing countries, which have non-existent petroleum reserves, there is a progressive preoccupation with these issues. Several electricity production plants derived from solar and wind energy have been built or are currently under construction. As of now, there is no guiding or promotional policy for the production and use of biofuels.

In addition, Morocco's considerable potential has been enhanced by the Moroccan government's planned "Green Morocco" project, which is primarily aimed at developing industrial agriculture, particularly oilseed plants. Those efforts are estimated to generate substantial quantities of waste fats and biomass that can be recycled into primary and secondary biodiesels, respectively[27].

biodiesel production from waste feedstock is a relatively recent market in Morocco. Technically, there is no widespread biodiesel production in Morocco, and its manufacturing does not involve considerable capital investments[28].

The modern fabrication of biodiesel requires minimal investment in established capital; the used cooking oil and the necessary equipment are both extremely affordable. Nevertheless, the production process requires experienced employees, as it involves the use of toxic chemicals.

I.7. A general view of biodiesel

I.7.1 History of Biodiesel

Although a relatively novel type of alternative fuel, triglycerides have been used in diesel engines for decades. In 1892, Rudolf Diesel invented the typical modern diesel engine, which was exhibited in 1900 at the Paris Exposition.[29]The first use of vegetable oil in diesel engines was evaluated at the request of the French government to stimulate energy self-sufficiency in its colonies in Africa by reducing the costs associated with imported coal and liquid fuels. Indeed, the essential oil carefully chosen for the trials came promptly from groundnuts, which are abundantly grown in tropical countries.

By the end of World War II (1939 to 1945), when oil supplies were interrupted, vegetable oil was used as a fuel by various countries, including Brazil, Argentina, China, India and Japan. Once the war was terminated, the oil reserves returned as cheap and plentiful.[30]

The Renewable Energy Policy Network for the 21st Century (REN21) report in 2014, indicates that biodiesel and ethanol are responsible for most of the renewable fuels in the transportation sector. In Brazil, as in the United States and some European countries, the two biofuels have a growing market share. Biodiesel, particularly, has seen the greatest improvement among biofuels over the past decade, growing 15 times. As well as in the U.S., biodiesel production has grown rapidly in Asia. Indonesia, for example, has significantly increased its biodiesel production since 2013 as the desired result of new national biofuel policies, placing the conquered country among the largest biodiesel producers in the world[31].

I.7.2 The biodiesel's types of production.

Biodiesel has many physical properties similar to conventional diesel, such as viscosity, flash point, and cetane number. It is considered a more environmentally friendly fuel because of its reduced emission of toxic gases during combustion[32].

Generally, biodiesel is produced from any type of oil source. It is obtained through transesterification processes in the presence or absence of a catalyst, by enzymatic interesterification, by micro emulsification, or by pyrolysis.

I.7. 2.1 Micro-emulsion

Microemulsification is the complex formation of organic co-solvents (microemulsions) that accurately represent a potential solution to solve the problem of the high viscosity of vegetable oils. The microemulsion is defined as relaxation at the colloidal equilibrium of visually isotropic fluid microstructures with dimensions generally between 1 and 150 nm, formed spontaneously from two

normally immiscible liquids and one or more ionic or non-ionic amphiphiles.[33]Microemulsion fuels are also known as "hybrid fuels", which are precisely complex mixtures of conventional diesel fuel and vegetable oils. Microemulsions are clear, isotropic, and stable fluids composed of three essential components: an oil phase, a water phase, and a surfactant. The blending of vegetable oil and diesel as an alternative fuel to biodiesel has sufficiently been recognized as one of the promising techniques used effectively to reduce the viscosity of vegetable oils.[34]

I.7.2.2 Pyrolysis

The pyrolysis process involves the transformation of an organic compound into another one by applying heat or heat with the addition of a catalyst. The pyrolyzed substance can consist accurately of vegetable oil, animal fat, natural fatty acids, or fatty acid methyl esters[35]. The thermal cracking of vegetable oils and animal fats composed mainly of triglycerides is a promising technology for biodiesel production. Whereby biomass thermal decomposition is carried out in the absence of oxygen[36]. Further, the thermal cracking and pyrolysis systems are expensive for moderate output. Even though the main products are chemically similar to petroleum-derived gasoline and diesel fuel, the potential elimination of oxygen during thermal processing also removes any potential environmental benefit of using an oxygenated fuel. It typically produces some low-value materials and sometimes more gasoline than diesel fuel[37].

I.7.2.3 Tansesterification

The most frequently applied process to produce biodiesel is the transesterification of oils (triglycerides) with alcohol, resulting in biodiesel (fatty acid alkyl esters, FAAE) as the leading product and glycerine as a by-product. The basic transesterification reaction is shown in ***Figure.I.6***. Transesterification involves a substantial group of organic reactions in which the exchange of the alkoxy moiety results in the transformation of one ester into another as per. The transesterification efficiently is an equilibrium reaction that typically consists of the alcoholysis of carboxylic esters, generally realized in the presence of a conventional catalyst to accelerate the equilibrium adjustment to obtain higher yields of esters. The most important process variations affecting the transesterification process are reaction temperature, time, pressure, alcohol/oil ratio, catalyst concentration and type, mixing intensity, and feedstock type.[38]

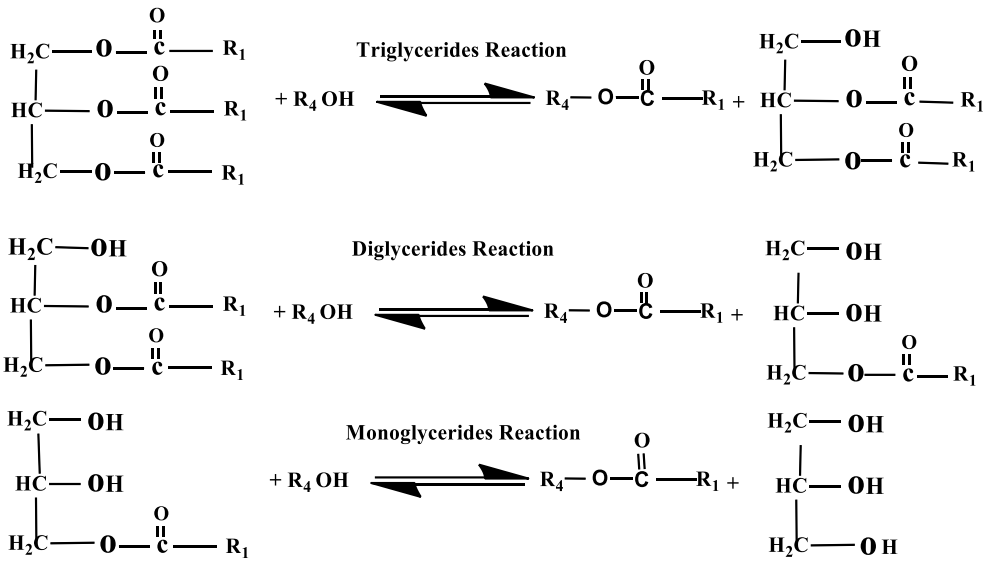

Figure.I.6: Transesterfication reaction .

I.8. An overview of vegetable oils

I.8.1 Definition

The vegetable oils are extracted from seeds, kernels and fruits. The oilseeds are those which are used to produce oil industrially and are grown for this purpose. Some of the plants cultivated for their oil are peanut, olive, rapeseed, castor, soybean and sunflower. In general, all seeds contain oil.

Vegetable oils are substances that are insoluble in mineral solvents, consisting mainly of glycerol esters of fatty acids, called triglycerides[39].

I.8.2 Triglyceride

Triglycerides obtain esters in which three molecules of one or more other fatty acids are bound to glycerol alcohol, as illustrated in ***Figure.I.7***, they are named according to their fatty acid components example: Tristearin contains three molecules of stearic acid. The used types of triglycerides in animals vary typically depending on the species and the composition of fats in the food[40]. Triglycerides in animals and probably in plant seeds function as energy deposits. In mammals, they are conserved in adipose tissue until needed, at which time they are broken down into one glycerol molecule and three fatty acid molecules. Other rich sources of triglycerides are used in cooking oils (WCO) such as used palm oil, used rapeseed oil and used sunflower oil. as used palm oil, used rapeseed oil and used sunflower oil.

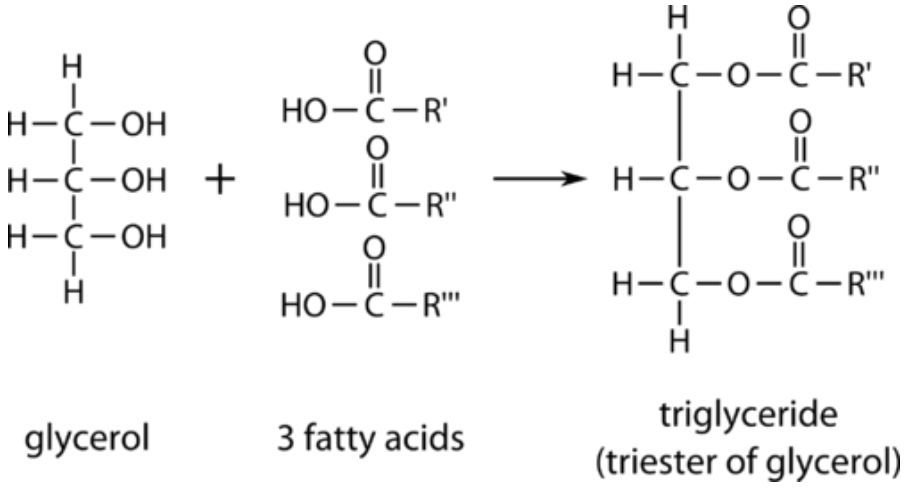

Figure.I.7: Triglyceride components.

I.8. 3 Properties of vegetable oils and Diesel

Vegetable oils can be considered biofuels because they are biodegradable, non-toxic, and clean. Their use and that of their derivatives as fuels in diesel engines lead to substantial reductions in emissions of sulfur oxides, carbon monoxide, polycyclic aromatic hydrocarbons, smoke, and exhaust gases. Their use and that of their derivatives as fuels in diesel engines lead to substantial reductions in emissions of sulfur oxides, carbon monoxide, polycyclic aromatic hydrocarbons, smoke, and particles. However, for refined vegetable oils to be typically used in a conventional unmodified diesel engine, they must meet certain rheological criteria (viscosity, pours points, density, etc.) as well as those relating to their ignition (cetane number, flash point, etc.)[41]***the Table .I. 1*** summarizes the values of certain physical parameters of some oils compared with the values obtained for conventional diesel.

Table .I. 1:summarizes the values of certain physical parameters of some oils.

Vegetable oil	Kinematic viscosity at 40°c (mm^2/s)	Cetane Numbers (°C)	pour point (°C)	flash point	density (Kg/l)
Corn	**34,9**	**37,6**	**-40**	**277**	**0,9095**
Cottonseed	**33,5**	**41,8**	**-15**	**234**	**0,9148**
Linseed	**27,2**	**34,6**	**-12,2**	**241**	**0,9236**
Crambe	**53,6**	**44,6**	**-12**	**274**	**0,9048**
Peanuts	**39,6**	**41,8**	**-6,7**	**271**	**0,9026**
Rapeseed	**37**	**37,6**	**-31,7**	**246**	**0,9115**
Safflower	**31,3**	**41,3**	**-6,7**	**260**	**0,9144**
Sesame	**35,5**	**40,2**	**-9,4**	**260**	**0,9133**
Soyabean	**32,6**	**37,9**	**-12,2**	**254**	**0,9138**
Sunflower	**33,9**	**37,1**	**-15**	**274**	**0,9161**
Palm	**39,6**	**42**	**-**	**267**	**0,918**
Babassu	**30,3**	**38**	**-**	**150**	**0,946**
Diesel	**3,06**	**50**	**-16**	**76**	**0,855**

Vegetable oils and natural animal fats are extracted or pressed to produce raw oils or fats. These generally include free fatty acids, phospholipids, sterols, water, odorous substances, and other impurities. Even praised oils and fats contain small amounts of free fatty acids that vary in carbon chain length and the number of unsaturated bonds (double bonds) as shown in **Table. I. 2**

Table. I. 2:Fatty acid composition of fat sources.

typycal fatty acid composition, wt%											
Fattyacid	vegetable sources					Anmial and fisher sources					
	Rapessed	Palm	Soybean	Sun Flower	Jatropha	Beef Fat	Chiken Fat	Yellow Grease	Lard	Tallow	Salmon
Capric (10:0)	0,56	0,48								0,1	
Lauric(12:0)	0,09		0,09	0,1	0,09			0,19		0,19	
Myristic(14:0)		1,05	0,09	0,1	0,28	3	1	0,78	2	2,55	3
Palmitic(16:0)	4,04	41,59	11,07	6,31	14,36	27	22	16,03	27	23,85	11
Palmitoleic(16:1)	0	0,19	0,18	0,1	0,93	11	6	0,85	4	2,55	5
Stearic(18:0)	2,1	3,6	3,72	3,55	5,88	7	6	6,9	11	17,86	4
Oliec(18:1)	57,26	40,41	22,61	21,39	38,94	48	37	43,34	44	41,42	25
Linoleic(18:2)	20,69	9,3	51,33	63,35	34,89	2	20	24,39	11	4,32	5
Linolenic(18:3)	8,08	0,29	5,63	1,46	0,28		1	1,07		0,88	5
Arachidic(20:0)	0,37	0,29	0,27	0,29	0,19			0,28		0,2	
Eicosenoic(20:1)	2,02	0,1	0,27	0,19	0,09			0,47		0,59	
Behenic(22:0)	0,28	0,1	0,27	0,58	0,19			0,38		0,1	
Erucic(22:1)	0,46		0,09	0,1	0			0		0,1	
Total Satureted	7,06	48,85	15,7	11,22	23,58			24,94	40	46,87	18
Total Unsatureted	88,8	50,28	80,39	88,69	75,31			75,06	59	51,21	80

I.8.4. The esters from vegetable oils and fats

Another way to improve the physical characteristics of vegetable oil to make it comparable to diesel fuel is to change its chemical makeup to an ester. During the 1940s there were over a dozen patents issued to Dupont, Colgate, and others to convert vegetable oils into esters. After World War II and on the practical recommendation of the Research Institute for Oils and Oilseeds in France (IRHO), used tests on esters were typically undertaken at the Bellevue station of the French Petroleum Institute (IFP). But it was in the 1980s that researchers introduced esters in new direct injection engines and the name biodiesel became significant for fuel of biological origin very close to fossil diesel [42].

The recurrent fuel crises have naturally attracted the focused attention of both academic researchers and politicians toward biodiesel as an alternative fuel to fossil diesel. Nevertheless, the production processes and the availability of the raw material have not yet allowed industrial production on the grand scale of fossil hydrocarbon.

I.9. Biodiesel production process

Biodiesel is made by the transesterification reaction of triglycerides in the presence of alcohol and a possible catalyst. This reaction leads to a mixture of esters and glycerin (unpurified glycerol) that can be used in several industrial sectors. The production of biodiesel can make an enormous contribution progressively reducing energy dependency, creating wealth and jobs, and modestly improving the quality of the environment. The cost of the raw material, vegetable oil, and animal fat, represents 75 to 80% of the price of the finished product. The choice of feedstock constitutes a critical step in producing a biofuel that meets standards and is cost-effective. One of the characteristics of biodiesel

production is the precise type of catalysis and how it works. In the case of the transesterification process, the most critical parameters that influence the procedure are the reaction temperature, reaction time, reaction pressure, alcohol/oil ratio, catalyst concentration and type, reaction time, and water temperature.

I.9.1. Catalytic biodiesel production

Generally, vegetable oils can be transesterified by heating in the presence of a catalyst and alcohol. There are three basic types of catalysts used in biodiesel production, the homogeneous and heterogeneous categories and enzyme.

The first is homogeneous catalytic transesterification occurring only when the catalyst is placed with the reactants in the same phase (liquid) throughout the transesterification process. In contrast, if the catalyst remains in a different phase (i.e., solid, immiscible liquid, or gas) than the reactants, the process is called heterogeneous catalytic transesterification.[43] For catalytic methods, proper catalyst selection is an important parameter to reduce the cost of biodiesel production.

Therefore, commercial biodiesel is currently produced by transesterification using a homogeneous catalyst solution. Another factor influencing the choice of catalyst type is the amount of free fatty acids (FFA) present in the oil. In the case of oils containing a low amount of FAA, the base-catalyzed reaction gives a better conversion in a relatively short time, while for oils containing a higher amount of FAA, acid-catalyzed esterification gives a better conversion in a relatively short time. Acid-catalyzed esterification followed by transesterification is appropriate[44]The enzymatic reactions have been reported to be insensitive to FAA and moisture levels in the oil. Therefore, enzymatic reactions can be typically used for transesterification of used cooking oil.

I.9.1.1 Heterogeneous catalytic transesterification

The production of biodiesel by heterogeneous catalysis has been studied in recent years. Typically, heterogeneous catalysts appear to be solid. On the other hand, they represent the opposite of homogeneous catalysts and therefore act differently in the liquid reaction mixture phase.

In addition, two types of heterogeneous catalysts are employed to produce biodiesel: alkaline catalysts and acid catalysts.

I.9.1.1.1 Heterogeneous alkaline catalysts

Heterogeneous catalysts have typically played an important role in the sustainable development of biodiesel production, usually due to their practical applications in a continuous process and easy separation.

Numerous metal oxides have been studied for the oil transesterification process, including alkaline earth metal oxides, transition metal oxides, mixed metal oxides, and supported metal oxides[45].

The utilization of a solid catalyst in the form of a fixed bed reactor system improves the separation of the catalyst from the transesterified product. In addition, the solid catalyst is effective in transesterification at a temperature near the boiling point of methanol.

The heterogeneously catalyzed methanolysis reaction is extremely complicated since it typically occurs in a three-phase system consisting of a solid (heterogeneous catalyst) and two immiscible liquid phases (oil and methanol). Furthermore, in parallel to the methanolysis, some side reactions occur such as the saponification of glycerides and methyl esters and the neutralization of free fatty acids by the catalyst as demonstrated in ***Figure.I. 8***.[46]

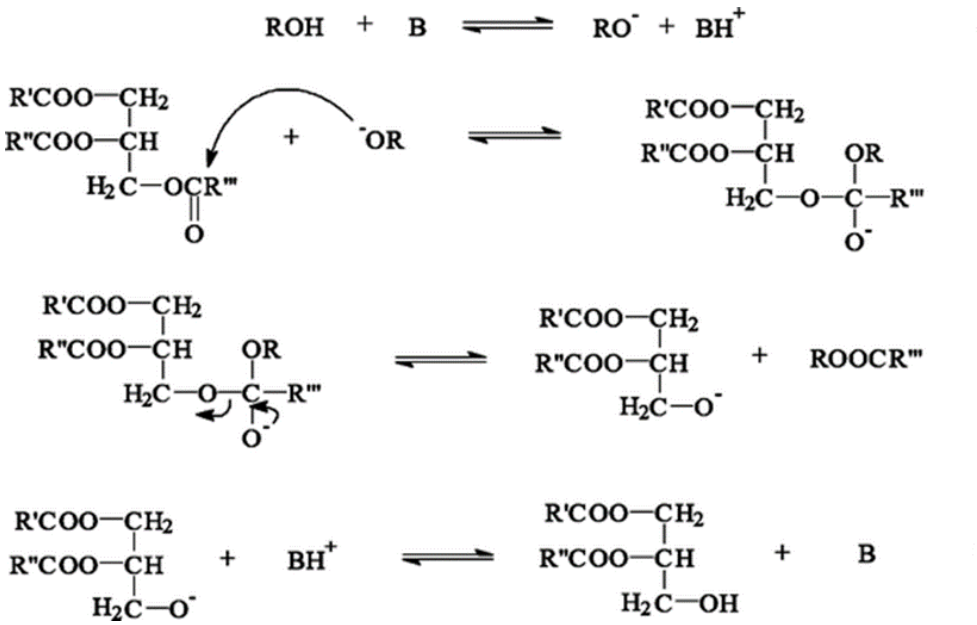

Figure.I. 8: Mechanism of transesterification in the presence of Heterogeneous alkaline catalysts.

I.9.1.1.2 Heterogeneous acidic catalysts

the heterogeneous acid catalyst utilization can eliminate the problems associated with homogeneous acid catalysts. Heterogeneous acid catalysts can be easily removed from the reaction mixture by filtration and recycled to the new process***(Figure.I. 9).*** Therefore, catalyst loss could be avoided. Thus, the reaction products are obtained with high purity. In addition, there is no soap formation from the free fatty acids, which makes it possible to use the acidic oils as soap stocks[47]. Several reports are available about the use of heterogeneous acid catalysts to produce biodiesel. In particular, (zeolites:

ETS-10 zeolite, Zeolite HY, Zeolite X) and **Al_2O_3 -SnO, KOH/K_2CO_3, Al_2O_3 -ZnO, Ca $(NO_3)_2$ /Al_2O_3 CaO/Al_2O_3, KOH/Al_2O_3, Al_2O_3 /KI, Sr$(NO_3)_2$ /ZnO, ZrO_2/SO_4^{-2}**

TiO_2 /SO_4^{-2} .

Indeed, the heterogeneous acid catalyst is commonly hydrophilic, and its activity will be decreased by the water yielded from the esterification of FFA.

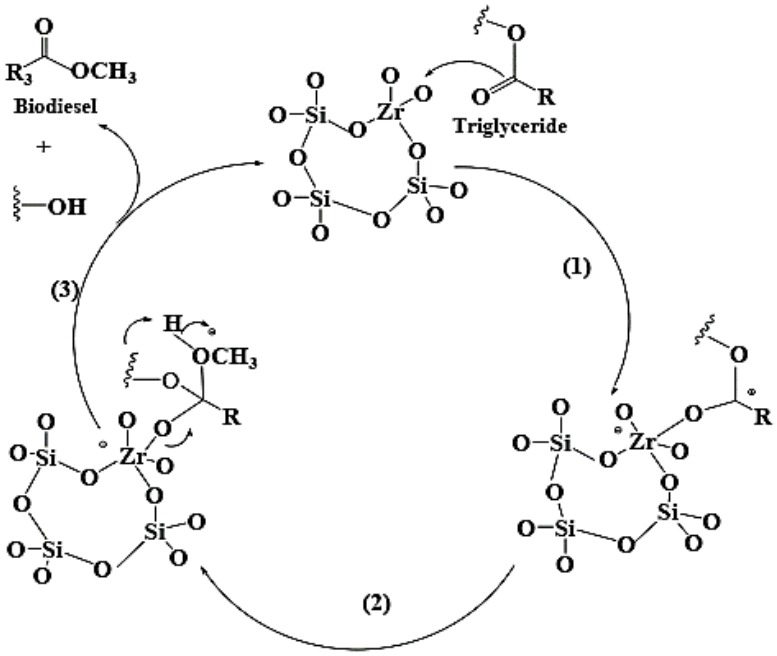

Figure.I. 9: Mechanism of transesterification in the presence of Heterogeneous solid acid catalysts.

I.9.1.2 Homogeneous catalytic transesterification

The homogeneous catalysts used in biodiesel production are divided into two specific types: alkaline homogeneous catalysts and acid homogeneous catalysts.

I.9.1.2.1 Homogeneous alkaline catalysts

Many researchers have employed alkaline catalysts (NaOH, KOH, CH_3-ONa) for biodiesel production because these catalysts are cheap and commercially available, especially basic catalysts.[48] They are favored by industrial processes for biodiesel production because they are non-corrosive and produce biodiesel with high purity and high yields in a short time compared to acid catalysts. The basic catalyst is consumed in producing soap and reduces catalyst efficiency. The soap causes an increase in viscosity and formation of gels which reduces ester yield and makes the separation of glycerol difficult(***figure.I. 10).***

However, this process has some limitations, such as high energy consumption, which in turn leads to a considerable increase in capital equipment costs and safety issues. In addition, this process is extremely sensitive to the water and free fatty acid (FFA) content of the raw material.

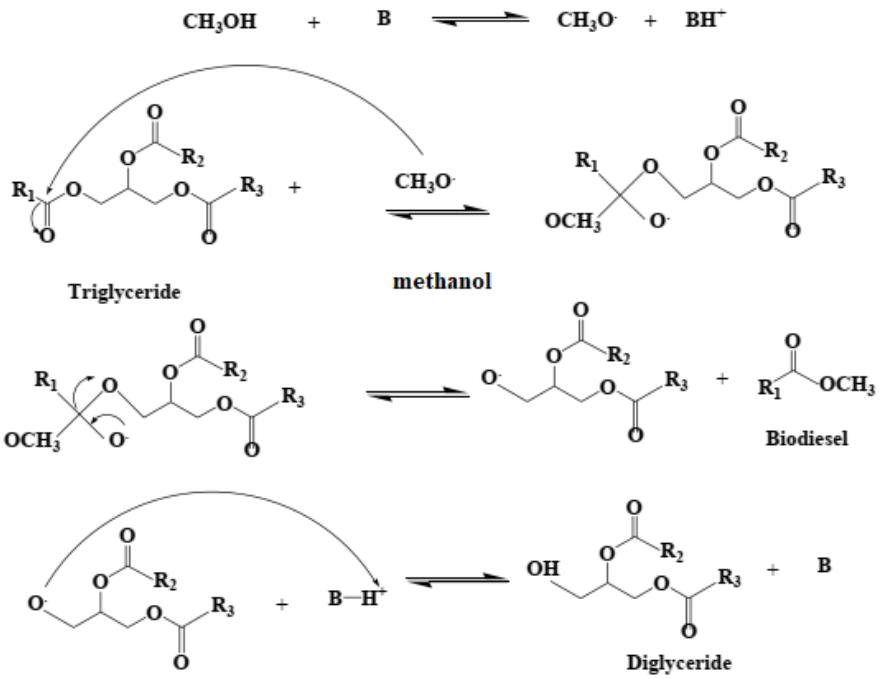

Figure.I. 11: Mechanism of transesterification in the presence of a homogeneous alkaline catalyst.

I.9.2.2.2 Homogeneous acidic catalysts

The homogeneous acid catalysts are also most tolerant of moisture or water during the reaction*(***Figure. I. 12***)* They are frequently used for reducing the FAAs content of waste cooking oils and animal fats before complete transesterification with alkaline catalysts. The most widely applied type of acid catalysts for the transesterification process is sulfuric acid (H_2SO_4), sulfonic acid (HSO_3R) and hydrochloric acid (HCl)[49].

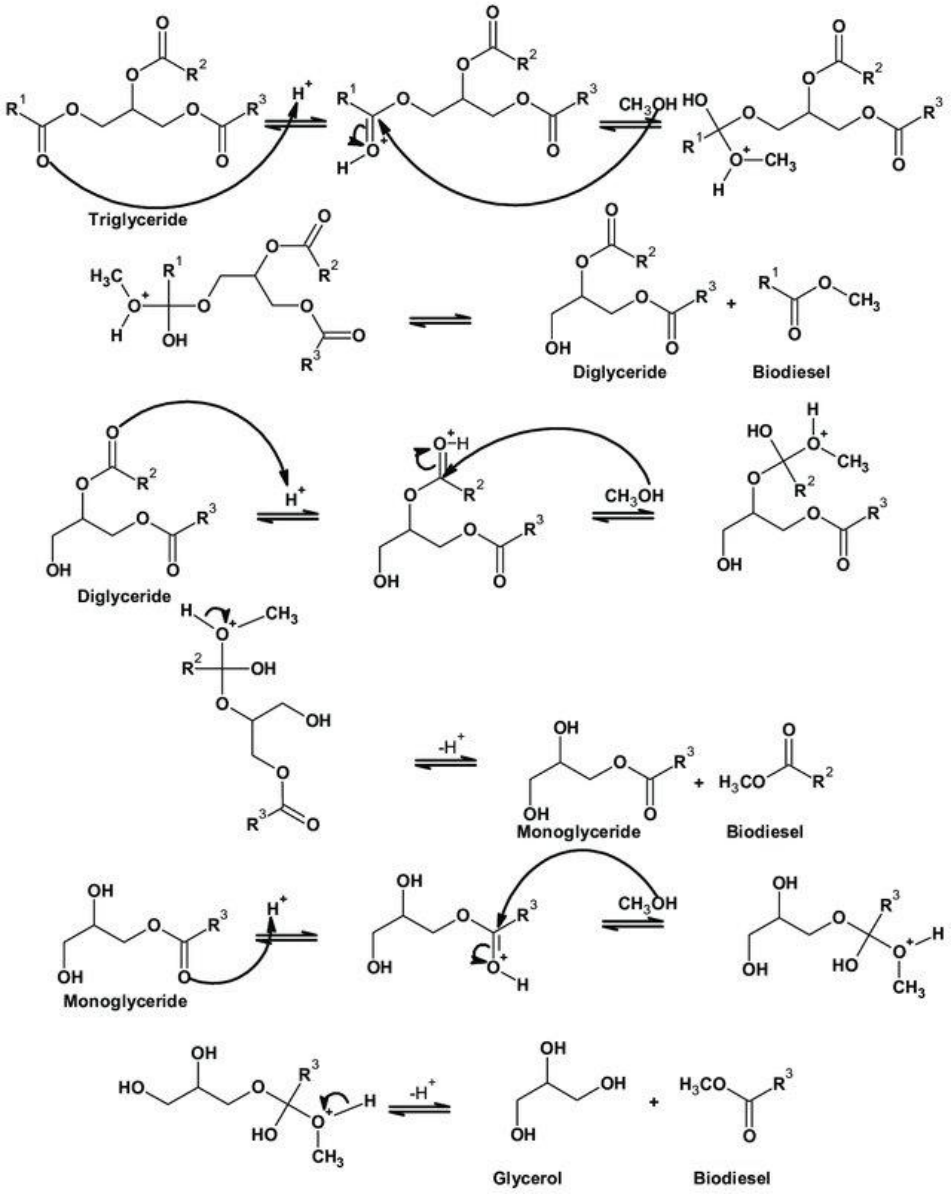

Figure. I. 12:Mechanism of transesterification in the presence of a homogeneous acid catalyst.

Ultimately, due to their corrosive nature, they require special (more expensive) processing equipment.[50] Indeed, a homogeneous acid catalyst reacts more than 4000 times slower than an alkaline catalyst[51]. However, acid catalysts also demand a high reaction temperature and have a higher alcohol/oil molar ratio. Therefore, they are rarely used in this field.

I.9.1.3 Enzymatic catalytic transesterification

Enzymes obtain commonly successful biocatalysts to have Features of a substrate, functional group specificity, and stereospecificity in an aquatic medium. Indeed, the chemical reactions may also be activated using lipase directly in organic media. The carboxylic acid-alcohol esterification reaction in aqueous media is difficult to achieve, whereas this reaction proceeds readily in the organic medium. This kind of biodiesel production has grown in significance during the last years, is hoped eventually to eliminate the usage of metal catalysts. Lipases occur naturally and can carry out transesterification processes for biodiesel production as shown in ***Figure.I. 13***. Although biodiesel fuel production through the enzymatic method has been unadopted industrially. Because of the expensive costs of an enzymatic catalyst.

Enzyme production can be achieved from both extracellular and intracellular lipases. Principally, an immobilized enzyme is consumed, thereby eliminating downstream processes like separation and recycling. Therefore, in all works reported in the literature, immobilized enzymes (extracellular) or immobilized intact cells (intracellular enzymes) are employed for catalytic processing. Both procedures are considered extremely efficient.[52]Various lipase immobilization techniques exist, including adsorption, covalent bonding, entrapment, encapsulation, and cross-linking, these immobilization methods have been used in recent years to improve lipase stability for biodiesel production. Adsorption remains the most widely used method for lipase immobilization[53].

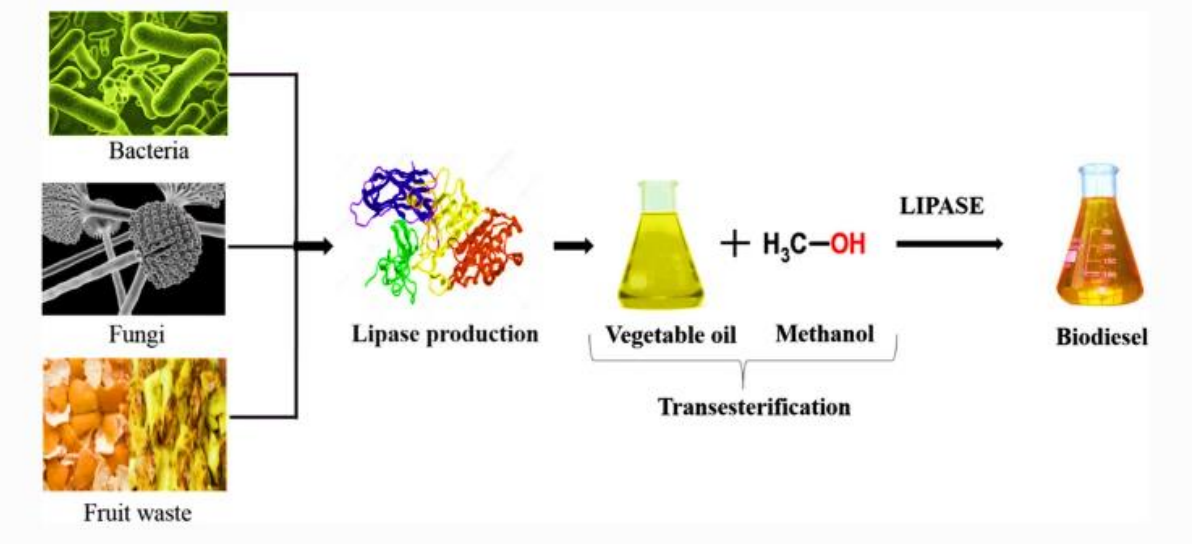

Figure.I. 13: the enzymatic catalytic transesterification in biodiesel production.

I.9. Advantages and disadvantages of biodiesel

Biodiesel has its advantages and disadvantages when considered as an automation fuel. Due to some unfavorable properties of biodiesel, such as its high viscosity and FFA content, moisture absorption and oxidation stability, and highly corrosive nature, a detailed and accurate assessment of the CI engine's short and long-term durability is usually required before use.

I.9.1 Advantages

Biodiesel typically reduces the environmental effect of a waste product and can be made out of used cooking oils and lards[54]. Because of its biodegradability characteristics, lower toxicity, sulfur content (a positive factor for not increasing pollution), hydrocarbon and carbon monoxide exhaust emissions (due to the presence of oxygen), particulate matter, and lower CO2 emissions, biodiesel is described as advantageous over fossil diesel in terms of engine operation. Because it has a higher cetane number (about 60–65 depending on the vegetable oil) than petroleum diesel (53) and may not require engine modification up to B20[55]. Higher mixes, on the other hand, may necessitate some small alterations. According to its greater flash point (over 100–170 °C) than petroleum diesel (60–80 °C), higher blends may require some modest adjustment and is safe for transportation, handling, distribution, usage, and storage.[56]

I .9.2 Disadvantages

Biodiesel has a 12 % lower energy content than diesel, resulting in a 2-10% increase in fuel usage. Furthermore, biodiesel has a greater cloud point and pour point than diesel and higher nitrogen oxide emissions. It has lower volatility, which leads to engine deposits as a result of incomplete combustion characteristics, more nitrogen oxide emissions than diesel, and lower volatility, which leads to engine deposits as a result of incomplete combustion characteristics[57]. It has a greater viscosity (11-18 times that of diesel) and lower volatility than diesel, necessitating higher injection pressure. Biodiesel has poorer oxidation stability than diesel. It can be oxidized to fatty acids in the presence of active air, causing corrosion of the fuel tank, pipe, and other components. Biodiesel can cause corrosion in engine materials (copper and brass), such as fuel system obstruction, seal problems, clogged filters, and injection pump deposits.

The use of biodiesel in an internal combustion engine can cause issues such as injector cocking, filter blocking, and piston ring sticking, which can lead to corrosion in engine materials (copper and brass), such as fuel system obstruction, seal problems, clogged filters, and injection pump deposits[58].

I.10. Biodiesel Corrosivity

Corrosion causes materials to disintegrate by typically reacting with biodiesel when they come into contact[59]. Corrosion of materials leads to the formation of modest scales and other products that adversely affect heat transfer and result in decreased thermal efficiency of the equipment. This requires periodic descaling and cleaning in a hydrochloric acid solution, resulting in increased costs. However, the considerable extent of corrosion varies for metal ions, typically depending on the oxidation potential and other conditions prevailing in the fuel.

However, the extent of corrosion varies for metal ions depending on oxidation potentials and other conditions in the fuel. Yet, biodiesel handling guidelines have reported that copper, brass, bronze, lead, tin, and zinc, which are the materials used for biodiesel production and transportation, are corroded by biodiesel, resulting in biodiesel instability and degradation[7]. The level of corrosion in biodiesel is specified by the copper strip corrosion test and determined by the American Society for Testing and Materials. (ASTM).[60]

II. Overview of corrosion

II. 1. Introduction

In a widespread aspect, corrosion can be defined as the deterioration of a material, generally by chemical or electrochemical action from the environment, whether or not associated with mechanical stresses. Corrosion is the transformation of a metallic material or a metallic alloy by its chemical or electrochemical interaction in a given medium of exposure, leading to the formation of corrosion products and the release of energy. Chemical corrosion occurs at high temperatures in the absence of water. The problem of corrosion has considerable importance nowadays, given the increasing use of metals and alloys in modern life. The study of corrosion is located at the crossroads of various fields: electrochemistry, solid-state physics, metallurgy, chemistry, physics, thermodynamics, etc. In addition to its interdisciplinary scientific interest, it responds to an important industrial issue. Corrosion occurs when a metal is oxidized to its ionic species, resulting in an electron flow between an oxidizing agent and the metal, resulting in an excess of electrons at the metal's surface. As a result of the transfer of electrons to electrochemically active species present in an electrolyte solution, the oxidation reaction is electrochemical in nature and usually occurs at the separating surface between the metal and the corrosive medium. Therefore, corrosion is a means of destroying the metal by progressing along its surface. When a metal is oxidized to its ionic species, an electron flow between the metal and an oxidizing agent occurs, resulting in an excess of electrons at the metal's surface. s: appearance, maintenance of the coating used to protect the metal, interruption of a production process or contamination of the product, loss of material due to leaks from pipelines and tanks, which can cause environmental contamination and health and safety problems.

II .2. Definition

Corrosion remains the phenomenon of interaction between a metal or metal alloy and its environment that results in a deterioration of the beneficial properties of the metal, allowing it to return to the stable sulfide or oxide state that it had before the manufacturing and extraction operations[61]. Nonmetallic compounds are unincluded in this definition. Plastics may swell or crack, wood may melt or open, granite may erode, and Portland cement may leach, but the term "corrosion" is here limited to the chemical attack of metals.

II .3. The types of corrosion

The corrosion of a metal or an alloy can develop according to different processes, which characterize a type of corrosion. We can adequately distinguish three types of corrosion:

- Chemical corrosion.
- Electrochemical corrosion.
- Bacterial corrosion (biocorrosion)

II.3.1. Chemical corrosion (drying):

Chemical corrosion is typically known as corrosion that does not involve the passage of an electric current between the solid and the gas or liquid. It is a heterogeneous reaction between a solid phase and a gas or liquid phase. In the case where the reagent is gaseous (this is the case of oxygen, which has been studied the most), a phenomenon of dry corrosion appears. If the reagent is a liquid, the metal is attacked by the formation of corrosion products on its surface, usually at an elevated temperature, without an exchange of electrons between a metal and an oxidant[62].

The reaction that occurs is of the form:

$$M(s)+X(g) \rightarrow MX(s) \quad (1)$$

II. 3.2 Bacterial corrosion (biocorrosion)

Bacterial corrosion is due to the existence of numerous bacteria colonies, which are known as anaerobic bacteria, that grow in water containing sulphates. The fight against this form of corrosion is currently essentially of a biological nature. It is carried out by the injection of bacterial products into the corrosive medium (***Figure. I. 14)***. [63]

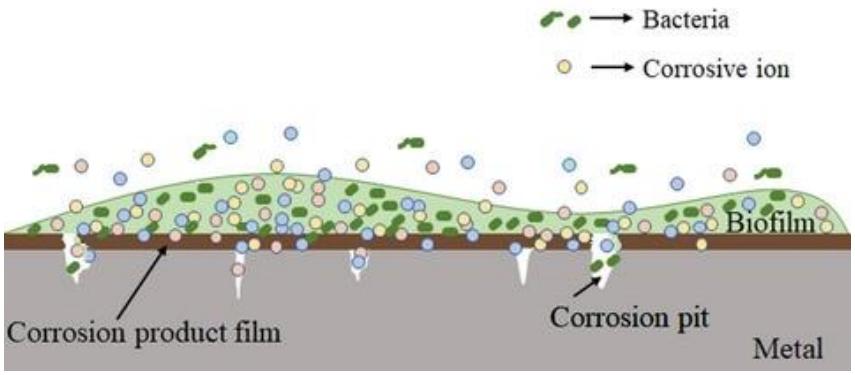

Figure. I. 14: Bio corrosion

II. 3.3 Electrochemical corrosion (humid)

It is characterized by the corrosion of metals and alloys in contact with a solution containing a dissolved electrolyte(***Figure.I. 15***) . It appears that when one of the constituents of the metal-forming couple is heterogeneous, the reaction results in the formation of batteries or micro-batteries, anodes, and cathodes on the same part of the metal structure. The corrosion of the anode part is accompanied by the passage of a current in the electrolyte, a current that goes from the anode to the cathode[64].

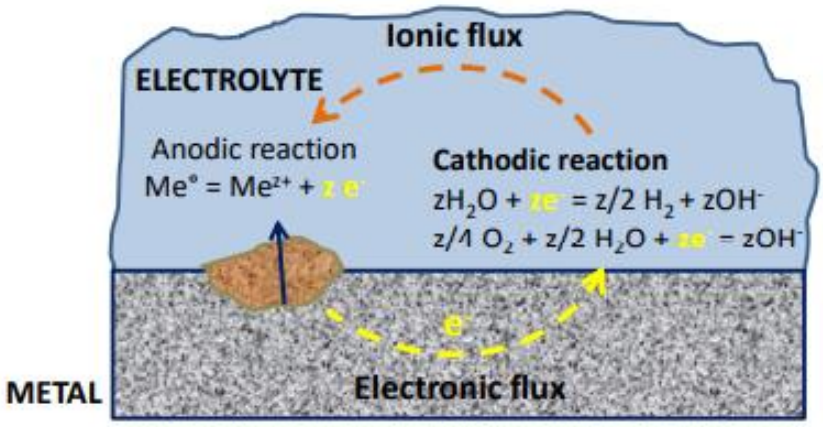

Figure.I. 15: Electrochemical corrosion process.

II. 4. The different forms of corrosion (morphology)

Depending on the type and location of the attack, the most important types of corrosion are classified into two major groups: generalized and localized corrosion (***Figure.I. 16***). A clear distinction is made between anodic and cathodic areas. The main forms are presented and described in ***Table I .3***.

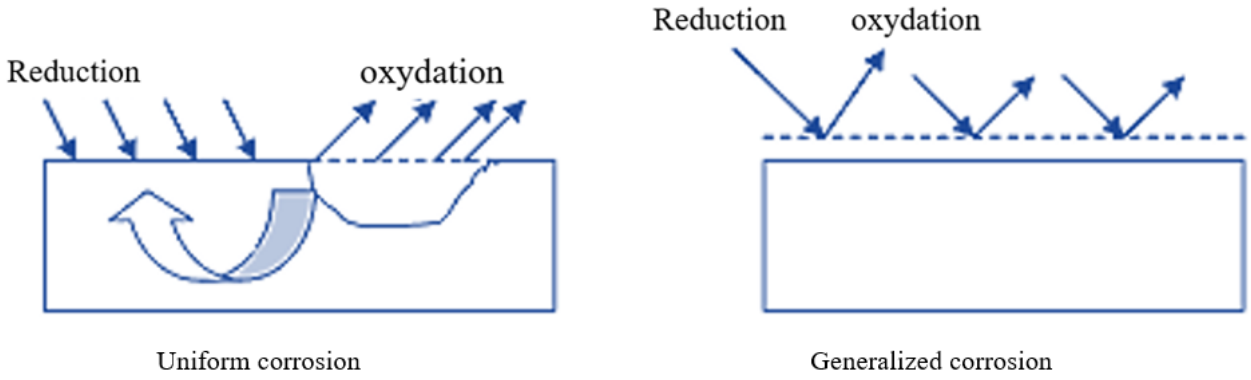

Figure.I. 16:corrosion morphology.

Table I .3:The main forms of corrosion

Corrosion forms	**causes**
morphology	Uniform, by plates, alveolar, punctate or by the pit, intergranular, transgranular, filiform, by selective exfoliation, around the weld bead, and blistering by hydrogen.
Mechanical factors	Under tension, under fatigue, by friction, associated with erosion; Atmospheric,
Causes or mechanisms	By aeration, electrolytic or by leakage currents, galvanic, associated with mechanical stresses (corrosion under fracturing stress), around a weld bead, selective, blistering or weakening by hydrogen;
Corrosion medium	Atmospheric, soil, microorganism-induced, seawater, and molten salts;
Location of attack	Pite uniform; intergranular; transgranular;

II.1. Uniform or generalized corrosion

Uniform corrosion occurs when the metal surface is in contact with the solution and is attacked in the same way. It is expressed by a chemical or electrochemical reaction that occurs uniformly over the entire surface, also called "generalized corrosion." It occurs in the presence of a homogeneous environment and when the metal exhibits sufficiently homogeneous behavior concerning the environment. Uniform or generalized corrosion occurs at the same speed at all points of the metal, leading to a regular decrease in the thickness of the metal. or simply a color change (tarnishing). the

same speed at all points of the metal, leading to a regular decrease in the thickness of the metal. or simply a color change (tarnishing). In this way, there are different classifications for the types of corrosion.

II. 2. Localized corrosion

The phenomenon occurs, on the contrary, when the material is put in the presence of an environment exhibiting selective behavior towards it (***Figure. I. 17***). This selectivity can have multiple origins both at the level of the material (hetero-phasic alloy, presence inclusions, locally defective surface protection, bimetallic material, etc.) and in the environment (a local variation of the composition, pH, or temperature)[65].

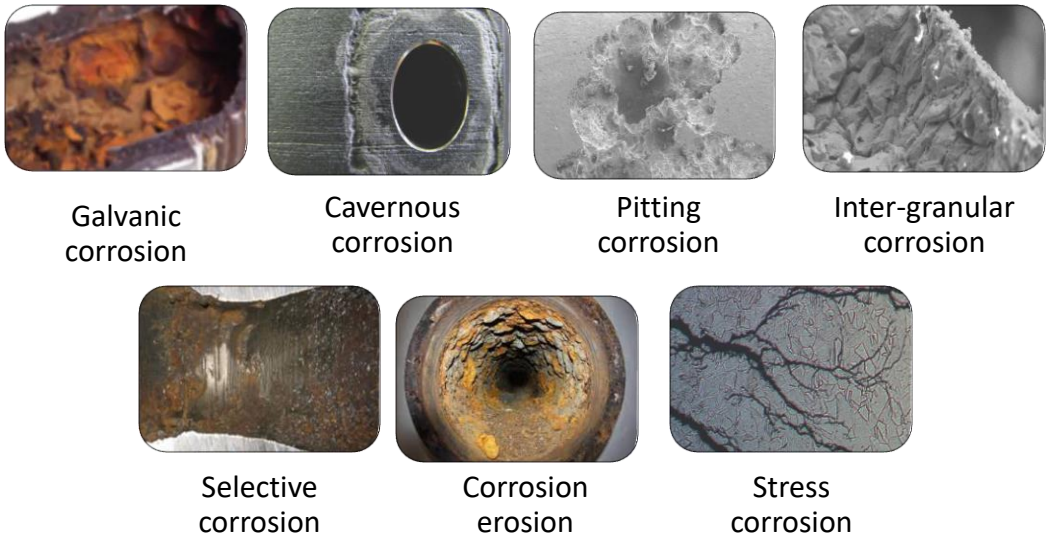

Figure. I. 17:Localized corrosion.

This form of corrosion occurs at some point on the surface of a material, and we distinguish several types of localized corrosion, which we can schematize as follows ***Figure. I. 18***:

Figure. I. 18: Macroscopic and microscopic forms of localized corrosion .

In our work, we were interested in the electrochemical corrosion of metals.

The prevention of corrosion of metals can be considered in different ways, the three most important ones being the following:

- Practical applications of coatings
- Use of passivizable alloys,
- Protection by inhibition

II.5. Corrosion factors

The nature and degree of corrosion depend on the metal and the environment. The main factors that can influence the corrosion process are as follows ***Table I. 4***:

Table I. 4: The main factors that can influence the corrosion process

The corrosive environment:	**Nature of metal:**	**Conditions of use:**	**Time index:**
• Reactant concentration; • Oxygen content; • PH of the medium; • temperature; • Impurities; • Pressure.	• the material composition of the metal or alloy; • process of elaboration; • Heat treatments; • Protective additions; • impurities.	Surface conditions; • Means of protection; • The shape of parts; • Use of inhibitor; • Mechanical stresses; • Assembly processes (welding, brazing, etc.)	• Metals not subject to ageing; • Mechanical stresses; • Modification of protective coatings.

II.6. Fight against the corrosion

The economic cost caused by the annual degradation of materials has provoked the implementation of protection methods. These methods aim to save material and energy, to which many constraints are added, notably non-pollution. Any effective and sustainable solution can only be a compromise considering all these factors, including economic and scientific constraints. In terms of corrosion protection, it is possible to act on the material itself (judicious choice, adapted shape, etc.).

In terms of corrosion protection, it is possible to act on the material itself (Judicious choice, adapted shape, constraints according to the applications,), on the surface of the material (Coating, painting, any type of surface treatment, ...) or on the environment with which the material is in contact (corrosion inhibitor).

The considerable reduction of the aggressiveness of the environment, by adding inhibitors, has a wide industrial application, in particular in the pickling and descaling industry, oil well stimulation and closed circuits. It is an easy and often cost-effective process. However, improper application conditions can lead to dangerous consequences.

II.6.1 Corrosion Inhibitors

II.6.1.1 Definition

An inhibitor of corrosion must lower the metal's rate of corrosion while preserving its physicochemical properties. Corrosion of metal is decreased, slowed down, or stopped when small amounts of corrosion inhibitors are added to the environment where it would typically corrode.

Furthermore, a corrosion inhibitor must reduce the corrosion rate of the metal while maintaining its physicochemical characteristics. It must not only be stable in the presence of the other constituents of the medium but also not influence the stability of the species contained in this medium. It is recognized as such if it is stable at the temperature of use and effective at a low concentration[66].

II.6.2. Current industrial applications

Theoretically, inhibitors can be used in most cases of corrosion (with, as major limitations, a too large volume of the corrosive medium or the impossibility of incorporating additives). traditional fields of application:

- The treatment of water treatment (sanitary water, industrial process water, boiler water, etc.);
- The petroleum industry includes drilling, extraction, refining, storage, and transportation. The use of corrosion inhibitors is essential for the protection of installations at all stages of this industry;
- The temporary protection of metals, whether during acid pickling, cleaning of installations, or storage in the atmosphere (volatile inhibitors, incorporation into temporary protection oils and greases) or for the treatment of cutting oils;
- In the metal painting industry, where inhibitors are additives that ensure the anti-corrosion protection of metals.

II.6.3. The classes of inhibitors

The inhibitors can be classified in several ways as played in ***Figure.I. 19***:

- classification according to the nature of the molecules of the inhibitor
- Mechanisms of electrochemical action,
- By reaction mechanism,

- According to the field of application.

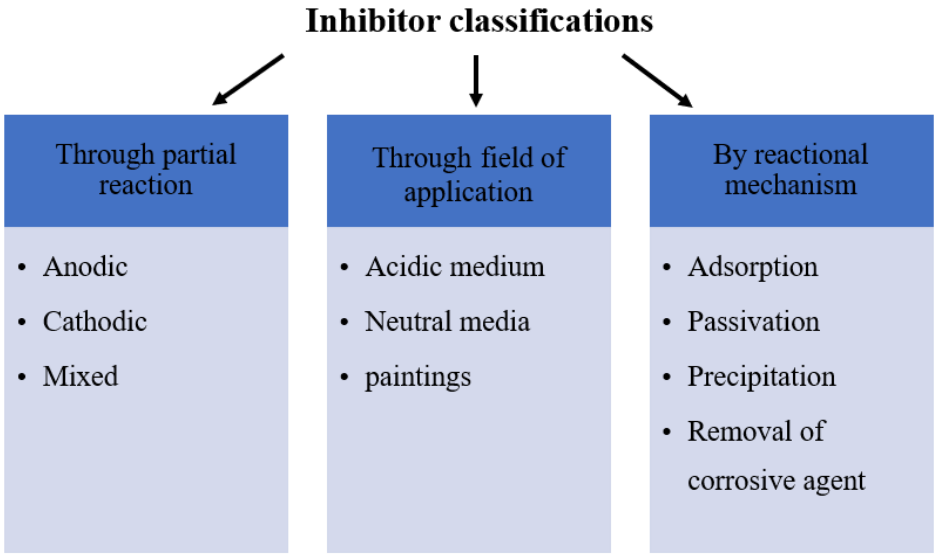

Figure.I. 19:Inhibitor classifications

a) Classifications based on the nature of the inhibitor's molecules

a-1) The inorganic inhibitors

Inorganic molecules are most often used in a near-neutral environment, or even in an alkaline environment, and more rarely in an acidic medium. The products dissociate in solution and it is their dissociation products that ensure the inhibition phenomena (anions or cations). The most important inhibiting cations are Ca^{2+} and Zn^{2+} and those that form insoluble salts with certain anions such as hydroxyl OH^-. The principal inhibiting anions are the oxo-anions of type XO_4^{n-} such as chromates, molybdates, phosphates molybdates, phosphates, and silicates[67].

The number of molecules now employed is more and more restricted because most of the useful goods have a detrimental side to the environment[68]. Nevertheless, novel organic complexes of chromium III and other cations (Zn^{2+}, Ca^{2+}, Mg^{2+} new organic complexes of chromium III and other cations (Zn^{2+}, Ca^{2+}, $Mg^{2+,}$ Mn^{2+}, Sr^{2+}, Al^{3+}, $Zr^{2+,}$ $Fe^{2+,}$...) effective against corrosion and non-toxic have been developed [69].

a-2) The organic inhibitors

Organic molecules are more than likely to develop in terms of corrosion inhibitors; their use is currently preferred to that of inorganic inhibitors for reasons of eco-toxicity in particular. They possess

at least one active centre that can exchange electrons with the metal, such as nitrogen, oxygen, phosphorus, or sulfur. The usual functional groups, allowing their fixation on the metal, are amine (NH_2), mercapto (-SH), hydroxyl (-OH), and carboxyl (-COOH). The inhibitory action of these organic compounds, which is generally independent of anodic and cathodic corrosion processes, is related to the formation by adsorption of a more or less continuous more or less continuous barrier but of fine thickness, which prevents the access of the solution to the metal [70].

b) Mechanisms of electrochemical action:

Three different types of inhibitors can be distinguished according to their effect on the rate of partial electrochemical reactions:

- Anodic inhibitors,
- Cathodic inhibitors,
- Mixed inhibitors.

b-1) The anodic inhibitors

Anodic inhibitors are numerous. Their mode of action is to decrease the anodic partial current density and shift the corrosion potential in the positive direction. However, while anodic inhibitors are very effective and often used, they generally have an undesirable property: if the inhibitor content is progressively lowered, the metal surface is no longer completely covered, and it functions as an anode, thus promoting a dangerous combination. A small anode and a large cathode lead to pitting corrosion. In such a case, the inhibitor does more harm than good. For this reason, it is frequently referred to as dangerous.

b-2) The cathodic inhibitors

These inhibitors work by reducing the solvent reduction current density and shifting the corrosion potential in the opposite direction. Because they are less likely to encourage localized corrosion due to their mode of action than anodic inhibitors, cathodic inhibitors are thought to be safer. They are typically cations that can migrate to the cathodic surface, where they can precipitate as basic salts or hydroxides to form compact, adherent films.

b-3) Mixed inhibitors:

The mixed inhibitors reduce the rate of both partial reactions by slightly changing the corrosion potential. They possess both the properties of anodic and cathodic inhibitors.

c) According to the field of application

c-1) In the aqueous environment

An electrochemical attack on the steel during pickling or descaling is one of the uses for the inhibitors for acid media. Additionally, neutral or alkaline media inhibitors are frequently used to safeguard the pipes in cooling circuits.

c-2) In the organic medium

The corrosion inhibitors are used in large quantities in engine lubricants, gasoline, and paints, such as inorganic pigments or tannins. They often contain traces of water and ionic species that can cause corrosion.

c-3) Gas phase inhibitors

These inhibitors are generally used for the temporary protection of various packaged objects during transport and storage (precision instruments, components, machines, etc.). They are usually high-pressure organic compounds, including some amines.

d) Based on their interfacial mode of action

d-1) Inhibitor molecule absorption on the metal surface

Ordinarily, organic inhibitors are those that act by adsorption. Due to the absence of an oxide layer on the steel's surface in this instance, this type of inhibitor is typical of acidic environments. By physisorption or chemisorption, which involve electrostatic bonds in the first case and covalent bonds in the second, the inhibitor is directly adsorbed onto the metal surface. As a result, the inhibitor forms a mono- or multilocular layer on the surface of the steel that serves as a defense against aggressive species[71].

d-2) Passivation inhibitors

Passivation inhibitors are normally mineral ones. They provoke the spontaneous passivation of the metal by reinforcing the oxide layer naturally formed on the metal surface. Therefore, they reduce the pores of the more or less protective oxide/hydroxide layer that simply forms on the metal surface. Although chromate ion is one of the best passive inhibitors, its carcinogenicity and high toxicity considerably reduce its use[72].

II 6.4. Factors affecting the inhibitor adsorption

To better comprehend the mechanism of inhibition of these substances, it is crucial to be aware of the variables that affect the phenomenon of the adsorption of inhibitors.

II.6.4.1 Adsorption type

The adsorption of organic compounds can be explained by two primary types of interaction: physical adsorption and chemisorption. Thus, the nature of the metal charge, the chemical composition of the organic product, and the type of electrolyte all have an impact on these two types of adsorption[73].

a) Physical adsorption (physisorption)

Physical adsorption involves weak bonds. The identity of the molecules that are adsorbed is preserved in this type of adsorption. Three types of forces are to be distinguished[74]:

- Although always present, the dispersion forces (Van der Waals, London) are insufficiently energetic to provide sufficient attachment to the metal surface.
- The polar forces brought about by an electric field
- Amino or hydroxyl groups are responsible for the hydrogen bonds.

These traits describe physisorption :

- The absence of direct contact between the inhibitor and the metal surface.
- The inhibitor-metal bond is assured through electrostatic interaction between the inhibitor's active sites and the surface of the electrically charged metal.
- Because of the low activation energy of the process, it is independent of temperature.
- Adsorption only depends on the charge that the metal is carrying; it is not type-dependent.

An electrostatic force exists between a positively or negatively charged metal and ions in a solution produced by the protonation or dissociation of organic inhibitors. The electric flow field present at the metal-solution interface is what causes the metal to produce a surface charge. Therefore, it depends on where the corrosion potential (E_{corr}) of the precious metal is concerning the metal's E_{PCN} zero charge potential.

- In the case where φ (φ = E_{corr}-E_{PCN}) is positive, the metal is positively charged, and anions adsorb;
- in the case where φ (φ E_{corr}-E_{PCN}) is negative, the metal is negatively charged, and cations adsorb.

b) Chemical adsorption (chemisorption)

Chemisorption consists of the pooling of electrons between the polar part of the molecule and the metal surface; this leads to the formation of much more stable chemical bonds based on higher bond energies.

The bulk of electrons come from the unpaired doublets of inhibitor molecules such as O, N, S, and P (all these atoms are distinguished from others by their high electronegativity). Chemical adsorption is accompanied by a profound modification of the distribution of electronic charges of the adsorbed molecules. Chemisorption is often an irreversible mechanism[75].

II.6.5 Molecular structure of the inhibitors

There are a very large group of organic substances available as inhibitors in corrosive media, including aromatic molecules and macromolecules with linear or branched chains; Their effectiveness is dependent, in addition, to their molecular structure and concentration (***Figure. I. 20)***[76].

The organic molecules used as inhibitors contain a non-polar, hydrophobic, and relatively bulky portion. A hydrophobic and relatively voluminous part composed primarily of carbon and hydrogen atoms, and a polar, hydrophilic part composed of one or more functional groups such as -NH_2 (amine), -SH (mercapto), -OH (hydroxyl), and so on. The molecule binds to the surface via its functional group, while its non-polar, more voluminous part partially blocks the active surface.

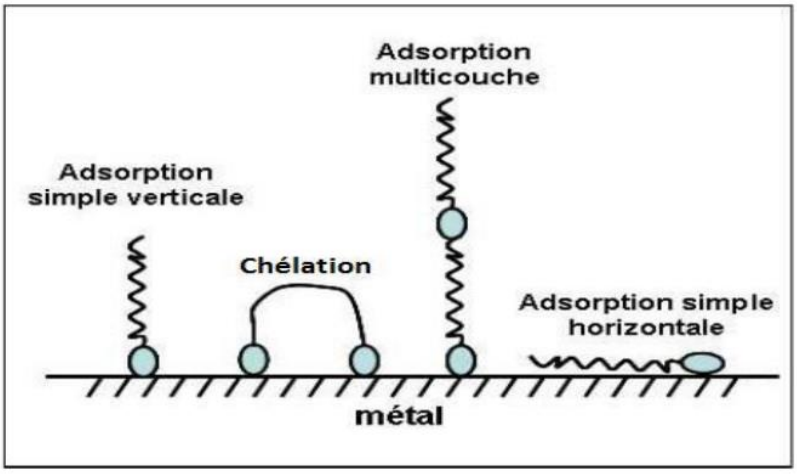

Figure. I. 20:The adsorption modes of inhibiting organic molecules on a metal surface are depicted schematically.

II.6.6 The Effect of Electron Density Inhibition

The process of inhibition under an acidic environment tends to involve the chemisorption of the inhibitor. The more likely the functional atoms are to create bonds with the metal by donating electrons, the more effective the inhibitors are. The efficacy of inhibition decreases inversely with the electronegativity of those functional atoms in a sequence of organic compounds that differ solely in their functional atoms [77].

Therefore, it increases in the following order:

$$O < N < S < Se < P$$

Unsaturated organic compounds (those with double or triple bonds) are electron carriers and can form bonds with metal atoms. These bonds will be associated with a positively charged metal surface if possible. The presence of an unsaturated bond can thus be very favorable to the inhibitory efficiency of an organic molecule or an electronic molecule in an acidic environment.

II.6.7 The effect of concentration

An adsorption isotherm expresses the relationship between the rate of coverage of an interface by the adsorbed species and the concentration of the species in the solution. The interface formed by the adsorbed species and the species concentration in solution The Langmuir and Temkin isotherms is the most commonly used models of adsorption isotherms. We will give a brief description of these isotherms and explain the conditions required for their validity in each case. There are several models of adsorption isotherms, of which two models are the most commonly used. There are several models of adsorption isotherms, of which two models are the most commonly used: the Langmuir isotherm

and the Temkin isotherm. We will give a brief description of these isotherms and explain the conditions necessary for their validity in each case.

a) Langmuir isotherm

The Langmuir isotherm assumes that the inhibitor causes capping of the coated surface θ by an adsorption monolayer and that the uncoated fraction (1- θ) reacts with the acid as if there is no inhibitor. The Langmuir equation links the ratio (θ / 1-θ) to the concentration :

The adsorption rate is proportional to the C_{inh} inhibitor concentration and the fraction of unoccupied adsorption sites (1-θ):

$$\mathbf{V_{ads} = K_{ads} (1-\theta) C_{inh}} \qquad \mathbf{(2)}$$

In contrast, the desorption rate is proportional to the fraction of sites occupied by the adsorbed gas:

$$\mathbf{V_{ads} = K_{ads}\theta} \qquad \mathbf{(3)}$$

At equilibrium: A l'équilibre : $\mathbf{K_{ads} (1-\theta) C_{inh}\theta}$ **(4)**

According to Langmuir, the surface coverage rate θ with (0< θ<1 is related to the inhibitor concentration **C** by the following relationship:

$$\mathbf{\theta / (1-\theta) = KC_{inh}} \qquad \mathbf{(5)}$$

This gives: $\mathbf{C_{inh}/ \theta = 1/K + C_{inh}}$ **(6)**

K = K_{ads}/K_{des}, where **K** is the adsorption coefficient or equilibrium constant of the adsorption process.

b) Temkin Isotherm

The adsorbate's adsorption-free energy is a linear function of the lapse rate θ, while the chemical rate constants are functions of θ. There is attraction or repulsion between species that have become adsorbent on the surface.

The recovery rate is determined by :

$$\mathbf{\theta = \frac{1}{f} \ln K_{ads} C_{inh} f} \qquad \mathbf{(7)}$$

With:

f: is a parameter in the adsorbed layer that accounts for surface heterogeneity and intermolecular interactions.

Cinch: the concentration of the inhibitor in the solution;

K_{ads}: is the adsorption process's equilibrium constant, which is related to the standard free enthalpy of adsorption **ΔG_{ads}**.

$$K_{ads}=\frac{1}{55.5}\exp\left(\frac{\Delta G_{ads}}{RT}\right) \qquad (8)$$

R: is the perfect gas constant, and T is the absolute temperature.

The value 55.5 represents the mole per liter concentration of water in the solution.

c) Frumkin Isotherm

The following relation can be used to express this type of isotherm[78]:

$$\frac{\theta}{1-\theta}\exp(-2a\theta) = kC \qquad (9)$$

a: A particle-adsorbed interaction constant

K is the adsorption coefficient.

C: The concentration of the inhibitor

II.6.8 Temperature effect

The effect of temperature on the effectiveness of inhibitors, particularly in acidic environments, has been the subject of several articles, particularly during high-temperature pickling and descaling and for removing corrosion products from metal installations. Inhibitors protect cells from acid attacks.

The Arrhenius-type dependence observed between corrosion current and temperature in these studies enables us to calculate the value of the activation energy:

$$V_{corr} = A\exp\left(\frac{-E_a}{RT}\right) \qquad (10)$$

With :
Ea: the activation energy.
A: a constant.
R: the constant of perfect gases.
T: the absolute temperature.
Vcorr: the corrosion rate.
Radovisi suggests categorizing inhibitors based on temperature action. We divide them into three categories:

- The inhibitors that **Eai ≥ Ea** adsorb on the substrate via electrostatic bonds (weak bonds). This type of bond is temperature sensitive and does not allow you to fight corrosion effectively as the temperature rises(physisorption).
- The inhibitors for which **Eai ≤Ea** has a temperature-dependent increase in protective power. The organic molecules of the inhibitor adsorb to the metal surface by strong bonds (chemisorption).
- The inhibitors where **Eai = Ea.** This category contains very few compounds and does not exhibit an evolution of protective power with temperature.

a) Adsorption of free energy

The free energy of adsorption can be estimated, knowing the value of the equilibrium constant determined from the equation of the corresponding isotherm, by the following formula :

$$\Delta G^{\circ}_{ads} = - RT\, Ln\, (C_{H2O}.\, K_{ads}) \qquad (11)$$

The values R, C_{H2O}, and T stand for universal gas constant, the pure water concentration in the solution, and temperature (°K) (R = 8.314 J mol^{-1} K^{-1} and $C_{H2O} = 10^3$ $g.L^{-1}$), respectively.

Negative ΔG°_{ads} values reflect the adsorption process's spontaneity and the adsorbed layer on the metal surface.

b) The enthalpy ΔHa and entropy ΔSa

The enthalpy and entropy of activation can be calculated using the following equation, using an alternative form of the Arrhenius equation:

$$I_{corr} = A \exp\left(\frac{-E_a}{RT}\right) \qquad (12)$$

From the Arrhenius equation (12) one can determine the activation energy (Ea) by plotting different values of ln (icorr) as a function of 1/T;

With Ea, the assumed activation energy of the corrosion process, R is the universal gas constant, T is the absolute temperature, and (A) is the pre-exponential Arrhenius factor.

$$I_{corr} = \frac{R \times T}{N \times h} \times exp\left(\frac{\Delta S_a}{R}\right) exp\left(\frac{-\Delta H_a}{R \times T}\right) \qquad (13)$$

Whereby Na Avogrado number, h Plank constant, ΔHa, ΔSa are the activation enthalpy, and activation entropy, respectively. A straight line is given by ln (Icorr)/T as a function of (1/T). Its slope is (-ΔHa / R), and its intersection with the ln (Icorr)/T axis gives the parameter ΔSa.

II.7. Biodiesel fuel-compatible materials

Materials suitable for biodiesel fuel have evolved over the years, introducing many more complex materials and alloys that have proven to be well-suited to improving engine performance and durability. Therefore, research on biodiesel compatibility with common internal combustion engine materials is essential[79]. Due to the autoxidation, or instability of biodiesel, in the presence of moisture in the operating environment. In addition, the amount of fuel that comes into contact with engine components varies with temperature, speed, load, and pressure. As a result, different engine parts and components in contact with biodiesel have different rates of corrosion, leading to problems such as metal thinning, sediment, and corrosion product formation, clogging of filters and injection pumps, and reduced durability and life of the engine[80]. The biodiesel fuel properties and composition may also be out of specification or degraded.

In general, various materials are found to exhibit different reactions in terms of corrosive characteristics, which behave differently in terms of corrosive nature and wear deterioration when in contact with fuel. These materials can be divided into metallic and non-metallic, as illustrated in **Figure.I. 21**[81]. It is equally essential to correctly determine the most compatible biodiesel blends that are capable of giving excellent corrosion properties by reducing metal loss and preventing degradation of biodiesel fuels when in contact with the respective metals.

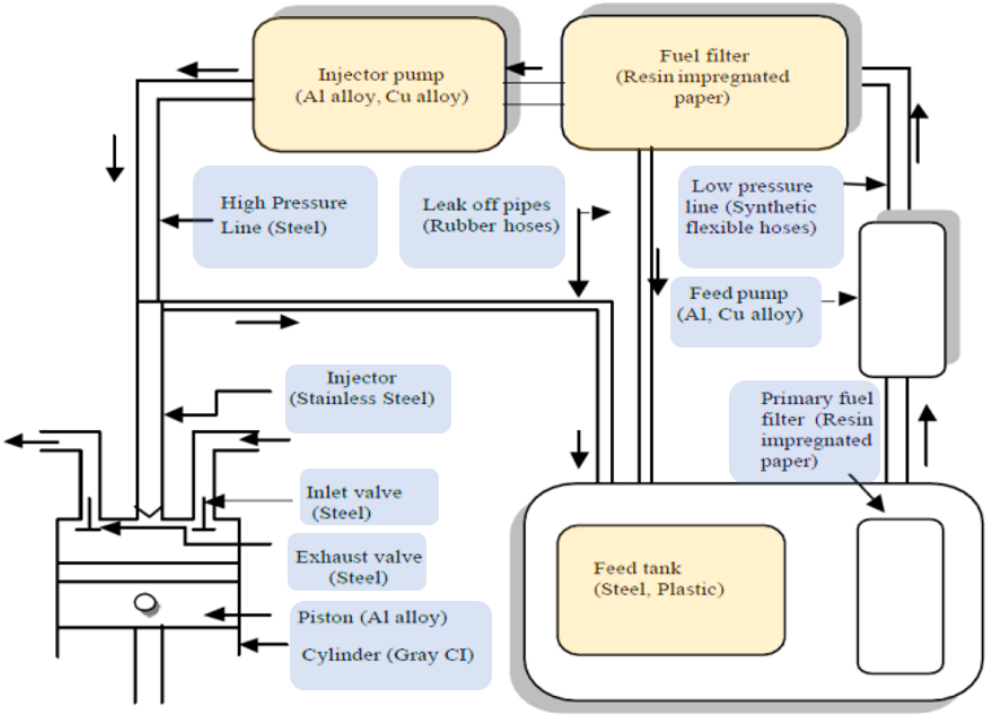

Figure.I. 21: Used material for the fabrication of parts in diesel engines.

II.8. Corrosion Mechanism in Biodiesel

Although the types of corrosion listed above are varied, the primary causes of metal corrosion in a biodiesel environment are thought to have the following origin: an electrochemical nature[82].

Corrosion can occur when a metal surface comes into contact with biodiesel. The oxidation stability of renewable fuel is functionally related to the susceptibility of biodiesel to corrosion[83]. Residues presented in biodiesel, including glycerol, unsaturated fatty acids, or metals, can cause oxidation instability due to inadequate processing[84].***Figure.I. 22*** illustrate Initiation, propagation, and termination are the three steps involved in the oxidation process of biodiesel (autoxidation) to form peroxides.

The peroxides are decomposed in a variety of different ways to produce secondary oxidized products, including acids, aldehydes, dimers, and several other polymer products.

The first stage of biodiesel oxidation is the initiation stage. In the initiation stage, the unsaturated fatty acid chains of a new carbon-based fatty acid radical, R*, form the reaction between the initiator radical, I*, and the unsaturated fatty acid chain. The presence of an initiator radical I* most likely comes from the catalyst used in the transesterification process. The second step in the oxidation of biodiesel is the propagation step. In the propagation step, there are two steps involved in this step. First, the fatty acid

radicals, R*, form the unstable fatty acid peroxide radical, ROO*, from the reaction with oxygen molecules. In the second step, the unstable fatty acid peroxide radical, ROO*, forms the fatty acid hydroperoxide or allylic hydroperoxide, ROOH*, and the new allyl radical, Rn+1*, from the reaction with the original unsaturated fatty acid chain. The previous step in the oxidation of biodiesel is the termination step. In the termination step, stable polymer chains are produced from the reaction of the two radicals. The end product of this step consists of non-radical substances like alcohols, ketones, esters, organic acids, etc. The increase in acid number due to the oxidation process can increase the corrosive property of the biodiesel.

The water and fatty acid content in biodiesel typically remain the principal causes of corrosion in biodiesel. Also, during the transesterification process, many contaminants are present in biodiesel.
Due to its hygroscopic properties, however, water molecules are typically attracted to the FAME chains in biodiesel during the hydrolysis process. Over time, the water accumulates and forms a thin layer that sinks to the bottom of the fuel storage tank. The water acts as an electrolyte, while the metals act as an anode and a cathode.
The corrosion between the metal and the water is illustrated in:

- **Reaction at anode:** $M \rightarrow M^{n+} + ne$ **(14)**
- **Reaction at cathode:** $O_2 + 2H_2O + 4e \rightarrow 4OH^-$ **(15)**

  $2H_2O + 2e \rightarrow H_2 + 2OH^-$

When a metal is brought into contact with an aggressive solution, the following behaviors may occur:

- corrosion of metal.
- immunity of metal.
- The passivity of metal.
- coating of metal by a mineral compound.

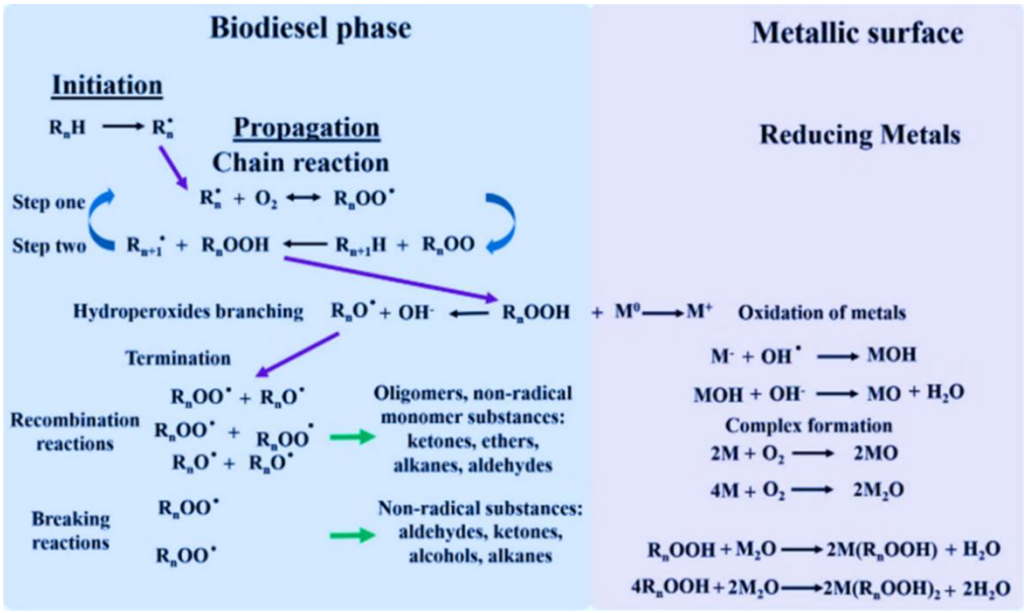

Figure.I. 22:Detailed mechanism and step involved in the oxidation process of biodiesel.

III. Molecular Modelling by DFT and MDS

III.1 Introduction

The advancement of computer tools has resulted in a significant increase in the number of theoretical studies, as well as the emergence of numerous applications. There have been a lot of numerical calculations on systems with increasingly more atoms over the past 30 years. Even though the systems being studied are becoming more complex and voluminous, it is crucial to establish relationships between experimental data and theoretical calculation results.

Furthermore, Copper (Cu), aluminum (Al), and iron (Fe) corrosion can be reduced by changing their surfaces with organic/inorganic corrosion inhibitors[85]. These inhibitor molecules adsorb on the metal surface and form a corrosion-resistant layer. The degree of interaction between the inhibitor molecules and the metal surface determines how well an inhibitor can prevent corrosion. Adsorbed inhibitor molecules alter the cathodic and anodic corrosion reactions, or they physically block the active sites that are present on the metal surface or in the solution, to modify the corrosion process[86,87].

However, the use of theoretical studies, such as density functional theory (DFT) and molecular dynamics (MD) simulation, has recently become more common. Therefore, a review of the literature demonstrates that there is a substantial body of literature in which experimental work has been performed to understand the process of the corrosion mechanism[88].

This chapter will primarily focus on stating the chosen methods, namely density functional theory and molecular dynamics simulation. The remainder of the tools used in the various theoretical chemistry approximations will allow comparison of the use of the different theoretical chemistry methods, their limits, and the fields of their applications;

III.2 Modeling Method

III.2.1 Density Functional Theory approach (DFT)

Quantum electrochemistry is a field that includes quantum mechanics, electrochemistry, and electrodynamics. In general, quantum electrochemistry is an application of density functional theory (DFT) to study electrochemical processes such as electron transfer to electrode surfaces.

Density functional theory (DFT) is a methodology that is similar to Hartree-Fock's theory in that it attempts to provide a solution to the electronic state of a molecule directly from the electronic density.

In terms of basic functions using orbitals and the use of the vibrational principle to locate the lowest energy wave function, it can be seen that the methods are not essentially analogous for this discussion. However, the primary difference is the inclusion of terms to account for both exchange and correlation when evaluating the energy of the wave function, which results in a much better description of the electronic structure.

III.2.2 Fundamentals of quantum computing

One of the most important equations in physics and quantum mechanics is the Schrödinger equation (14). Its resolution allows one to describe a many-body system (the nucleus and electron) and obtain all the information about the electronic structure of the system. However, this resolution is only available in the case of hydrogen. For systems with more than two particles, the solution of the Schrödinger equation is required[89].

$$\ddot{H}\Psi = E\Psi \qquad (16)$$

where is :

Ḧ:corresponds to the Hamiltonian operator which governs the motions of the nuclei and electrons of the system under study.

Ψ: is the wave function of the system, the function of the coordinates of the nuclei, electrons and contains all the information of the system,

E: is the total energy.

The general form of the Hamiltonian operator in the molecular context considers five contributions to the total energy of the system: the kinetic energy of the electrons and nuclei, the attraction energy between the electron and the nucleus, the attraction energy between the electron-electron, and the energy of repulsion between the nucleus -nucleus.

This Hamiltonian has the following general expression in mathematics **(17)**:

$$\ddot{H} = \sum_i \frac{1}{2}\Delta_i - \sum_i \frac{1}{2m_A}\Delta_A - \sum_{i,k} \frac{Z_A}{r_{iA}} + \sum_{i<j} \frac{1}{r_{ij}} + \sum_{A<B} \frac{Z_A Z_B}{r_{AB}}$$

Where:

i and **j** represent the electrons,

A and **B** represent the nuclei,

Δ_A the Laplacian operator applied to the particle **A,**

$\mathbf{m_A}$ and $\mathbf{Z_A}$ respectively the mass and the atomic number of the nucleus **A,**

$\mathbf{r_{AB}}$ is the distance between the particles **A** and **B**.

The first two terms in equation (15) are the operators for the kinetic energies of nuclei and electrons, the second and third terms are the operators for the energies of nucleus-nucleus and electron-nucleus repulsion, and the final term is the energy d electron-nucleus attraction.

A<B is intended to prevent duplicate counting of interaction terms in $\frac{1}{r_{ij}}$ Where $\frac{1}{r_{AB}}$.

The Schrödinger equation is an eigenvalue equation with an infinite number of solutions that are challenging to apply to polyatomic molecules. To do this, we must employ approximations such as the Born-Oppenheimer approximation.

III.2.3 Approximation de Born-Oppenheimer

Since the Hamiltonian operator defined in equation (15) renders it very complicated to solve, Born and Oppenheimer proposed simplifying the determination by separating the electronic part from the nuclear part in the wave function. The Born-Oppenheimer Approximation[90]. The latter involves considering nuclei to be fixed due to their large mass and, as a result, slower speed when compared to electrons. The kinetic energy of the nuclei is considered negligible in this approximation, and the nucleus-nucleus interaction term is assumed to be constant.

$$\ddot{H}_{el}\Psi_{el} = E_{el}\Psi_{el} \qquad (18)$$

$$\ddot{H}_{el} = -\sum_i^n \frac{1}{2m_i}\nabla_i^2 \; - \sum_I^N \sum_i^n \frac{Z_i}{r_{Ii}} + \sum_{j>i}^i \frac{1}{r_{ij}} + cte \qquad (19)$$

Based on this simplification, several methods have been developed to solve the Schrödinger equation. Which consists in describing the wave function Ψ_{el} as a Slater determinant. The DFT is an alternative method proposing electron density as a basic quantity of calculations in replacement of the wave function.

III.2.4 Hohenberg-Kohn theorem

The Thomas-Ferm model is the foundation of the DFT method[91]. Even though this model has simplified the quantum approach by reducing the number of variables to three from the traditional 3n (n being the number of electrons in the system) with the approach, due to the inaccurate approximation

of the kinetic energy, a theory proposed in 1927 used the electron density function to determine the properties of the fundamental state of a system made up of electrons interacting with fixed nuclei.

III.2.4.1 first Hohenberg-Kohn theorem

Based on the famous Hohenberg-Kohn theorem, they typically received the Nobel Prize in Physics in 1964 for their work on DFT[92]. Thus, Hohneberg and Kohn proposed a first theorem stating that the electron density ρ(r) is sufficient to define all the properties of a system in its ground state. Moreover, a second theorem showed that the ground state energy could be calculated by involving the variational principle in the electron density[93]. The total ground state energy of an N-electron system is expressed in DFT by the potential external v(r) and the three-dimensional electronic density ρ(r) in the ground state in the form that the system's ground state energy obtains the value that minimizes it E[(r)].

$$E[\rho(r)] = F_{HK}[\rho(r)] + \int \rho(r) v_{ext}(r) d^3r \qquad (20)$$

Where :

$$F_{HK}\,\rho(r)] = T[\,\rho(r)\,] + V_{ext}[\,\rho(r)\,] \qquad (21)$$

F_{HK}[(r)] is the universal function that is independent of the systems under consideration and contains all of the system's electronic contributions, and $v_{ext}(r)$ is the nuclei's external potential. The understanding of **T[r]** facilitates all molecular systems but the precise form of this function is at the moment far from being known and known and it is necessary to resort to approximations.

III.2.4.2 Second Hohenberg-Kohn Theorem:

The declaration of the second theorem is as follows: "For a test density ρ(r) such that ρ(r) ≥ 0 and The following inequality is true when = (r)dr n: ∫ρ = (r)dr n, the following inequality holds:

$$E_0 \leq E[\tilde{\rho}] \qquad (22)$$

The condition for a function like E_0 to admit an extremum is that its derivative cancels.
According to the definition:

$$\delta E = \int \frac{\delta E}{\delta \rho} d\rho dr \qquad (23)$$

The relationship $\delta E = 0$ is confirmed if and only if the following conditions are met:

$\frac{\delta E}{\delta \rho} = 0.$

The solution then consists of attempting to minimize E[ρ] while keeping the constraint in mind

$\int \tilde{\rho} \mathbf{dr} = \mathbf{n}$.

We thus obtain the fundamental equation of the DFT :

$$\boldsymbol{\mu} = \frac{\boldsymbol{\delta E}\,[\boldsymbol{\rho}]}{\boldsymbol{\delta \rho}} = \boldsymbol{v}(\boldsymbol{r}) + \frac{\boldsymbol{\delta F_{HF}}\,[\boldsymbol{\rho}]}{\boldsymbol{\delta \rho}} \qquad (24)$$

where the quantity μ is called the "chemical potential" of the system. The approach allowing to take advantage of these two theorems in a satisfactory calculation method appeared in 1965: it is the SCF methodology of Walter Kohn and Lu Sham.

III.2.5 Kohn-Sham equations: Orbital approach

The first fundamental concept is to imagine a fictitious system of electrons with no interactions.
as the density of the ground state is the density of the real system with which the electrons interact
The functional E[(r)] is then divided into five contributions:(25)

$$\mathrm{E}\left[\rho(\mathrm{r})\right] = \mathrm{T}_{\mathrm{ni}}\left[\rho(\mathrm{r})\right] + \mathrm{V}_{\mathrm{ne}}\left[\rho(\mathrm{r})\right] + \mathrm{V}_{\mathrm{ee}}\left[\rho(\mathrm{r})\right] + \Delta\mathrm{T}\left[\rho(\mathrm{r})\right] + \Delta\mathrm{V}_{\mathrm{ee}}\left[\rho(\mathrm{r})\right] \quad \textbf{(25)}$$

T $[\rho(r)]$ is the electrons' kinetic energy without interactions, V_{ne} $[\rho(r)]$ is the electron-core attraction potential, V (r) $_{ee}[\rho(r)]$ is the classical electron-electron repulsion potential, and ΔT $[\rho(r)]$ is the correction.

ΔV (r) $_{ee}[\rho(r)]$ the set of nonclassical corrections for the electron-electron repulsion potential and the kinetic energy derived from the true electron interaction this function can be rewritten by expressing the density in terms of orbitals as follows :

$$\boldsymbol{E}[\boldsymbol{\rho}(\boldsymbol{r})] = \sum_{\boldsymbol{i}}^{\boldsymbol{N}} \langle \boldsymbol{\chi_i} \left| -\frac{\mathbf{1}}{\mathbf{2}} \Delta_{\boldsymbol{i}} \right| \boldsymbol{\chi_i} \rangle - \langle \boldsymbol{\chi_i} \left| \sum_{\boldsymbol{K}}^{\boldsymbol{M}} \frac{\boldsymbol{Z_K}}{\boldsymbol{r_i - r_k}} \right| \boldsymbol{\chi_i} \rangle + \sum_{\boldsymbol{i}}^{\boldsymbol{N}} \langle \boldsymbol{\chi_i} \left| \frac{\mathbf{1}}{\mathbf{2}} \int \frac{\boldsymbol{\rho(r)}}{\boldsymbol{r_i - r}} \boldsymbol{dr} \right| \boldsymbol{\chi_i} \rangle + \boldsymbol{E_{xc}}\,[\boldsymbol{\rho}(\boldsymbol{r})] \quad (26)$$

The density is expressed by a wave function of Slater determinant type, where N is the number of electrons and M is the number of nuclei.

$$\boldsymbol{\rho} = \sum_{\boldsymbol{i=1}}^{\boldsymbol{N}} \langle \boldsymbol{\chi_i} | \boldsymbol{\chi_i} \rangle \qquad (27)$$

The two terms ΔT $[\rho(r)]$ and $\Delta V_{ee}[\rho(r)]$ were combined into a single term called the exchange-correlation energy, $E_{xc}\,[\rho(r)]$.

The concept of considering a system of electrons without interactions allows the Hamiltonian to be expressed as a sum of monoelectronic Hamiltonians known as Kohn-Sham operators:

$\widehat{h}_i^{KS}$:

$$\widehat{h}_i^{KS} = -\frac{1}{2}\Delta_i - \sum_k^M \frac{Z_k}{r_i - r_k} + \int \frac{\rho(r')}{r_i - r'} dr' + V_{XC} \quad (28)$$

With: $V_{XC} = \frac{\delta E_{XC}}{\delta \rho}$

The χ orbitals that minimize the energy must satisfy the equations:

$$\widehat{h}_i^{KS} \chi_i = \varepsilon_i \chi_i \quad (29)$$

Given that the energy we minimize is precise, the orbitals must define the density. To find the associated coefficients for these orbitals χ, which are expressed as linear combinations of basis functions, one must solve the secular determinant, as in the case of the Hartree-Fock method.

Kohn and Sham have thus made DFT an effective tool for studying chemical systems. This formalism is currently used to perform the vast majority of DFT calculations. The following approximations, which will be briefly described, are within the Kohn-Sham formalism.

III.2.6 The exchange-correlations functionals

Until today, the DFT seems to be an exact method we need a formulation of Exc(), which requires an approximation, to make the DFT and Kohn-Sham equations applicable in practice; For the approximate definition of this term, there are two generations of functionals: the Local Density Approximations (LDA) and the Generalized Gradient Approximations (GGA)[94].

III.2.6.1 The Local Density Approximations (LDA)

LDA (Local Density Approximation); these functionals rely solely on the density at each point of the system, ignoring any influence of the system's electronic density inhomogeneity. They produce accurate results when the density varies slowly along the studied system.

The LDA method outperforms Hartree-Fock calculations in real-world applications[95]. We do observe that this approximation typically tends to underestimate activation barriers for chemical reactions, overestimate binding energies, and shorten bond lengths in molecules. The vibration frequencies, on the other hand, are generally in good agreement with the experiment.

The most common source of error in the LDA method is an underestimation of the exchange energy, whereas the correlation energy is frequently overestimated, even though its contribution to the total energy is smaller in absolute value.

III.2.6.2 Generalized Gradient Approximation (GGA)

Improved approximations to approximate the exchange-correlation function are required to increase the accuracy of DFT computations. Some authors devised a density function related to its derivatives to account for the system's inhomogeneity[96].

With the inclusion of information on the spatial variation of electron density in the GGA, it is now possible to describe real-world materials with more flexibility. The GGA, on the other hand, does not allow for the representation of the properties of strongly correlated material systems, such as magnetic systems and transition metals. Furthermore, delocalized and localized orbitals with significant on-site Coulombic interactions are addressed with an extra component, the "Hubbard U parameter," which improves the AGG's accuracy. Although neither technique transfers the Hubbard U-parameter from one to the other[97].

III.2.6.3 Hybrid Functional

Kohn and Sham mentioned the potential value of an exact treatment of exchange when they proposed their approach in 1965. They had developed a formal expression for the exchange-correlation energy based on the Hartree-Fock approximation for exchange, with the correlation term unchanged from the LDA. Similarly, they discovered that by employing this hybrid function, the effective potential would exhibit the correct asymptotic behavior (in 1/r) when positioned at a distance from the atom. Although this concept is effective for the treatment of atoms, the results for molecules were disappointing. In most cases, the GGA functions were more accurate and had higher precision. Furthermore, the error is due to the artificial separation of the exchange-correlation terms since the nonlocal combination exchange hole (Hartree-Fock) with a local correlation hole (LDA) ignores the self-consistency of the local hole description[98].

III.2.6.4 The functional basis of DFT

The function is a function of another function, the electron. In light of this, various functions have been developed and are listed *in* ***Table I .5*** based on fundamental quantum mechanics and experimental findings[99].

The generations of functional density are numerous. The first generation, referred to as the "X" method, is the simplest. J.C. Slater created this function while working on the Hartree-Fock approximation, but he found the simplest one for the DFT by accident[100]. The X_α function included electron exchange but no correlation. The results obtained by the X_α method are as accurate as those obtained by the HF method, but in some cases, they are better.

The second-generation functional map takes advantage of both the density and its gradients. The first gradient-corrected energy function was proposed in 1986. Becke, Perdew[101], and Wang proposed the Perdew exchange and correlation[102,103].

The third generation is a hybrid functional and is more advanced than the GGA. In this case, the function consists of both a Hartree-Fock exchange and a DFT exchange computed from the orbitals. In 1998, a hybrid function called the B3LYP function was introduced[104].

Table I .5: List of density functional:

ACRONYMS	NAME	TYPE
XA	X alpha	Exchange only
HFS	Hartree -Fock Slater	HF with LDA exchange
VWN	VWN Vosko, Wilks, and Nusair	LDA
BLYP	Becke 3 term with Lee, Yang, and Parr	Hybrid exchange
PW91	Perdew and Wang 1991	Gradient-corrected
G96	Gill 1996	Exchange
B96	Becke 1996	Gradient-corrected
P86	Perdew 1986	Gradient-corrected
B3P86	Becke exchange, Perdew correlation	Hybrid
B3PW91	Becke exchange, Perdew and Wang	Hybrid correlation

III.2.6.5 The basis sets

Different basis sets are employed in the DFT computation[105]. STO-3G is the most basic. Three Gaussians provide 1s in this basis set, and three others provide 2s, 2px, 2py, and 2pz. The basis set can be improved by introducing two 1s functions for hydrogen two 2s functions and two 2p functions for

second-row elements such as carbon. These are known as split valence basis sets. The valence and core orbitals are represented by two function sets and a single function set, respectively[106]. Here's an example:

- **3-21G**: has three Gaussians for the 1s combination, the same two Gaussians for the 2s and 2p combinations, and the same Gaussian for the 2s' and 2p' combinations.
- **6-31G:** six gaussian for the 1s combination, three gaussian for the 2s and 2p combination, plus 2s' and 2p' the same gaussian.
- **6-311G:** This basis set consists of three sets of valence functions, each of which has three, one, and one Gaussians, and six Gaussians.

The fundamental difference between multiple valences and split valence basis sets is that in the former, all orbitals are typically divided into two, three, and so on specific sets of functions. With various basis sets, different coefficients were applied to the s and p orbitals[107]. Therefore, by including functions that correspond to the orbitals with higher angular momentum, the calculation of the electronic structure can be improved.

This is outlined as follows: P-functions are added to the hydrogen atom; d-functions are added to carbon, nitrogen, oxygen, etc.; and f-functions are introduced for the transition metals[108]. These functions are illustrated by an asterisk added to the base set and the p, d, and f functions specified. The following example illustrates this:

- **6-31G or 6-31G (d):** Add d functions to the second row's components (C, N, O, and so on).
- **6.31G or 6-31G (d, p):** Apply the d function to the second line's elements (C, N, O, and so on) and the p function to H.

The single pair of electrons on the heteroatoms can be confused by merging scattering functions and adding diffuse functions, which are represented in the basic set by the + and ++ signs. The polarization and diffuse functions are significant for other atoms like carbon, nitrogen, and oxygen, but not so much for the hydrogen atom[109]. As an illustration:

- **6-31+G** denotes the addition of diffuse functions to the elements of the second row (C, N, O, etc.).
- **6–31++G:** represents that diffuse functions have been added to the elements of the second row and H.

III.2.7 DFT chemical concepts and reactivity indices

III.2.7.1 FMO frontier molecular orbital theory

We can determine a molecule's electrical structure and forecast its shape according to its molecular orbitals (MOs). Understanding chemical reactivity is a further aim of OM theory. This refers to a molecule's capacity to change or interact with other molecules. However, it might occasionally be too difficult to make rapid generalizations when applying the whole mathematical argument to the OM theory. It's crucial to be able to create qualitative methods based on OM theory's core ideas that may be used without requiring laborious computations. A qualitative application of the OM theory is the analysis of the interactions of the orbitals of the governing molecules. As the molecules approach each other and the reaction progresses, there is a reciprocal disruption of the orbitals, which takes place until the reaction is complete and the new product is formed.

The frontier orbitals are two types of molecular orbitals (MO):

- the HOMO (an acronym for highest occupied molecular orbital), which is the highest energy molecular orbital occupied by at least one electron, and the HOMO (an acronym for highest occupied molecular orbital). The higher the energy of this MO, the more easily the molecule will give up electrons. The molecule will readily give up electrons.

  The value of EHOMO is expressed in eV and is directly related to the ionization potential I :

$$\mathbf{I=- E_{HOMO}} \quad (30)$$

- The LUMO orbital (an acronym for "lowest unoccupied molecular orbital") is the lowest energy orbital that is not occupied by an electron. It reflects the molecule's electro-acceptor (electrophilic) properties. The lower the energy of this OM, the easier it is for the molecule to accept electrons.

  E_{LUMO} also expressed in eV, is directly related to the electronic affinity of the molecule:

$$\mathbf{A=- E_{LUMO}} \quad (31)$$

These two orbitals play an important role in reaction processes. The major interaction in polar or ionic reactions occurs between the HOMO of the donor (nucleophile) and the LUMO of the acceptor (electrophile).

Molecular orbitals (HOMO-LUMO) and their characteristics, such as E_{HOMO}, E_{LUMO}, and gap energy (ΔE), are extremely valuable to physicists and chemists and are critical factors in quantum chemistry.

These are critical parameters in quantum chemistry. Molecular orbitals (HOMO) and (LUMO) are the primary orbitals involved in chemical stability.

III.2.7.2 The electronegativity

The electronegativity of an atom in a molecule measures its ability to attract electrons. There are various electronegativity scales: Pauling, Mulliken, Gordi... etc..., all of which are based on different criteria on the energy of the bond. The electronegativity $\boldsymbol{\chi}$, measured in eV, is a parameter that reveals a molecule's capacity. The opposite of the chemical potential, it can attract electrons. Additionally, it can be said in E_{HOMO} and E_{LUMO} 's functions.

$$\boldsymbol{\chi = \frac{E_{HOMO}+E_{LUMO}}{2}} \qquad (32)$$

III.2.7.3 Overall Hardness and Softness

Hardness is denoted by **η** and is the reciprocal of softness with **σ**. These terms are generally used to qualitatively explain the selectivity of chemical reactions[110]. In general, a "hard" molecule has a weaker polarizability and a stronger electronegativity and vice versa for a "soft" molecule; the overall hardness equation represents (31) :

$$\boldsymbol{\eta = \frac{E_{HOMO}-E_{LUMO}}{2}} \qquad (33)$$

While a hard molecule has a higher value of ΔE denotes the hard nature of the molecules, a soft molecule has a small ΔE. Unlike hard molecules, soft molecules can more easily provide electrons to the acceptor system due to the small value of ΔE. Therefore, the reactive site of the molecule, where $\boldsymbol{\sigma}$ has the highest value, can be absorbed.

The softness is written as the inverse of the overall hardness, as given in the flowing equation (32):

$$\boldsymbol{\sigma = \frac{1}{\eta} = \frac{2}{E_{HOMO}-E_{LUMO}}} \qquad (34)$$

III.2.7.4 Electronic chemical potential

The chemical potential electronic potential may be defined as the Lagrange multiplier. This definition is identical to the one determined by Pearson[111]:

$$\boldsymbol{\mu = -\chi = \frac{E_{HOMO}+E_{LUMO}}{2}} \qquad (35)$$

III.2.7.5 Overall Electrophilic Index

An electrophile can absorb electrons when submerged in a stream of free electrons. Comparing the electrophilic strength of various species is made possible by this electron count and the resulting energy stabilization[112].

The reactivity indices defined in the conceptual framework of DFT can be used to theoretically characterize the electrophilic and nucleophilic behaviors of organic molecules, and we have introduced the following definition of the electrophilic index of a molecule as a function of its chemical composition: Equation (34) describes a molecule as a function of its chemical potential and chemical hardness.

$$\boldsymbol{\omega = \frac{\mu^2}{\eta}} \qquad (36)$$

III.2. 8 Fukui Function

The Fukui function describes the electron density after a certain number of electrons have been added or removed. It can predict where the most electrophilic and nucleophilic sites are on a molecule.

The Fukui function is implemented as a finite charge change. By default, one whole electron is added or removed, but the calculation is not limited to this amount[113]. Electron fractions are permitted.

The Fukui equation for the electrophilic attack**,** $\boldsymbol{f^-}$**,** is given for the case where one electron is removed.

$$\boldsymbol{f^- = \rho(N)-\rho(N-1) = \rho^{LUMO}} \qquad (37)$$

For the case where one electron is added, the Fukui function for a nucleophilic attack, $\boldsymbol{f^+}$, is given.

$$\boldsymbol{f^+ = \rho(N+1)-\rho(N) = \rho^{HOMO}} \qquad (38)$$

It should be noted that in all cases, the electron density is calculated using the neutral state geometry. The dual descriptor connects the two Fukui functions. When it is electrophilic, it has a positive value; when it is nucleophilic, it has a negative value. The difference between the Fukui plus and Fukui minus functions is used to implement it.

The Fukui function can be used to describe local chemical reactivity. Using the condensed Fukui function, this can even be done per atom.

$f^{-k} = q^k(N) - q^k(N-1)$ for electrophilic attack (39)

$f^{+k} = q^k(N+1) - q^k(N)$ for nucleophilic attack (40)

$f^0 = [q(N+1) - q(N-1)]/2$ for a radical attack (41)

Where,

$q^k(N)$: electronic population of the atom k in the neutral molecule,

$q^k(N+1)$: electronic population of the atom k in the anionic molecule,

$q^k(N-1)$: electronic population of the atom k in the cationic molecule.

It has been shown for reactions controlled by the boundary orbitals a large value of the Fukui index indicates a high reactivity of the site[114].

III.2.9 Electrostatic potential "ESP"

The basic idea behind these methods, which date back to the mid-1980s, is to align the atomic charges as closely as possible to the previously calculated molecular electrostatic potential (MEP for molecular potential or ESP for electrostatic surface potential). The only limitation is that the total of the atomic charges must be less than one to correspond to the molecule's global charge. The electrostatic potential V(r) is determined by the CLOA method at point rA[115].

III.2.10 Electronic transfer ΔN

The electron transfer fraction (ΔN) between inhibitor molecules and metal surfaces is calculated using Pearson's method. According to Pearson, electrons move from a system with low electronegativity to a system with high electronegativity when they are in contact. When the chemical potential of the two systems equalizes, this flow of electrons ceases[116,117]. To calculate the fraction of electron transfer we used the following equation :

$$\Delta N = \frac{\chi_{Metal} - \chi_{inh}}{2(\eta_{Metal} + \eta_{inh})} \qquad (42)$$

Where:

χ_{Metal} : denote the absolute electronegativity value of the used metal.

χ_{inh} : denote the absolute electronegativity value of the used inhibitor.

η_{Metal} and η_{inh} denotes the absolute hardness of the metal used and the inhibitor respectively.

III.2.11 Molecular Dynamic Simulation MDS

Molecular dynamics (MD) simulations have enabled significant advances in many scientific disciplines, including chemical physics, materials science, and biophysics. This computational methodology has proven to be very useful in the detailed characterization of biomolecular systems, such as supplementing experimental data, optimizing experimental design, and predicting properties relevant to chemical systems that are expensive or difficult to manipulate experimentally. It has been used to characterize disease development processes and in the early stages of drug design and development, among other things[118].

Molecular dynamics is a computer modeling technique that describes the time evolution or trajectory of a molecule using classical Newtonian mechanics principles[119]. The intramolecular motions of inhibitor molecules are simulated in molecular dynamics to visualize the true picture of the corrosion inhibition process[120]. The molecular dynamics simulation calculation has two goals:

- Intramolecular motion simulation and calculation of thermodynamic properties such as entropy, free energy, and so on.
- Efficient molecular structure optimization by annealing the simulation process to avoid multiple minima. Each simulation takes between 10^{14} and 10^{10} seconds.

III.2.12. Methodology of DFT &MDS

Several commercial computer programs can be used to perform molecular dynamics calculations. When commercial programs are used, the time required to prepare the scripts and computer files is greatly reduced. In this study, the Materials Studio 7.1 program from Accelrys was used for building meshes, molecules, and computer calculations [121]. Materials Studio is an efficient molecular modeling program containing different modules like DMol3, MesoDyn, Gaussian, QSAR, Discover, etc. All these modules allow a wide variety of calculations, from ab initio to mesoscale simulations. For molecular dynamics, the Discover module has been used[122].

Additionally, Materials Studio provides an easy-to-use graphical interface for designing molecules and building meshes for simulations. Each cell represents a box in which each atom and each bond are represented, much like a crystal cell. There are many parameters for the dimensions of the mesh, depending on the length of the edges and the angle of the sides (a, b, c, $\alpha.\beta.\gamma$). Cartesian coordinates (x, y, z) determine the positions of the atoms in the cell, and links are defined by the atoms they connect.

The meshes enable calculations to be performed under periodic boundary conditions. Each mesh is surrounded by virtual meshes that are identical to it. A molecule can leave the mesh, but the atoms that do so are replicated on the other side. We can represent solid materials in this way.

To predict the properties of systems in molecular mechanics, it is necessary to make them last in time. Minimization is only an energy optimization and does not allow you to track the system's temporal evolution. This is why we use molecular dynamics. By observing the system's energy fluctuations, one can track the system's development over time. Understanding the operation of a system is impossible without molecular dynamics. These simulations can be performed under a multitude of conditions.

III.2.12.1 Force field:

The force field is the first parameter considered in molecular dynamics simulations. This parameter is by far the most important for obtaining relevant data. The force field is a collection of formulas and constants that describe all of the potential energy parameters that act on atomic nuclei. Experiment data and ab initio calculations are used to parameterize the force fields.

Various force fields are available, depending on their application. For this study, calculations were performed using the COMPASS force field. COMPASS stands for "Condensed-phase Optimized Molecular Potentials for Atomistic Simulation Studies"[123]. In addition to being performed based on ab initio calculations, COMPASS was parameterized via different experimental data on organic compounds consisting of H, C, N, O, S, P, halogens, and metals[124]. This force field covers the vast majority of organic polymers, crystals, and metals.

III.2.12.2 Minimization:

When a cell, or even a single molecule, is created by molecular modelling, it is rarely in its optimal configuration. It is therefore necessary to reach the minimum energy level of the studied system. The system is then brought to atomic positions close to those of the potential energy minimum by using established mathematical methods of function minimization. This type of calculation is called "minimization".

Minimization is essential because each step in the process of creating a molecular model requires minimization to obtain the most representative mesh possible.

III.2.12.3 Canonical NVT:

The sum of the force field equations that one applies to a molecular model allows the time evolution of a system. However, as the constants of the formulas are fixed and the number of atoms does not change, the energy should theoretically remain the same, which is rarely the case in nature. For this purpose, methods have been created to simulate the conditions to which the systems are subjected, allowing the reproduction of various sets of dynamics. One set leaves one dynamic parameter variable while it fixes the others. The variation of several parameters is simply fundamentally impossible in molecular mechanics. The micro-canonical ensemble, (NVE), and Canonical ensemble (NVT). NPT (Isobaric-isothermal ensemble) and NPH (The isobaric-isohenthalpic ensemble). With these ensembles, the energy can vary during the simulation. For corrosion inhibition simulations, the canonical system is widely used. For this system, the number of atoms (N), the volume of the mesh (V), and the temperature (T) of the system are fixed. Only the pressure can vary the energy inside the mesh. This set is ideal for stabilization dynamics.

III.2.12.4 Temperature:

One of the difficulties in molecular dynamics is the control of temperature and pressure. Temperature is a thermodynamic state variable for the system. Although the initial temperature is assigned at the beginning, it does not remain constant throughout the simulation, as the motions of the molecules on the potential energy surface cause changes in the velocity of the atoms and thus in the temperature. This is why algorithms have been created to control the temperature. They are called thermostats.

ChapII

Methods of investigation & experimental conditions

Chapter II: The investigation methods and the experimental conditions

II.1 Introduction

Biodiesel is a fuel derived from renewable sources, primarily vegetable oils, animal fats, used cooking oils, algae oils, and other similar substances. The biodiesel source must meet two critical criteria. It must be distinguished by its durability, availability, and reasonable cost. However, production costs are high, which is due to the high price of vegetable oil and some technological problems. The majority of commercial biodiesels are made from vegetable oils (primarily rapeseed, soybean, and sunflower).

Indeed, there is the possibility of using either proven non-edible vegetable oils, such as jatropha oil, or large-scale edible oils, such as palm oil. Brazil (jatropha), India (jatropha, palm, etc.), and Malaysia (palm) have all taken this route. In addition, some African countries, such as Mali, Senegal, and Burkina Faso, are interested in establishing Jatropha.

The experimental work consists of producing biodiesels from a soybean waste cooking oil source collected from the restaurant at Rabat's Faculty of Sciences, as well as commercial sunflower vegetable oil, in the presence of homogeneous (KOH) and heterogeneous ($KOH/FeSO_4.5H_2O$) catalysts, as well as anhydrous Methanol of 99.95% purity.

With the processing and analytical methods, we have created specifically for this purpose, we advise handling and identifying used vegetable oils.

II.2.Pre-treatment of the raw material

II.2.1 Filtration

Filtration is a separation process that uses a porous medium to separate the constituents of a mixture with a liquid and solid phase.

The oil was filtered through cellulose, recycled paper, and fabric filters. The aim is to remove solid particles and some water from the oil. When compared to the methods described in the rest of this work, filtration is not an expensive method.

II.2.2 Drying process

The oil was simply heated for 20 minutes at 100°C to dry it. This period was calculated by keeping track of weight loss during heating. To avoid increased fatty acid levels and triglyceride hydrolysis, longer exposures should be avoided.

II.3 Biodiesel physicochemical analysis technique

II.3.1 Acidity Determination

The acid index, which measures the amount of potassium hydroxide (KOH) needed to neutralize the free fatty acids in 1 g of fat, is used to define acidity.

According to the ASTM D 974, AFNOR T 60 - 112 method, the acidity was assessed. A test sample of oil that "weighs exactly" is dissolved in a solution of absolute ethanol and dimethyl ether (2V/V). After that, a simple acid-base assay is performed using phenolphthalein as a colour indicator by adding a volume of VKOH to a 0.1N titrated KOH solution. The solution changes colour to pink once all free fatty acids have been neutralized.

The following relationship determines the oil's acidity index:

$$IA = \frac{M_{KOH} V_{KOH} N_{KOH}}{m_{oil}} \qquad (43)$$

With :

M_{KOH} : The molar mass of KOH.

V_{KOH} : The volume at equivalence.

N_{KOH} : The normality of the KOH solution.

m_{oil} : The mass of the oil sample.

The acid index is expressed in (mg KOH/g oil).

II.3.2 Density

The relative density of a substance is the ratio of its density to the density of a reference substance. For liquids, a density meter is used for an accurate measurement of the density.

The sample is heated to a prescribed temperature. The test sample is placed in a test tube, and then a density meter is introduced and left until it reaches temperature equilibrium. The scale value of the densimeter is read along with the temperature of the test sample. Finally, the density is converted to 15°. The experimental device is represented in the**Figure.II. 1**

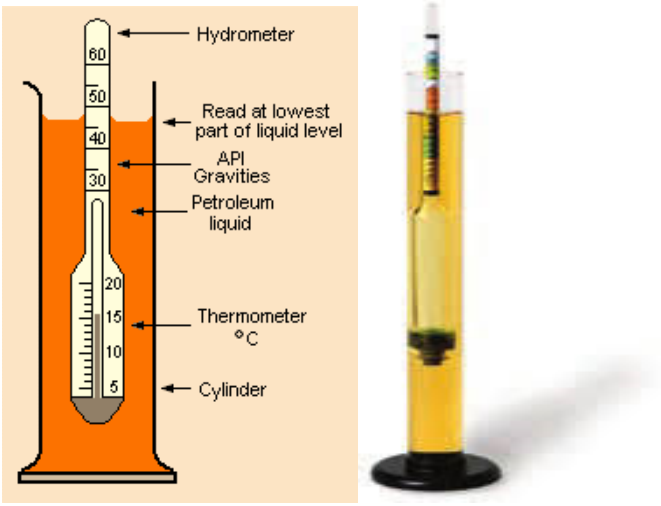

Figure.II. 1:Densimeter instrument.

II.3.3 Viscosity

Viscosity is a property of resistance to uniform, turbulence-free flow in the bulk of a material. It is represented by a coefficient that represents the shear stress required to produce a flow velocity gradient of one unit in the material.

The UBBELHODE viscometer is shown in ***Figure. II. 3****It* is a viscometer for clear liquids with two-gauge lines. The kinematic viscosity is calculated from the time of flow of a specific volume of substrate in a calibrated capillary under specific conditions. Following the measurement of the product's flow time, the viscosity is calculated using the following expression: viscosity = C.t, where C is the viscosity constant and t is the flow time; the centistoke "Cst" is the unit of measurement for viscosity.

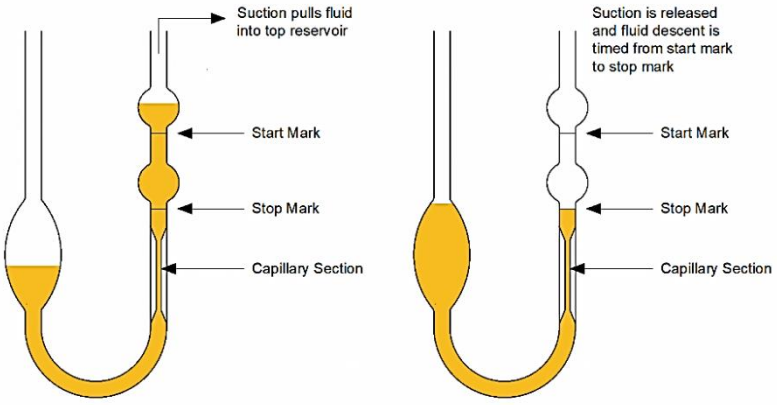

Figure.II. 2:Viscosimeter UBBELHODE.

II.3.4 Flow point

This indicates the ability of oil or fuel to flow at a low operating temperature. The lowest temperature at which the fluid will flow when cooled to the required conditions is referred to as the pour point. The ***Figure. II. 4*** represents the instrument of the flow point.

Figure. II. 5:Measurement of the flow point.

- **Method principles:**

The test sample is placed in a hermetically sealed test tube with a cap containing a thermometer held vertically and well-centered. The thermometer's capillary starts 3 mm below the product's surface. The tube is heated to 45°C, then cooled to 32°C before being placed in a 3°C flow bath until the product solidifies. After determining the freezing point, a +3 °C coefficient is applied to determine the boiling point.

II.3.5 Flashpoint measurement

The flash point is the lowest temperature at which a fluid exhibits instantaneous combustion, but it is higher than the minimum temperature at which it burns continuously. The flash point is a crucial sign of a petroleum product's inherent fire and explosion risks. The **Figure. II. 5** depicts the Instrument for flash point determination

Figure. II. 6:Instrument for flash point determination.

The sample is introduced to a predetermined level in the vessel. It is heated rapidly at first, then slowly and steadily to near the flash point temperature. A small flame is passed over the vessel at specified temperature intervals. The flash point is defined as the lowest temperature at which the application of a flame causes the ignition of the vapors emitted at the liquid's surface.

II.3.6 Determination of sulfur content

The sulfur content is determined using energy-dispersive X-ray fluorescence. The principle involves oxidizing sulfur-containing liquid compounds in the presence of oxygen at 1050 °C. The result is SO_2, whose known sulfur concentration can be calculated. Sulfur determination was carried out using a Jena instrument illustrated in After homogenizing the biodiesel, a previously weighed test sample is injected into the Karl Fischer apparatus's titration vessel, which contains a stirring solvent. The water is titrated with the KF reagent until the potentiometric end point (250 mV) is reached.

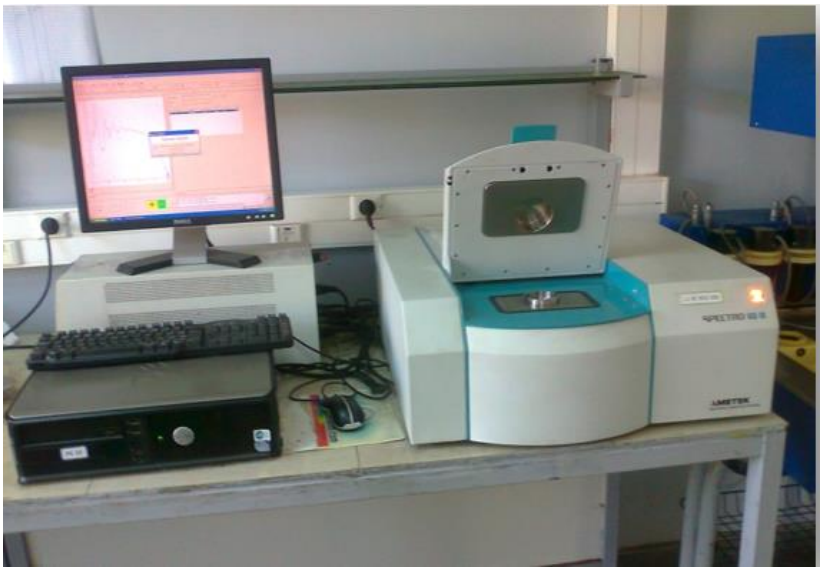

Figure. II. 7: instrument for the determination of sulfur in biodiesel.

II.4 Inhibitor Preparation

II.4.1The coffee grounds preparation

Coffee grounds are the insoluble residue that remains after coffee beans have been dried, ground, and infused coffee beans. There are two sources: those generated by the soluble coffee industry, which accounts for roughly half of the world's coffee harvest each year, and those generated by coffee shops and the general public, which accounts for the other half.

The trash coffee ground (grains acquired after making the drink, 100% Arabica type) was collected from a cafeteria at the University of Science in Rabat, Morocco. After that, the wasted coffee grounds were dried in an oven to eliminate moisture. To dry coffee grounds and remove all moisture were placed in a drying oven at a controlled temperature for 24 hours as shown in the figure

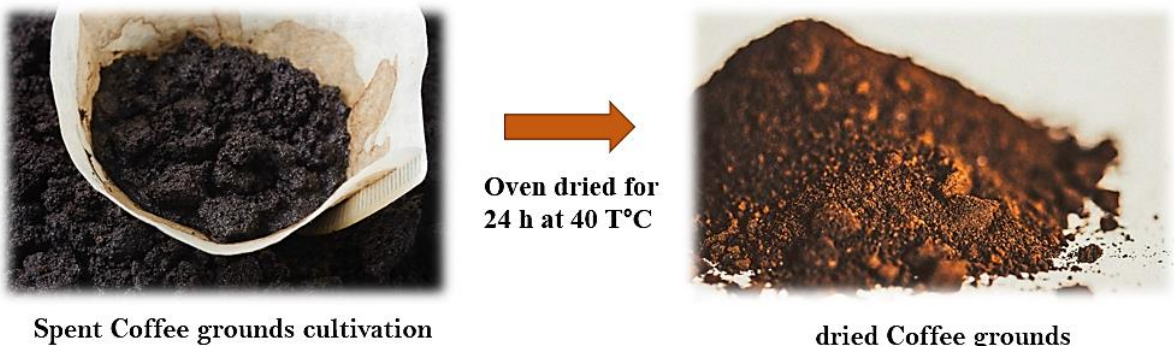

Figure. II. 8: the coffee grounds spent treatment setup.

II.4.1 Extraction of the coffee grounds spent

The hydroalcoholic extract of coffee grounds was obtained using the Soxhlet process. The HECG was obtained using 100 g of coffee ground placed into a cartridge with 450 ml of methanol introduced into a Soxhlet extractor for a 5-hour at a temperature of 65°C. After the extraction had been accomplished, the solvent was evaporated under a vacuum at 40 °C to remove excess methanol, the steps of extracting the inhibitor are described.

The extraction yield is determined using the following relation:

$$\% \ R = \frac{m_{ext}}{m_{coeffe}} * 100 \qquad (44)$$

$m_{extracted}$: the mass in grams of the extracted

m_{coeffe}: the mass in grams of the sample taken for the test,

Figure.II. 9:The hydroalcoholic extraction setup of coffee grounds using the Soxhlet process and rotavapor.

II.5 Characterization of biodiesel & inhibitor

II.5.1 Analysis by Fourier transform infrared spectroscopy(FTIR)

Infrared spectroscopy is based on the absorption of infrared radiation by the material being studied. It detects vibrations typical of chemical bonds to analyze the chemical functions present in the compound. The sample to be analyzed is either liquid or powder in nature. The sample is placed in contact with an IR-absorbing crystal with a refractive index greater than 2.5 (germanium, diamond) in ATR mode. (When the incident wave reaches the sample, it is completely reflected.) This band, however, is known as an attenuated total reflection because it is slightly absorbed in the interface. The samples were

analyzed using a JASCO 4600 FT-IR instrument. The ATR crystal is made of diamond, a material with a spectral range of 4000 to 400 cm1. A scan of 30 scans with a resolution of 4 cm-1 is selected.

Figure. II. 10:Spectroscopy apparatus (FT/IR JASCO 4600).

II.5.2 Analysis by gas chromatography coupled to mass spectroscopy (GC/MS).

The technique used is gas chromatography coupled to mass spectrometry (GC/MS) is a general-purpose instrument used in the quantitative and qualitative analysis of liquid and gaseous molecules. GC-MS is a hyphen analytic technique. Is composed of two instruments combined as a series to produce robust analytical results. In this instrument, gas chromatography separates the components of a sample, and the results are displayed as a chromatogram, where the intensity of the bands provides information on the number of analytes and the number of bands representing the different molecules present in the sample. The number of analytes and the number of bands represent the different molecules in the mixture. Mass spectrometry, on the other hand, provides a discrete number in the form of peaks that represent either the mass of the molecule or its fragments, which is characteristic of the different components of the mixture. By combining these techniques, it is possible to analyze quantitatively and qualitatively the compounds in a given mixture.

GC/MS used in this work is a Perkin Elmer Clarus 680 with a Restek RTX-5 silica column (5% diphenyl, 95% dimethyl polysiloxane) (30 m 0.25 mm) and an electronic impact ionization detector. The carrier gas is helium, and the flow rate is constant at 0.2 ml /min. The injector, transfer line, and ion source were all set to 220, 200, and 200 °C, respectively. The energy of ionization was set to 70 eV. The automatic setting produced the electron multiplier (EM) voltage. All data were collected by collecting full-scan mass spectra ranging from 20 to 600 m/z. The sample volume injected was 0.1 ml,

with a split ratio of 50:1. The oven temperature program was as follows: 140°C for 5 minutes, 4°C/min (heating rate), and 250°C for 5 minutes.

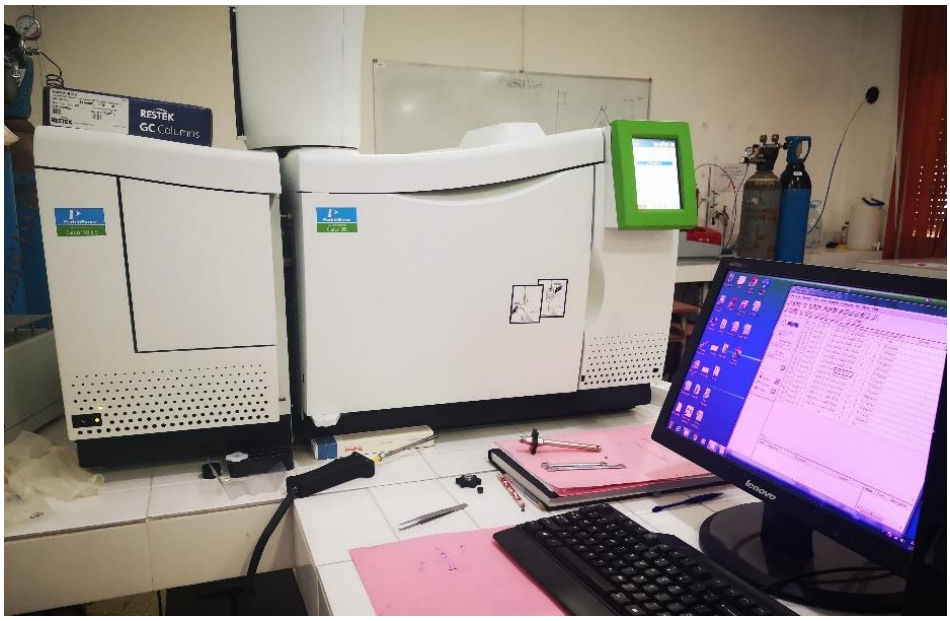

Figure.II. 11:Instrument of Gas chromatography coupled to mass spectroscopy (GC/MS).

II.6 Experimental methods and techniques

II.6.1 Sample Preparation

Automobile engines are constructed from many types of materials. Although, materials that are commonly used for engine fuel system components are chosen for corrosion testing with biodiesel. The specifications of the tested material samples, such as stainless steel ((19%Cr, 9% Ni, 2.72% Mo, and 0.98% C), aluminum (95.73% pure), and copper (95.37% pure).

All of these compounds have a positive effect on the corrosion resistance. Indeed, the Ni percentage increases the corrosion resistance by increasing the critical potential, while the Cr percentage results in a high corrosion resistance thanks to the protective oxide layer formed on the surface. Finally, the percentage of Mo improves the corrosion resistance and facilitates the passivation after the breakage of the passive film[125,126].

The samples were prepared from a round bar by machining, grinding, and polishing. Each sample was drilled with a 1cm² Diameter hole to suspend it by Teflon when immersed in the fuel samples. The biodiesel samples were stored in a glass beaker. Before being immersed in the glass beakers, the material samples were polished with silicon carbide abrasive paper (grade 180 to 1200 grit), then washed and degreased with acetone.

II.6.2 Evaluation technique of corrosion inhibiting efficiency

II.6.2.1 Gravimetric technique

Mass loss measurements are the first approach to the study of metal corrosion in electrolytic media. The corrosion rate is determined using this method.

This rate can be expressed in several ways, according to the literature: as a percentage of mass loss, milligrams per square centimeter per day, and grams per square inch per hour. The most desirable unit for expressing corrosion rate is millimeters per year. In the corrosion test, this parameter is calculated from the mass loss of the metal or alloy sample during corrosion. The corrosion rate is expressed by the following relationship:

$$\boldsymbol{W_{corr} = \frac{\Delta m}{S * t}} \qquad \textbf{(45)}$$

Where $\boldsymbol{W_{corr}}$ is the corrosion rate (mg /cm² / d), Δm is the mass loss in mg, S is the surface exposed in cm² and t is the immersion time in d.

The inhibition efficiency η_{WL} % can be determined using the corrosion rate $\boldsymbol{W_{corr}}$ (in the blank) and $\boldsymbol{W_{corr}^{inh}}$ (with inhibitor) as follow :

$$\boldsymbol{\eta_{WL}\ \% = \frac{W_{cor-}\ W_{corr}^{inh}}{W_{corr}} * 100} \quad \textbf{(}46\textbf{)}$$

II.6.2.2 Electrochemical method

The approach of the mechanisms involved in the corrosion process cannot be determined using weight loss to determine inhibitory efficiency. Electrochemical measurements, on the other hand, are a more comprehensive technique because they investigate the very basis of the corrosion phenomenon, the electrochemical process.

Electrochemical techniques allowed us to approach the study from two perspectives. Either by using a cyclic voltammeter with a high sampling rate or by monitoring the open circuit potential over time, which is characteristic of the change in the interface of a metal with its environment. The most quantitative aspect (polarization curves with moderate sampling speed, polarization, impedance spectroscopy, etc.) gives access to the reaction rate and to the values of the physical parameters describing the state of the system (double layer capacitance, transfer resistance, film capacitance, etc.).

The evaluation of the effectiveness of corrosion inhibitors of materials was carried out by electrochemical methods such as stationary methods and transient methods.

II.6.2.2.1 Evolution of the free potential as a function of time

When the corrosion potential of a metal is measured, it is observed that it generally does not reach a stationary value immediately. A stationary potential takes some time to develop because there aren't any metal ions present when the metal is submerged in the solution. The metal-solution interface, on the other hand, can be altered by the formation of a gas, such as hydrogen, or an insoluble corrosion product. Potential-time curves reveal various characteristics.

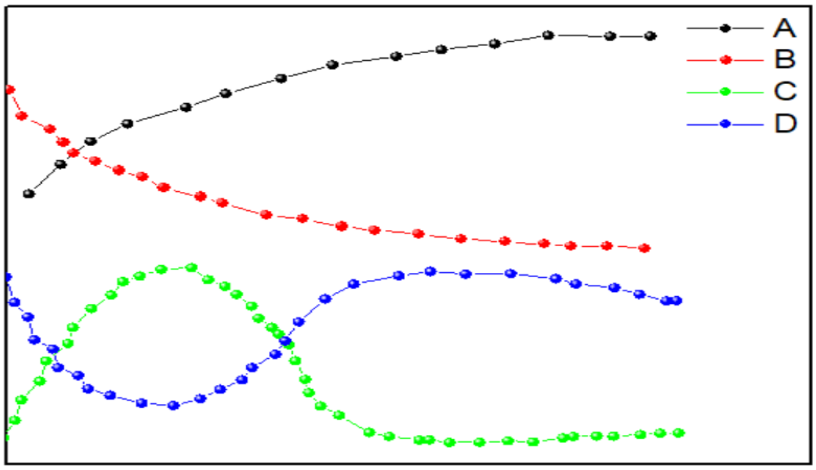

Figure.II. 12:Schematic of the potential monitoring as a function of time.

Curve A: As the potential becomes more noble, the metal is passivated by the formation of an insoluble corrosion product on the surface.

Curve B: The potential only decreases, and the material becomes less and less noble, by a continuous attack of the metal.

Curve C: the potential initially becomes more negative, then tends towards more positive values; there is an attack followed by passivation.

Curve D: the potential becomes more noble and then moves towards more negative values. This is the case when, at the time of immersion, the metal is covered with a protective layer, which develops over a more or less long period and is then destroyed. The metal is then exposed.

II.6.2.2.2 Stationary method: Polarization curve

Stationary techniques permit to study of a steady-state system by applying a potential ramp with the lowest possible sweep rate. These methods consider all of the redox couples in the solution to provide

information on the various electrochemical reactions involved. They are widely used in laboratories for general corrosion research.

To determine the polarization curve, different potentials are applied between the working electrode and a reference electrode using a potentiostat. We are talking about the stationary current that forms after a certain amount of time in the electrical circuit between this working electrode and a counter electrode. The value of Icorr was first determined by Stern and al[127].

The curves LogI =f(E) represent the polarization curves (***Figure. II.* 13***)*These curves allow an accurate determination of the main electrochemical parameters of a metal in contact with an electrolyte via a potentiostat. These parameters are the instantaneous corrosion rate (Icorr), the corrosion potential (Ecorr), the polarization resistance (Rp), the passivity current density (Ip), the passivity potential (Ep), and the transpassivity potential (Ep). The determination of corrosion rate from polarization curves is closely related to electrochemical kinetics. Pure activation, passivation, and transpassivity kinetics are the three main categories of kinetics

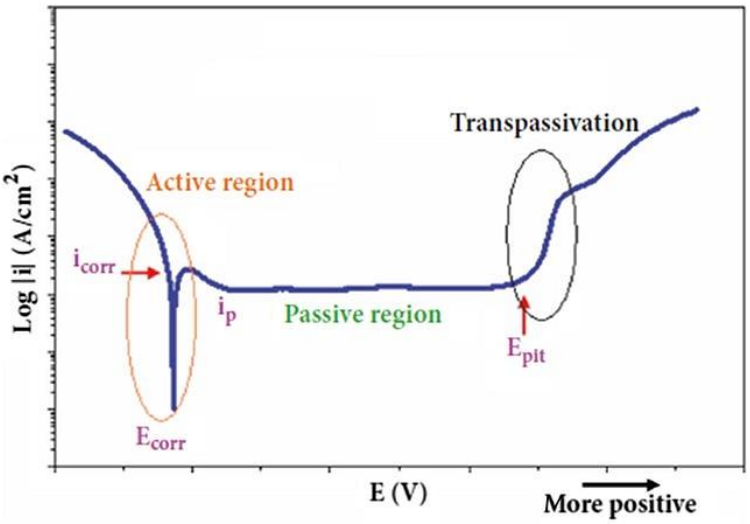

Figure. II. 13:Potentiodynamic curves of a steel log I=f(E).

The exploitation of the anodic and cathodic branches equated to Tafel lines on the log(I)=f(E) curve leads to the point (Icorr, Ecorr). Polarization curve plots showing the anodic and cathodic regions and

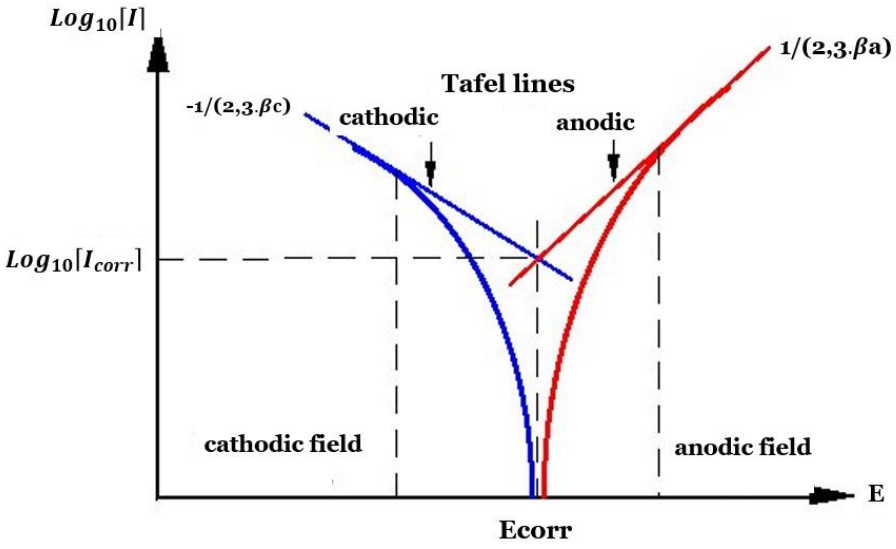

Figure.II. 14:Determination of the electrochemical parameters from the Tafel lines.

the Tafel extrapolation method in estimating the corrosion potential (Ecorr) and corrosion current density (Icorr) as shown in ***Figure.II. 14***.

The current-potential curves are acquired using the potential-kinetic mode and a sweep rate of 1 mV/S. With this speed, we were able to position ourselves in nearly stationary conditions and achieve good reproducibility. These curves are recorded in a potential range with a precise specification (mV/ECS).

The effectiveness of an inhibitor can be determined by measuring a metal's corrosion current in a corrosive solution containing a known amount of inhibitor (i_{corr}^{inh}). It is defined by the following equation:

$$\eta_{PDP}(\%) = \frac{i_{corr} - i_{corr}^{inh}}{i_{corr}} * 100 \qquad (45)$$

With :

$\mathbf{i_{corr}}$ (in the blank) and $\mathbf{i_{corr\ inh}}$ (in the presence of the inhibitor).

II.6.2.2.3 Transient method: electrochemical impedance spectroscopy

Non-stationary methods are divided into two types: large-amplitude perturbation methods (cyclic voltmeters) and small-amplitude perturbation methods (electrochemical impedance meters). Previous research demonstrated that electrochemical impedance spectroscopy (E.I.S.)[128]. It Can identify the elementary steps involved in the overall process occurring at the metal/solution interface in the form of different time constants.is used today in the following fields:

- Photo-electrochemistry,

- the semiconductor/electrolyte interface,
- organic electrochemistry and the study of adsorption phenomena,
- biochemistry,
- corrosion and its inhibition

The impedance spectroscopy approach involves measuring the response of the electrode to a sinusoidal modulation of the potential with a modest amplitude as a function of frequency. An anodic or cathodic potential imposed on the corrosion potential can be modulated in this way.

The EIS offers various benefits in the realm of corrosion. It enables an exact assessment of the corrosion rate even when the metal is protected by a protective coating. Furthermore, the EIS also allows for the assessment of the inhibition rate, the characterization of various corrosion events (dissolution, passivation, pitting, and so on), and the investigation of reaction mechanisms at the electrochemical interface.

II.6.2.3.1 Principle

Electrochemical impedance spectroscopy is a nonstationary method that provides information about the basic steps in the entire electrochemical process. Its principle is to overlay a modulation of the sinusoidal potential with a small amplitude on the electrode potential to follow the current response for different frequencies of the interference signal. The current response is also sine, superimposed on a current in the steady state but offset in phase by an angle regarding the potential. Conversely, one can impose a current and record the potential(***Figure. II. 15***).

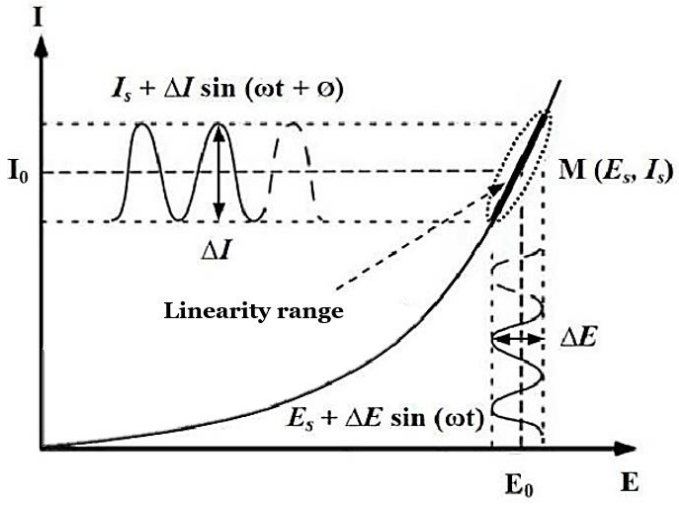

Figure. II. 15:Diagram of a non-linear electrochemical system submitted to sinusoidal disturbance.

The electrochemical system can be considered a "black box" that reacts by emitting a signal when subjected to a disturbance ***Figure. II. 15.***

The two signals are then linked by a transfer function **H(ω)** such as:

$$\mathbf{Y(\omega) = H(\omega)\, X(\omega)} \qquad \mathbf{(47)}$$

X(ω) and **Y(ω)** and being respectively the Fourier transforms of x(t) and y(t).

The total voltage expression is given in the flowing equation :

$$\mathbf{E_0\,(t) = Ea + |\Delta E|\ \sin(\omega t)} \quad \mathbf{(48)}$$

With ω= 2πf (pulsation), where Hz is the frequency of the disturbance.

After a relaxation time, the sinusoidal current response is superimposed on the I_0 bias current, which defines the steady state under study, with a phase ϕ shift between ΔE and ΔI. Its expression is the

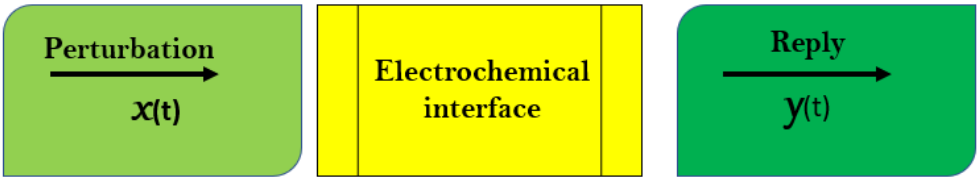

Figure.II. 16:Scheme of a Transfer function.

following :

$$\mathbf{I_0\,(t) = I_0 + |\Delta I|\ \sin(\omega t)} \quad \mathbf{(49)}$$

The impedance around the operating point (I_0;E_0) is then defined for each excitation frequency as the ratio of the disturbance signal to the associated response:

$$\boldsymbol{Z(\omega) = \frac{\Delta E(\omega)}{\Delta I(\omega)} = \frac{[\Delta E]\exp(j\omega t)}{[\Delta E]\exp(j\omega t+\varphi)} = |Z|\exp(j\varphi)} \quad \mathbf{(50)}$$

The impedance is a complex number characterized by its modulus $|Z|$ and phase ϕ . It can be written as follows:

$$\boldsymbol{Z(\omega) = jZ_{Im}(\omega)} \qquad \text{with} \quad \boldsymbol{j = \sqrt{-1}} \qquad \mathbf{(51)}$$

The modulus is : $$\boldsymbol{|Z| = (Z_{Re}^2 + Z_{Im}^2)^{1/2}} \qquad \mathbf{(52)}$$

and the phase: $$\boldsymbol{\varphi = tan - 1\,(Z_{Im}/Z_{Re})} \quad \mathbf{(53)}$$

The frequency analysis of the electrochemical impedance will allow for the differentiation of the different elementary phenomena according to their characteristic frequencies (or time constants). Each disturbed process returns to its stationary state with its own response time.

The partial reactions that occur at the electrode/electrolyte interface can thus be distinguished: Charge transfer is a type of fast electrochemical phenomenon. are encouraged at high frequencies, whereas slow phenomena (material transport: diffusion, adsorption) occur at low frequencies.

Electrochemical impedance spectroscopy (EIS) has several advantages in the field of corrosion. It enables accurate corrosion rate determination even when the metal is protected by a protective layer. EIS can also be used to calculate the inhibition rate, characterize corrosion phenomena (such as dissolution, passivation, and pitting), and investigate reaction mechanisms at the electrochemical interface.

II.6.2.3.2 Traditional data representation

Impedance diagrams are commonly represented in two ways as presented in ***Figure. II. 17*** They can be plotted in cartesian coordinates in the Nyquist complex plane by putting Z_{Re} on the abscissa and $-Z_{Im}$ on the ordinate. It is necessary to use orthonormal reference points for this representation; otherwise, the diagrams will be distorted, and the interpretation will be distorted. The Bode representation is another traditional method for visualizing diagrams[129].

In this case, the modulus of impedance |Z| (represented in the logarithmic scale) and phase shift ϕ are plotted as a function of frequency, which is also represented in the logarithmic scale. These two different visions of the same result are complementary, not competitive; each of them shows a different aspect of the impedance diagram.

The Nyquist representation makes it possible to see the various ***"loops and lines"*** of the plot but often masks the results at high frequencies. This representation enables the calculation of parameters such as electrolyte resistance (Rs), charge transfer resistance (Rt), and double-layer capacitance (Cdl)(***Figure. II. 17).***

The Bode representation offers a complete vision of the frequency domain but is less able to identify some characteristic phenomena.

The charge transfer resistance Rt is defined as the intersection of the loop with the real axis at low frequency. The electrolyte resistance is the limit of the high-frequency impedance. The double-layer capacitance Cdl is determined from the following relationship:

$$C_{dl} = \frac{1}{R_t 2\pi f} \qquad (54)$$

Where f is the frequency corresponding to the top of the half-loop

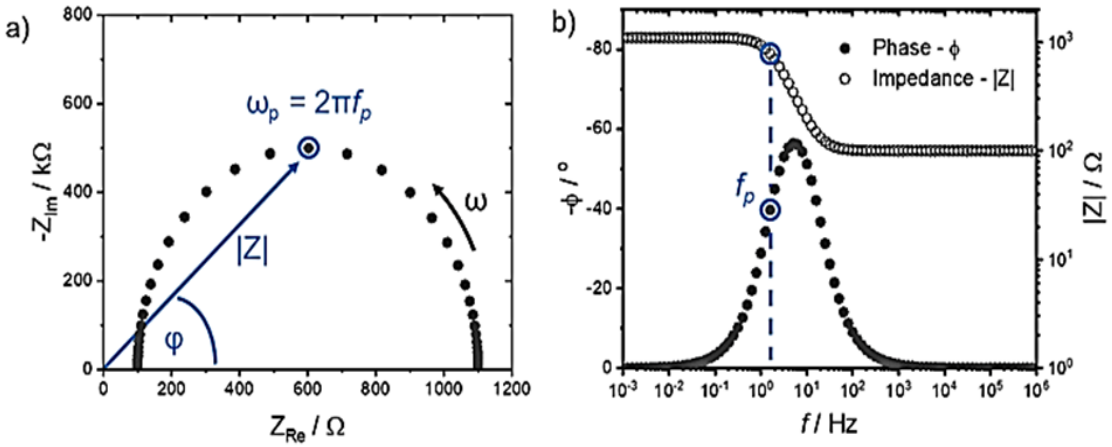

Figure. II. 17:Representation of the electrochemical impedance in Nyquist (a) and Bode (b).

II.6.2.3.3 Use of equivalent electric circuits

The impedance of an electrochemical system, whatever it is, can indeed be analogous to an electrical impedance. We can therefore associate this system with an equivalent electric circuit (EEC) where each physicochemical phenomenon taking place at the metal/electrolyte the metal/electrolyte interface can be modeled by an electrical component[130].

We should mention that the interpretation of experimental impedance diagrams employing CEE must respect two conditions:

- all the elements of the circuit must have a precise physical meaning, associated with the physical properties of the system;
- the spectrum simulated from the CEE must be as faithful as possible to the experimental spectrum and the error must not present a systematic character according to the frequency;

This double layer is described by three main models: Helmotz, Gouy-Chapman, and Stern[131]. The behavior in the dynamic regime of a redox reaction in the absence of concentration gradient of the electroactive species is therefore analogous to that of the electrical circuit behavior of a redox reaction

in the absence of a concentration gradient of electroactive species is analogous to that of the electrical circuit called the generalized Randles circuit.

there are many other types of equivalent circuits, each of them describing a particular system. How each component is connected and the order in which they appear is important the way each component is connected and the order in which they appear are important, both for the calculation of the impedance and for the readability of the model. The physical logic of the system must be followed: successive processes are connected in series while simultaneous processes are connected in parallel.

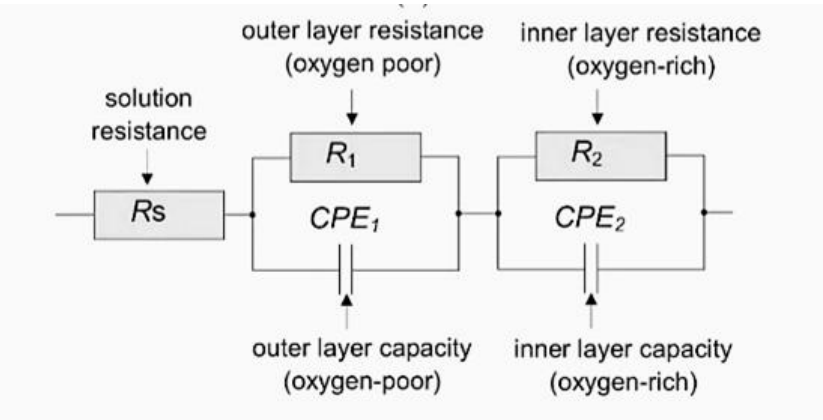

Figure. II. 18:Equivalent circuits of EIS electrochemical impedance spectra: (a) two-layer model, and (b) one-layer model.

The electrical circuit consists of three resistors and two capacitors. Rs is the resistance of the solution. Constant phase elements (CPE) were applied to represent the capacitances of the different layers. The parameters R1 and CPE1 are related to the outer layer, which corresponds to the top layer of the oxygen-rich region as shown in ***Figure. II. 18***

II.6.3. Techniques for analyzing corrosive solutions

II.6.3.1 Spectroscopy UV-Vis analysis

In chemistry, ultraviolet-visible spectroscopy (UV-Vis) is one of the most well-known and frequently used techniques for qualitative and quantitative analysis. This technique is useful for determining the concentrations of organic and inorganic chemical compounds that are absorbed in this electromagnetic domain.

A radiation source, a wavelength selection device, a sample compartment, a detector, and an output device comprise the fundamental method. A wavelength selector, a sample compartment, a detector, and an output device are all present.

Figure.II. 19:Jasco model V-730 UV-Vis spectrophotometer.

The absorbance spectra of the samples were obtained at room temperature using a UV-Vis spectrophotometer (model Jasco V-730)*(***Figure.II. 19***)*. We are interested in the analysis of transition metal ions and their complexes, which are generally colored and exhibit an absorption tendency due to electronic transitions involving the 3d and 4d orbitals. This technique allows us to detect the presence of chemical elements that make up the iron alloy in the solution to assess the degree of corrosion.

II.6.3.2 Flame Atomic Absorption Spectroscopy

In the 1960s, the analytical method known as flame atomic absorption spectroscopy (Flame AAS or FAAS) was first made available for purchase. This technique has remained popular over the years due to its dependability and simplicity. Atomic absorption spectrometry is an analytical technique for determining the concentration of specific elements in a sample. About 75% of the chemical elements in the earth are metals. A material's metal content may be desirable in some circumstances, but metals can also be contaminants or poisons. As a result, determining metal content is crucial in a variety of applications, which we will discuss further in this article. For now, suffice it to say that it is used for a variety of purposes, including environmental testing, toxicology, and quality control.

II.6.3.2.1the principle of atomic absorption spectroscopy

FAAS's fundamental principles are as follows: First off, the light at particular and distinct wavelengths can be absorbed by all atoms or ions. When a specimen made of copper (Cu) and nickel (Ni) is exposed to light with the characteristic wavelength of copper (Cu), only the copper atoms or ions absorb the light. The concentration of the absorbing ions or atoms is directly proportional to the amount of light absorbed at this wavelength.

An atom's electrons have different energy levels. The electrons transition from a ground state to an excited state when the atom is exposed to the light of its wavelength. The electrons' ability to absorb radiant energy is directly related to the transition that takes place during this process. The absorbed radiation also represents a distinct property of each element and can be measured because the electronic structure of each element is distinct.

The AAS applies these fundamental principles to practical quantitative analysis. A typical atomic absorption spectrometer is made up of four major components: the light source, the atomization system, the monochromator, and the detection syste*m* ***Figure. II. 20.***

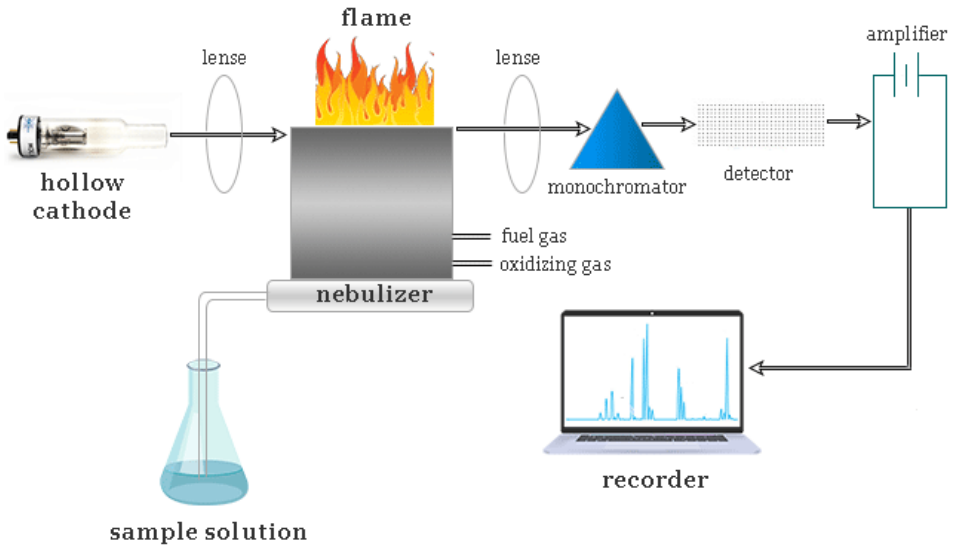

Figure. II. 21: overview of an atomic absorption spectrometer procedure.

II.6.3.2.2 The preparation of the samples

For sample preparation, various methods are available, each with its own set of benefits and drawbacks. Samples with high organic content, such as biodiesel, make F atomic absorption spectrometry difficult to analyze. This issue can be solved by diluting it with an appropriate organic solvent, though this lowers the detection limit of the procedure. In biodiesel analysis, the majority of sample processing techniques are based on emulsification, and microemulsification[132].

a) Emulsions method

Emulsions are dispersions formed by combining two immiscible liquid phases with a surfactant and mechanical shear to form a single fluid(products containing a molecule with both a polar and non-polar structure) are usually added to the oil-water mixture to improve the kinetic stability of such a system;

thus, the stability of emulsions can be designed to range from a few seconds to several years depending on the application[133].

The main advantages of using emulsions are that they do not require the prior destruction of organic samples or the use of organic solvents as diluents, and they behave similarly to aqueous solutions, allowing calibration with aqueous standard solutions. When one liquid (dispersion medium or continuous phase) is dispersed in another, it creates an emulsion, which is a kinetically stable system. They do not form spontaneously because they are thermodynamically unstable systems and must be stirred manually or mechanically by centrifugation or agitation.

b) Microemulsion

A microemulsion is a mixture of the aqueous and oil phases in the proper proportions, along with a surfactant and/or co-surfactant, that is thermodynamically stable, optically transparent, and microscopically homogeneous. These systems have distinct properties, such as low viscosity and the ability to solubilize both polar (aqueous) and non-polar (oil-soluble) substances. The ability to prepare calibration solutions using aqueous standards rather than unstable organometallic standards is one of the main advantages of using micro emulsification for sample preparation[134,135].

From an environmental and toxicology standpoint, the use of micro emulsification as a sample preparation method for the direct analysis of high lipid samples is appealing because it allows for direct analysis without the need for dilution with relatively toxic organic solvents.

The Microemulsions are very different from emulsions in many respects: formation, droplet size (about 500 times smaller), physicochemical characteristics (e.g., interfacial tension is lower (about 1000 times) and specific surface area is higher), and appearance (emulsions are opaque and microemulsions are transparent). Furthermore, the O/W and W/O morphologies, which make up the two main types of emulsions, suggest the presence of biphasic behavior at equilibrium[136].

II.6.3.2.3 Preparation of the samples by microemulsion

The atomic absorption analyses were carried out by spectrometer controlAA300 (Analytic Jena AG, Jena, Germany). Hollow cathode lamps of Fe, Ni and Cr, Cu, and Al were used as radiation sources functioning at a particular current for all elements. Air pressure was used to oxidize Fe, Ni and Cr, Cu, and Al, and the combustible was acetylene for all elements. The primary instruments, sample suction rate, and acetylene flow rate that were employed to generate maximal and steady absorbance readings are listed *in* ***Table.II . 1***.

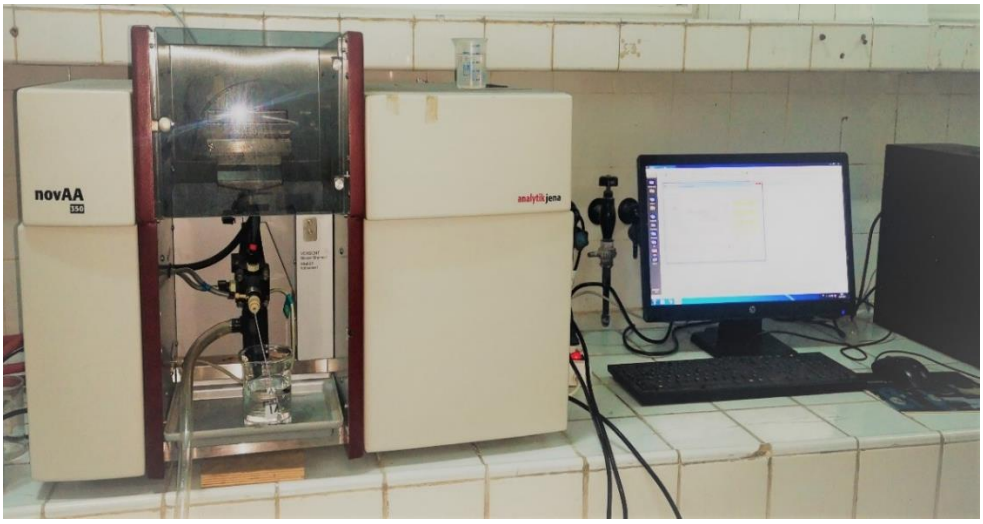

Figure. II. 22:controlAA300 (Analytic Jena AG, Jena, Germany), FAAS Instruments.

The ME analysis was performed at room temperature using a mixture of 0.0017 kg biodiesel, 1.1×10^{3} L aqueous phase water, and approximately 0.0054 kg saturated n-propanol in a final volume of 10×10^{-3} L. Nitric acid (1.4 mol L^{-1}) was added to increase the stability of these analytes. By lowering the quantities of biodiesel, dilute nitric acid, and n-propanol, the ternary diagram phase was created; apparent transparency was seen. ME calibration standards were made by substituting 0.0017 kg of oleic acid for sunflower biodiesel and adding mineral metal standards to the aqueous phase. A blank solution containing oleic acid, aqueous phase (1.4 mol L^{-1} HNO_3), and n-propanol was also created. In 10×10^{-3} L volumetric vials, standards were created by adding to the amount of the aqueous phase previously reported aqueous solutions to reach concentrations in the ranges of 1→5 mg L^{-1} for Fe, 0.025→5 mg L^{-1} for Ni and Cr, and 1→6 mg L^{-1} for Cu and Al.

Table.II . 1:Instrumental parameters for FAAS measurement of Fe, Ni, and Cr using the micro-emulsion sample preparation method.

	Flame composition C_2H_2/air (Fe, Cr, Ni)	***Aspiration rate (mL min^{-1})***	***Burner height (mm)***	***Wavelength (nm)***	***Lamp current (mA)***	***Slit (nm)***
Fe	**0.081**	**3.1**	**6**	**248.3**	**6**	**0.2**
Cr	**0.342**	**4.0**	**5**	**357.9**	**6**	**0.2**
Ni	**0.340**	**2.8**	**5**	**232.0**	**6**	**0.2**
Cu	**0.082**	**3.0**	**7**	**309.3**	**5**	**0.8**
Al	**0.430**	**2.8**	**7**	**324.8**	**7**	**0.8**

II.7. Surface analysis and characterization techniques

II.7.1 UV-Vis-NIR spectroscopy

Spectroscopy is fundamentally based on the phenomenon of light energy absorption by a substance. Because high energy electrons are transferred by atomic or molecular orbitals when a material is exposed to light, spectroscopy in the ultraviolet (UV), visible (Vis), and near-infrared (NIR) regions of the electromagnetic spectrum are frequently referred to as "electron spectroscopy"[137].
To scan the spectrum at the desired X intervals, the instrument typically employs one or two light sources and a monochromator.

The following relationship expresses the relationship between the energy absorbed in an electron transition and the frequency (υ), wavelength (λ), and wavenumber ($\bar{\nu}$) of the radiation producing the transition**.**

$$\Delta E = h\upsilon = h\frac{c}{\lambda} = h\bar{\upsilon}c \qquad (55)$$

Where "h" denotes Planck's constant, "c" denotes the speed of light, and "E" denotes energy absorbed during the electronic transition of a molecule from its ground state (lower energy) to its excited state (higher energy).

The spectrophotometer (model Jasco V670) presented in **Figure.II. 23**, was set to record from 190 nm to 2700 nm before and after the studied alloys were immersed in the tested solutions. These spectra were then adjusted by considering the smoothing of Savitzky-Golay and the second derivative to improve the result of the bands and remove the baseline[138].

The minimum on the second derivative curve indicates the position of an absorption band, while the difference in ordinate between the minimum and the next maximum determines its amplitude[139].

Figure.II. 23: UV-Vis-NIR Spectrophotometer (Jasco model V670).

II.7.2 Scanning electron microscopy and energy dispersive spectroscopy.

Scanning electron microscopy (SEM), a technique for surface characterization, enables observations at the nanometric level. This approach does not depend on the detection of secondary electrons that are attracted to the sample by bombardment[140].

SEM is a widely used technique for microscopic topography. The principle of scanning electron microscopy is to scan the surface of a sample with an electron beam. A detector measures the flow of secondary or backscattered electrons emitted by the irradiated sample. A beam of electrons emitted by a thermionic gun strikes the surface of the material to be observed. The latter, under the impact of primary electrons, reacts by emitting different types of signals. A synchronous detection between the beam scanning and the electrons emitted by the material allows reconstituting of a signal observable on a video screen.

Figure.II. 24:Scanning electron microscopy.

The SEM is typically equipped with an X-ray spectrometer, which allows for the qualitative characterization of the microstructure and the chemical composition of the corrosion products on the material's surface using the EDX (Energy Dispersive X-ray) technique. The scanning electron microscope JEOLJSM-IT100 (***Figure.II. 24***), which enables the analysis of elements by X-ray energy dispersion, is used in our research to observe the sample's surface. Using 20 kV of voltage, the electrons are accelerated. The resolution is 3 nm and the magnifications can go from 6x to 106x.

II.7.3 X-ray diffraction

X-ray diffraction (XRD) is a technique used to determine the structure of crystalline materials and to identify unknown compounds, allowing crystal structures to be created. Each substance has a distinct X-ray diffractogram that can be used to identify it directly by comparing it to pre-existing crystallographic databases. This is referred to as the substance's "fingerprint."

II.7.3.1 Equipment and protocol

The process of X-ray diffraction is based on the constructive interference of monochromatic X-rays with a target and crystalline sample. X-rays are produced in an electron cathode tube and directed to a copper anode plate after being filtered to produce monochromatic radiation.

When a photon beam collides with an ordered set of atoms in a crystal plane, the electrons elastically scatter it into regular spherical waves. Although the majority of these waves experience destructive

interference, they add up constructively. It is important to keep in mind that diffraction only happens when Bragg's law is met, which means that wave diffraction only happens at specific angles known as Bragg angles where the wave patterns of the beam leaving the atomic planes are in phase (constructive interference)[141].

Bragg's law, which he developed in 1914, is as follows:

$$2d \sin_{hkl} \theta = n \lambda \qquad (56)$$

Where :

- $\mathbf{d_{hkl}}$: inter-reticular distance expressed in Å.
- **n**: integer number corresponding to the order of reflection.
- **λ**: wavelength of the radiation used (nm) related to the nature of the anticathode.
- **θ**: diffraction angle (°).

The scattered waves from each atom in the various planes will be in phase with each other, according to this law. The required conditions are depicted in ***Figure.II. 25.***

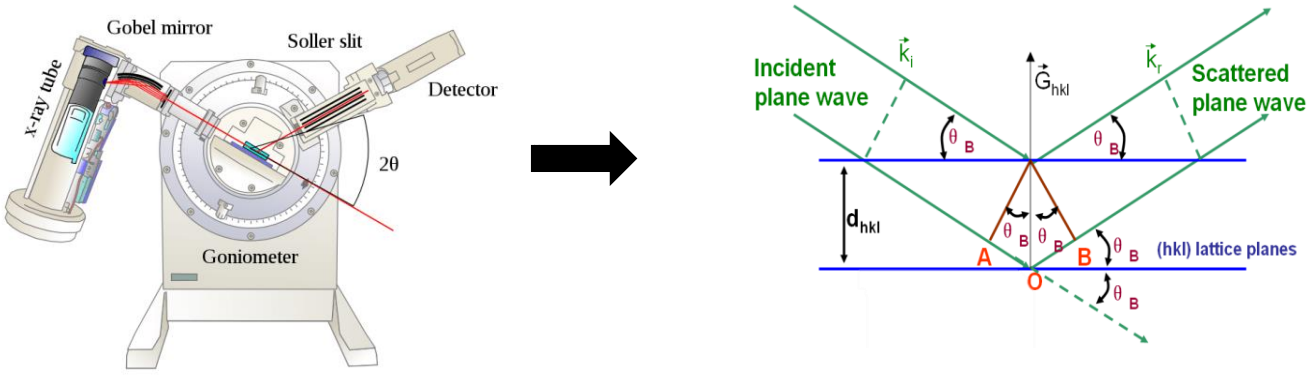

Figure.II. 26:Diagram of the X-ray diffraction phenomenon.

An x-ray electron detector measures the intensity of the diffracted X-ray beam as the number of current pulses per unit of time. Due to the random orientation of the material, all possible diffraction directions of the grating are reached by scanning the sample over a range of 2θ angles. Converting the diffraction peaks to d-spacing allows the element to be identified because each element has a unique set of spacings. Typically, this is accomplished by comparing the measured d-spacing to standard reference patterns.

XRD analysis was performed with a Shimadzu 6100 diffractometer (**Figure. II. 27***)* equipped with a copper anticathode (λCuKα = 1.541838 Å), a THA-1101 thin film attachment, and a THA-1101 thin-film attachment directly on the surface of the alloy at room temperature. 13) equipped with a copper anticathode (λCuKα = 1.541838 Å), a THA-1101 thin film attachment and an anticathode (λCuKα =

1.541838 Å), a THA-1101 thin film attachment and a CM-4121 monochromator counter monochromator CM-4121. The samples were scanned between 40 and 120° (2θ) at a speed of 2°/min with a tube voltage of 40 kV and a current of 30 mA.

Figure. II. 27:Shimadzu 6100 Diffractometer.

II.8. Molecular modeling by DFT and MDS

II.8.1 DFT calculations

The Material Studio (MS, version 7.1) software from Accelrys Inc.'s DMol3 module was used to carry out the DFT calculations[142,143]. A "double digital plus polarization" (DNP, 4,4 parameters) basis set was used to calculate the molecular structure of the studied compounds, its bulk quantum descriptors, and Fukui function indices using the generalized gradient approximation (GGA) and Perdew-Burke Ernzerhof (PBE)[144,145]. For geometry optimization in all DFT calculations, the default Dmol3 convergence criteria were used, with a "fine" quality.

The Chemical reactivity of the methyl linoleate molecule was described by the following parameters: HOMO energy, LUMO energy, energy gap (ΔE), ionization potential (I), electron affinity (A), electron chemical potential (μ), electronegativity (χ), overall hardness (η).[110]

The transferred electron fraction **(ΔN)** between the metals and the molecule was calculated according to Equation (64), where χ_{metal} and η_{metal} are electronegativity and hardness of the metal, respectively, while $\chi_{molecul}$ and $\eta_{molecule}$ are the corresponding molecular properties for the molecule.

$$\Delta E_{gap} = E_{LUMO} - E_{HOMO} \quad (57)$$

$$I = - E_{HOMO} \quad (58)$$

$$A = - E_{LUMO} \quad (59)$$

$$\mu = \frac{I+A}{2} \quad (60)$$

$$\chi = -\mu = \frac{I+A}{2} \quad (61)$$

$$\eta = \frac{I-A}{2} \quad (62)$$

$$\Delta N = \frac{\chi_{metal} - \chi_{molecul}}{\eta_{metal} - \eta_{molecul}} \quad (63)$$

To complete the local reactive characterization, the dual descriptor (Δf) (Eqs. (64), (65), (66), and (67) were computed at the same level of theory[147].

$$f_k^+ = q_k(N+1) - q_k(N) \quad (64)$$

$$f_k^- = q_k(N) - q_k(N-1) \quad (65)$$

$$f_k^\circ = q_k(N+1) - q_k(N-1) \quad (66)$$

$$\Delta f = f_k^+ - f_k^- \quad (67)$$

II.8.2 Dynamics molecular simulations.

MD simulations were also performed within the framework of the DFT approach in a system that included all of the factors controlling the adsorption behavior of the molecule on the surface of the materials studied. The MD simulations were carried out using the Material Studio program's Forcite module.

The crystalline metals imported from the Materials Studio database were cleaved along the (110) and (111) planes with a plate thickness of 16 A°. The reason for using the (110) and (111) planes was that they were found to have high stabilization energy values and an extremely compact structure. The metals (110) and (111) were first built and relaxed by minimizing their energy using molecular mechanics, then their surface was enlarged and their periodicity was adjusted by building a supercell, and finally a 30 A° thick vacuum plate was built on their surface. Five layers of metal atoms were used to provide enough depth for the molecule to be involved only in non-bonded interactions with the metal atoms in the surface layers while not excessively increasing the computing time.

With the help of the Adsorption Locator module of the Materials Studio software [146]; the metal and solvent layers were assembled in a simulation box, size 25 × 25 × 16 Å. All simulations were performed using the Condensed Phase Optimized Molecular Potentials for Atomistic Simulation Studies (COMPASS) force field in the canonical NVT ensemble (constant number of molecules, volume, and temperature) at 298 K.

For all dynamic simulations, an integration time step of 1.0 fs, periodic boundary conditions, and a simulation time of 5000 ps was used. By applying equations 68 and 69, we estimated the strength of the interaction by the interaction energy and the total binding energy, respectively

$$\mathbf{E_{interaction} = E_{total} - (E_{Surface} + E_{Mol})} \quad \mathbf{(}68\mathbf{)}$$

$$\mathbf{E_{binding} = - E_{interaction}} \quad \mathbf{(}69\mathbf{)}$$

While, E_{total}, $E_{surface}$, and E_{Mol} are the total energy of the system, respectively.

Chap III

Results & discussions

PART A:

Investigation of the corrosion of stainless steel, copper, and aluminum in sunflower biodiesel solution: Experimental and theoretical approaches

Chapter III: Results & Discussions

PART A: Investigation of the corrosion of stainless steel, copper, and Aluminum in sunflower biodiesel Solution: Experimental and theoretical approaches

III.1 Introduction

The biodiesel industry demands the utilization of materials that are resistant to corrosion and degradation due to the characteristics of the chemical reagents and catalysts used in the biodiesel production process and those of the fuel itself.

The biodiesel feedstock supply chain starts with the production and logistics of the feedstock, followed by the biodiesel's production, storage, and distribution. The ultimate step is the end use. Along the biodiesel supply chain, there is an enormous variety of systems, equipment, and components made of metallic and polymeric materials. Biodiesel comes into contact with many of these, primarily at the modern stages of production, storage, distribution, and end-use.

Previous studies have shown that biodiesel is more corrosive than diesel fuel. This can lead to problems like interaction with metallic surfaces and degradation of fuel properties. Degradation of the fuel by contact with the metal can also vary depending on the metal.

Many engine components are made of metals like aluminum, copper, and alloys, which can corrode when exposed to biodiesel. The characteristics of biodiesel cause numerous operational issues, including material incompatibility, the formation of heavy deposits on the engine, clogging of injectors, filter blocking, and piston ring delamination.

The goal of our research is to investigate the corrosion behavior of copper, aluminum, and stainless steel in biodiesel during production at room temperature and assess its impact on fuel property degradation using electrochemical, SEM/EDS, X-ray diffraction, and spectroscopic analysis. To further our understanding of the adsorption phenomenon, quantum chemical calculations (DFT) and molecular dynamics simulations (MDS) were carried out. Due to their extensive range of applications in automotive component production, these metals were chosen for the study.

III.2. Experimental procedure

III.2.1. Biodiesel production

Biodiesel is typically produced through the transesterification process [148]. The biodiesel used in this study was made by combining potassium hydroxide as basic catalyst and 99% of methanol in an ideal molar ratio of 6:1 by using vegetal sunflower oil [149].The ***Figure III . 1*** below describes the assembly used for studying three-metal corrosion during the production of biodiesel.

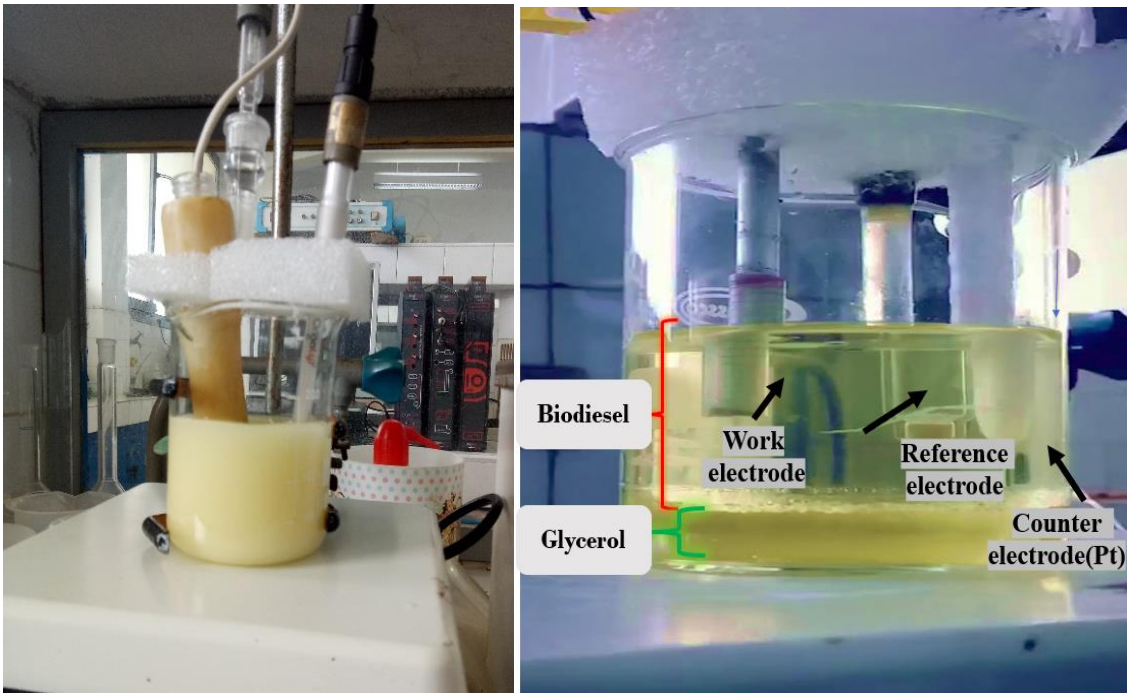

Figure III . 1: Electrolysis cell for the corrosion of the three metals in biodiesel production.

III.2.2. Characterization of synthesis biodiesel

III.2.2.1 Physicochemical characterization

The physio-chemical characteristics of the used and synthesized sunflower biodiesel, such as viscosity, density, and acidity index, were determined and presented in *Erreur ! Source du renvoi introuvable.It* is seen that this produced biodiesel has similar characteristics to EN 1421.

Table III . 1:: Physicochemical parameters of the synthesis of biodiesel.

	Standard Test Methods	Unit	Results
Density at 20 °C	ASTM D4052	kg/m³	890.2
Ester content	EN 14103	(wt.%)	93.50
Acid value	ASTM D664	(mg KOH/g)	0.451
Viscosity at 40°C	ASTM D455	(mm^2/s)	4.30
Cold Soak Filtration Test	ASTM D7501	°C	-3
Sulfur content	ASTM D5762	µg /l (ppm)	10
Flash point	EN ISO 2719	°C	70

III.2.2.2 GC/MS analysis

In the GC/MS analysis presented in Figure III . 2, we assessed the chemical composition of synthetic biodiesel. We know that the most important components of biodiesel depend heavily on the nature of the oil used;

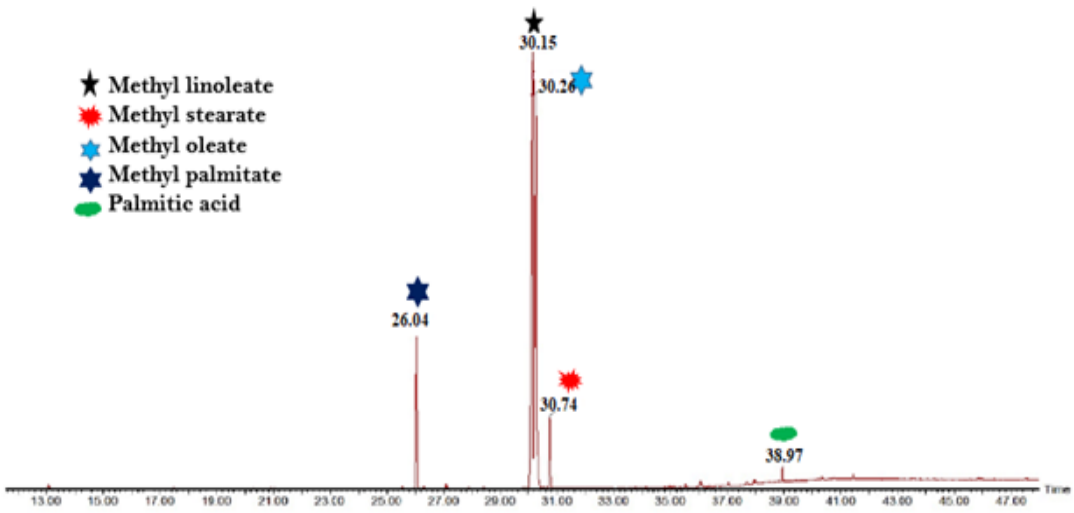

Figure III . 2: GC/MS Chromatogram of biodiesel

The CG/SM chromatogram identified five main peaks which characterize our biodiesel obtained after the electrochemical test. We found that the three solutions tested by GC/MS presented the same compounds, so we chose stainless steel for a more detailed study.

Although the contents of the compounds methyl palmitate (C17), palmitic acid (C16), methyl linoleate (C19), methyl oleate (C19) and methyl stearate (C19) are presented in the biodiesel (in molar percentages) as 13.43%, 0.36%, 50.36%, 31.12% and 4.75%, respectively ***Table III. 2***. It is obtained

that the biodiesel generally produced by direct trans-esterification processes contains fatty acids in the C16-C20 range, the discrepancy is attributable to the fatty acid contents of natural oils. In reality, climate conditions, soil type, and the growing season, as well as the plant's maturity and genetic variety, are all elements that influence fatty acid compositions[150,151].

Table III. 2: Fatty acid composition in the biodiesel product.

Fatty acid type	Retention time (min)	Identified compounds	Chemical formula	mole conc. (%)
Methyl octadeconoate	26.04	methyl stearate	$C_{19}H_{38}O_2$	13.43
9,12-octadecadienoic acid (z,z)-, methyl ester	30.15	methyl linoleate	$C_{19}H_{34}O_2$	50.36
9-octadecenoic acid (z)-, methyl ester	30.26	methyl oleate	$C_{19}H_{36}O_2$	31.12
Tetradecanoic acid, 10,13-dimethyl-, methyl ester	30.74	methyl palmitate	$C_{17}H_{34}O_2$	4.75
Tetradecanoic acid, 12-methyl-, methyl ester	38.96	Palmitic acid	$C_{16}H_{32}O_2$	0.36

III.2.2.3 Infrared spectroscopy (FTIR) analysis

The FT-IR spectra were used to identify the functional groups and bands that correspond to the different stretching and strain vibrations in the biodiesel samples. The position of the carbonyl group in FT-IR is known to be sensitive to the effects of both the substituent and the molecular structure[152].

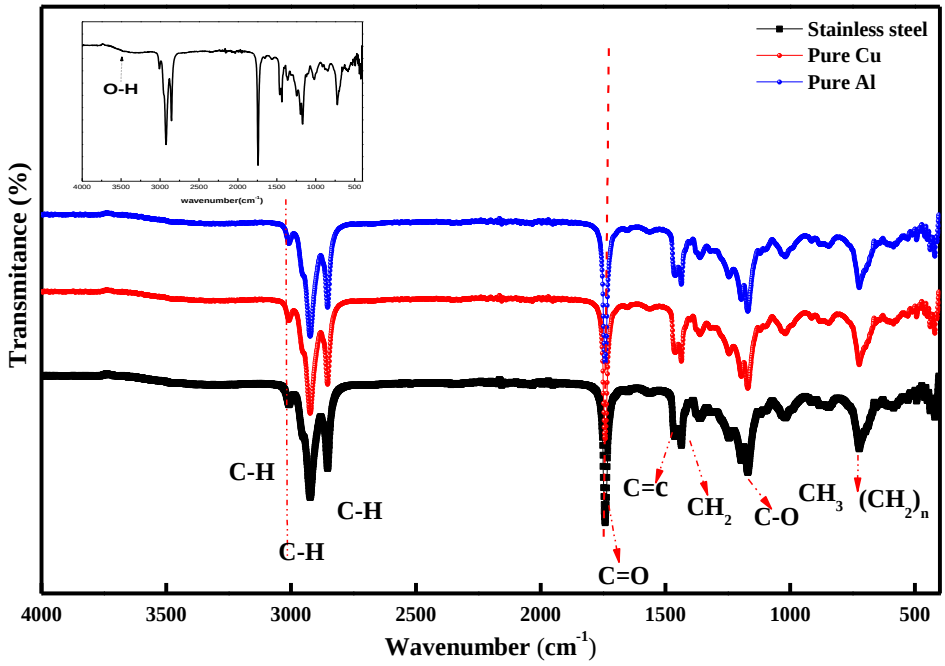

Figure III . 3: FTIR spectrum of the synthesis biodiesel with different used substrates.

From ***Figure III . 3***, the esters show two strong absorption bands, those of carbonyl ($\nu_{C=O}$) at 1750-1730 cm-1 and C-O (antisymmetric axial stretching and asymmetric axial stretching) at 1300-1000 cm-1. Other functional group peaks in biodiesel were detected in the spectra, including sp2 C-H stretching vibration at 3194 cm-1, sp3 C-H at 2916, 2855, 2731, and 2677 cm-1, and C-C stretching vibration at 1597 cm-1. In addition, bending vibrations of CH2 were recorded at 1458 cm-1, CH3 at 1373 cm-1, C-C at 872 cm-1, and (CH2S)n at 725 cm-1. The peak at 3472 cm-1 is generally attributed to the O-H bands, which are thought to be caused by the FFAs in the biodiesel and the residual glycerol in the biodiesel[153].

Concerning the spectrum of the copper in biodiesel, we notice the presence of peaks in the region of ~540, ~610, and 3323 cm-1 looks to indicate the presence of CuO, Cu2O, and the hydroxyl group (-OH), respectively. In addition, the peaks observed in the regions ~1020, 1434, and 1740 cm-1 are more likely to be attributed to the carboxylate anion (COO-). The -OH group appears indicative of Cu(OH)2, while the presence of the carboxylate anion (COO-) suggests that the film is composed of a mixture of metallic CuO and carboxylate derivatives (corrosion compounds).

Similarly, the spectrum of stainless steel in biodiesel, shows a peak at 583 cm-1, suggesting the creation of the Fe2O3 compound. In addition, the 1020 cm-1 and 1327 cm-1 areas showed the presence of corrosion products such as γ-FeO(OH), and α-FeO(OH). The peak observed at 1710 cm-1, indicates the formation of Fe2O2CO3. Thus, free hydroxyl groups (-OH) are either detected in the area between

3601 cm^{-1} and 3788 cm^{-1} indicating the presence of Fe(OH)3. Furthermore, the spectrum of the aluminum shows an absorption band at wave number 588.29 cm-1 suggesting the presence of Al-O stretching.

III.2.3. Electrochemical measurements

III.2.3.1 Evolution of the Eocp versus time

Figure III. 4 depicts the E**ocp** values as a function of time for the three metals examined during sunflower biodiesel generation after 120 minutes of submersion. all E_{OCP} values were negative and nearly stable, indicating that biodiesel was produced.

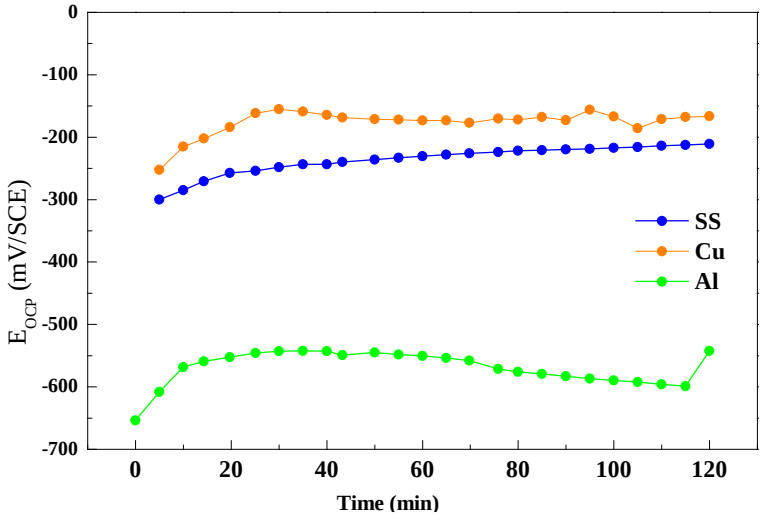

Figure III. 4:The variation of E_{OCP} values of stainless steel, aluminum, and copper in sunflower biodiesel.

The results of our research indicate that the negative E_{OCP} values suggest that the metal surfaces used in biodiesel had high electrochemical activity during the production process. These observations may be related to an increase in the corrosion activity of the metal surfaces caused by the oxidation of biodiesel, which could lead to the formation of corrosion products on the metal surfaces.

Based on the nature of these corrosion products, they may or may not have a protective effect. According to the literature, several of these compounds have been found in the surface metals of biodiesel. Fe_2O_3, $Fe_2O_2CO_3$, and $Fe(OH)_3$ corrosion products were found on the stainless steel exposed during the synthesis of sunflower biodiesel, as well as the formation of Cr_2O_3 and Al_2O_3 on the aluminum substrate[154]. However, when the copper substrate was exposed to palm biodiesel, corrosion products such as Cu_2O, CuO, and $Cu(OH)_2$ were produced[155].

III.2.3.2 Potentiodynamic polarization

Figure III. 5 presents the potentiodynamic curves of aluminum and copper, and stainless-steel during biodiesel production at various times (t=0, and t=120 min). The respective electrochemical parameters (corrosion potential $\mathbf{E_{corr}}$, corrosion current density $\mathbf{i_{corr}}$, and **Ip** passive current density, and Tafel constants (β_a, β_c) were derived from Tafel plots and displayed in the table

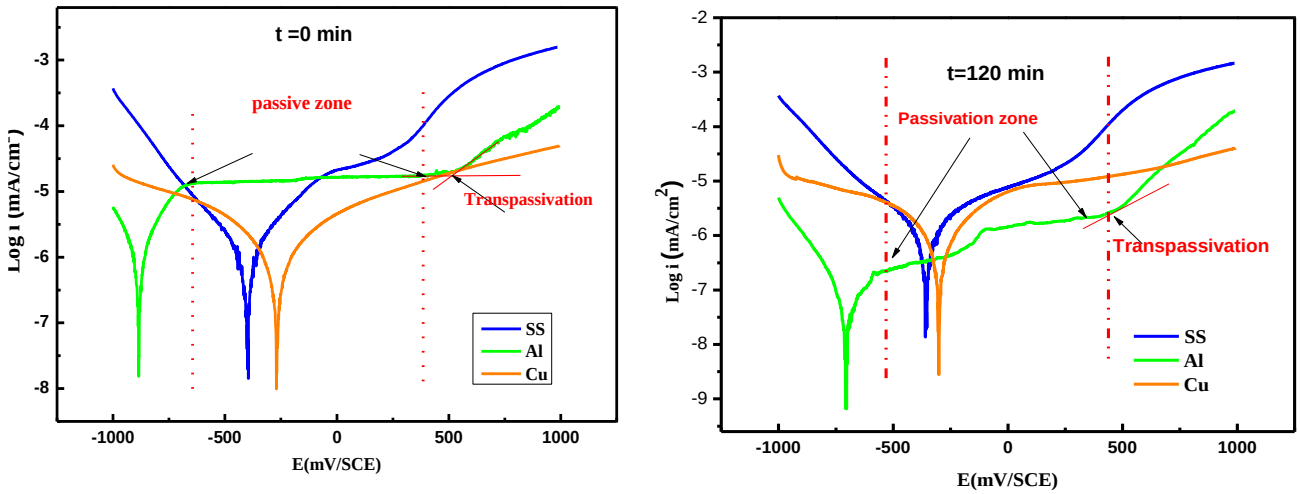

Figure III. 5: Potentiodynamic polarization curves of Al, stainless steel, and Cu at different times of biodiesel production.

From the potentiodynamic curves, it is evident that both aluminum (Al) and stainless steel (Ss) exhibit a passive behavior. This behavior is characterized by the formation of a thin and protective oxide layer on the surface of the metal, acting as a barrier against further corrosion.

At the beginning of the test (t=0 min), we can observe the passive behavior of aluminum, indicating the formation of a stable passive system(-648 mV/SCE to 386 mV/SCE). Over time, this passive behavior is also observed at the end of the test (t=120 min) but is unstable. The passive zone typically occurs at a higher potential in the presence of oxygen from the environment, resulting in the formation of aluminum oxide (Al2O3). This oxide layer effectively prevents further corrosion. Moreover, within the unstable passive zone, both the corrosion current density and the passive current density values show no changes due to the oxidation of biodiesel, as stated in the essay's conclusion.

Regarding stainless steel, during the initial stage of the test(t=0), disturbances in passivity are observed in the anodic part. This behavior can be attributed to the instability of the biodiesel. The anodic polarization curves reveal the presence of a pseudo-passive region within a potential range of (-181 mV/SCE to 398 mV/SC) for t=0 and of (-183 mV/SCE to 400 mV/SC) at the end of the test. This suggests that the solution has achieved quasi-stationary stability due to the formation of a protective

passive layer on the stainless steel surface. However, at higher potentials, this passive layer disappears, which can result in either uniform or pitting corrosion.

On the other hand, copper is known to be susceptible to corrosion in the presence of fatty acids, which are present in biodiesel. These fatty acids could react with copper to form soaps resulting in the degradation of the metal's surface and potential corrosion.

In addition, based on ***Erreur ! Source du renvoi introuvable.***. The variation in corrosion current density illustrates an unstable behavior related to the instability of the solution conductivity. This indicates that the fresh species involved in the reaction are not reaching the active surface of the electrode, or the corrosion products are not diffusing away from the active surface. The lower corrosion current density Icorr (0,963-0,1**($\mu A/cm^2$)**) was measured for the pure AL durant the test. Moreover, the IP increased with time. This implied the higher resistance of AL Durant the biodiesel production. furthermore, the copper's corrosion current density displayed the high values which mean a high corrosion rate .

Table III . 3:Electrochemical parameters of the tree metals in Sunflower biodiesel production durant 120 min.

	Time (min)	**E_{corr}**	**I_{corr}**	**Ep**	**Ip**	**E_{Br}**	**I_{Br}**	**β_a**	**$-\beta_c$**
Metals		**(mv/SCE)**	**($\mu A/cm^2$)**	**(mv/SCE)**	**($\mu A/cm^2$)**	**(mv/SCE)**	**($\mu A/cm^2$)**	**(mV/dec)**	**(mV/dec)**
AL	**0**	-884,773	0,963	208,0	1,8201	507,5	1,7377	227,4	215,5
	120	-706,141	0,1	203,0	3,2610	491,2	2,489	274,6	250,2
SS	**0**	-398,40	0,98					230,5	252,8
	120	-357,92	0,825					423,1	164,2
Cu	**0**	-268,56	1,824					603,9	504,9
	120	-272,19	1,298					419,3	441,4

III.2.3.3 Electrochemical impedance spectroscopy

Figure III . 6 shows the EIS data in both Nyquist and Bode form for the various testing metals used in the synthesis of sunflower biodiesel at various immersion times.

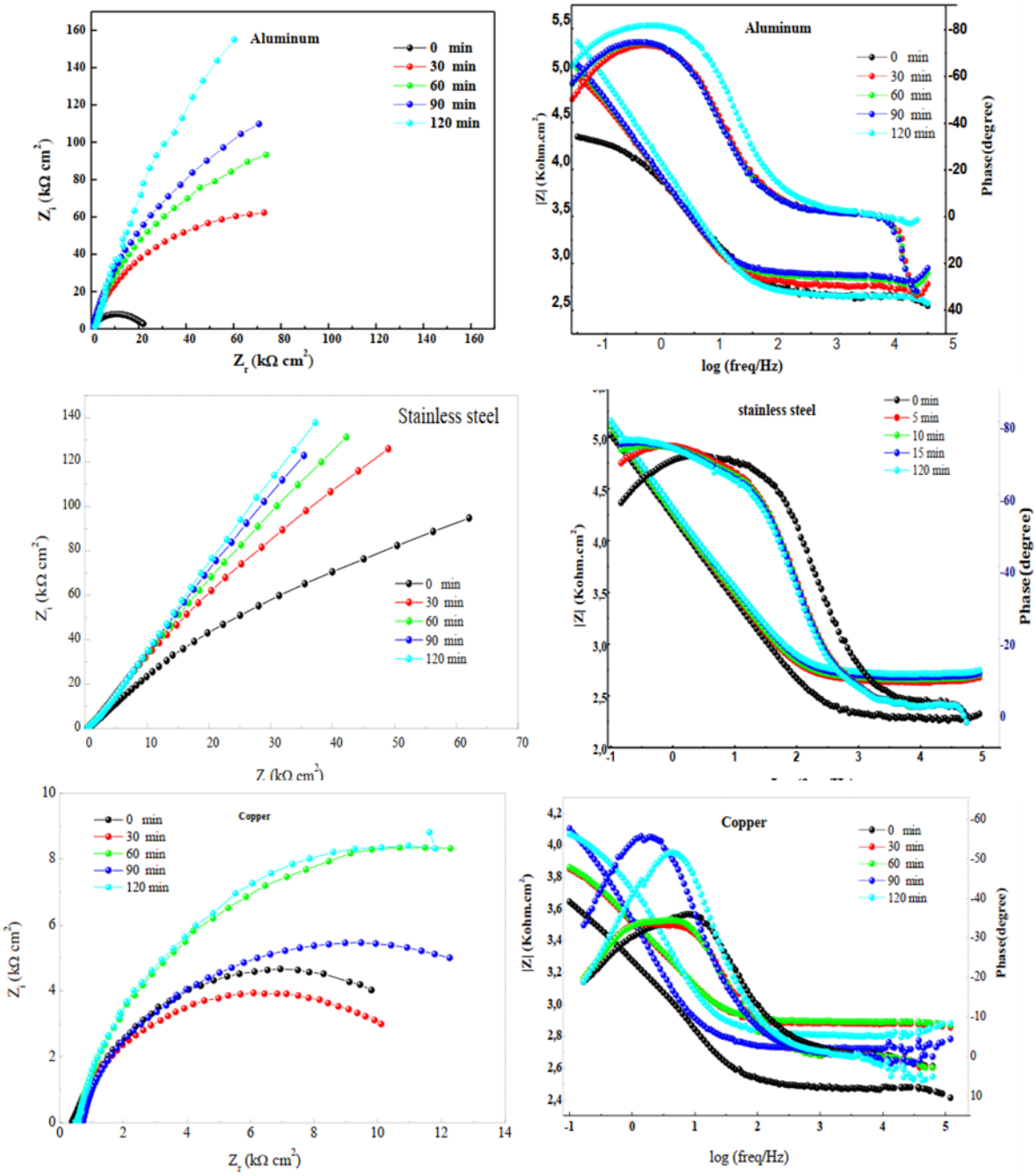

Figure III . 6:Nyquist (right) and Bode (left) plots of different used metals after biodiesel tests production at the EOCP .

Figure III . 6 depicts the electrochemical impedance spectra following the Nyquist representation, which reflects the influence of time on the metal's (Ss. Al. Cu) corrosion resistance during biodiesel production.

Furthermore, this approach provides information on the resistive and capacitive behavior at the interface and allows for the evaluation of the investigated compounds' efficacy as metal corrosion inhibitors. The strength of this approach is that it distinguishes response events based on their

relaxation time. We were able to approximate the intrinsic characteristics of the contact using the values of the transient electrochemical parameters.

The Nyquist plots obtained show a unique flattened capacitive semicircle for all three metals with two capacitive time constants typically appearing in the Bode diagrams. The semicircle in the Nyquist plots is characteristic of work electrodes that show a dispersion of the impedance frequency for all the samples and their deviations are attributed to the inhomogeneity and roughness of the exposed surface. The diameter of the semicircle for each material changes significantly from 10 minutes of biodiesel production to 60 minutes for each material. This could be due to the formation of corrosion products that protect the surfaces of the materials, notably stainless steel and aluminum by creating an oxide layer, known as a passive layer.

As outlined earlier in the E_{OCP} data, the loop diameter progressively decreases with time due to an increase in corrosion activity on the metal surface caused by the oxidation and degradation of biodiesel and the creation of certain corrosion products on the metal surface. Thus, beyond 65 min, the EIS spectra indicated that the corrosion resistance values increase with time in the case of aluminum and stainless steel which prevented the metals from oxidation and prevented active species from diffusing on the electrode surface allowing for lower corrosion rates. In contrast, the copper spectra show that the diameter of the loops is unstable and changes with time [156].

In addition, the Bode diagrams reveal a significant solution resistance that diminishes with time, as well as two slopes indicating the presence of two-time constants. The first is based on the resistance of the film layer, while the second demonstrates the charge transfer mechanism (Rct). Furthermore, it is discovered that the modulus value increases with time for up to 60 minutes before becoming stable. It has also been observed that the value of the phase angle decreases with time at higher frequencies. It decreases for 60 minutes at low frequencies before increasing. These findings might be related to the formation of a long-lasting protective layer[157].

Further to that, for high frequencies, the phase angle is near 0 and the values of |Z| are between -1 and 5 cm^2, indicating that the impedance is regulated by the kinetics of the transfer resistance. Indeed, the phase angle values approach the maximum at 80, demonstrating the passive film's capacitive nature. The values of |Z| drop at low frequencies, representing the resistance of the passive film formed in the metal surfaces [158].

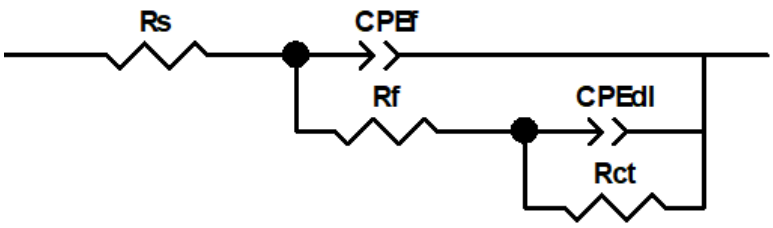

Figure III. 7:Proposed electrical circuit for the metal/solution interface.

The EIS parameters were simulated by the proposed electrical circuit illustrated in ***Figure III. 7,*** whereby **Rs** is the solution resistance, $\mathbf{R_{ct}}$ is the charge transfer resistance, $\mathbf{CPE_{dl}}$ is a constant phase element, $\mathbf{R_f}$ is the resistance of the film formed by the corrosion products and CPEf is the constant phase element. **CPE** is often attributed to time constant distributions induced by interfacial heterogeneity and roughness, the magnitude of which is of the order of 1-2%.

CPE is frequently attributed to time constant distributions induced by interfacial heterogeneity and roughness, the magnitude of which is defined by the divergence of the CPE constant from the ideal capacitive behavior. and its impedance $\mathbf{Z_{CPE}}$ is given by[159] :

$$\boldsymbol{Z_{CPE} = \frac{1}{Y_0(i\omega)^n}} \qquad (70)$$

where Y_0 is the $\mathbf{Z_{CPE}}$ constant, ω is the angular frequency (in rad s-1), i2 = -1 is the imaginary number and n is a $\mathbf{Z_{CPE}}$ exponent which can be used as an indicator of surface heterogeneity and roughness.

Electrochemical impedance characteristics from fitting the EIS data to the expected electrical circuit are given in **Table III . 4**.

The high value of solution resistance in this table was typical of biodiesel. As the test progresses, this number rises gradually, indicating both a reduction in electrochemical processes and a decrease in corrosion rate as a function of time. A further commonality is that irrespective of the chemical composition of the metal, the corrosion product resistance, $\mathbf{R_f}$, is significantly higher than the charge transfer resistance, $\mathbf{R_{ct}}$, suggesting that the corrosion resistance of the metal is formed by the film generated by the corrosion products.

Table III . 4:Electrochemical parameters used to fit the EIS data for metals in biodiesel tests.

Metal	Time (Min)	Rs(KΩ.Cm²)	$10^{-6}Q_{dl}$ (F Sn Cm²)	n_{ct}	R_{ct}(Ω.Cm²)	Q_f (F Sn. Cm²)	n_f	R_f (Ω.cm²	R_p(Ω. Cm²)
	0	204.3	36.9	0.74	1.34E+03	1.63E-05	0.865	1.63E+02	1.50E+03
	30	446.9	8.07	0.87	2.08E+04	2.37E-06	0.8045	9.66E+02	2.18E+04
Ss	60	459.3	8.37	0.86	2.08E+04	2.16E-06	0.8343	1.83E+03	2.26E+04
	90	484.3	7.63	0.87	1.87E+04	2.88E-06	0.8222	3.01E+03	2.17E+04
	120	520.06	7.73	0.86	2.21E+04	2.67E-06	0.8369	5.14E+03	2.72E+04
	0	447.7	44.47	0.86	1.93E+04	1.64E-04	0.5623	3.85E+04	5.78E+04
	30	502.8	46.07	0.9	2.50E+04	3.12E-04	0.6997	4.58E+06	4.61E+06
Cu	60	550	53.96	0.86	1.94E+04	4.36E-04	0.5804	2.43E+05	2.62E+05
	90	527.3	30.71	0.82	1.61E+04	2.02E-05	0.8849	2.61E+04	4.22E+04
	120	529.5	66.17	0.83	2.14E+04	1.44E-04	0.9111	1.20E+04	3.34E+04
	0	441.1	11.81	0.800	2.21E+04	1.10E-07	0.8	9.73E+04	1.19E+05
	30	584.2	15.12	0.92	7.44E+04	3.12E-06	0.8018	1.08E+05	1.82E+05
Al	60	718.5	18.1	0.84	5.91E+04	1.75E-05	0.999	1.76E+05	2.35E+05
	90	779.7	9.04	0.9	4.63E+05	3.04E-06	0.5462	4.19E+06	4.65E+06
	120	797.3	9	0.891	1.02E+04	6.10E-07	0.5031	3.67E+05	3.77E+05

III.2.4 . Spectroscopies Analyses

III.2.4.1 UV–Vis-NIR spectroscopy

The purpose of this research is to determine the impact of biodiesel production on the chemical composition of corrosion products generated on the surface of the substrates under investigation (Al, Cu, and SS). So, the studied region is between 190 nm and 2700 nm, and the spectra are interpreted according to the second derivative of the absorbance curve. Indeed, the absorbance curve's second derivative has been used to display weak absorption bands and improve the outcomes of bands formed by various electronic or vibratory transitions in corrosion goods. The minimum in these curves indicates the position of absorption bands, while the difference between the minimum and the next maximum determines its amplitude, which can be used for quantitative analysis according to the literature[160,161]. The obtained UV–Vis-NIR absorbance spectrum for three metals in biodiesel solution is presented in ***Figure III . 8.***

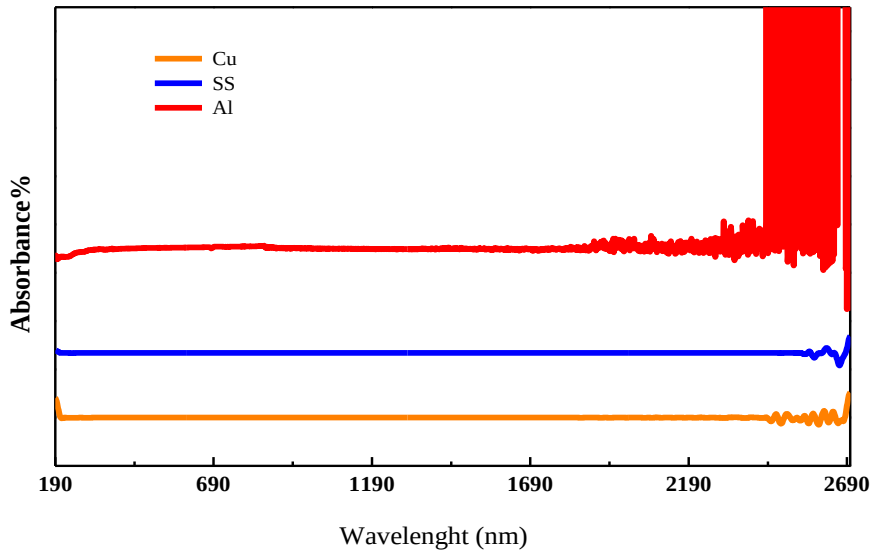

Figure III . 8:UV–Vis-NIR absorbance Spectrum for aluminum, Stainless steel and Copper in biodiesel solution.

Therefore, the aluminum reflectance spectrum presented in ***Figure III . 9*** shows the formation of the oxide layer on its surface and displays the main corrosion products at their different wavelengths. Specifically, the peaks between 205 nm and 265 nm are attributed to the aluminum oxide Al_2O_3, which protects almost the entire surface from corrosion attack.

Indeed, the detected peaks located at 242 nm and 344 nm are related to the AlOOH product. The amplitude of the obtained peaks is significantly reduced after the production of biodiesel, which indicates a diminution of the content of corrosion products on the aluminum surface.

On the other hand, the UV–Vis-NIR spectra of stainless steel in biodiesel solution are presented in ***Figure III . 9*** At different wavelengths, these spectra explain the principal corrosion compounds.

The discovered peaks at 210 nm and 250 nm are attributable to char

ge transfer between Lepidocrocite (γ-FeOOH) and maghemite (γ-Fe_2O_3), respectively ***(Figure III .*** 9***a)***, and the intense bands at 2668 nm and 2688 nm are attributed to the -OH group with unique coordination into the maghemite structure(**Figure III . 9 *b***). In addition, the peaks detected at 412 nm, 606 nm, and 726 nm are chromium oxides (Cr_2O_3), and the peaks at 380 nm, 432 nm, 680 nm, and 712 nm are nickel (Ni_2O_3) oxides (NiO) [162].

After immersing the sample in the biodiesel solution, the amplitude of the peaks increases, indicating an increase in the composition of the stainless-steel surface, which is a symptom of the degradation of the biodiesel. Moreover, the peaks found between 500 and 2200 nm had a higher amplitude than those observed between 200 and 500 nm. This result is consistent with the XRD analysis of the iron oxide product presented below.

Moreover, the reflectance spectrum of copper in the biodiesel solution is presented in ***Figure III . 9***. This figure illustrates the growth of the oxide layer on the copper surface and reveals the dominant corrosion products at their different wavelengths. Additionally, the observed peaks between 258 nm and 275 nm are associated with copper oxide CuO, and the reflectance peaks at 345 nm, 388 nm, and 550 nm are attributed to Cu_2O products[163,164]. The amplitude of the observed peaks increases dramatically following biodiesel synthesis, showing an increase in the content of produced corrosion products on the copper surface and explaining the significance of the biodiesel degradation-induced dissolving process. These results were verified later by using SEM/EDS analyses.

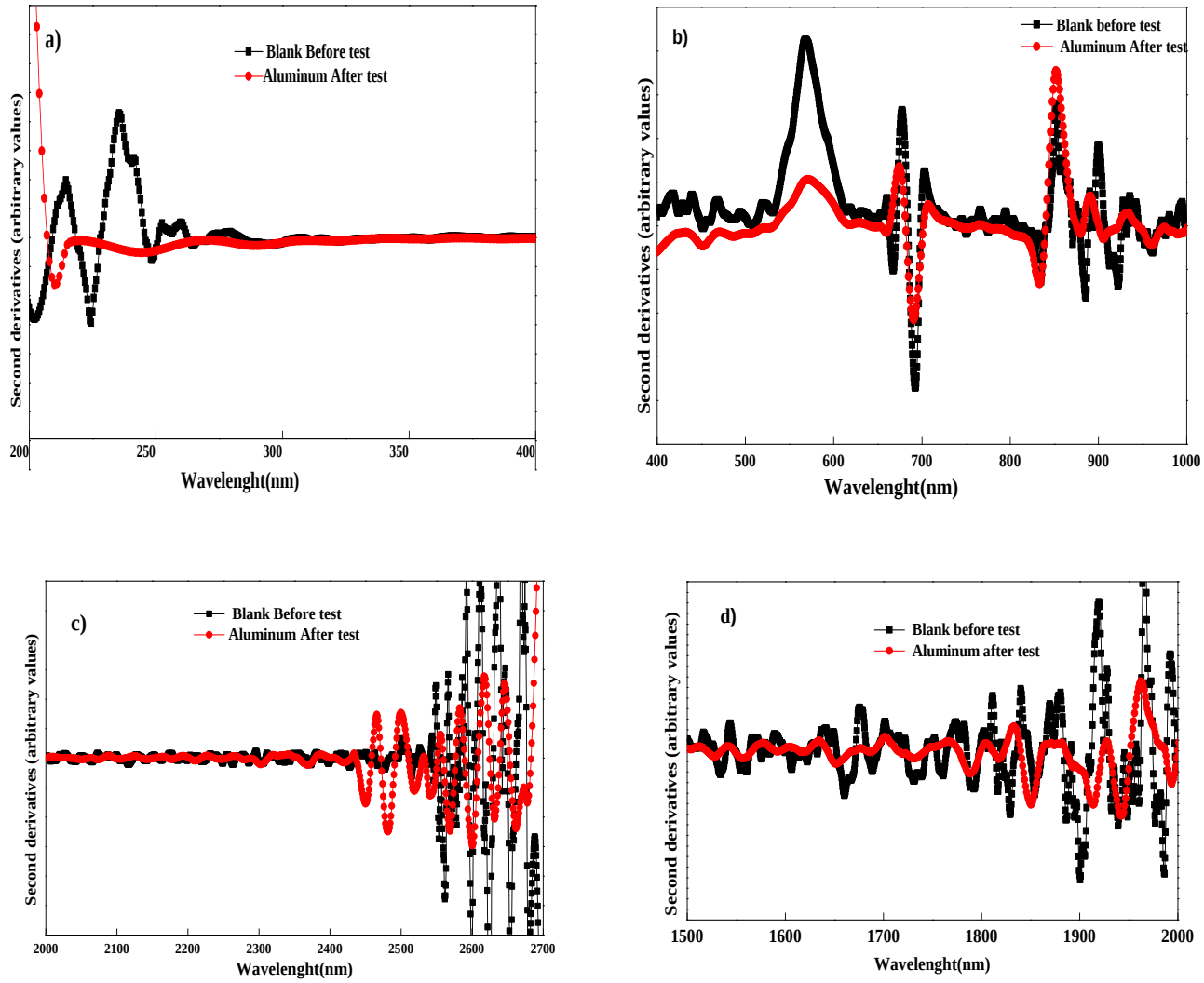

Figure III . 9:Second derivative absorption spectra of the aluminium substrate before and after the test.

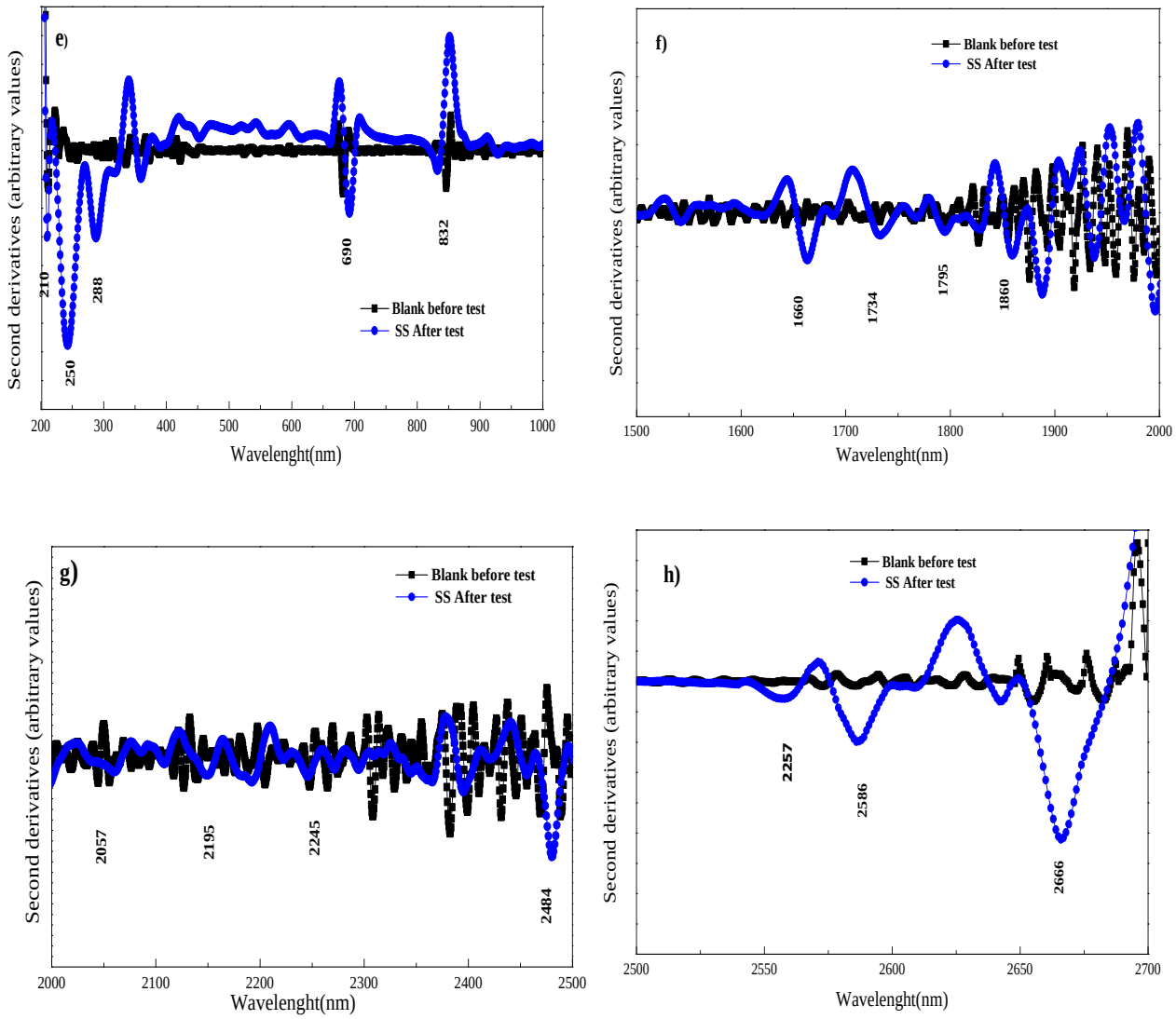

Figure III. 10: Second derivative absorption spectra of stainless-steel substrate before and after the test.

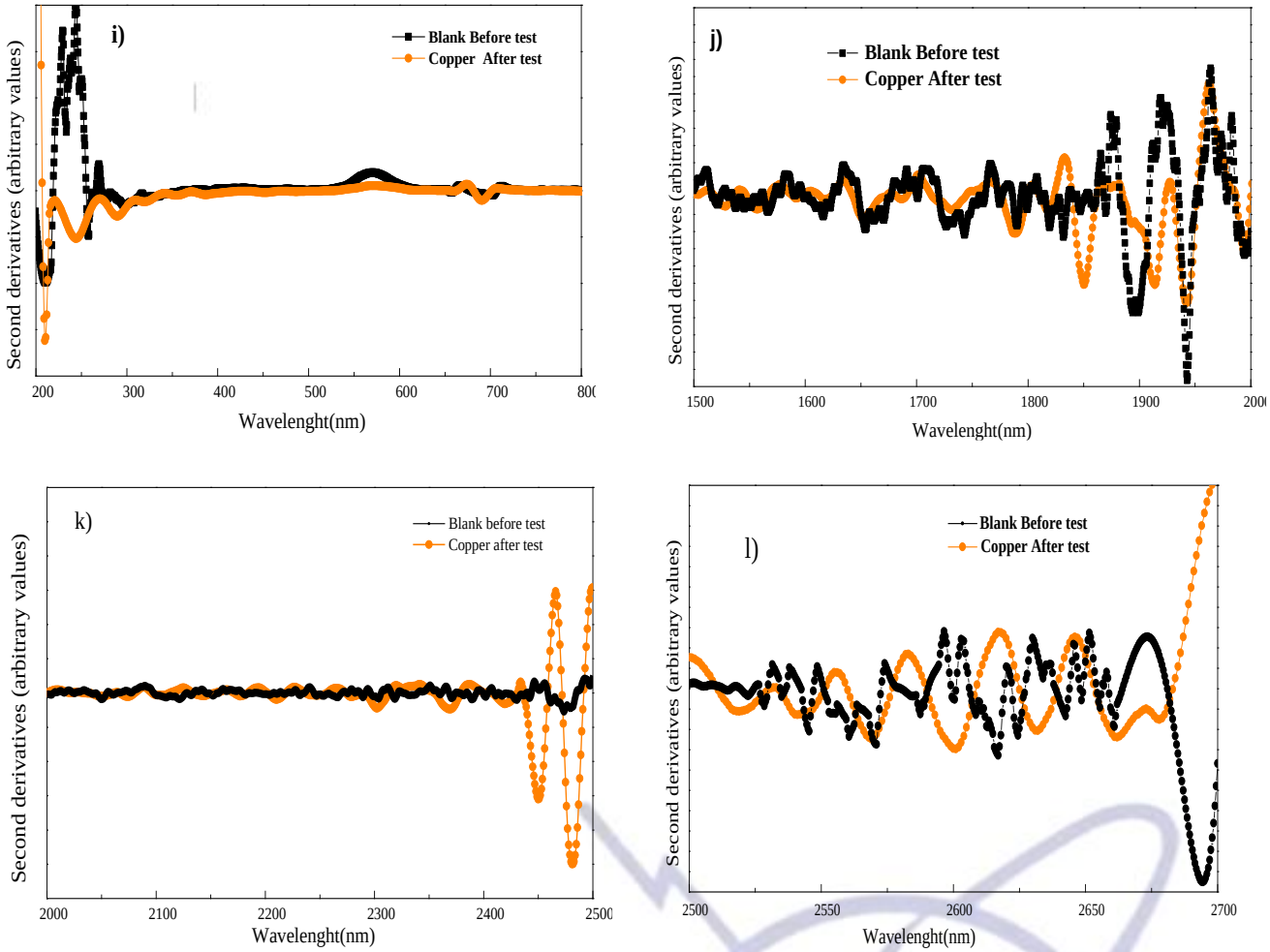

Figure III. 11:second derivative absorption spectra of the copper substrate before and after the test.

III.2.4.2 UV/Vis absorption spectroscopy analysis

In the current research, we performed UV-vis spectroscopic analysis to detect the amount of metal ions released during biodiesel production.

Figure III. 12 shows a variation in the absorption bands of metals in contact with the generated biodiesel. As a result, the copper ions present in the biodiesel solution have a stronger absorption band. This significant increase in UV-vis absorption in the range of 225-262 nm correlates with the oxidation process of copper. It further resulted that compared to copper, the UV-vis absorption band of stainless steel and aluminum is tiny. This indicates that the levels of oxidation products are lower, implying that the resistance of the metals inhibits oxidation (SS and Al)[165].

Furthermore, the difference in intensity of these bands was of particular interest for the subsequent oxidation steps. Indeed, the oxidation compounds with a double conjugated bond absorb energy in the ultraviolet and visible regions. It is widely recognized that conjugated dienes of linoleic acid exhibit an absorption peak at 235 nm due to $\pi \rightarrow \pi*$ transitions, and an absorption band centered at 262 nm due to π-$\pi*$ transitions in the linoleic acid structure[166–168].

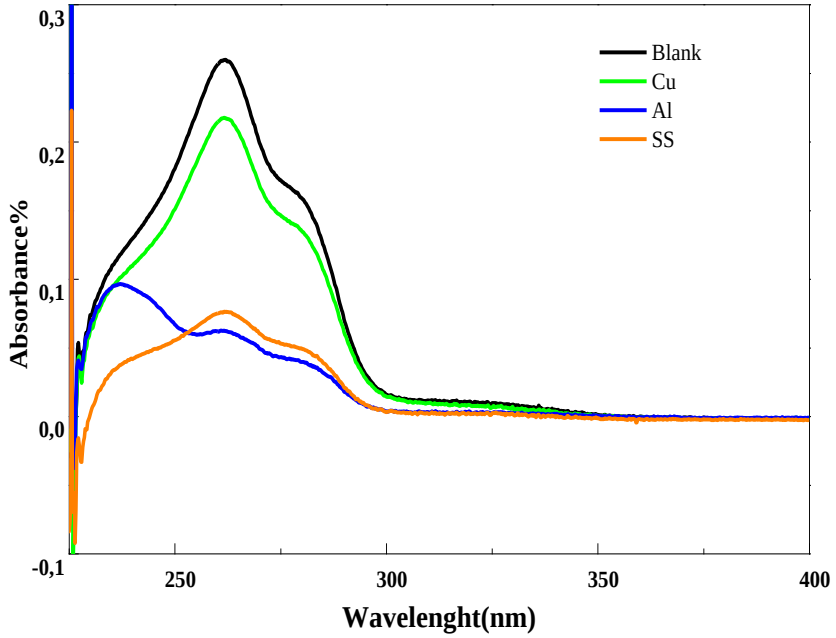

Figure III. 12:UV–Vis spectra of sunflower biodiesel after the test.

III.2.4.3 Flame atomic absorption spectroscopy

The goal of the study here described was to evaluate the combination of a microemulsion sample preparation procedure and the introduction of microemulsions by discrete aspiration using FAAS for biodiesel analysis. The improvement of sensitivity using FAAS for the determination of metals in biodiesel microemulsions can be reached by adopting a discrete aspiration procedure for sample introduction into the flame.

Using a discrete aspiration approach for sample input into the flame improves sensitivity when using FAAS to determine metals in biodiesel microemulsions. This technique allows for the entry of a lower volume of sample into the atomizer without negatively compromising the figures of merit. Moreover, the intensities of transient signals are recorded in peak area mode, yielding higher sensitivity as compared to standard continuous aspiration.

Figure III. 13 displays the result of the FAAS analysis. All metals, such as Fe, Ni, Cr, and Cu, release some of their elements into the sunflower biodiesel solution. Moreover, compared to aluminum and stainless steel, biodiesel synthesis produces a high concentration of released copper. On the contrary, Ni and Cr have negative values, indicating that their concentrations are below the detection limit of the instrument. The previously mentioned SEM/XRD examination revealed the difference in concentrations under the degradation of the metal by the production of corrosion products on the metal surface;

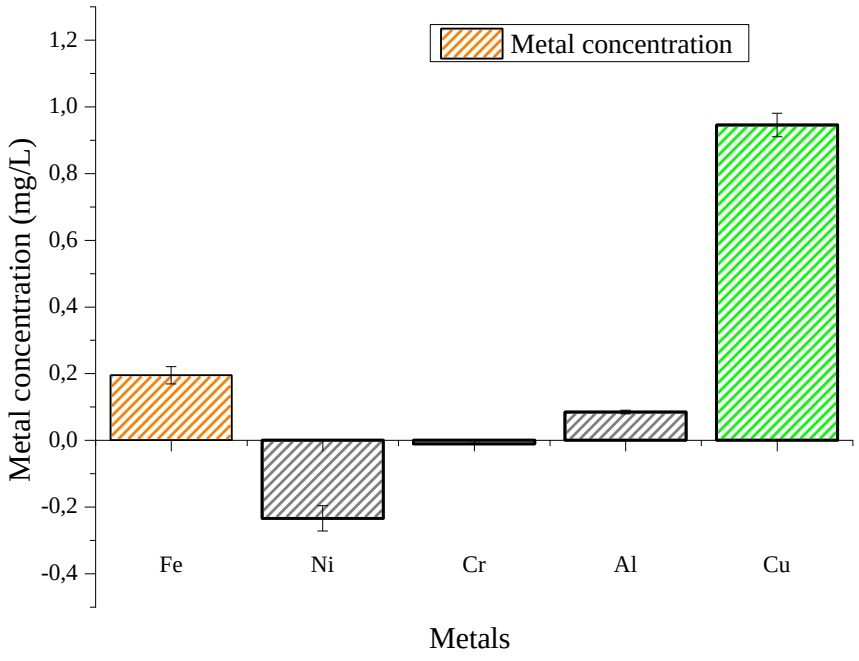

Figure III. 13: FAAS analysis of release metal elements into the sunflower biodiesel solution.

III.2.5. Surface analysis

III.2.5.1 SEM/EDS analysis

The SEM/EDS analyses of stainless steel, copper, and aluminum surfaces during biodiesel production are reported in the figures below. Here on the metal surface, the elemental distribution of corrosion products was mapped. Many of the adhering metal oxides that form on the surface of corroded metal are made of carbon and oxygen, while some organic deposits come from biodiesel. The rapid oxidation of metal into different oxides and subsequent further oxidation in the presence of oxygen are known properties of metal.

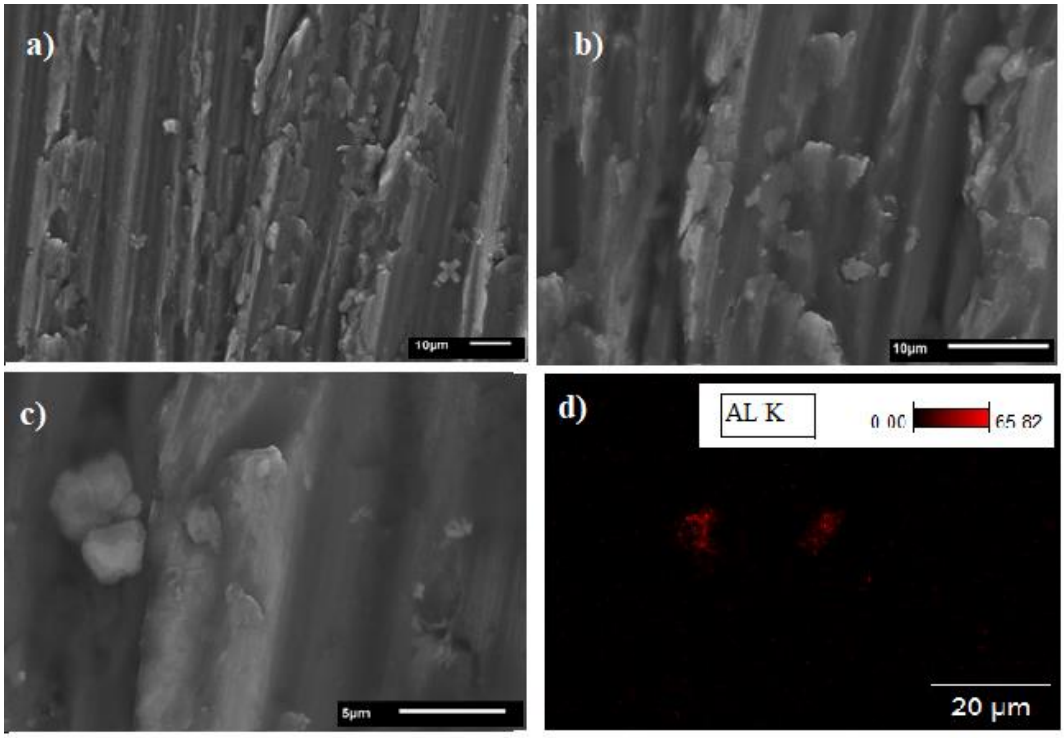

Figure III. 14: SEM micrographs of aluminum after the biodiesel production.

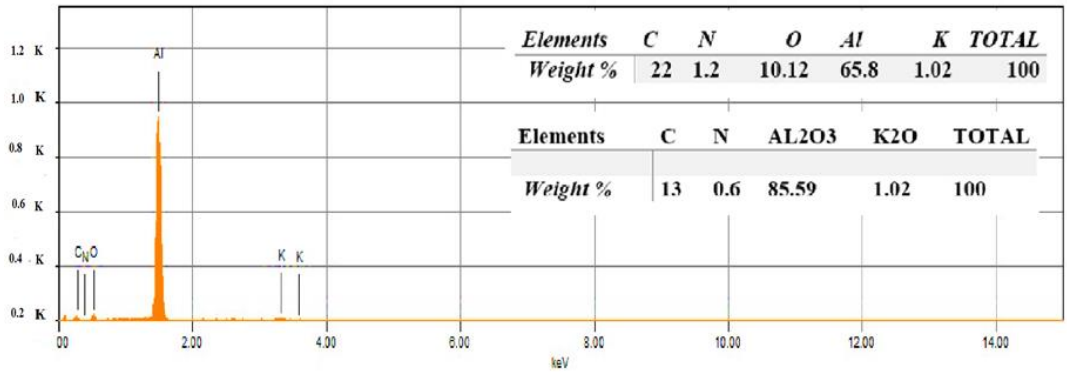

Figure III. 15:EDS spectrum of aluminum after biodiesel production.

However, according to several corrosion tests of aluminum in contact with different types of biodiesel, their corrosion rate varies with the biodiesel content[169]. Additionally, these investigations were carried out with aluminum used only with biodiesel from one type of sunflower, whereas in the current study, the aluminum showed high contact resistance during the production test, as indicated by SEM micrographs, with the appearance of a phase on its surface. The formation of a robust protective Al_2O_3 oxide coating (85.59%) on the metal surface is believed to be responsible for this effect. Moreover, the saturated and monounsaturated components of the fatty acid methyl ester composition are less vulnerable to oxidation processes, resulting in less material deterioration[170]. However, the SEM/ESD scans on the copper surface during biodiesel production are given in *Figure III . 16.*

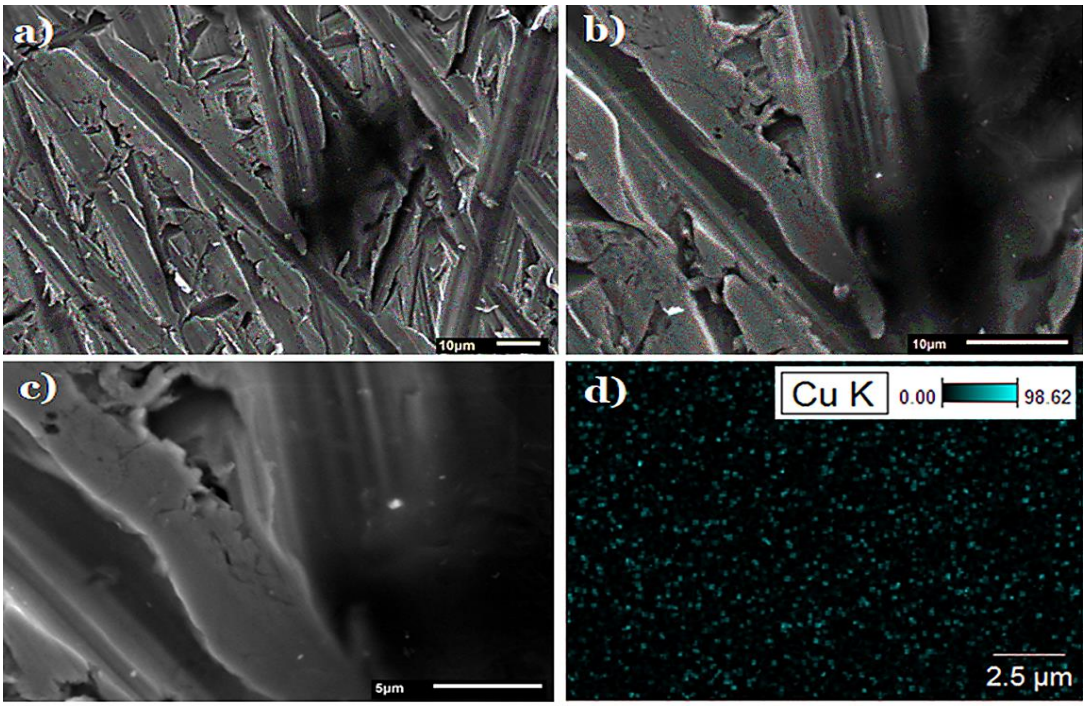

Figure III. 16:SEM micrographs of copper after biodiesel production.

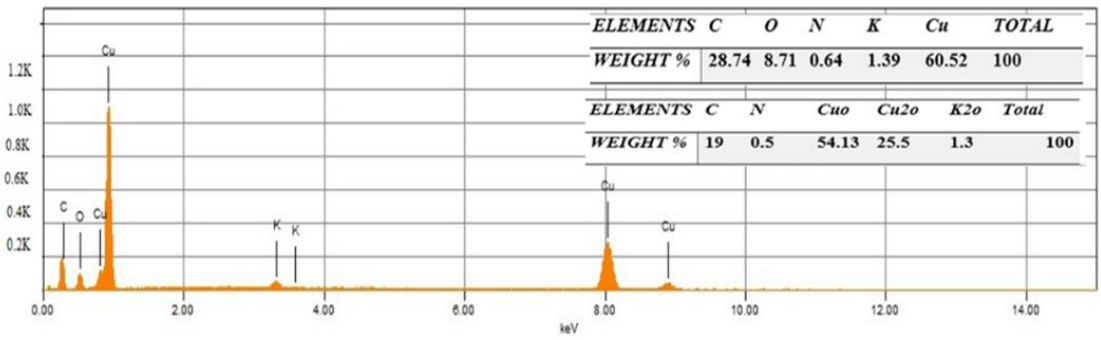

Figure III. 17:EDS spectrum of copper after biodiesel production.

Furthermore, the surface chemical composition of copper (***Figure III. 17)*** indicates the detection of corrosion products, mainly containing 28.74 wt% C and 8.71 wt% O, which proves that oxygenated molecules were still present in the Cu-rich material. Besides, the EDS demonstrated that the biodiesel is corroded, which proves that the fatty acid composition and profile of biodiesel have a significant impact on metal corrosion. This is most likely due to the water content and the presence of oxygen in the fatty acid molecules, and the activated oxygen atom in biodiesel causes the formation of metal oxide (CuO and Cu_2O)[155].

Besides, ***Figure III . 18****, and* ***Figure III. 19*** illustrate the SEM/EDS analyses carried out on the stainless-steel surface during biodiesel production. This indicates that the concentration of chromium, nickel, molybdenum, and iron released from the intermetallic surface of the stainless steel is very rich in these

elements, as indicated by the EDS spectrum. Thus, the small indentations, caused by the roughness of the coupon, form active regions where micro-pitting has occurred as a result of the iron reactions. Also, during biodiesel production, the volatile chemicals in the fuel were found to condense on the surface as soluble solids. Furthermore, the environment has created a corrosion situation, which is most likely induced by the presence of water, condensed volatile substances, and closer proximity to ambient oxygen. This most likely encouraged the emergence of chemical processes producing oxygenated compounds, which damaged the materials[171].

The EDS analysis indicated the presence of 5.65 wt% carbon and 2.83 wt% oxygen, both associated with the creation of corrosion products such as Fe_2O_3, FeO, K_2O, etc. This suggested the material had been submerged in a lower oxygen environment, which made it less corrosive, and demonstrates that the stainless steel is resistant in contact with biodiesel solution owing to a passive layer containing Cr_2O_3 and/or MoO_3[172].

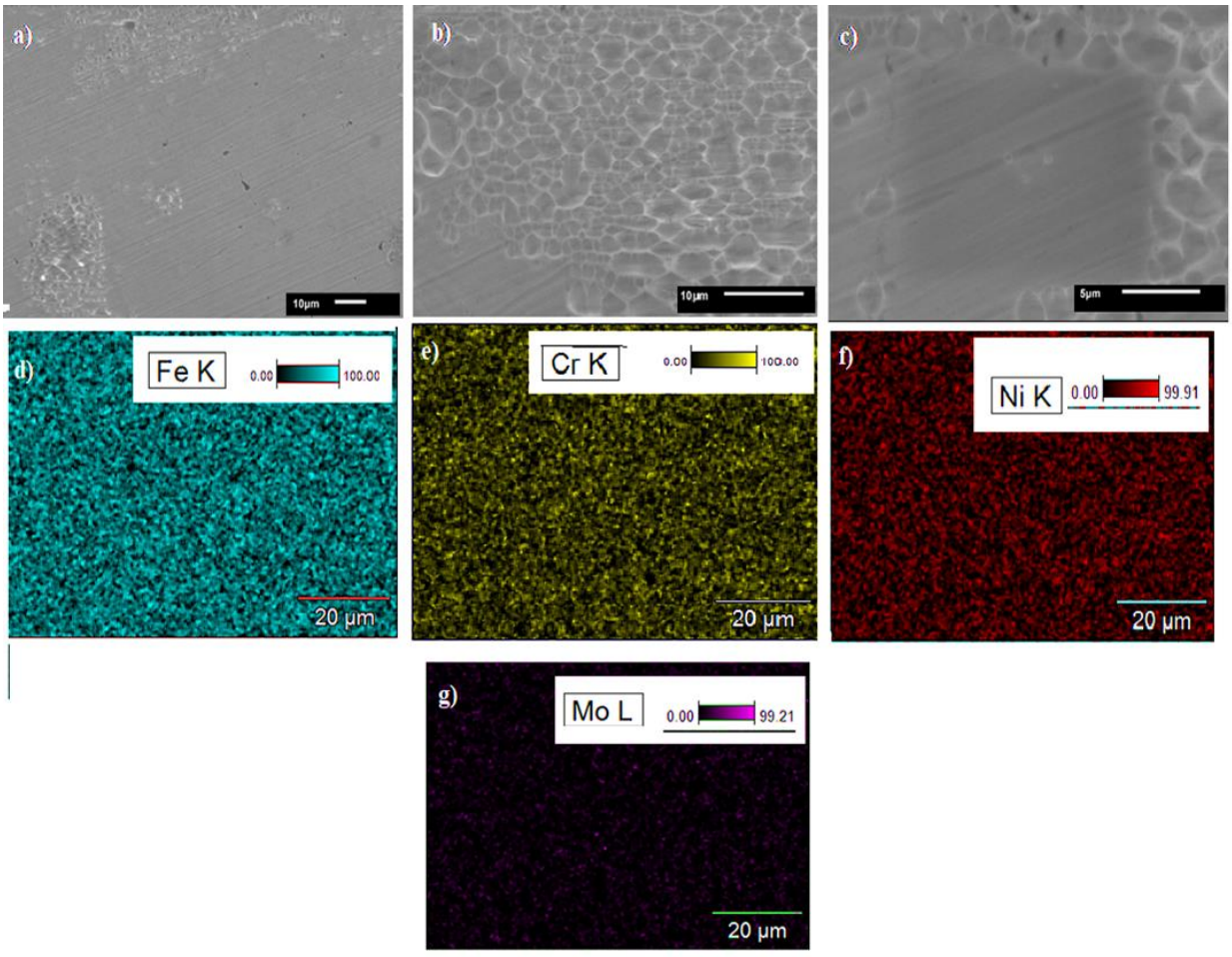

Figure III . 18:SEM micrographs of stainless steel after biodiesel production.

In summary, copper has higher corrosion rates than stainless steel and aluminum when in contact with biodiesel. The same behavior was observed in previous studies where copper and lead were put in contact with palm oil biodiesel[173,174].

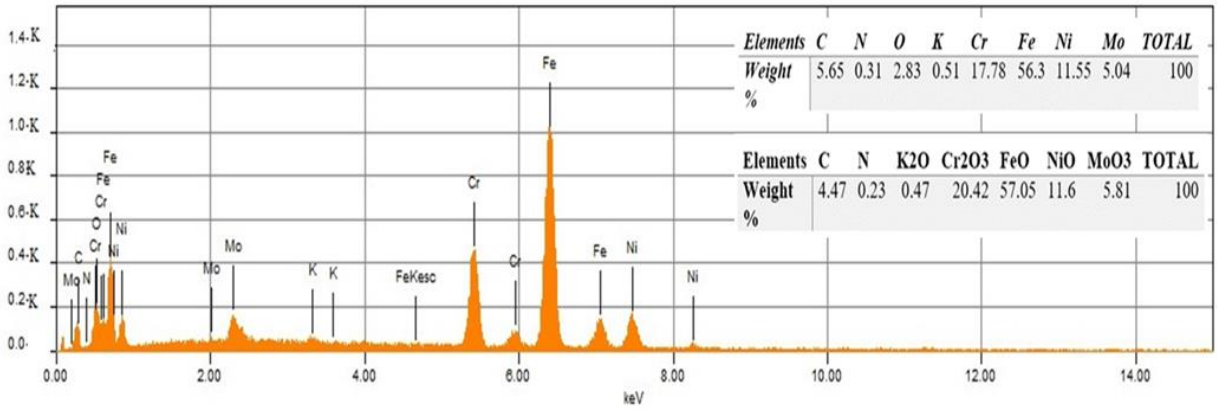

Figure III. 19:EDS spectrum of stainless steel after biodiesel production.

III.2.5.2 X-ray diffraction analysis

The XRD patterns of aluminum, stainless steel, and copper after being immersed in a biodiesel solution are shown *in* ***Figure III. 20*** It is noted that the XRD spectra reveal in particular the so-called base metals (aluminum, copper, and iron) as well as rarely significant proportions of AlO(OH) (***Figure III. 20.*** a), Fe_2O_3, $Fe(OH)_2$ and Cr_2O_3 (***Figure III. 20*****b**) CuO, and $Cu(OH)_2$ (***Figure III. 20*****c**)**.** Furthermore, the aluminum surface in contact with biodiesel shows the presence of an oxide protective layer with the formation of crystalline aluminum hydroxide (Boehmite, AlOOH) (***Figure III. 20*****a**). The presence of oxygen in the fuel also resulted in the development of another oxide film (Al_2O_3). This Al_2O_3 film is a solid layer that is not easily broken by biodiesel acids, but the oxyhydroxide film is not so strong and can be easily penetrated by acids.

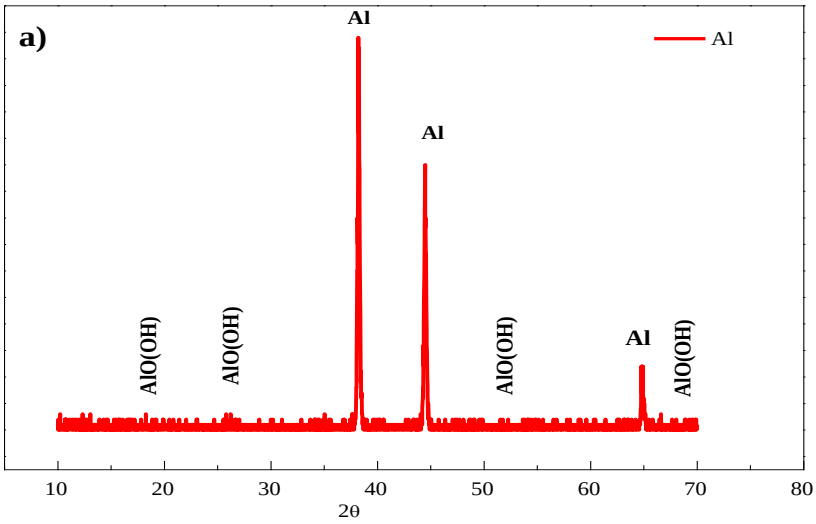

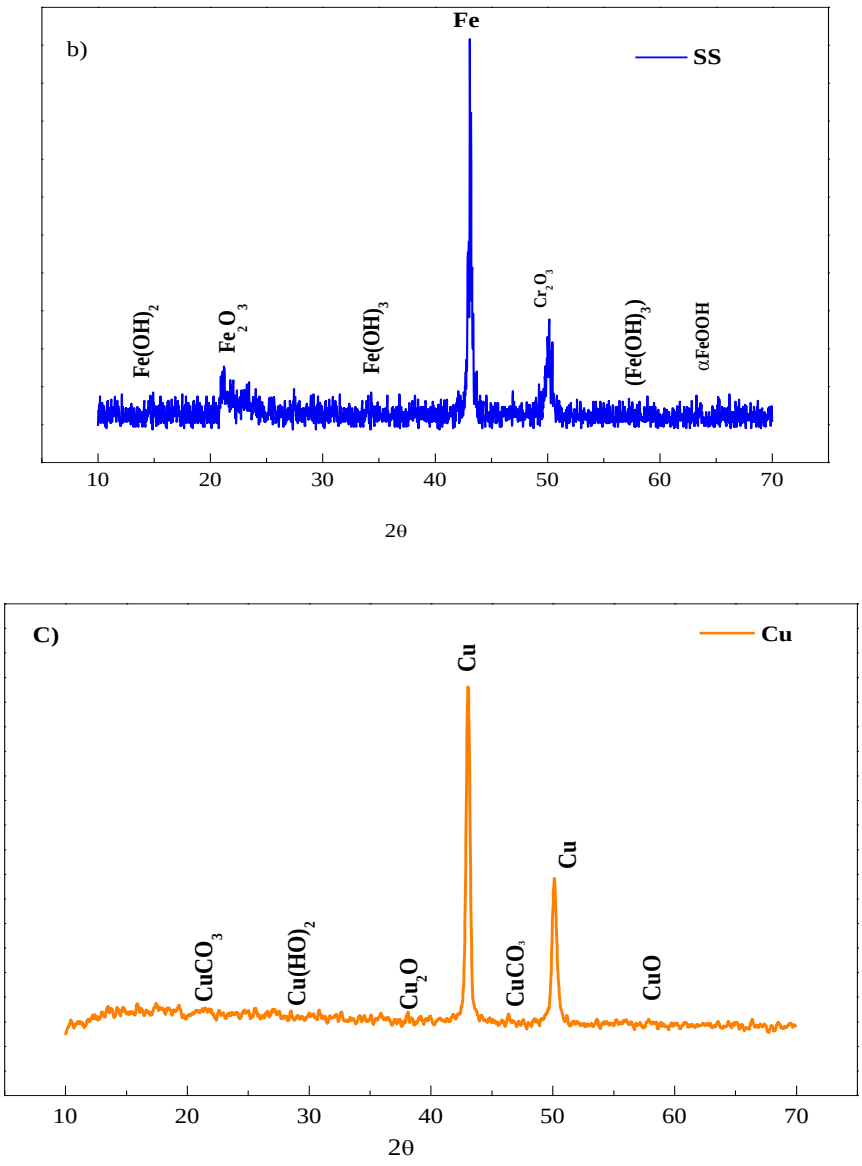

Figure III. 20: XRD pattern of (a) aluminum, (b)stainless steel, and (c)copper after immersion test.

Mechanism

The electrochemical reactions may occur on the lower metal surface. Based on the EDS and XRD findings, it is assumed the following reactions can occur at the metal surface when it is exposed to sunflower biodiesel. In the presence of dissolved oxygen and water from the biodiesel, copper leads to the formation of Cu(OH)2, Cu2O is unstable and is very quickly transformed into a more stable CuO. Equations (70-73)[175]. When iron is brought into contact with oxygen and water in biodiesel, the following chemical reactions have been reported(74-79)

$$2Cu + \frac{1}{2}O \rightarrow Cu_2O \qquad (71)$$

$$Cu_2O + \frac{1}{2}O_2 \rightarrow 2CuO \quad (72)$$

$$2Cu + O_2 + 2H_2O \rightarrow 2Cu(OH)_2 \quad (73)$$

$$CuO + H_2O \rightarrow Cu(OH)_2 \quad (74)$$

$$4Fe + 3O_2 \rightarrow 2Fe_2O_3 \quad (75)$$

$$4Fe + 4H_2O + 2O_2 \rightarrow 4Fe(OH)_2 \quad (76)$$

$$4Fe(OH)_2 + 2H_2O + O_2 \rightarrow 4Fe(OH)_3 \quad (77)$$

$$4Fe(OH)_2 + O_2 \rightarrow 2Fe_2O_3.H_2O + 2H_2O \quad (78)$$

$$R - COOR + Fe \rightarrow R - COO^{\circ} + R^{\circ} \quad (79)$$

$$2R - COO^{\circ} + Fe \rightarrow FeCO3 + R - R + CO \quad (80)$$

When compared to copper and stainless steel, the corrosive effect of biodiesel on aluminum is negligible. Following the exhibition tests, XRD investigations reveal a small amount of AlO(OH), which is most likely due to the reaction of aluminum with dissolved oxygen and water in biodiesel.

III.2.6.“FMO” frontier molecular orbital reactivity

The DFT based on Dmol3 has been used to study and evaluate the adsorption behavior and the interaction process of methyl linoleate (ML) on metallic surfaces, respectively iron (Fe (1 1 0)), aluminum (Al (1 1 1)) and copper (Cu (1 1 1)) to further investigate the reaction procedure. Moreover, this method is based on the electron density distribution of frontier molecular orbitals (FMO) in the majority of ML molecules, so it is considered useful for the calculation of several global descriptors of chemical reactivity[175].

The optimized structure and the electron density distributions of FMO for ML are represented ***Figure III . 21, Figure III . 22.*** The ML structure is in the final geometry form with minimal energy and represents maximum stability with positive frequencies. Concerning the electron distribution with maximum LUMO density, we see that the LUMO density is centralized around the ester group (R-COO-CH_3) of ML, which shows that this part has a great possibility to receive electrons from the electron donor sites located on the metallic surfaces such as Fe (110), Al (111) and Cu (110). However, the HOMO density is concentrated on the two double bonds (C=C) of the linear chain, indicating an electron donor power towards the vacant acceptor centers of the metal surfaces of the selected elements. Thus, the active regions (HOMO/LUMO) are likely influenced by the adsorption process on the surface of the investigated metals by horizontal adsorption characteristics.

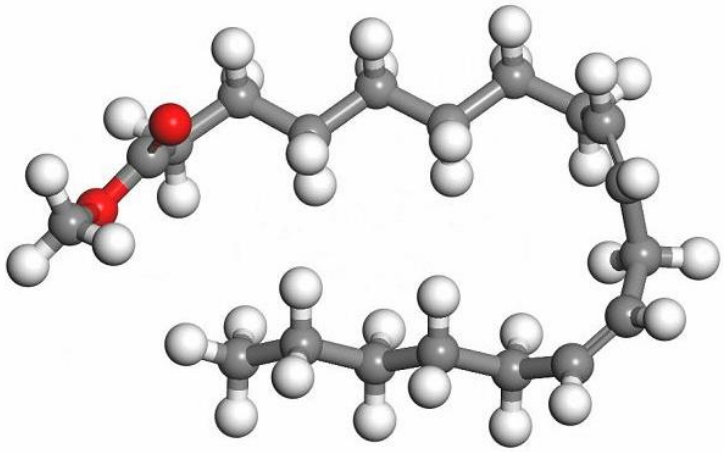

Figure III . 21:optimiezd methyl linoleate.

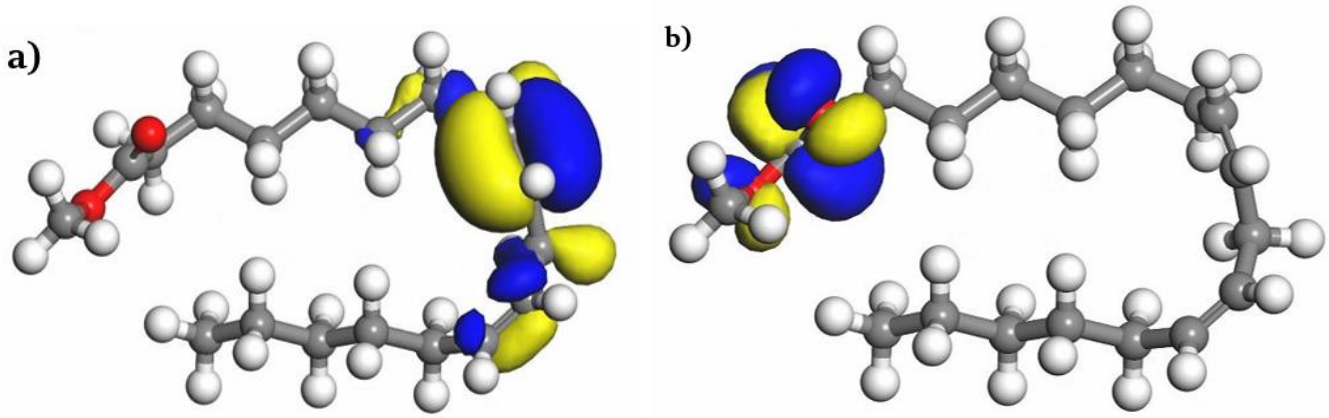

Figure III . 22: The electron density distributions of FMO for ML; a) HOMO, b) LUMO.

Table III . 5, lists the global descriptors that were assessed in this latest study. The energy gap (E) between HOMO and LUMO gives us information about the molecule's total reactivity[175]. A molecule with a low E is the most polarizable and is frequently linked with strong chemical activity and low kinetic stability, as well as increased metal surface adsorption. In our case (ΔE = 5.157 eV) this value indicates that the molecule is strongly reactive with the metal's surface, and has a strong ability to adsorb on the metal surface.

The absolute electronegativity (χ) and Absolute hardness (η) are varied in the sense of the reactivity of this species[176]. The electronic exchange at the metal surface/inhibitor molecule interface is also dependent on the electronegativity variation. Electrons can move from the protector compound (low electronegativity) to the metal support (high electronegativity), to equalize the chemical potentials.

As examined *in* ***Table III . 5*** the electronegativity value of optimized major compound ML (2.774 eV) is lower than those of $\chi_{Fe\,(110)}$ (4.820 eV), $\chi_{Cu(111)}$ (4.480 eV) and $\chi_{Al(111)}$ (5.600 eV). These data show that our inhibitor will

be possible more reactive with the aluminum surface (Al (111)) and the reactivity increases with the rise of electronegativity of each metal investigated.

Another important parameter that must be considered is the fraction of electrons transferred (ΔN). The literature assumes that if ΔN is strictly positive, the electrons are migrated from the molecule to the substrate, and if ΔN is strictly negative from the substrate to the molecule. The calculated ΔN values are grouped in ***Table III . 5***and are proportional to the values of the electronegativity of each selected metal in the most stable lattice planes (Fe (110), Al (111), and Cu (111)). From the ΔN values shown *in**Table III . 5** we* certainly notice that ΔN > 0 for all the metals examined, which explained that ML was the electron donor and the metal surface was the electron acceptor [177]. These results support the proposal that the adsorption of the molecule onto the metal surface can occur based on donor-acceptor interactions between the p-orbital of ML and the d-orbitals of Cu and Fe and the sp-orbital for Al. As observed that the high value of $\Delta N_{Al\,(111)}$ (5.600) shows that the reactivity by electron donor effect is very important between ML and Al (1 1 1), this reactivity grows with the increase of the value of ΔN according to the following order: $\Delta N_{Al\,(111)} > \Delta N_{Fe\,(110)} > \Delta N_{Cu\,(111)}$. These data confirm the results obtained by the experiments realized.

Table III . 5:Global descriptors analyzing the responsiveness of ML.

Descriptors of reactivity	
E_{HOMO} (eV)	**-5.352**
E_{LUMO} (eV)	**-0.195**
ΔE (eV)	**5.157**
η_{ML} (eV)	**2.579**
χ_{ML} (eV)	**2.774**
$\chi_{Cu(111)}$ (eV)	**4.480**
$\chi_{Al(111)}$ (eV)	**5.600**
$\chi_{Fe\,(110)}$ (eV)	**4.820**
$\Delta N_{Fe\,(110)}$	**0.397**
$\Delta N_{Al\,(111)}$	**0.548**
$\Delta N_{Cu\,(111)}$	**0.330**

To predict the preferred site of the nucleophilic or electrophilic attack, we used two of the most famous methods, namely the Fukui indices (FI) and the electrostatic potential (ESP)[178].

Both methods are analyzed and calculated via Material Studio (MS, version 7.1) software. The variation of electron density is given by the following calculated Fukui function.

$$f_k^+ = q_k(N+1) - q_k(N) \quad (81)$$

$$f_k^- = q_k(N) - q_k(N-1) \quad (82)$$

$$\Delta f = f_k^+ - f_k^- \quad (83)$$

where $\mathbf{q_N}$, $\mathbf{q_{N+1}}$, and $\mathbf{q_{N-1}}$ are the electronic densities of the atom **k** in neutral, anionic, and cationic systems, respectively[179]. The data obtained from these two methods (FI and EPS) of local reactivity are illustrated *in* ***Figure III. 24*** and summarized *in* ***Table III . 6***.

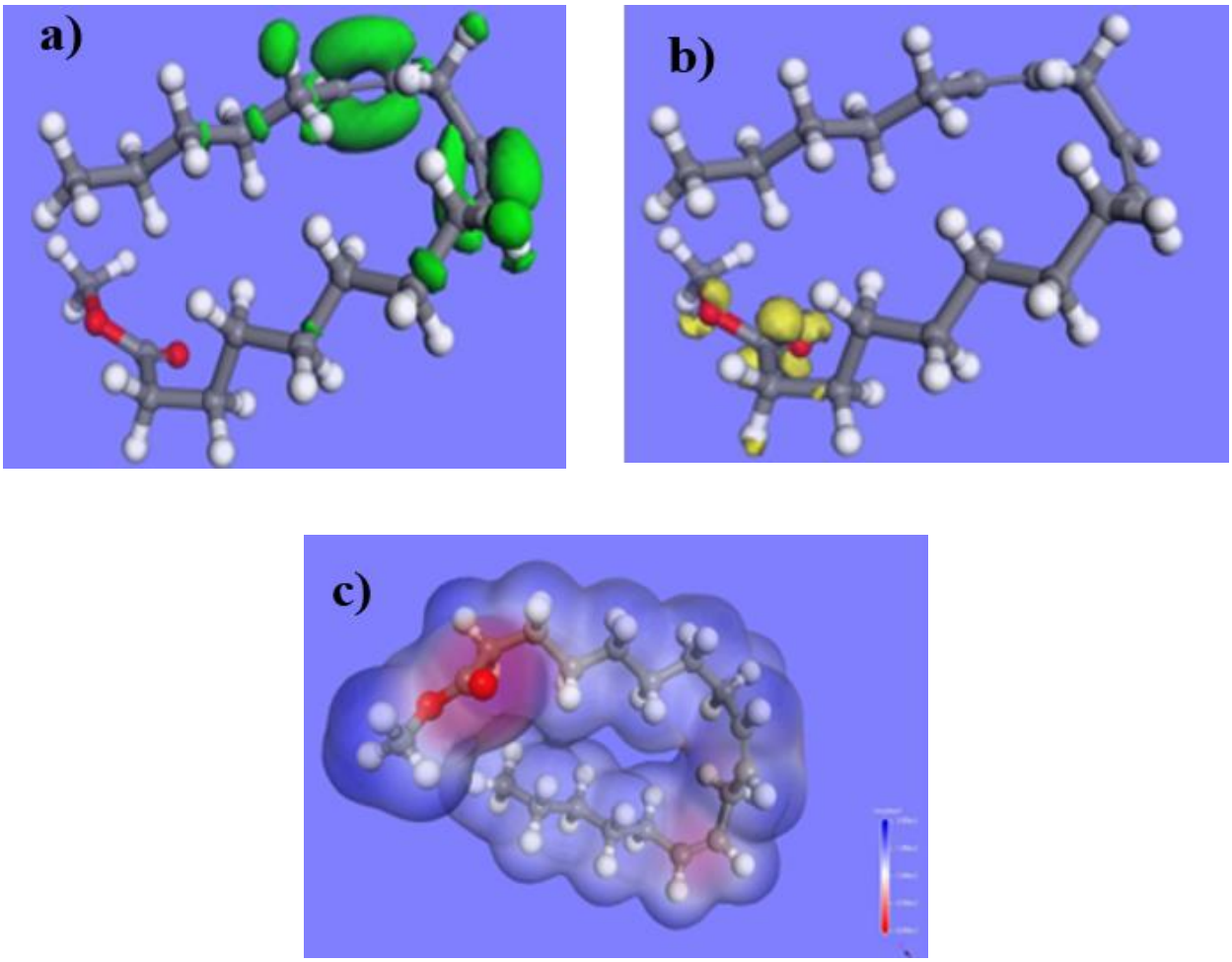

Figure III . 23:the Fukui indices a-b and EPS-c distributions on ML.

For a deeper understanding of the active sites of ML, we adopted the Fukui indices f_k^+ and f_k^- characterized the parts of this molecule in terms of their chemical behavior characteristics using the dual descriptor **(Δf)** developed by Morell & al[180]. This provided a more accurate estimation of the local reactivity of molecules and also a better predictive ability to identify electrophilic or nucleophilic attacks of an atomic site. Electrophilic/nucleophilic aggressors may be controlled for the maximum values; The f_k^+ maximum values tend to accept surface charges, while f_k values tend to give surface charges. Based on the results listed in ***Table III . 6*** and appeared in ***Figure III . 23***, we note that O (1) 0.074; O (2) 0.158; and C (17) 0.162, and show a positive density of change, implying that these are the preferred sites for nuclear attacks.

However, C (13) 0.097; C (15) 0.072; C (18) 0.138, and C (19) 0.125 are the sites best suited for electrophile attacks. Let us emphasize here that the distribution of the sites of the Fukui function agrees with the distribution HOMO/LUMO.

As described in Figure 22, the electrostatic potential **(ESP)** for the molecule under study was calculated to provide an overview of the adsorption phenomenon in terms of charge distribution. Under the **blue-white-red (BWR)** transition color, the blue and red areas reflect positive and negative electrostatic potentials, respectively, indicating an electron-rich or electron-deficient region, while the white area indicates a region with an ESP value of zero.

Table III . 6:Sites of locale reactivity using FI method of ML.

Atoms	f_k^+	f_k^-	Δf
O (1)	**0.074**	0.002	-0.072
O (2)	**0.158**	0.002	-0.156
C (3)	0.005	0.004	-0.001
C (4)	0.002	0.002	0.000
C (5)	0.001	0.002	0.001
C (6)	0.005	0.012	0.007
C (7)	0.010	0.003	-0.007
C (8)	0.006	0.015	0.009
C (9)	0.031	0.003	-0.028
C (10)	0.000	0.008	0.008
C (11)	0.002	0.003	0.001
C (12)	0.027	**0.097**	0.07
C (13)	0.005	0.022	0.017
C (14)	0.001	0.004	0.005
C (15)	0.026	**0.072**	0.046
C (16)	0.009	0.019	0.01
C (17)	**0.162**	0.001	-0.163
C (18)	0.022	**0.138**	0.116
C (19)	0.025	**0.125**	0.100
C (20)	0.003	0.007	0.004
C (21)	0.024	0.002	-0.022

III.2.7. Molecular dynamics (MD) simulations

A detailed explanation of the ML's adsorption and interactions with the metal surfaces tested (Fe (110), Al (111), and Cu (111)) is required to adequately evaluate the performance of this molecule from a theoretical standpoint utilizing the Forcite module through Material Studio (MS, version 7.1) software[181].

The simulation system for each calculation considered the study medium (K^+, OH^-, H_2O, and CH_3OH), the selected metal surfaces, the majority of the molecule, and the temperature of the experiments. The results for each simulation give many different adsorption configurations with different energy values,

but the configuration that has low energy is considered the adsorption configuration of ML on metal surfaces[182].

Figure III . 25-25depict snapshots of the top and side views of the molecule obtained when the MD simulations reach the equilibrium state. As visualized in these figures, it is clear that the major molecule ML absorbs almost totally on the Fe (110), Al (111) and Cu (111) surfaces. The literal and upper views show that the linear chain of the ML molecule aligns with the metal surfaces to occupy the vacant sites on the cubic lattice of the metal surface by a strong trend in the adsorption pattern. This adsorption behaviour leads to maximum contact with the metal surface, which results in larger surface coverage. Moreover, this sort of adsorption by ML allows for reducing the corrosion rate of the studied metals

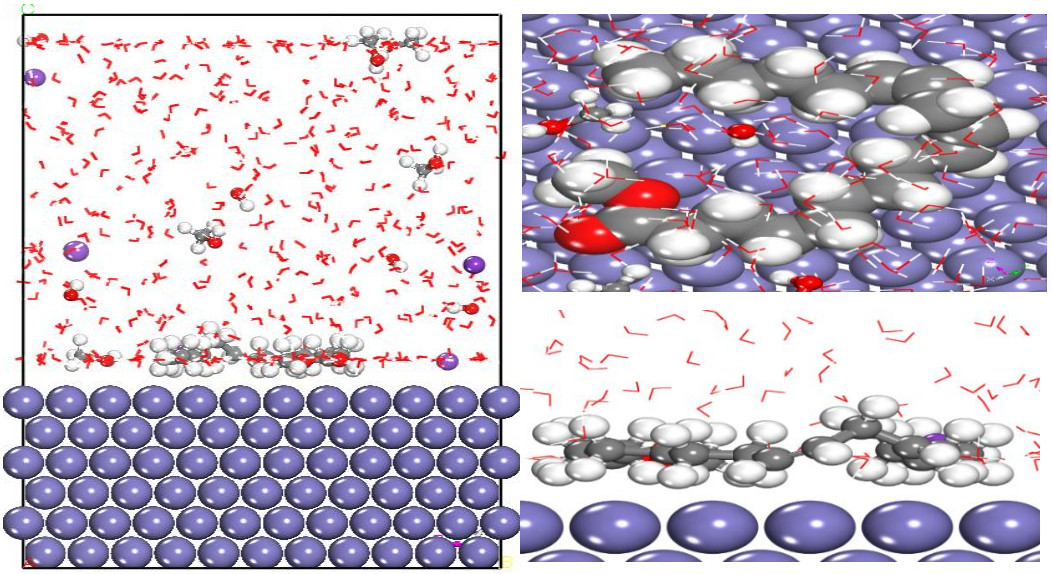

Figure III . 25:Snapshots of the top and side views of the molecule ML adsorbed onto the Fe (110) surface.

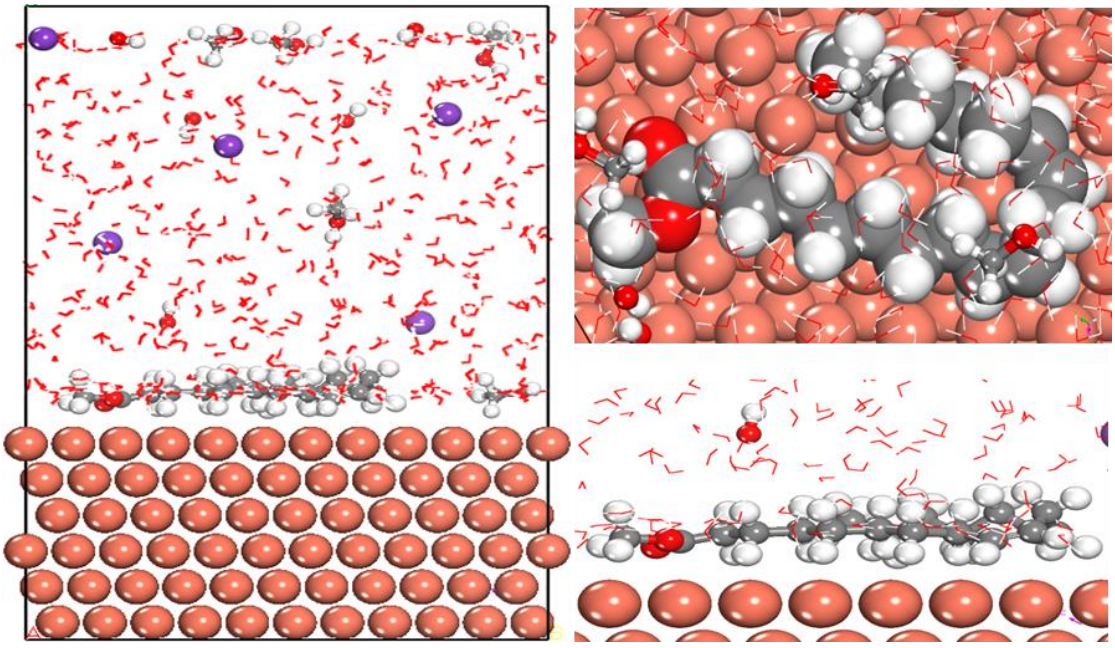

Figure III . 26::Snapshots of the top and side views of the molecule ML adsorbed onto the Cu (111) surface .

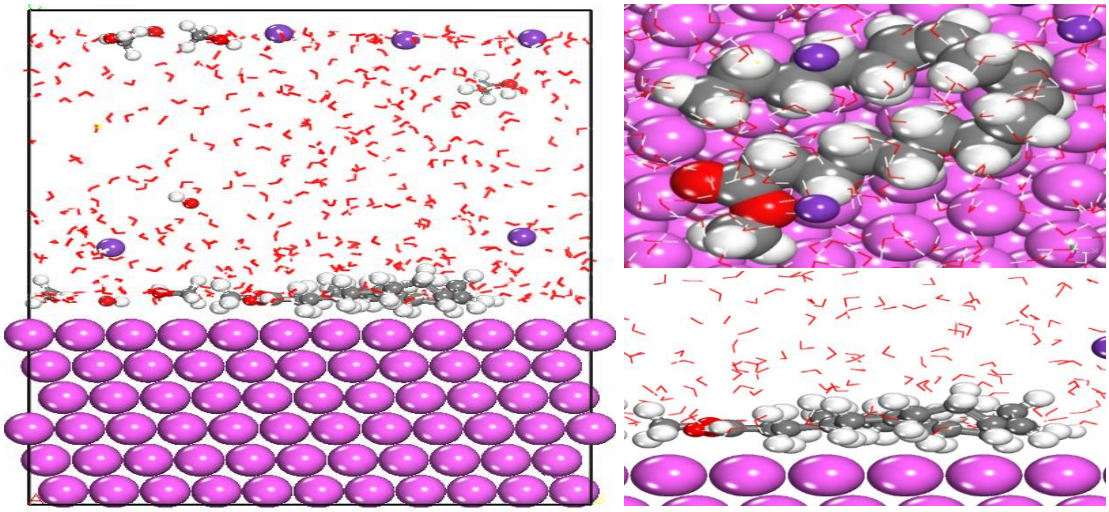

Figure III . 27:Snapshots of the top and side views of the molecule ML adsorbed onto the Al (111) surface.

The more stables adsorption configurations are associated with the lowest interaction energy ($\mathbf{E_{interaction}}$) and high binding energy ($\mathbf{E_{binding}}$), these two energy terms are determined by the following equations[182]:

$$E_{\text{Interaction}} = E_{\text{Total}} - (E_{\text{Surface+ Solution}} + E_{ML}) \text{ and } E_{\text{Binding}} = - E_{\text{Interaction}} \quad (84)$$

The obtained energy values of the simulated systems are collected in ***Table III . 7***.

Table III . 7:$E_{\_Interaction}$ and $E_{\_Binding}$ values of Fe (110)/ML, Cu (111)/ML, and Al (111)/ML systems.

SYSTEMS	$E_{\text{Interaction}}$ (KJ MOL^{-1})	E_{Binding} (KJ MOL^{-1})
ML/FE(110)	-901.201	901.201
ML/CU(111)	-891.083	891.083
ML/AL(111)	-939.921	939.921

The better interactions of the ML molecule onto the studied metallic surfaces depend generally on low values of $E_{\text{Interaction}}$. It is well confirmed in the literature that high values of E_{Binding} indicate strong adsorption[183,184]

From the data in ***Table III . 7*** we find that the ML/Al (111) system has the lowest value of the $\boldsymbol{E_{Interaction}}$ **(-939.921 kJ mol^{-1})** and the highest value of the $\boldsymbol{E_{Binding}}$ **(939.921 kJ mol^{-1}).** This indicates that the ML molecule covers the aluminum surface well and establishes a more effective energy barrier. Furthermore, the adsorption density and its performance are given as follows: Al (111)/ML > Fe (110)/ML > Cu (111)/ML. This order confirms the experimental values.

The radial distribution function (RDF) allows the easy calculation of the interatomic distance between the atoms of a molecule and iron. Mathematical calculation based on the previously established g(r) function allowed the RDF approach to be determined[185,186]**.** For a given interatomic distance r, this function g(r) provides the probability density for an atom of element X to have a neighbor of element Y. In addition, g(r) is derived by averaging the density of species of Y over all shells in proximity to species X. As shown in the literature, if the distance r is between 1 and 3.5 Å, the nature of their interaction is assumed to be chemisorption, while if this distance is at positions greater than 3.5 Å, it is physisorption[187].

The results of this analysis are presented in ***Figure III . 28***. The selected active sites (O19 and O20)-ML/Fe (1 1 0), (O19 and O20)-ML/Cu (1 1 1), and (O19 and O20)-ML/Al (1 1 1) have distances of less than 3.5 Å, which shows that these distances are more bonded and more rigid to the corrosion phenomenon. This method also shows that the bond lengths of the (O19 and O20)-ML/Al (1 1 1) system are the shortest, indicating that the interactions between the majority molecule of interest and the aluminum surface are maximal compared to the other remaining systems.

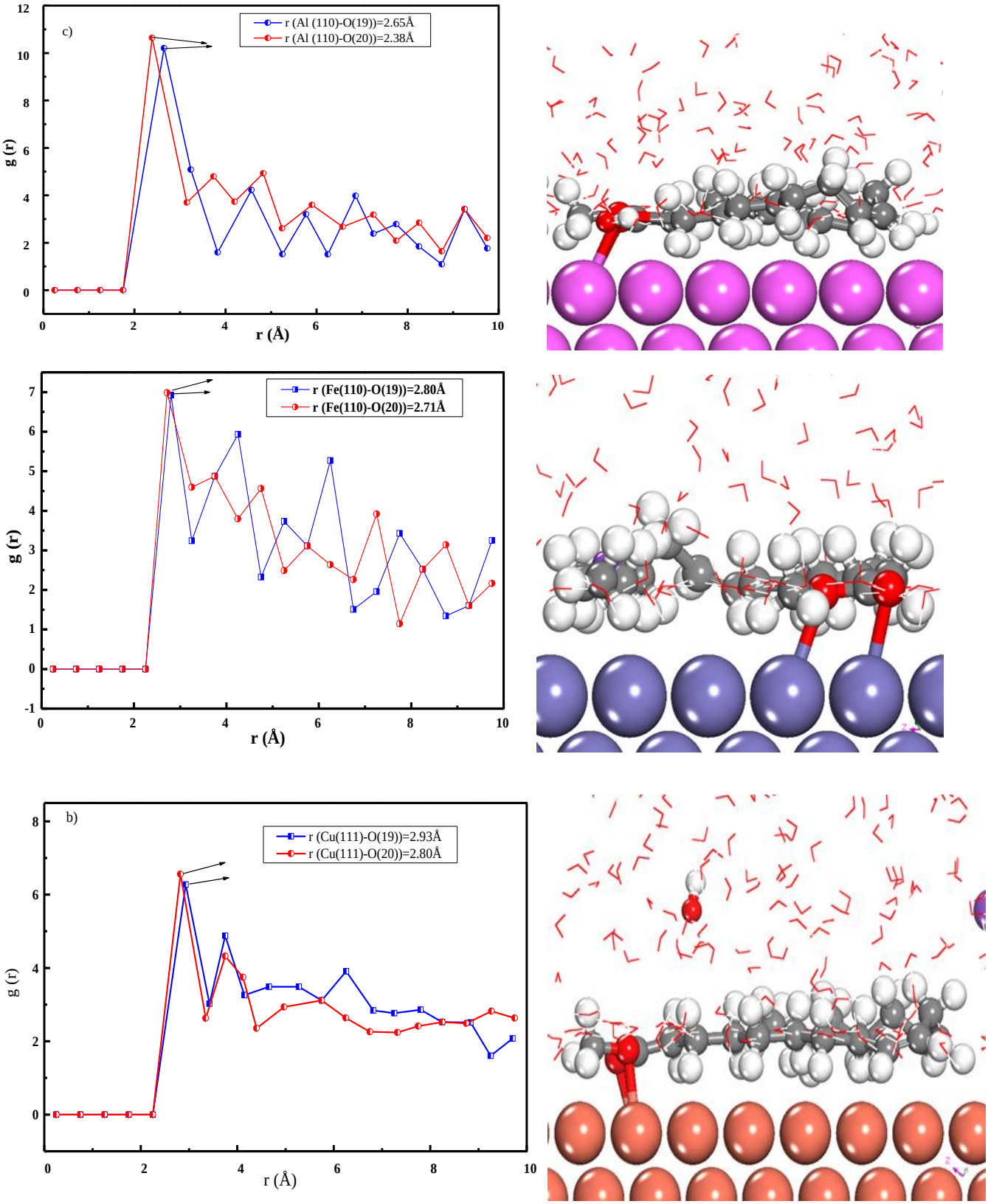

Figure III . 28: RDF of ML on Fe (110), Al (111), and Cu (111) surfaces.

III.2.8. MSD and FFV

Mean Square Displacement was used to assess the anti-corrosion capabilities of 60 ML molecules in a supercell containing corrosive ions (3 K+ & 3 OH-) (MSD). Molecular dynamics simulation is used for this analysis, and the Forcite module that is built within the Materials Studio 7.1 program is used. The diffusion coefficient (Dion) can be calculated using this model as [188]:

$$D_{ion} = \frac{1}{6N_{\alpha}} \lim_{x\to\infty} \frac{d}{dt} \sum_{i=1}^{N_{\alpha}} \left\langle \left[R_i(t) - R_i(0) \right]^2 \right\rangle \quad \textbf{(85)}$$

$$MSD = \left\langle \left[R_i(t) - R_i(0) \right]^2 \right\rangle \quad \textbf{(86)}$$

denotes the number of diffusive atoms N_{α}, while Ri (0) and Ri (t) respectively show the positions of corrosive ions at the origin time ((0)) and a later time (t). In the ML molecule film, the diffusion, FFV, and MSD curves of OH- and K+ are displayed in ***Figure III . 29***.

As illustrated in ***Figure III . 29*** **(a),** the ML molecules are denser in the created cell, indicating that the majority of the molecules form a superior barrier layer. This result suggests that the diffusion coefficient (Di) of the examined corrosive ions has difficulty penetrating the film created by the ML molecules. [189]. A low Dion value indicates a high inhibitory activity and consequently a high inhibitory effectiveness. [190].

In the supercell including the ML molecules, the values of the Dion for the OH- (DOH-) and k+ (Dk+) ions obtained by varying MDS vs. simulation length are shown in ***Figure III . 29 (b).*** The Dion data in this Figure reveal that the value of DOH- (0.011 10-12m2/s) is less than that of Dk+ (0.044 10-12m2/s), indicating that the OH- anion may permeate the microscopic pores encountered in the ML film to a lower extent. This finding indicates that the high density of the built-up coating reduces the number of corrosive ions reaching the surface of the examined metals.

The fractional free volume (FFV) calculation is another way for studying the variables that may influence the diffusion of corrosive species[190]. Large cavities in the inhibitory film may increase corrosive ion mobility and reduce inhibition efficacy, whereas tiny holes in the inhibitory film may have the opposite effect and reduce inhibition performance. The Connolly surface (***Figure III . 29 (c))*** has been used to detect free (V_f) and occupied (Vo) volumes in produced amorphous systems. As a result, the FFV has been computed [191]:

$$\mathbf{FFV}(\%) = \boldsymbol{V_f} \times \left[\boldsymbol{V_f} + \mathbf{V_o}\right]^{-1}(\%) \quad \textbf{(87)}$$

Keep in mind that the bigger FFV may be explained by the presence of a large Vf space inside the ML film, and therefore by the corrosion inhibitor film's lesser influence on species diffusion in diffusion and infiltration[192]. The calculated FFV percentage for ML molecules is 13.06 percent. The low FFV found indicates that the ML coating acts as a protective barrier, preventing corrosive ions from reaching the surface of the investigated metals.

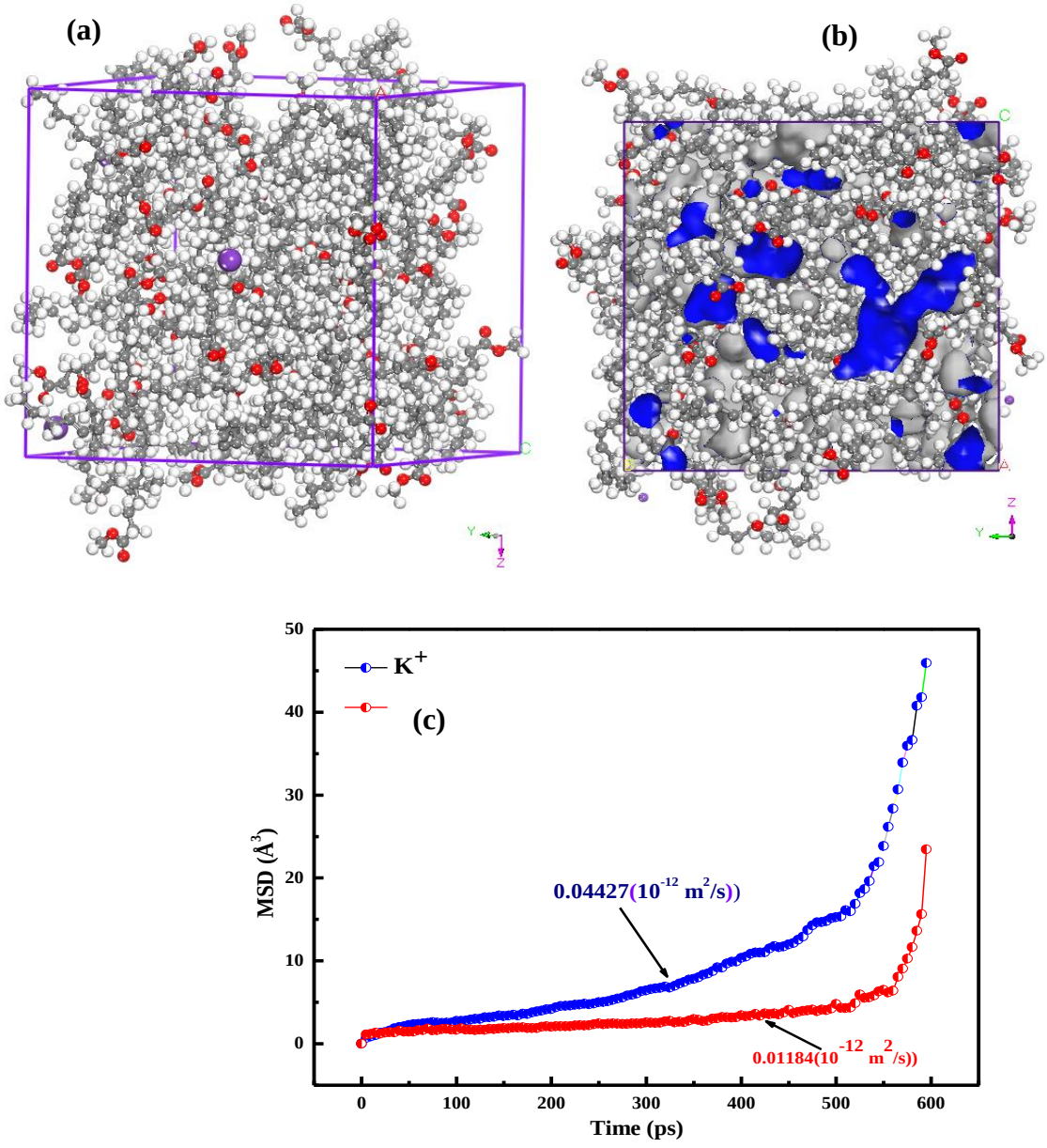

Figure III . 29: (a) Diffusion, (b) FFV, and (c) MSD curves of OH- and K+ in the ML film.

Conclusion

The corrosion behavior of stainless steel and pure aluminum and copper in sunflower biodiesel solution was investigated. From the electrochemical techniques, it is found that the R_p values of aluminum are high than stainless steel and pure copper. This signifies that aluminum is more resistant than stainless steel and copper at the time of biodiesel production. In addition, through the beginning of biodiesel production, the corrosion rate was higher for all metals. Beyond 65 minutes, the corrosion resistance increases in the case of aluminum and stainless steel. This could be due to the creation of a protective layer on the metal surface, which prevent the active substances from reaching the electrode surface. A high ratio of Fe to Ni, as well as Cr, Al, and Cu in the solution, were discovered using spectroscopic techniques (UV-Vis-NIR) and FAAS, showing that corrosion products are forming on the metal surface. These results are in line with those obtained by electrochemical techniques. SEM/EDS analysis confirmed that the methyl esters had a slight impact on metal deterioration, with a modest corrosion rate and the formation of localized micro-pitting on the metal surface. The FAAS analysis also revealed the existence of a low concentration of metal ions released into the solution. The results of the experiment are supported by DFT and MD simulation data; for a film of ML molecules, the computed fraction of FFV (percentage) is 13.06 percent. The low values of the diffusion coefficient indicate an important action of ML, implying a high inhibitory efficiency. Therefore, the correlation approach (DFT and molecular dynamics simulations (MDS)) was applied to support the experimental results that favored aluminum as the base metal for biodiesel synthesis due to its low corrosion rate during the process.

PART B:

Evolution of 307 L Stainless Steel Corrosion on the Oxidative Stability of Biodiesel During Storage

PART B: Evolution of 307 L Stainless Steel Corrosion on the Oxidative Stability of Biodiesel During Storage

III.3 Introduction

Biodiesel is widely recognized around the world as an alternative solution to conventional diesel because it is a renewable source. Biodiesel degrades, causing significant changes in its original composition and properties and leading to metal corrosion through direct contact. The current study aims to investigate the relationship between biodiesel degradation and the corrosion behavior of the 307 L stainless steel used for storage. Transesterification with a heterogeneous catalyst and methanol results in the production of biodiesel from used soybean cooking oil (SWCO). The corrosion effect was evaluated using electrochemical methods, SEM/EDS microscopy techniques, X-ray diffraction (XRD) analysis, and UV-VIS -NIR absorbance, while the various changes in biodiesel composition were studied using FTIR, GS-MS, and UV absorbance. The results show that methyl ester has a weak influence on metal degradation, indicating a low corrosion rate with localized micropitting on its surface. Furthermore, flame atomic absorption spectroscopy (FAAS) revealed the presence of a small number of metal ions, and electrochemical assays such as electrochemical impedance spectroscopy (EIS) and polarization curves (PC) revealed that the 307 L stainless steel has a high corrosion resistance due to the formation of a passive film.

III.3.1 Experimental procedure

III.3.1.1 Pre-treatment of Soybean Waste Cooking Oil (SWCO

A nearby restaurant provided the soybean oil used 2-3 times. To separate suspended impurities from the waste oil, filter paper was used. The oil was then centrifuged at 3000 rpm for 30 minutes to remove small particles and then heated at 100 °C for 30 minutes to remove the contained water.

III.3.1.2 Synthesis of biodiesel

The biodiesel used in the current study was prepared from SWCO and methanol 99 % in the presence of heterogeneous acid catalyst $FeSO_4$, 7 H_2O/ KOH by using the trans-esterification process for 2 hours. The best conditions for producing 98 percent biodiesel are a volume ratio of 6:1, a temperature between 60 and 65 degrees Celsius, and a catalyst of 1% KOH and 2% $FeSO_4$, $7H_2O$ [193,194]. For 30 minutes, the reaction product was exposed to air to evaporate excess methanol. Then it was allowed to lay for 6 hours to produce the two distinct phases.

III.3.2 Biodiesel characterization

III.3.2.1 Physicochemical characterization

The physicochemical parameters of the biodiesel generated from local WCO, such as viscosity, density, and acid number, were determined using well-established procedures [24]. ***Table III . 8*** highlights the findings observed. Overall physicochemical characteristics of WCO biodiesel could be determined to be following ASTM D6751- 02 [25]. The major physical and chemical properties (kinematic viscosity, acid number, and density) are, nonetheless, extremely close to the norms.

Table III . 8:parameters physico-chimie of SWCO Biodiesel .

Test	**Means**	**Specifications**	**EN 14214 methods**
Kinematic Viscosity (40° C) (Cs)	4.33	3.5–5.0 max	EN ISO 3104
Density (15 °C) G/Cm^3	0.882	0.860–0.900 max	EN ISO 12185
Acid Number Mg Koh/G	0.453	0.5 max	EN 14104

III.3.2.2 Fourier Transform Infrared Spectroscopy (FTIR) analysis

Figure III. 30 depicts the FT-IR spectra of SWCO biodiesel. Thus, the major spectral features of biodiesel are stretching vibration C-H at 3010 cm-1, three bands at 2960.5 cm-1, 2929.4 cm-1, and 2851.7 cm-1, which are assigned to the -CH2 group for asymmetrical vibration stretching, the -CH3 group for asymmetrical vibration stretching, and the group of two distinct vibration bands observed between 1700 cm-1 and 1755 cm-1, respectively. Furthermore, the band at 1735.5 cm-1 is assigned to carbonyl ester C=O, whilst the bands at 1460 cm-1, 1381 cm-1, and 902 cm-1 are attributed to the deformation vibrations of the carboxylic acid's -CH2, -CH3, and -OH groups, respectively[193,195]. The lack of bands in the 3200-3600 cm-1 range indicates the absence of residual hydroxides in SWCO biodiesel before and after immersion. However, after being exposed to 307 L stainless steel under certain test circumstances, the FT-IR spectra of biodiesel revealed the presence of a peak at 583 cm-1, indicating the creation of the oxide Fe_2O_3. Peaks found at 1020 cm-1 and 1327 cm-1 are attributable to γ -FeOOH and α-FeOOH as corrosion products, respectively. Furthermore, the existence of $Fe_2O_2CO_3$ produced during the exposition was revealed by the band about 1710 cm-1[196].

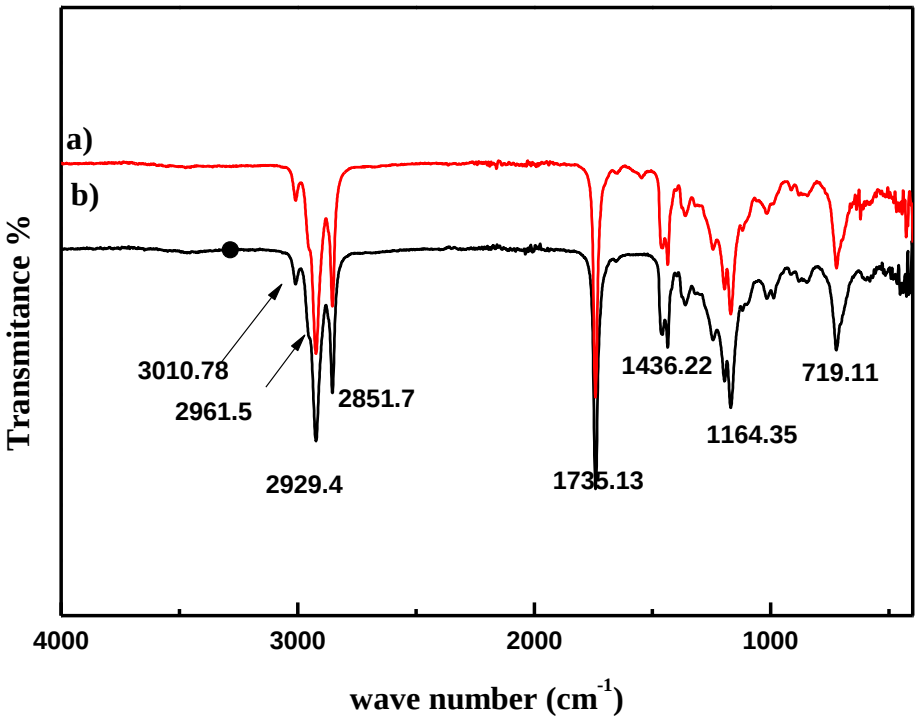

Figure III. 30:FTIR spectrum of SWCO biodiesel before (a) and after(b) 264h immersion of stainless steel.

III.3.2.3 GC-MS analysis

The GC-MS measurements were performed to examine the chemical composition of the synthesized biodiesel and the resulting chromatogram is shown in ***Figure III . 32***. The presence of four major chemicals was observed in the fatty acid methyl ester content of the SWCOs, corresponding to the proportional peaks (***Table III . 9***). However, the FAMEs were identified by analyzing the standards

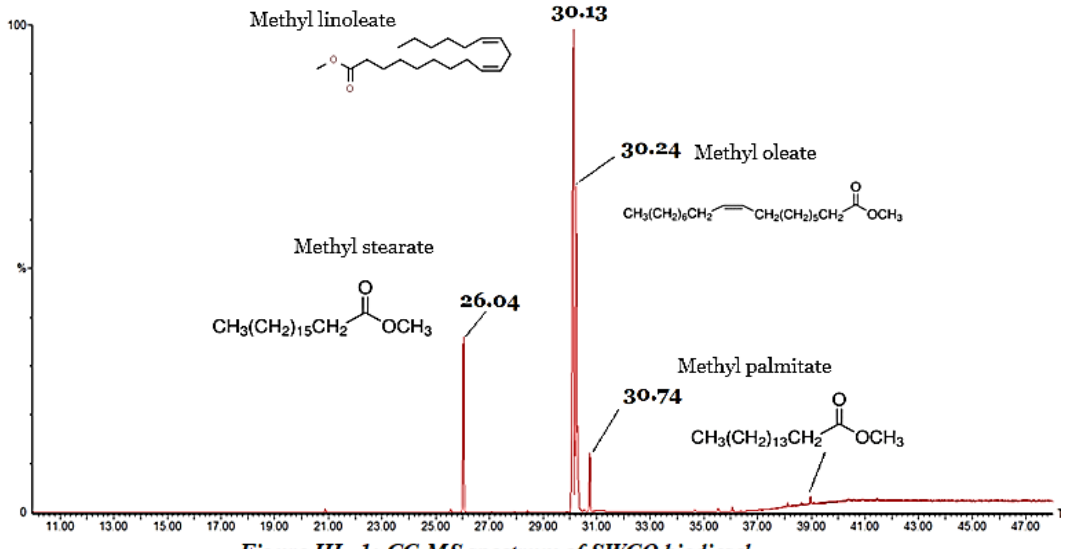

Figure III . 31:GC-MS spctrum of SWCO biodiesel.

under identical experimental conditions and weighting the results of the corresponding retention times.

Table III . 9:Chemical composition of SWCO biodiesel.

Fatty Acid Type	R.T (MIN)	IDENTIFIED COMPOUNDS	CHEMICAL FORMULA	MOLE CONC. (%)
n-Octadecanoic acid, methyl ester	26.04	methyl stearate	$C_{19}H_{38}O_2$	13.48
9,12-Octadecadienoic acid (Z, Z)-, methyl ester	30.13	methyl linoleate	$C_{19}H_{34}O_2$	50.52
9Z-octadecenoic acid, methyl ester	30.24	methyl oleate	$C_{19}H_{36}O_2$	31.23
Hexadecanoic acid, methyl ester	30.74	methyl palmitate	$C_{17}H_{34}O_2$	4.77

III.3.4 Electrochemical measurements

III.3.4.1 Open circuit potential (E_{OCP})

The variation of EOCP with time for the 307 L stainless steel electrode exposed to SWCO biodiesel is shown in ***Figure III. 33*** .In the first 24 hours of exposure, the EOCP is observed to be negative before moving to more positive values. This finding suggests that the 307 L stainless steel surface was coated with a protective film, where its reactivity was very weak. However, this film becomes more porous over time and less sticky to the metal's surface, causing the corrosion rate to increase. It is recognized that biofuel instability can lead to the formation of oxidation products such as aldehydes, alcohols, short-chain carboxylic acids, gums, and sediments in biodiesel[197]. Thus, depending on the type of these oxidizing compounds, they can be protective or non-protective of the metal surface against corrosion[198]. According to the results obtained, the compounds formed on the 307 L stainless steel exposed to WCO biodiesel are Fe_2O_3, $Fe_2O_2CO_3$, $Fe(OH)_3$, NiO, and Cr_2O_3(see XRD below). However, after 120 hours, the E_{OCP} values were approximately the same for the rest of the test period.

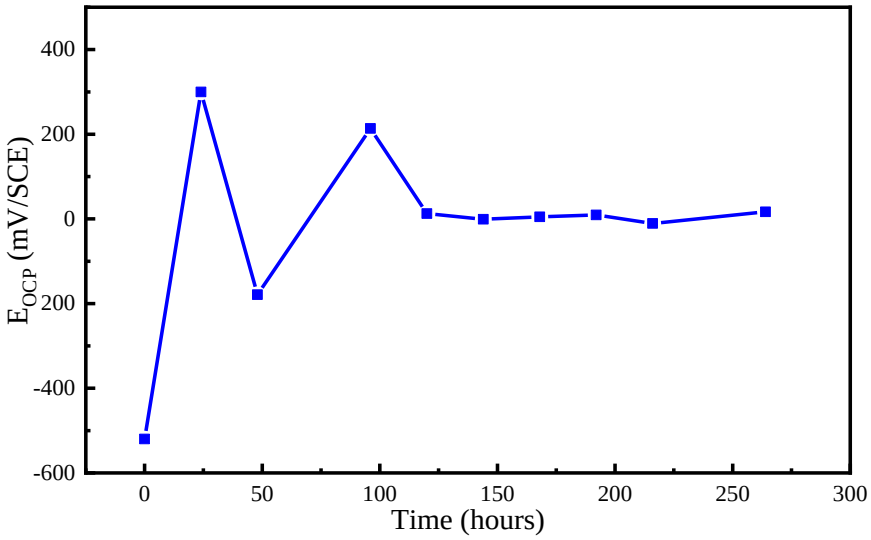

Figure III. 33:OCP variation value versus time for stainless steel.

III.3.4.2 Potentiodynamic polarization curves

The potentiodynamic polarization curves of 307 L stainless steel exposed to SWCO biodiesel produced at different immersion times are shown in ***Figure III. 34*** and relevant electrochemical parameters such as corrosion potential (Ecorr), corrosion current density (icorr), anodic (βa), and cathode (βc) slopes of Tafel are grouped into ***Table III. 10***. Curves have shown that corrosion potential moves from negative values to positive values, while - current density (icorr) increases with immersion time.

In the meantime, it can be noted that at the beginning of the test, the anode part exhibited a passivity disturbance behavior that may be caused by the instability of the biodiesel. This result could be related to the increase in the corrosion activity of the 307 L stainless steel due to the degradation of the SWCO biodiesel and the development of some corrosion products on its surface [199]. Furthermore, based on ***Table III. 10***, the anodic polarization curves show at 24 hours a pseudo-passivation in the potential range [248 mV/SCE; 368 mV/SCE], which suggests that the solution has acquired quasi-stationary stability through the formation of a passivity layer. This layer disappears at higher potentials, causing uniform corrosion or pitting [200]. After 48 hours, the corrosion current density shows an unstable variation related to the instability of the conductivity of the solution, which means that the fresh species of the reaction do not reach the active surface of the electrode, or that the corrosion products do not diffuse away from the active surface. Thus, the increase in $\mathbf{i_{corr}}$ values is probably due to the breakdown of a protective film created on the stainless steel, which in this case is Cr_2O_3. Furthermore, this reduction in the current density value is due to the re-establishment of such a protective film. However, the presence of chromium in the passive film may be the main cause of the shift of E_{corr} towards the noble direction of the term and the reduction of the active/passive current density[201]. Thus, if the chromium

content of the passive film is less than 12% by weight, the passive film may be subject to localized corrosion.

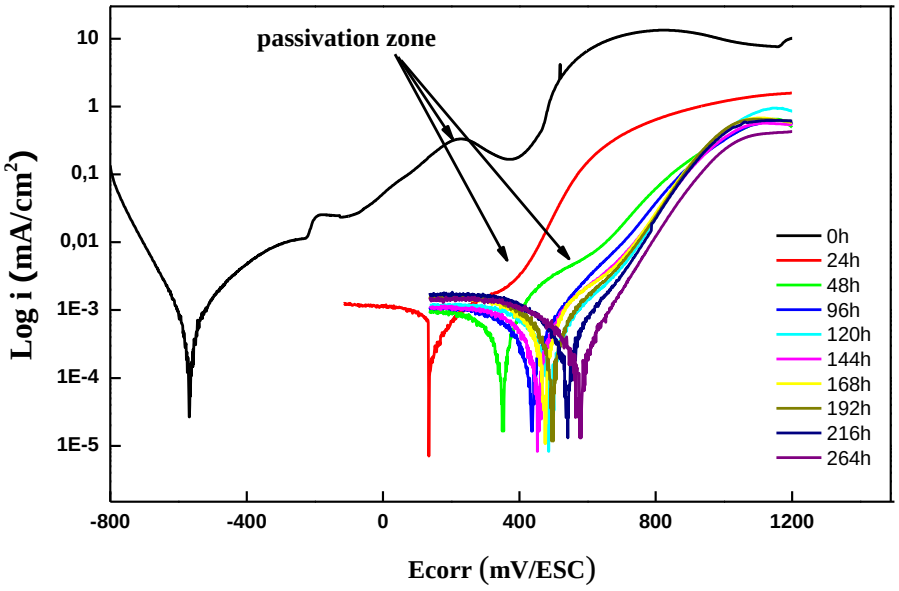

Figure III. 34:Potentiodynamic polarization curves of 307 L Stainless steel in SWCO biodiesel at different immersion times.

Table III. 10:Electrochemical parameters of 307 L stainless steel in SWCO biodiesel at different immersion times.

Time (h)	E_{corr} (mv/SCE)	I_{corr} (10^{-4}mA/cm^2)	β_a (mV/dec)	$-\beta_c$ (mV/dec)
0	-569.80	2.03	155.50	105.10
24	137.60	3.14	340.40	390.40
48	350.01	3.88	201.00	905.00
96	436.94	1.92	164.74	329.20
120	491.49	2.53	205.20	380.60
144	454.81	3.35	235.60	629.20
168	474.84	3.50	266.20	675.50
192	495.48	2.12	203.50	340.80
216	540.86	1.26	154.80	217.80
264	578.28	1.36	141.70	367.00

III.3.4.3 EIS measurements

Figure III . 35 and ***Figure III . 36*** show the EIS data in the form of Nyquist and Bode plots for 307 L stainless steel tested in SWCO biodiesel at different immersion times. Indeed, it is well established that the passive layers have a depressed semicircle shape, generally referred to as frequency dispersion and also attributed to the roughness or inhomogeneity of the electrode surface[202].

Thus, in the Nyquist plots (***Figure III . 35***), the shape of the loops does not change with immersion duration, indicating that the corrosion process is regulated by charge transfer. Furthermore, the diameter of the semicircle decreases within the first 48 hours of immersion in biodiesel, most likely owing to stainless steel disintegration. However, its diameter reduces marginally with immersion time after 48 hours. This finding is attributed to an increase in the corrosion activity of the 307 L stainless steel surface caused by SWCO biodiesel oxidation and degradation[203]. Furthermore, above 168 hours, the EIS spectrums revealed that corrosion resistance improves with immersion duration, which might be related to the creation of a protective layer at the metal/solution interface, preventing active species migration to the electrode surface.

As a result, the 307 L stainless steel displayed typical behavior for a mechanism regulated by species diffusion at the metal/solution interface. This behaviour validates the strong corrosion resistance of 307 L stainless steel in biodiesel solution as well as the potentiodynamic polarization data.

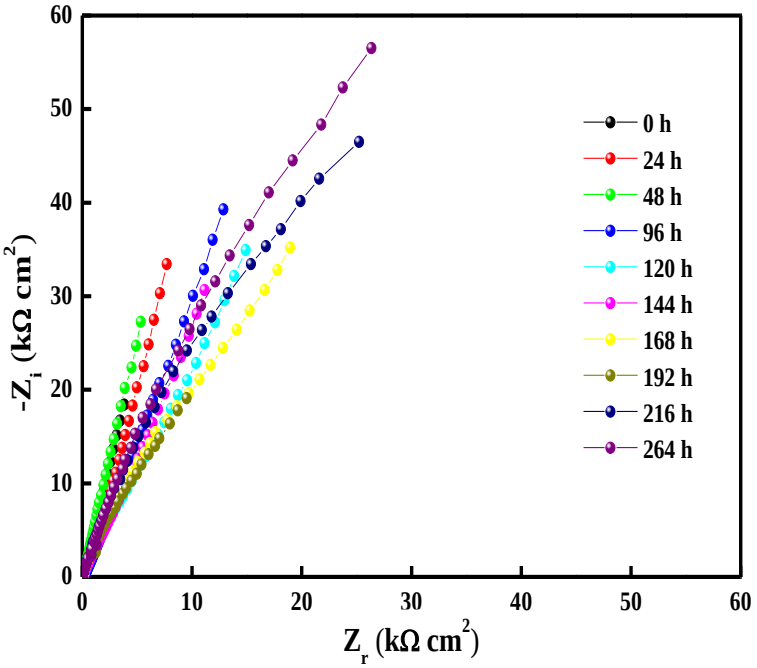

Figure III . 35:Nyquist plots of 307 L stainless steel electrode in SWCO biodiesel at different immersion times.

Alternatively, ***Figure III . 36*** reveals that as time elapses, the solution has a high resistance and the impedance modulus decreases. On the other hand, the existence of two slopes indicates the presence of two-time constants. The first depends on the charge transfer process (Rct), and the second frequency depends on log Z and the phase angle. It is observed that the log Z modulus increases at 24 hours, decreases up to 168 hours and increases again. This can be explained by the formation of a stable layer, which improves the immersion time.

The electrochemical impedance parameters achieved from fitting the EIS data, according to the proposed electrical circuit (in ***Figure III. 7)*** are regrouped in ***Table III . 11***. It is observed that the R_{ct} value at the beginning of the test is higher, which implies low conductivity and therefore low corrosion rates. Nevertheless, the solution resistance slightly diminishes after 168 hours, which may be related to the degradation or oxidation of the biodiesel, and the absorption of water from the environment. This occurrence causes the formation of a passive layer on the 307 L stainless steel surface[204]. On the other hand, the oxide film formed on the 307 L stainless steel presents slightly higher R_f values compared to those of R_{ct}, which proved that the metal corrosion resistance is provided in a better part by the produced corrosion products on the interface metal/solution.

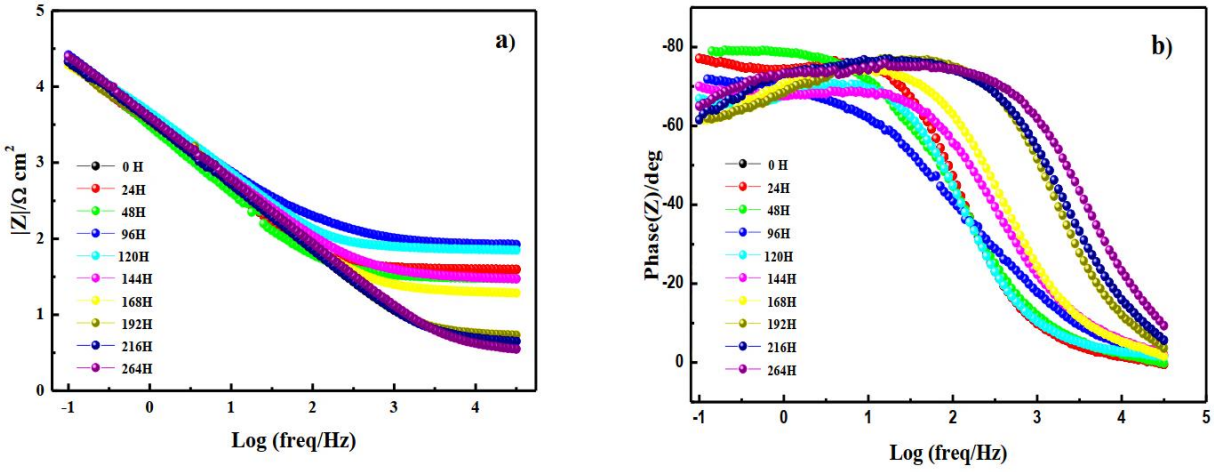

Figure III . 36:Bode-module-phase plots of 307 L stainless steel in SWCO biodiesel at various immersion times.

Furthermore, both R_f and R_{ct} values diminish over time, which reveals an augmentation in the rate of corrosion due basically as mentioned above to the development of several secondary oxidation products by biodiesel degradation like aldehydes, alcohols, short-chain carboxylic acids, and higher molecular weight polymers, causing a rise in the biodiesel corrosivity. Additionally, when the value of n is close to 1, it means that the roughness of the 307 L stainless steel surface is low because of the low corrosion rate. Therefore, the n_{ct} value stays almost equal to 1, throughout immersion time testing, but n_f value

diminishes over time, due to a rise in metal roughness as the corrosion rate increases because of biodiesel degradation as mentioned above[205].

Table III . 11:Electrochemical impedance parameters for 307 L stainless steel in SWCO biodiesel at different immersion time.

Time (h)	R_S (Ω cm²)	$10^{-5}\times Q_{dl}$ (F s^{n-1} cm^{-2})	n_{ct}	$10^{2}\times R_{ct}$ (Ω cm²)	n_f	$10^{-5}\times Q_f$ (F s^{n-1} cm^{-2})	$10^{5}\times R_f$ (Ω cm²)	$10^{5}\times Rp$ (Ω cm²)
0	134.30	6.50	0.88	3.03	1.00	1.41	2.19	2.19
24	63.61	3.37	0.91	2.31	0.91	1.15	20.3	20.6
48	61.86	2.31	0.99	4.51	0.85	3.14	4.99	5.00
96	133.00	2.73	0.75	8.70	0.89	74.5	25.2	25.2
120	113.10	3.82	0.81	1.21	0.91	1.47	15.1	16.3
144	48.46	3.82	0.80	1.08	0.74	39.9	4.82	4.93
168	11.61	1.20	0.50	0.32	0.88	2.09	3.34	3.34
192	11.94	2.45	0.86	4.71	0.83	2.28	1.29	1.76
216	11.22	2.08	0.87	4.64	0.66	77.5	2.18	2.65
264	8.631	1.88	0.85	3.02	0.76	36.1	2.94	3.24

III.3.5 Surface characterization " SEM/EDS& XRD"

The surface morphology and chemical composition of 307L stainless steel after immersion in SWCO biodiesel for 264 hours is illustrated in ***Erreur ! Source du renvoi introuvable.*** and ***Figure III . 39*** by SEM/EDS analysis.

Erreur ! Source du renvoi introuvable. shows the basic distribution of the passive film formed on the surface of the 307L stainless steel. It also shows that the corroded surface of the steel has adherent metal oxides composed of carbon and oxygen such as NiO, MoO_3, Fe_2O_3, and Cr_2O_3. In addition, there are also many organic deposits on the surface of the steel immersed in SWCO biodiesel, due to the reaction of many unsaturated fatty acids with the metal oxide. As a result, partial corrosion products adsorb/adhere to the surface of the steel and are led to more carbon and oxygen from the SWCO biodiesel. On the other hand, these SEM results showed the presence of localized corrosion attacks .

However, *Figure III. 37* shows the XRD pattern of 307 L stainless steel immersed in SWCO biodiesel for 264 hours of immersion. Accordingly, the corrosion products identified on the surface of the steelare

$Fe(OH)_3$, $Fe(OH)_2$, Fe_2O_3, Fe, Cr_2O_3 and $Fe2O2CO3$. The presence of $Fe_2O_2CO_3$ may be due to the reaction with moisture, oxygen, and CO_2 absorbed from the air, which is a product of the reaction between H_2CO_3 and FeOOH. In addition, FeOOH results from the decomposition reaction of $Fe(OH)_3$ while H_2CO_3 is produced by the reaction between water and CO_2 in the air**.**

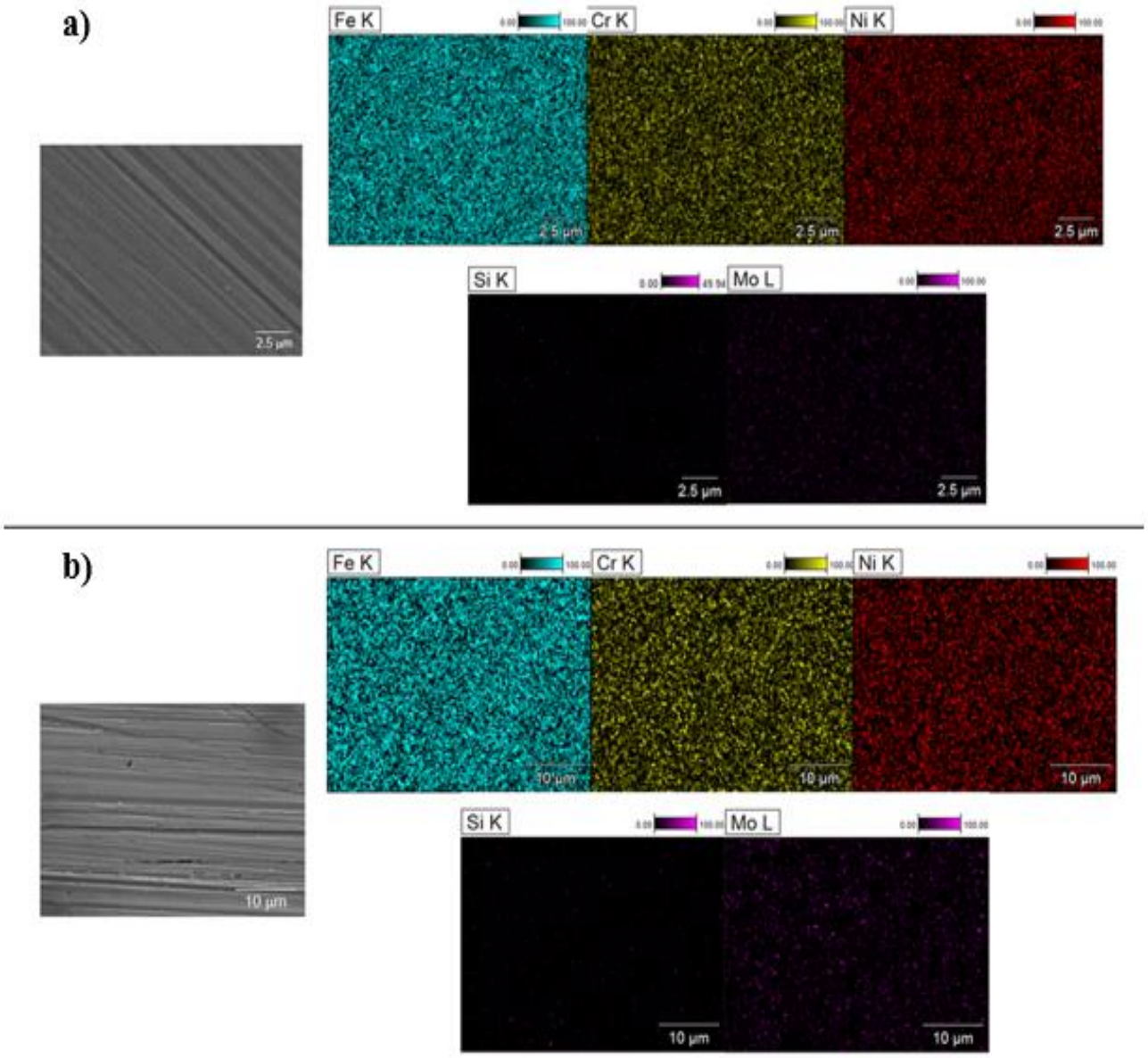

Figure III . 38: SEM of 307 L stainless steel before (a) and after (b) immersion in SWCO biodiesel during 264 hours of immersion

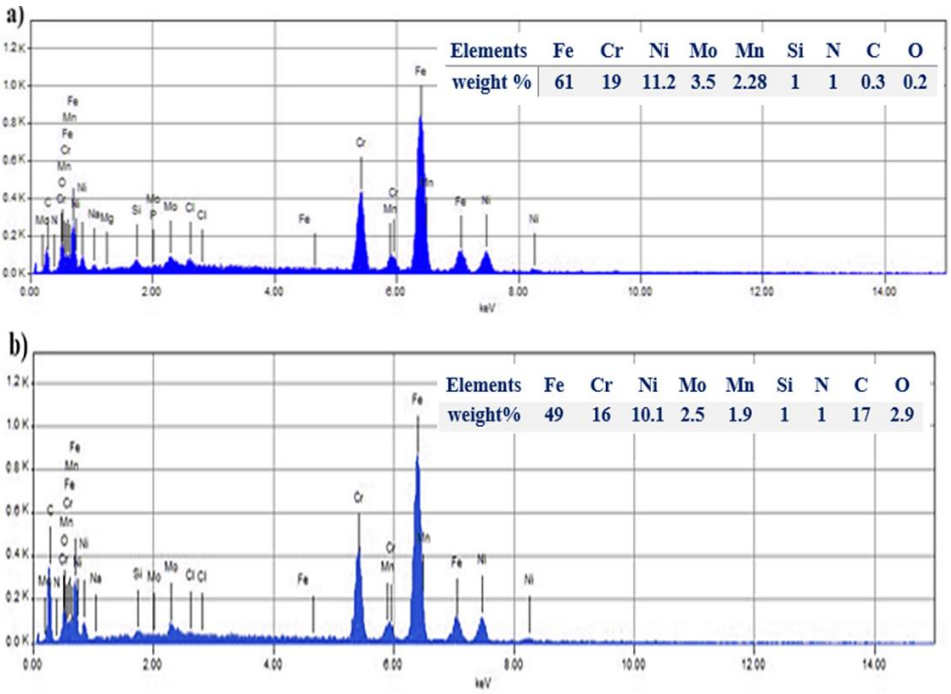

Figure III . 39: The EDS results of stainless steel before (a) and after (b) immersion in SWCO biodiesel during 264 hours of immersion.

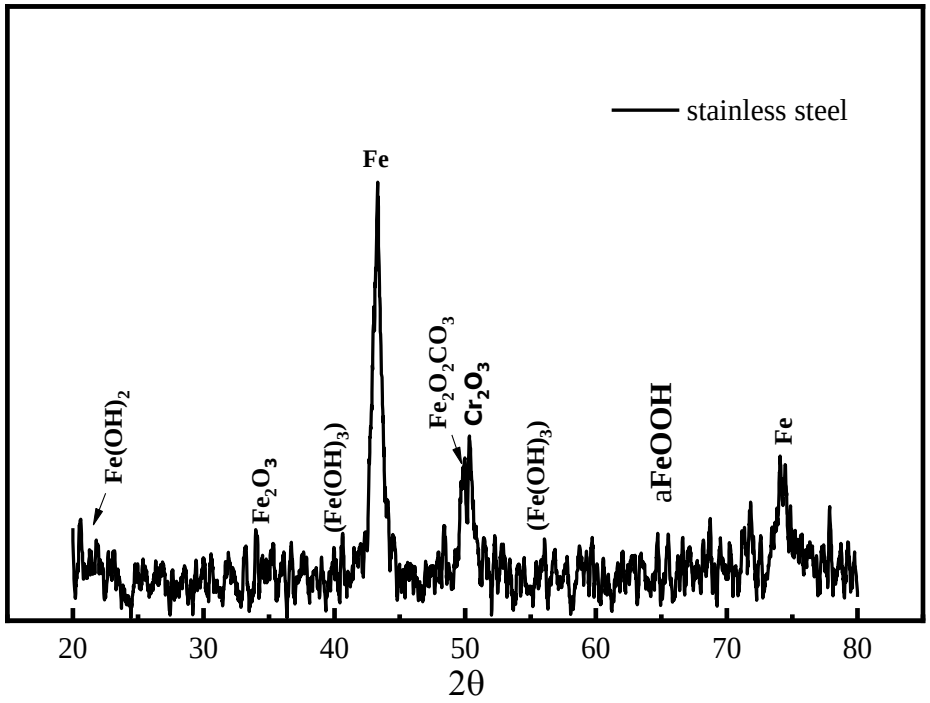

Figure III . 40: The XRD pattern of 307 L stainless steel immersed in SWCO biodiesel during 264 hours of immersion.

III.3.6 UV-Vis-NIR spectroscopy

The UV-Vis-NIR analysis was carried out to determine the nature of the compounds formed by corrosion on the surface of 307 L stainless steel immersed for 264 hours in SWCO biodiesel solution at ambient temperature are shown in ***Figure III . 41.***

Prior to immersion, the spectrum of the steel surface revealed that the most significant constituent elements are iron and chromium, as identified by other researchers[162]. Therefore, the secondary derivative of the absorbance curve was performed to show the weak absorption bands and to improve the result of the bands generated by the different electronic or vibrational transitions in the corrosion products. The least curve indicates the position of an absorption band, while the difference between the minimum and the next maximum defines its amplitude, which can be used for quantitative analysis[206].

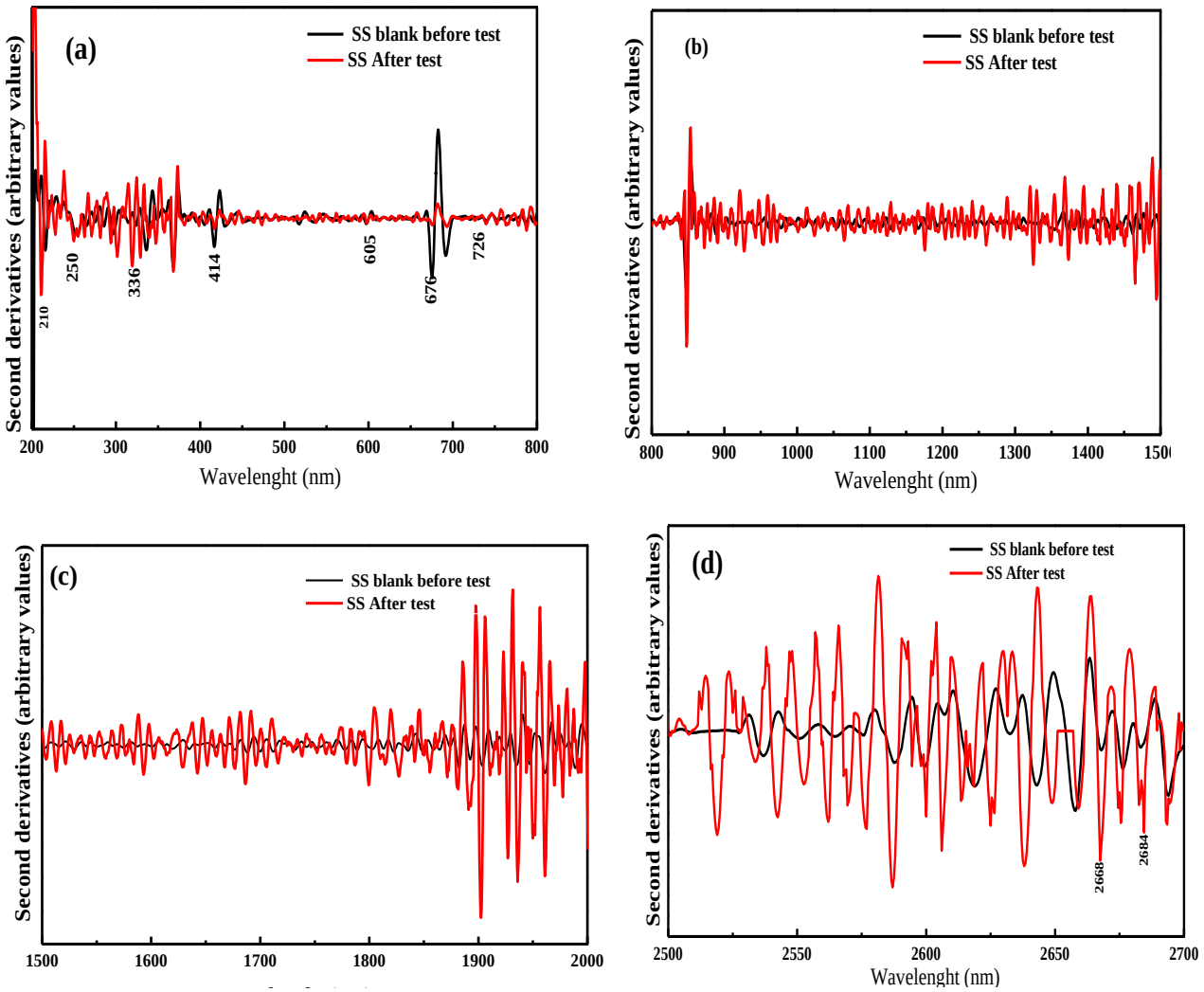

Figure III . 41:Second derivative absorption spectra of the 307 L Stainless Steel surface before and after immersion in SWCO biodiesel.

Before its immersion, the spectrum of the 307 L stainless steel surface showed that the most important component elements are iron and chromium such as identified by others researchers [137,162]. However, the second derivative of the absorbance curve has been conducted to show weak absorption bands and improve the result of the bands generated from the different electronic or vibratory transitions in corrosion products. The curve least implies the position of an absorption band, whereas the difference between the minimum and the next maximum defines its amplitude, which can be used for quantitative analysis [207]. The UV-vis spectra show the main corrosion products at various wavelengths. So, the peaks at 210 nm and 250 nm are attributed to the Lepidocrocite (γ-FeOOH) and maghemite (γ-Fe_2O_3), respectively (Figure 11a). The intense peaks at 2668 nm and 2688 nm are correlated to hydroxide (OH) with single coordination in γ-Fe_2O_3 structure (Figure 11e) [3]. The bands between 412 nm, 606 nm, and 726 nm can be associated with chromium oxides (Cr_2O_3). The peaks at 380 nm, 432 nm, 680, and 712 nm can be attributed to nickel oxides (NiO) [208]. On the other hand, it is observed that the amplitude of the peaks increases after immersion of the 307 L stainless steel in SWCO biodiesel solution, suggesting an increase in the composition of the 307 L stainless steel surface, and the importance of the dissolution mechanism caused by biodiesel degradation. Besides, peaks at 500 nm and 2200 nm have a higher increase in amplitude than those between 200 nm and 500 nm. In correlation with the XRD analysis, these peaks may be attributed to iron oxide.

III.3.7 UV-Vis spectroscopy analysis

The UV-vis spectra of SWCO biodiesel before and after immersion and their deconvolution using the Free Peak Fit software are shown in ***Figure III . 42*** & ***Figure III . 43***respectively. The results obtained, in terms of amplitude, centre, total width at half maximum (TWHM) and analytical area of each peak, are presented in ***Table III . 12***.

In the illustration of ***Figure III . 42***, two absorption bands detected at 235 nm and 274 nm and related to methyl linoleate are shown, where their intensity increases accordingly with the immersion time. According to the literature, the absorption peak of the band at 235 nm of linoleic acid-conjugated dienes can be attributed to $\pi \rightarrow \pi$ transitions, whereas the absorption band centred at 274 nm correlates with $\pi \rightarrow \pi^*$ transitions[209,210].Furthermore, the difference in band strengths of these two peaks is of special significance since it allowed the oxidation processes to be evaluated based on their amplitude ratios. Previously, the amplitude ratio between peaks 1 and 2 was rather low, suggesting that the oxidation process was only getting started. As the oxidation progresses, this ratio increases with the peroxide amount and decreases with longer oxidation periods[211].

In addition, ***Figure III . 43*** showed that the lipid auto-oxidation mechanism underwent a step change after 264 hours, which was due to the conjugation between the two double bonds of linoleic acid, which occurred during oxidation[212].

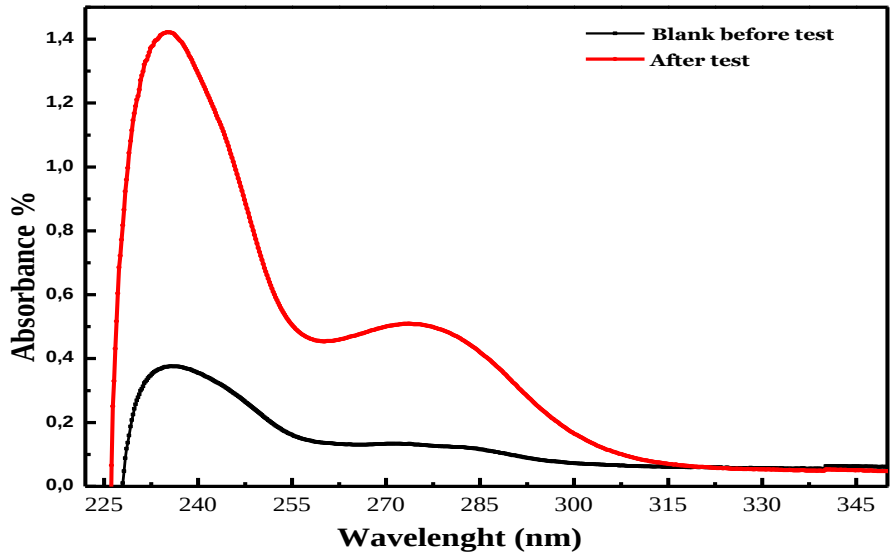

Figure III . 42: The UV-Vis Spectrum of SWCO biodiesel before and after the test.

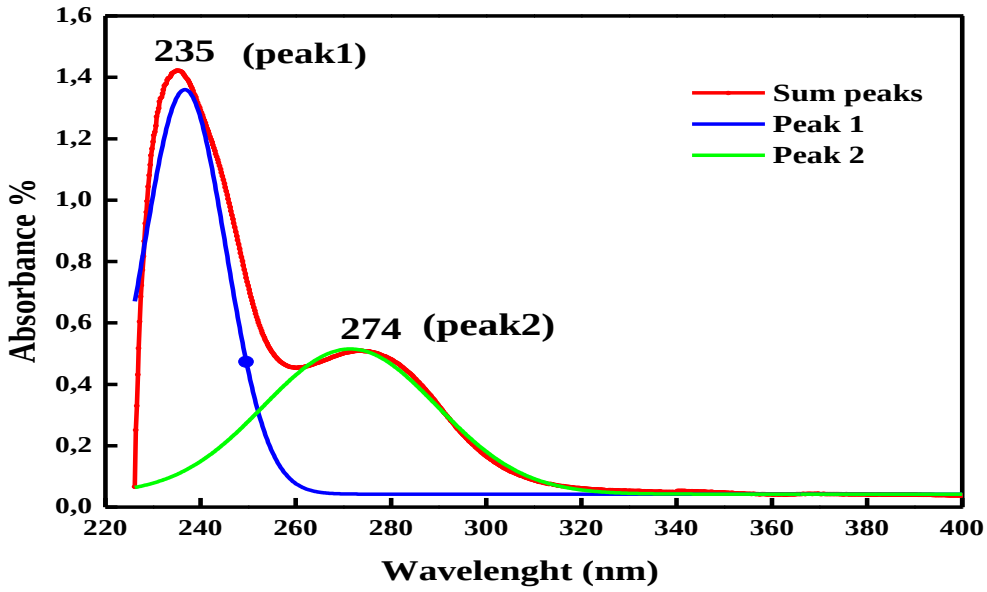

Figure III . 43: De-convolution of UV-vis spectrum.

Table III . 12:Data of the de-convolution of UV-Vis spectra .

Samples	Peak 1	Peak 2
Centre (nm)	235	274
Amplitude (a.u.)	1.3174	0.472
Area (a.u.)	28.48	21.6
FWHM (nm)	20.32	42.93
R^2	0.974	0.974

III.3.8 Flame atomic absorption spectroscopy using micro-emulsion method (ME)

Figure III . 44 shows the results of the FAAS analysis. We notice that after immersion in SWCO biodiesel, the 307 L stainless steel releases some of its elements such as Fe, Ni, Cr into the solution.

Based on the figure, we notice a high concentration of released iron in the WCO biodiesel compared to nickel and chromium. This negative result of Ni and Cr indicates that the concentrations of the elements are below the detection limit of the instrument, implying that the corrosion products are formed on the metal surface, which was confirmed by XRD and SEM analysis.

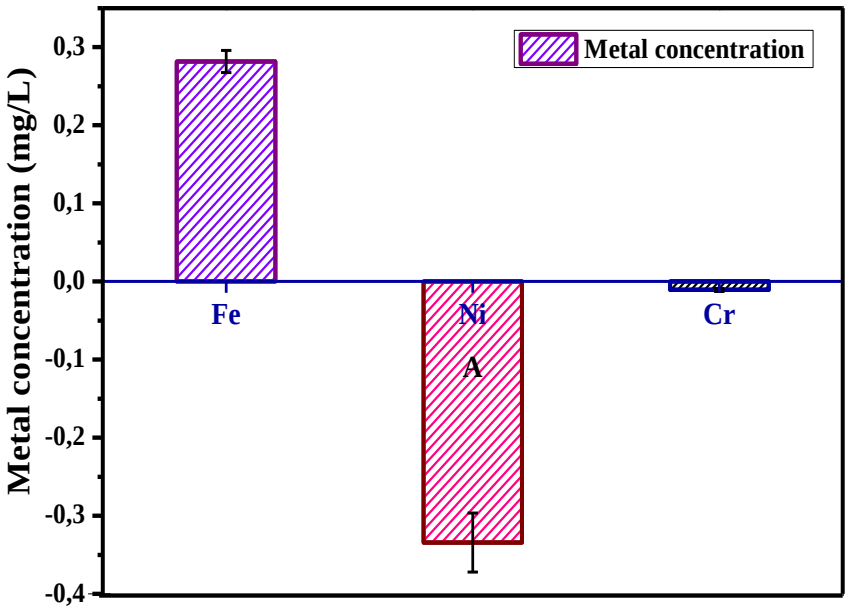

Figure III . 44:FAAS results employed for the determination of metals elements in WCO biodiesel solution.

Conclusion

The corrosion behaviour of the 307 L stainless steel in the SWCO biodiesel was studied using electrochemical methods and analyses spectroscopies. It is found that the corrosion rate of the 307 L stainless steel was very high at the beginning of the immersion time before decreasing after 24 hours due to the formation of a protective layer the chromium oxide (Cr_2O_3) on its surface. Furthermore, after 48 hours of immersion, the corrosion rate of the 307 L stainless steel continuously increases due to the breakdown of the formed passive film, and above 168 hours, the corrosion rate becomes to decrease with the re-establishment of the passive film. In addition, the 307 L stainless steel showed a corrosion resistance with the lowest corrosion rate presenting as localized corrosion such as pitting mostly due to the oxidation of biodiesel, which can enhance the corrosion compounds. The spectroscopic techniques (UV-Vis -NIR, and FAAS) indicated the high content of Fe compared to Ni and Cr in the solution, which means that the corrosion products are formed on the 307 L stainless steel surface.

PART C:

The evolution of the inhibiting activity of spent coffee ground extract on stainless steel in SWCO-Biodiesel solution.

PART C: The evolution of the inhibiting activity of spent coffee ground extract on stainless steel in SWCO-Biodiesel solution.

III.4 Introduction

Green chemistry focuses on preserving raw materials and energy resources while respecting the environment and consumer well-being to meet many of the world's current environmental challenges, which is part of the growing demand for modern science and technology in the environmental chemistry sector. Considerable attention has been focused on the application of green inhibitors in recent decades.

The most effective way to protect metals against corrosion reactions is to use corrosion inhibitors derived from low-cost, renewable sources, which provide high inhibition efficiency while having little or no environmental impact. Further, corrosion inhibitors can adsorb on metal surfaces, which helps them block a variety of active sites, which is how they primarily stop corrosion.

This research aimed to investigate the recycling of coffee grounds as an environmentally friendly SCG inhibitor in SWCO biodiesel. It was efficiently produced using a Soxhlet extraction technique for a 6H inhibitor, and its chemical composition was analyzed using GC/MS and FTIR.

Furthermore, the anticorrosion properties of the extract have been thoroughly investigated using gravimetric methods, polarization potentiodynamic spectroscopy (PDP); Additionally, there is electrochemical impedance spectroscopy (EIS). On the basis of this funding, the extract studied showed excellent inhibitory efficiency, which increased moderately with a given concentration and generally decreased with increasing temperature. Further evidence that the inhibitor molecules primarily prevented biodiesel attack by physisorption came from the fact that the inhibitor was adsorbed onto the steel surface under the Langmuir adsorption isotherm model.

Additionally, after all the tests, SEM/EDS and X-ray diffraction (XRD) techniques were used to examine the metal surfaces in an aggressive solution (biodiesel). This approach confirms the protection of the stainless steel by the inhibitor used through the appearance of barrier protection products (Cr2O3, NiO, etc.), which causes a passive film to form on the metal surface, improving its corrosion resistance overall.

III.4.1 Experimental procedure

III.4.1.1 Synthesis of biodiesel

The soybean oil used for cooking (SWCO) and the 99% methanol used in the biodiesel in the current study were produced using a heterogeneous acid catalyst. The details of the synthesis were presented in Part B.

III.4.1.2 Inhibitor

III.4.1.2.1 Samples collection & coffee grounds extraction

The waste coffee grounds (beans obtained after the beverage was made, 100% Arabica type) were collected in a cafeteria at the University of Sciences in Rabat, Morocco. After that, the waste coffee grounds were dried in an oven to remove moisture. To dry, the coffee grounds and all the water were placed in a temperature-controlled oven for 24 hours.

The Soxhlet process was used to create a hydroalcoholic extract of ground coffee. HECG was extracted by placing 100 g of ground coffee in a cartridge with 450 ml methanol in a Soxhlet extractor for 5 hours at 65°C. After the extraction had been accomplished, the solvent was evaporated under a vacuum at 40 °C to remove excess methanol, the steps of extracting the inhibitor are described in ***Figure III . 45***.

The following relationship governs extraction efficiency:

$$\mathbf{R\%} = \frac{m_{ext}}{m_{ech}} * \mathbf{100} \qquad \mathbf{(88)}$$

where **:**

R: is the yield in per cent.

m_{ext} : is the mass of the extract after evaporation of the solvent in grams.

$\mathbf{m}_{ech}$: is the dry mass of the sample before extraction. Hydroalcoholic extraction has the particularity of extracting an inhibitor that is soluble in biodiesel, which is the case of the inhibitor studied.

The calculated yield of the extraction was approximately 12.3%. By dissolving 500, 7500, 1000, and 1500 ppm of the extract in 0.5 ml of 95% methanol and then gradually adding biodiesel until a final volume of 50 ml was reached, stock solutions of various concentrations of the extract were created.

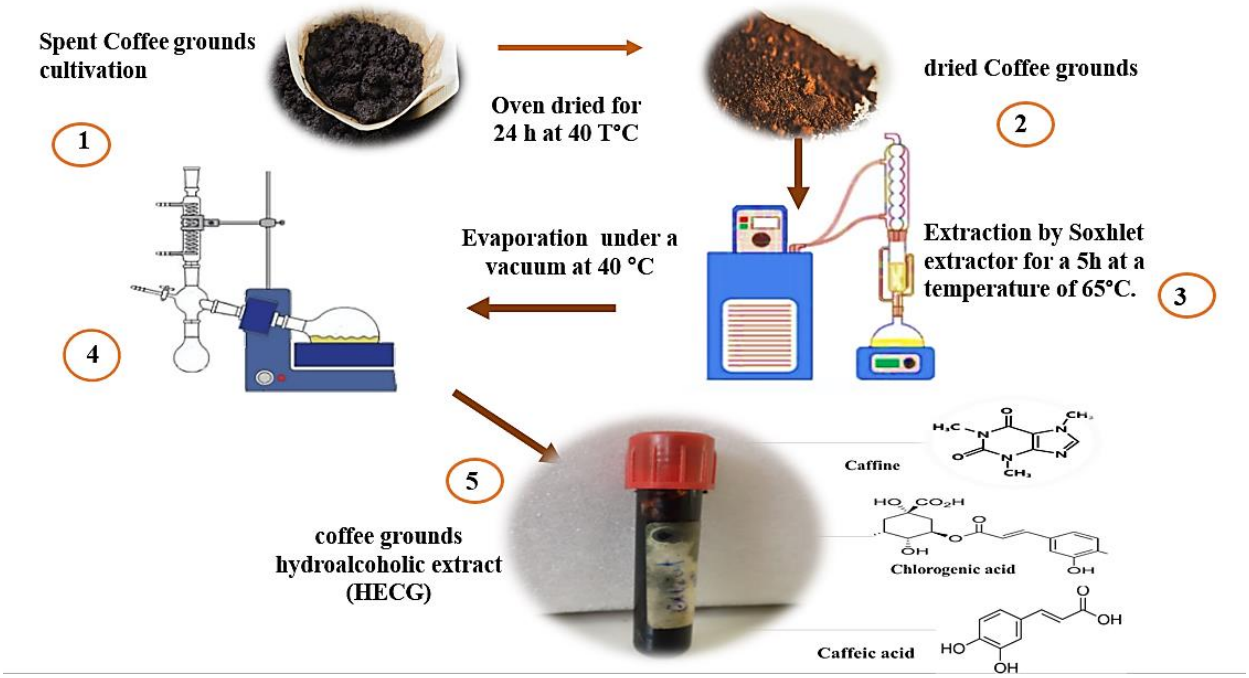

Figure III . 45: the coffee grounds hydroalcoholic extract steps.

III.4.1.2.2 GC/MS analysis of the HECG composition

The GC-MS chromatogram reveals volatile and bioactive compounds found in HECG with various retention times. According to the literature, the used coffee grounds extract is high in these compounds[213–215].

The following ***Table III . 13*** presents the chemical composition of HCGE. Twelve compounds were identified, revealing that the main components are B-Turmerone (32.49%), polyphenolic compounds such as caffeic chlorogenic acid and caffeine, and nitrogenous compounds like trigonelline. Moreover, these compounds are widely recognized for their antioxidant and antibacterial activity and their multiple applications in the agroalimentary sector, pharmaceutical, and veterinary industries[216–218].

Thus, the principle phenolic compound found in our extract was B-Turmerone due to its biological characteristics, such as its strong antioxidant activity, which could be responsible for the corrosion inhibition.

Table III . 13: the HCGC composition

	tr	%	Name of Compounds	Formula	Mol. W(g/mol)
1	10,48	32,49	B-Turmerone	C15H22O	218
2	5,44	8,68	Chlorogenic acid	C16H18O9	354,309
3	5,3	2,254	Caffeic acid	C9H8O4	180,16
4	3,466	5,695	2-Amino-4,6-dimethylpyrimidine	C6H9N3	123,15
5	1,84	7,64	4-Hydroxy-5-oxohexanoic acid	C6H10O4	146,14
6	9,732	1,67	4-methyl-Dibenzothiophene	C13H10S	198
7	11,37	18,01	Trigonelline	C7H7NO2	140,26
8	1	3,915	4-Vinyl-2-methoxy phenol	C9H10O2	150,17
9	1,43	4,368	3-pyridinol	C5H5NO	95,001
11	2,94	3,24	5-Methylfurfural	C6H6O2	110,11
12	3,94	2,69	3"-Hydroxy-geranylhydroquinone	C16H22O3	262,34
10	6,94	3,082	1-methyl-4-prop-1-en-2-ylcyclohexene	C10H18	138,25
11	6,276	7,64	Caffine	C8H10N4O2	194,19

III.4.1.2.3. Inhibitor Analysis (FT-IR)

The functional groups and spectral ranges characteristic of the coffee brand were identified using FTIR analysis as shown in ***Figure III . 46***. Inter and intramolecular hydrogen interactions are caused by hydrogen interactions between polymeric compounds such as ethanol, phenols, and carboxylic acids found in pectin, cellulose, and lignin.

The detection of a large band at 3334 cm-1 is mainly attributed to O-H stretching. The band between (2882-2829 cm^{-1}) that is attributed to the asymmetric elongation of C-H bonds of the methylamine (N-CH3) predominantly in the caffeine molecule, can be effectively exploited in the construction of prediction models for the quantitative study of caffeine[219]. Furthermore, the peak at 1700-1654 cm-1 can be attributed to being strongly bound to chlorogenic acids and caffeine. The C = O bond is stretched in a similar way to the peak at 1712 cm-1 in the presence of lipids and aliphatic esters. Indeed, the intensity of this peak increases as the concentration of these compounds in the sample

increases. The large band between 1135 and 952 cm1 results from C-O stretching vibration in C-O-H bonds such as glycosidic bonds and is associated with galactomannan polysaccharides' sugars[220].

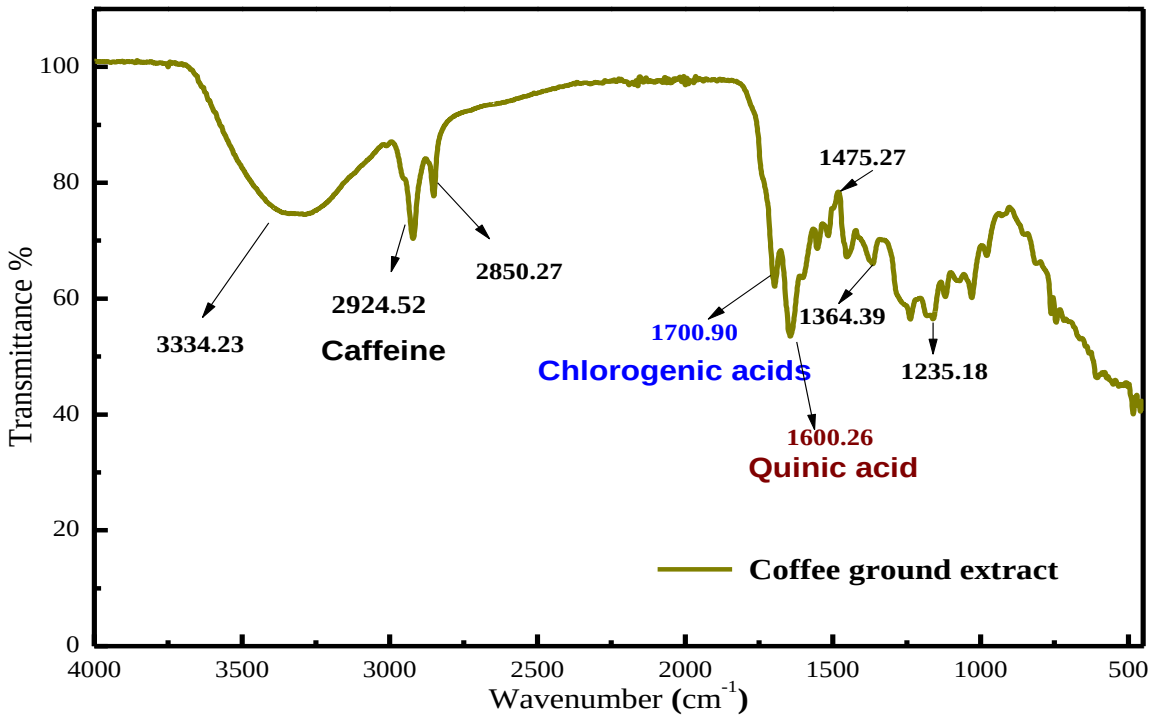

Figure III . 46:Fourier transforms infrared spectroscopy of the spent coffee grounds.

III.4.2 concentrations effects

III.4.2.1.Gravimetric method (weight loss)

The weight loss of all samples was measured before and after 1128 hours of immersion in SWCO biodiesel in a bath with different concentrations of HECG at a controlled temperature (303 K).

According to ***Table III . 14***, the corrosion rate of stainless-steel CR decreases from 1.13575E-2 to 3.38965E-4 (mg/cm2.h) as the inhibitor concentration increases from 500 to 1500 ppm, while the inhibition efficiency η_{WL} (%) increases from 78% to 97%. As the inhibitor concentration rises, the molecules of the inhibitor adhere to the stainless-steel surface, blocking more active sites for corrosion and more effectively halting mass loss[221,222].

Table III . 14:the parameters of Weight loss measurements after 1128h. Immersion in a controlled temperature (303 K) electrolyte containing various concentrations of HECG .

Conc. (ppm)	$10^2 \times C_R$ (mg/cm^2 h)	η_{WL} %
Blank	**1.1360**	
500	**0.2417**	**78.7**
750	**0.1744**	**84.6**
1000	**0.0722**	**93.6**
1500	**0.0339**	**97.0**

III.4.2.2.Electrochemical Measurements

III.4.2.2.1 Potentiodynamic polarization

Figure III . 47 illustrates the impact of HECG concentration in SWCO biodiesel on the stainless steel potentiodynamic polarization curves. ***Erreur ! Source du renvoi introuvable.*** summarizes the electrochemical characteristics obtained, In addition, as corrosion potential (Ecorr), corrosion current density (icorr), anodic (βa) and cathodic ((βc) Tafel constants and inhibition efficacy (%).

According to the polarization curves, increasing HECG concentration causes a decrease in both anodic and cathodic current densities, implying that metal dissolution at the anode and hydrogen release reactions at the cathode decrease. E_{corr} values changed noticeably, which was due to organic compounds in the extract adsorbing into the active sites on the electrode surface. This adsorption phenomenon may be attributed to the chemical inhibitor's interaction with the steel surface, which encourages the formation of a passive film, or it may be the result of the synergistic action of various organic corrosion inhibitor compounds.

The variation in E_{corr} between blank and inhibitors is much higher than 85 mV_{SCE}[223]. Based on these findings, we propose that HECG performs by inhibiting electrochemical anodic active sites on the SS surface and producing a protective layer, making it difficult to exchange the charge with the depth of the electrolyte[224].

In accordance with ***Erreur ! Source du renvoi introuvable.,*** As the concentration of HECG increased, the corrosion current density (icorr) decreased. The adsorption of HECG molecules on the stainless-steel

surface slowed the rate of the electrochemical reaction, implying that it was slowed. The anodic and cathodic Tafel slopes, ßa and ßc, were significantly different from the blank values.

Further examination of the table reveals that as the concentration of HECG extract increases, the anodic and cathodic Tafel constants change, demonstrating the impact of the plant extract on the cathodic and anodic reactions. Contrarily, it is clear that the addition of the products did not affect the corrosion potential (Ecorr) values for any concentration. These findings allowed us to calculate the inhibitory efficiency (%) EI, which rose with HECG inhibitor concentration to attain a maximum of 91.97% for 1500 ppm of HECG.

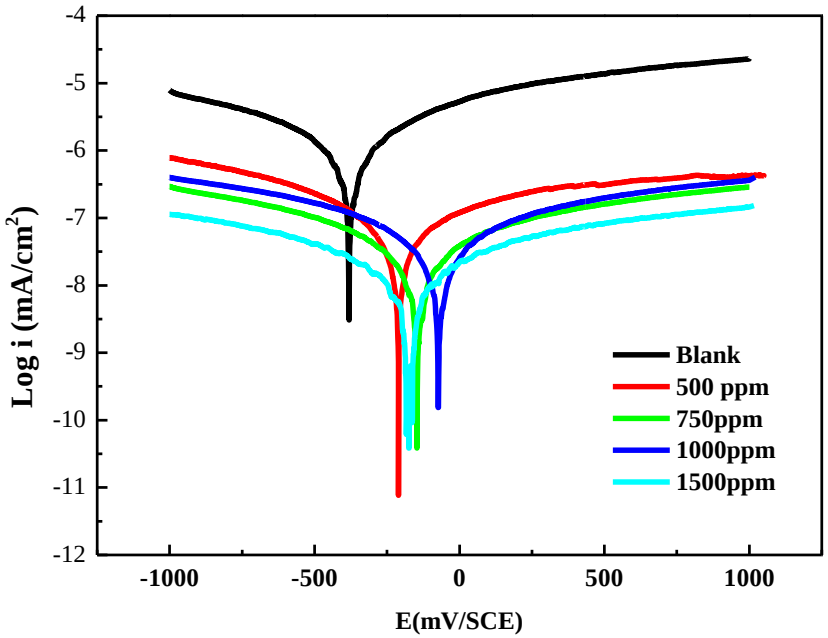

Figure III . 47:307L Stainless steel polarization curves in SWCO biodiesel without and with varying concentrations of HECG.

Table III . 15:Electrochemical parameters obtained from the polarization curves in the SWCO biodiesel solution with various concentrations of HECG

conc(ppm)	Ecorr(mV)	i_{corr}(nA/cm2)	βa	βc	% IE
Blank	-541,928	0,162	469	351,4	
500	-523,919	0,042	470,4	303,7	74,074
750	-172,56	0,029	478,8	306,7	82,098
1000	-147,135	0,017	480,1	389,5	89,506

1500	-210,114	0,013	501,1	339,9	91,975

III.4.2.2.2 Electrochemical impedance spectroscopy (EIS)

The corrosion inhibition properties of HECG on stainless steel were also investigated using electrochemical impedance spectroscopy (EIS). The **Figure III . 48** displays Stainless steel Nyquist plots obtained using the OCP in SWCO biodiesel with different concentrations of HECG.

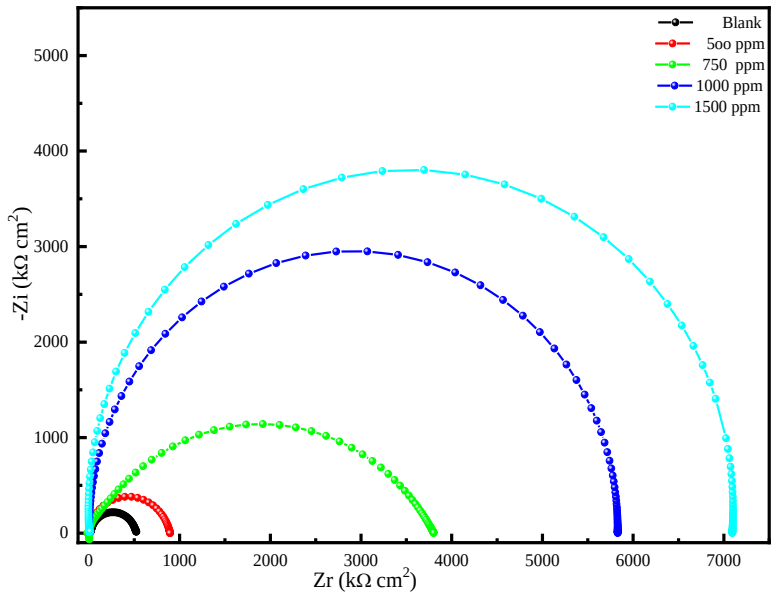

Figure III . 48 :Stainless steel impedance spectroscopy in SWCO biodiesel with varying HECG concentrations.

The previous figure shows that the impedance pattern size is modestly enhanced by adding HECG at different concentrations to the corrosive solution compared to that obtained with the pristine solution. Consequently, inhibition efficiency improved. This implies that there is a passive film formed by the adsorption of the inhibitor molecule on the steel surface.

The Nyquist representation allowed us to identify a few depressed semicircles with centres below the real axis, which pointed to the presence of a single capacitive loop. This is in accordance with the representation of the Bode diagram. This accuracy is typical of solid electrodes and could be related to the surface roughness and the metal electrode's inhomogeneity.

Furthermore, in these specific cases, the polarization resistance of the parallel array and the capacitance of the double layer is associated with the charge transfer process of metallic corrosion and the behaviour of the double layers[225]. This shows that the adsorption of plant extract molecules has reduced surface

inhomogeneity. In these cases, representing double-layer capacitors with a constant phase element (CPE) transfer function allows for a more accurate fit to the experimental data set.

The Bode plot and phase angle are depicted in ***Figure III . 49*** (a-b). Additionally, the Bode plot reveals the existence of a single constant phase element, which is typically the interface resistance. This finding indicates that charge transfer is primarily responsible for regulating the electrochemical process.

Furthermore, the absolute impedance of the Bode diagram at low-frequency values indicates that shielding increases with increasing HECG concentration [226]. The phase angle plot shows that increasing the concentration of the inhibitor produces an absolute value close to 88°. This is due to the high interaction of HECG molecules at higher concentrations on the stainless steel surface due to the formation of a passive layer, which prevents the metal from dissolving in the aggressive solution[227].

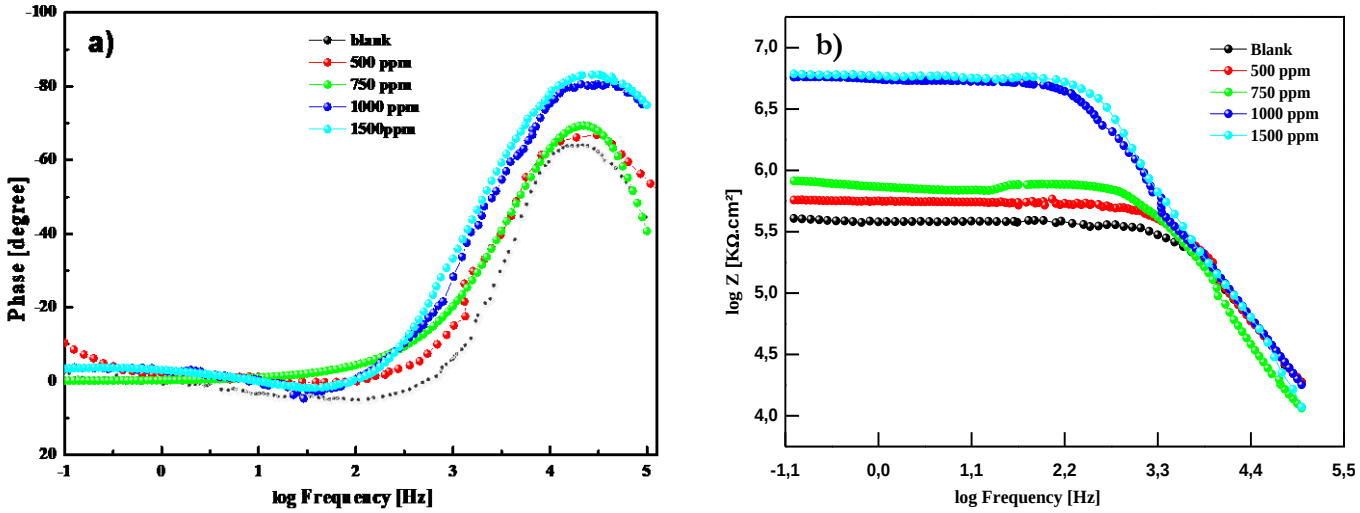

Figure III . 49:Bode-phase (a) and Bode-module plots (b) of stainless steel in SWCO biodiesel with different concentrations of HECG

Table III . 16: the electrochemical parameters found by fitting the EIS data

Conc. ppm	R_s (Ω $cm^{2)}$	CPE_{dl} (μF s^n cm^2)	n_{ct}	R_{ct} ($k\Omega$ $cm^{2)}$	CPE_f (μF s^n cm^2)	n_f	R_f ($k\Omega$ cm^2)	R_p ($k\Omega$ cm^2)	η
Blank	3865	1.18E-01	0.9110	1.22E+01	9.72E-4	0.9980	9.60E+04	1.08E+05	-----
500	1510	1.37E-4	0.9794	1.30E+01	1.12E-4	0.9976	3.77E+05	3.90E+05	74.5
750	3037	1.50E-4	1.0000	2.59E+02	1.18E-2	0.8343	5.32E+05	7.91E+05	82.0
1000	2953	1.43E-3	0.9996	2.46E+03	1.27E-2	1.0000	1.60E+06	4.06E+06	94.0
1500	2918	0.142E-3	1.0000	1.86E+03	4.41E-2	0.9823	2.52E+06	4.37E+06	96.2

is a representation of the electrochemical parameters found by fitting the EIS data to the electrical circuit shown in ***Figure III. 7*** for different concentrations of HECG in swco biodiesel.

From the ***Table III . 16*** Notably, a high blank solution resistance value means that the conductivity is low, which corresponds to a high corrosion rate. However, after adding various concentrations of HECG to the aggressive solution, we first found that the solution resistance was slightly reduced, which is mainly due to the oxidation of biodiesel with the adsorption of organic compounds on the metal surface[228]. Another interesting finding is that the resistance values of the corrosion product film **Rf** formed on stainless steel are slightly higher than the value of the charge transfer resistance **Rct**, whereas the decrease in **CPE_{dl}** may be due to a decrease in the local dielectric constant and/or an increase in the thickness of the electrical double layer. This implies that the metal's corrosion resistance is primarily due to corrosion products formed during the metal/solution relationship[229].

The EIS results also show that as the HECG concentration increases, the EI (%) improves steadily. In the case of 1500 ppm, the maximum value was 96.18%. Consequently, the outcomes suggest that this HECCG extract has the potential to be a successful corrosion inhibition

III.4.3 Temperature Effect

The environment and its temperature are the primary factors that influence the corrosion phenomenon. Recognize how stainless steel interacts with an aggressive environment with or without an inhibitor that can be adjusted according to the temperature.

Polarization experiments were performed in the temperature range of 298 K–350 K in a biodiesel solution in the absence and presence of an inhibitor at its optimum concentration (1500 ppm) as indicated in ***Figure III . 50***. The electrochemical parameters that were measured, including corrosion potential (Ecorr), corrosion current density (icorr), and nPDP inhibition efficiency (%), are also presented *in***Table III . 17** In general, based on these findings, we found that the icorr values in the presence of HECG increase slightly with rising temperature as opposed to the biodiesel medium, which exhibits a significant increase[170].

Under both inhibitory and non-inhibitory conditions, the corrosion rate of stainless-steel increases with temperature. Furthermore, a slight decrease in HECG compound inhibition efficiency at lower values (70% at 350 K) indicates that the inhibitor molecules are still adsorbed on the metal surface and active in the temperature range studied.

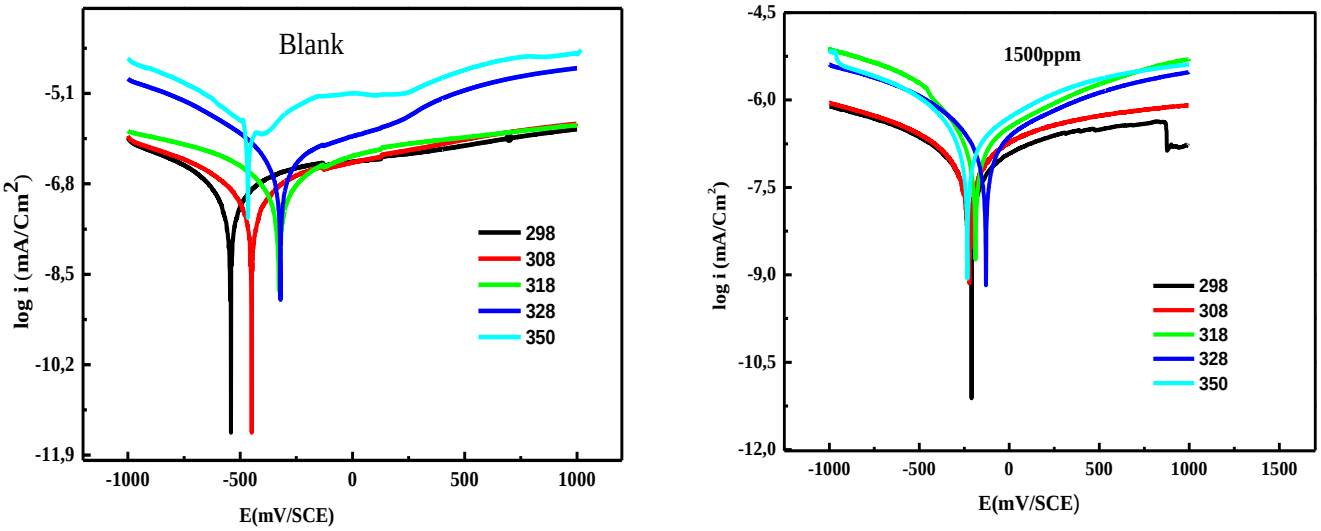

Figure III . 50 : Potentiodynamic polarization curves for the corrosion of S steel in a solution of SWCO biodiesel with and without 1500 ppm of HECG at various temperatures (298-350).

Table III . 17:Potentiodynamic polarization curves were used to calculate the stainless-steel corrosion parameters at a concentration (1500 ppm) of 298–350 K and without HECG

Medium	**Temp (K)**	E_{corr} **(mV_{SCE})**	i_{corr} **($\mu A/cm^2$)**	**% η_{PDP}**
	298	-541.9	162	
	308	-553.8	359	
Blank	318	-570.0	467	
	328	-613.0	483	
	350	-649.9	611	
	298	-210.1	13	92.0
	308	-232.1	64	82.2
1500 ppm	318	-283.3	93	80.2
	328	-329.6	100	77.2
	350	-357.8	230	62.4

The activation energies (**ΔEa**), enthalpies (**ΔHa**), and activation entropies (**ΔSa**) must also be determined in order to comprehend the mechanism of HECCG inhibition.

From the Arrhenius equation (88) one can determine the activation energy (Ea) by plotting different values of ln (icorr) as a function of (1000/T), one can thus calculate Ea *(***Figure III . 51***-a)* according to this equation:

$$i_{corr} = A \exp\left(\frac{-E_a}{RT}\right) \qquad (89)$$

with Ea representing the corrosion activation energy, R representing the universal gas constant, T representing the absolute temperature, and (A) corresponding to the pre-exponential Arrhenius factor.

$$i_{corr} = \frac{R \times T}{N \times h} \times exp\left(\frac{\Delta S_a}{R}\right) exp\left(\frac{-\Delta H_a}{R \times T}\right) \qquad (90)$$

Whereby Na Avogrado number, h Plank constant, ΔHa, ΔSa are the activation enthalpy, and activation entropy, respectively. A straight line is given by ln (Icorr)/T as a function of (1000/T) (***(Figure III . 51-b)*** Its slope is (-ΔHa / R), and its intersection with the ln (Icorr)/T axis gives the parameter ΔSa.

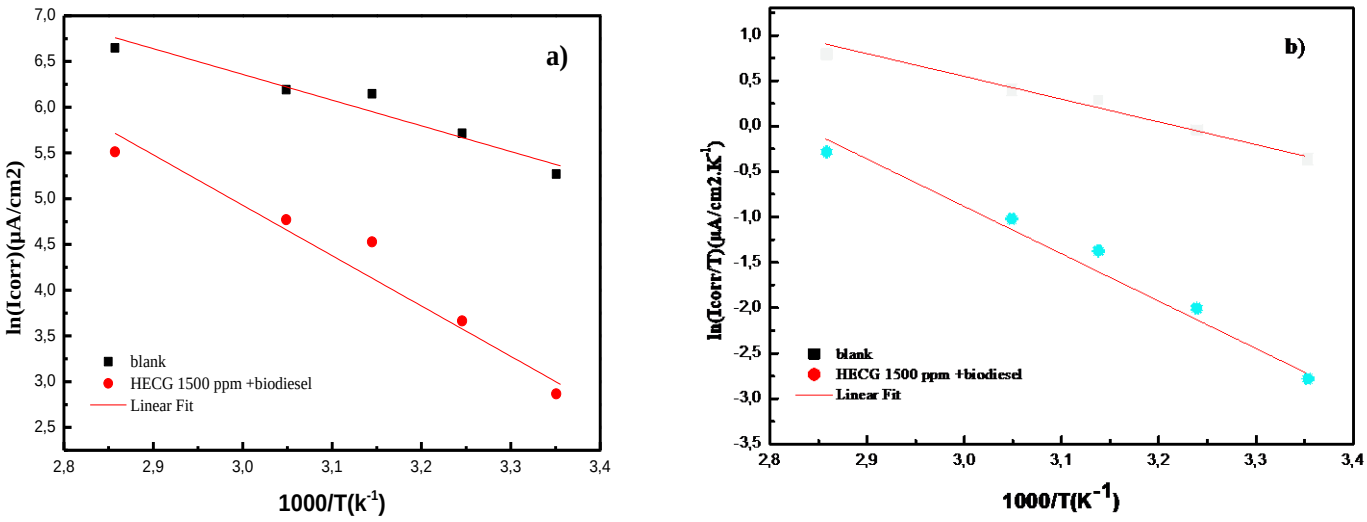

Figure III . 51:Plots of ln (icorr) versus 1/T and ln icorr/T versus 1/T for stainless steel with and without HECG at the optimal concentration (1500 ppm) and temperatures

Table III . 18: The calculated value of stainless-steel activation energy in SWCO biodiesel with HECG at its optimum concentration for different temperatures

Medium	**E_a (kj.mol^{-1})**	**ΔH_a (kj.mol^{-1})**	**Ea-ΔH_a (kj.mol^{-1})**	**-ΔS_a (j.mol^{-1} K^{-1})**
Blank	***23,40***	***20,71***	**2,69**	**130,99**
HECG inhibitor	***45,81***	***43,13***	**2,69**	**75,63**

As ***Table III . 18*** indicates, the higher values of ($\boldsymbol{E_a^\circ}$) in the addition of HECG represent a clear indication of the high inhibitory effect of the HECG by enhancing the corrosion process's energetic level. This may also be related to the increase in the double-layer thickness, which improves the ($\boldsymbol{E_a^\circ}$) of the corrosion process[230,231]. The increase in ($\boldsymbol{E_a^\circ}$) is frequently attributed to the formation of an absorbent physisorption film in the presence of an inhibitor[232]. We also notice that the activation enthalpy values $\boldsymbol{\Delta H_a^\circ}$ are both positive in the blank solution and in the presence of an optimum concentration, indicating that the process is endothermic. Besides, the $\boldsymbol{(\Delta S_a^\circ)}$ value of when HECG is present, it is greater than when it is not, indicating that the transition from a reactive to an activated complex has increased the degree of disorder hazard. We notice that the shift value of $\boldsymbol{(\Delta S_a^\circ)}$ to a more positive value by the addition

of the HECCG's concentration is the driving force that can overcome the barriers to the adsorption of the inhibitor on the stainless steel surface[233].

In addition, the difference in the average value between the E_a°-ΔH_a° is ***2.69 KJ.mol-1 at 298 K,*** which is relatively equal to the average value of RT (***2.47 KJ.mol-1)*** at the average temperature of the studied area. This result confirms that the corrosion process is a unimolecular reaction described by the known perfect gas equation (9):

$$E_a^\circ - \Delta H_a^\circ = \mathbf{RT} \qquad (91)$$

III.4.4 Adsorption isotherm

The effectiveness of an inhibitor can only be interpreted by investigating the inhibitor's ability to be adsorbed on the metal surface and the mechanisms by which this adsorption may occur. In fact, the surface oxide formation and adsorption of an organic corrosion inhibitor to the metal surface can reduce the metal's corrosion. The organic adsorbent's adsorption at the metal/solution interface can be described as a substitutional adsorption process involving organic molecules in the aqueous solution Org(sol) and water molecules on the metal surface H_2O(ads) (equation 100).

$$\mathbf{Org_{(sol)} + xH_2O_{(ads)} \rightleftharpoons Org_{(ads)} + xH_2O_{sol}} \qquad \mathbf{(92)}$$

With $Org_{(ads)}$, the organic molecules adsorbed on the metal surface, $H_2O_{(sol)}$ stands for water molecules in the aqueous solution, and x is the size ratio that represents the number of water molecules substituted by one organic adsorbate molecule.

To comprehend HECG's behaviour and adsorption strength on the stainless-steel surface. The experimental results were fitted to various adsorption isotherm models.

The model of **C/ θ vs C.** is shown in (Eq.101).

As shown in ***Figure III . 52*** a line demonstrating the fit of the Langmuir isothermal model is drawn using the surface coverage θ values obtained from potentiodynamic polarization measurements for various inhibitor C concentrations.

$$\frac{C_{inh}}{\theta} = \frac{1}{K_{ads}} + C_{inh} \qquad (93)$$

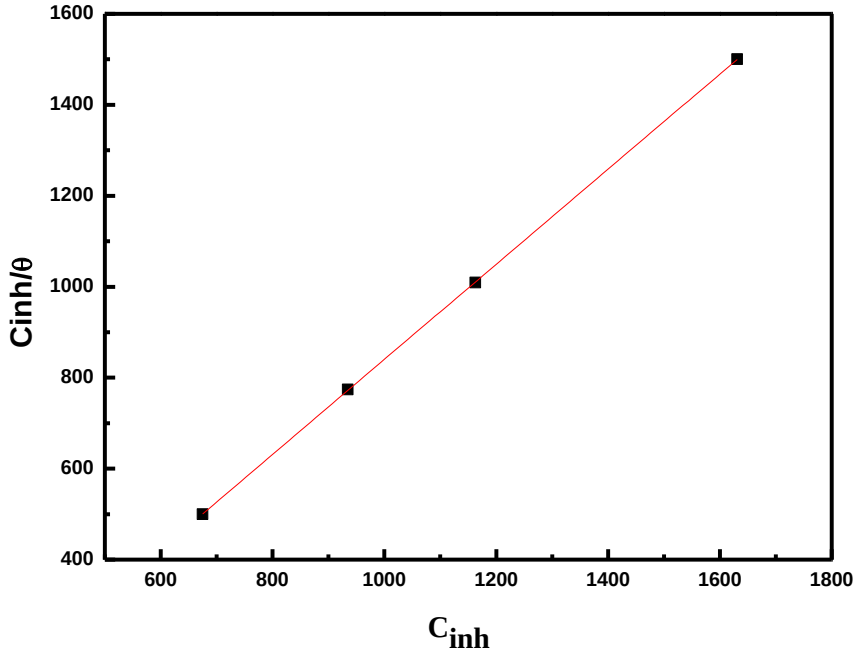

Figure III . 52: Langmuir adsorption isotherm of HECG on the S- steel surface at 298 K.

III.4.5 Analysis by UV-Vis-NIR spectroscopy

The characteristics of the corrosion products formed on the surface of S-steel immersed in SWCO biodiesel for 1128 hours in the presence and absence of HECG at 37°C were determined using UV-Vis-NIR analysis.

The UV-Vis-NIR spectra were analyzed with 2D derivatives using the Savitzky-Golay function. Additionally, by emphasizing sensitive absorption bands in the second derivatives of the absorption curve, it was possible to improve the results of bands that could be produced by electronic or vibrational transitions in the corrosion products. Furthermore, the ability of a material to defend itself from a corrosive environment can be quantified by measuring the difference in amplitude between the lowest and highest near points of the absorption bands.

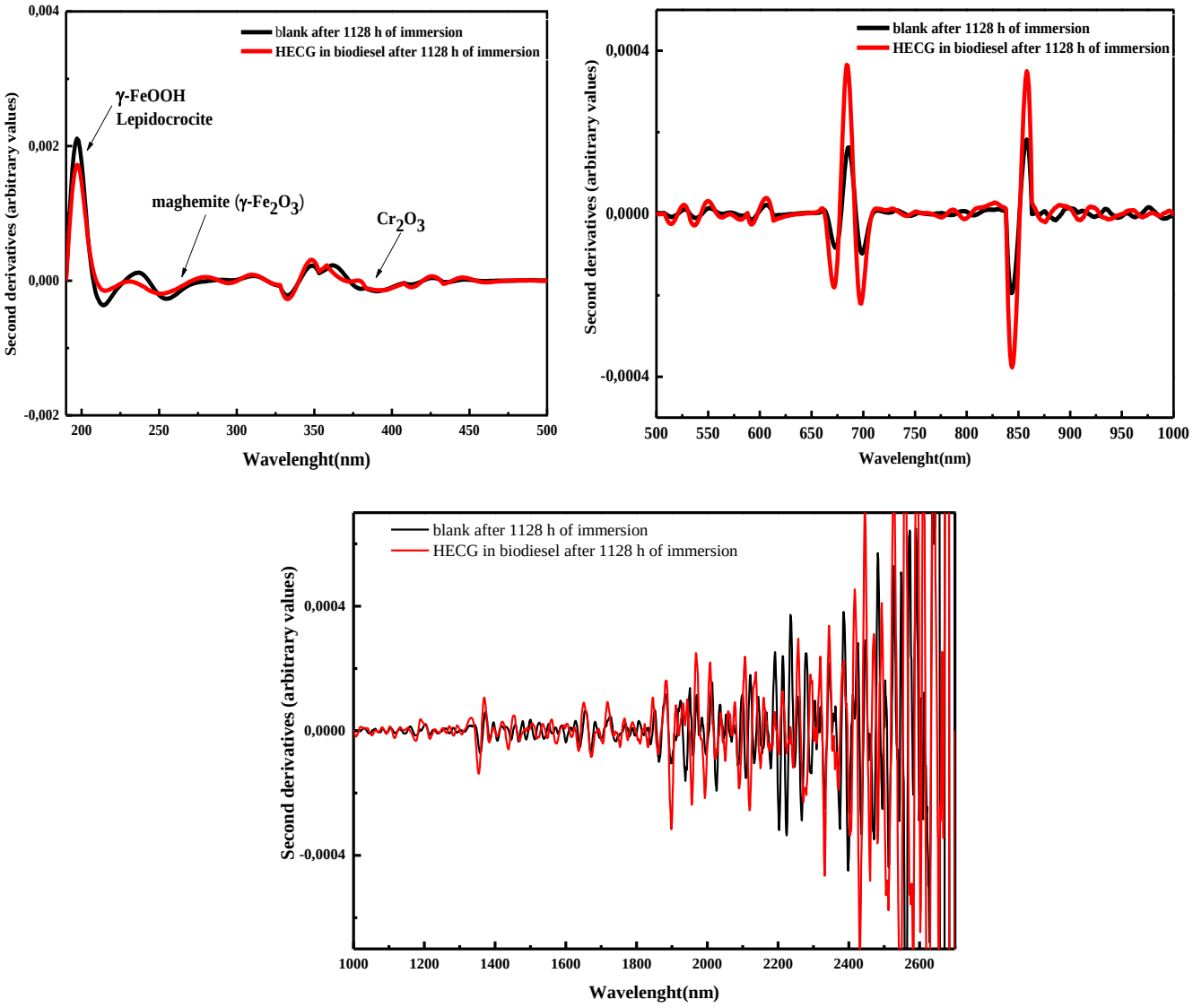

Figure III . 53 : Spectra of the s-steel surface's second derivative of the Savitzky-Golay function before and after 1128 hours in SWCO biodiesel (blank) and 1500 ppm HECG extract at 37 °C.

Besides ***Figure III . 53***, the surface of S steel showed that the maximum dominant constituent additives had been iron and chromium, as formerly suggested by different researchers [162].Therefore, Lepidocrocite (γ-FeOOH) and maghemite (γ-Fe_2O_3) are responsible for the peaks at 210 and 250 nm, respectively. Furthermore, the extreme peaks at 2668 -2688 nm connect with hydroxide (OH), with special coordination in γ-Fe_2O_3, and the bands at 412, 606, and chromium (Cr) oxides may be related to wavelengths of 726 nm. The peaks at 380, 432, 680, and 712 nm are attributed to nickel oxides[206,237]. For the HECG inhibitor, the amplitude of iron, chromium, and nickel oxides corresponding to the metal surface displays a difference in amplitude between the solution containing 1500 ppm and the blank

solution HECCG, this means that the surface was significantly protected from damage by forming a passive layer on the metal's surface, which was supported by XRD and SEM/EDS models.

III.4.6 UV–Vis Absorption Spectroscopy

The inhibitory effect of HECG in solution was evaluated using UV-Vis spectroscopy of the solution after 1128H immersion in the metal.

Figure III . 54 *d*epicts THE UV-vis spectrum, where the black line corresponds to SWCO biodiesel, and the red line corresponds to SWCO biodiesel with 1500 ppm of HECG inhibitor.

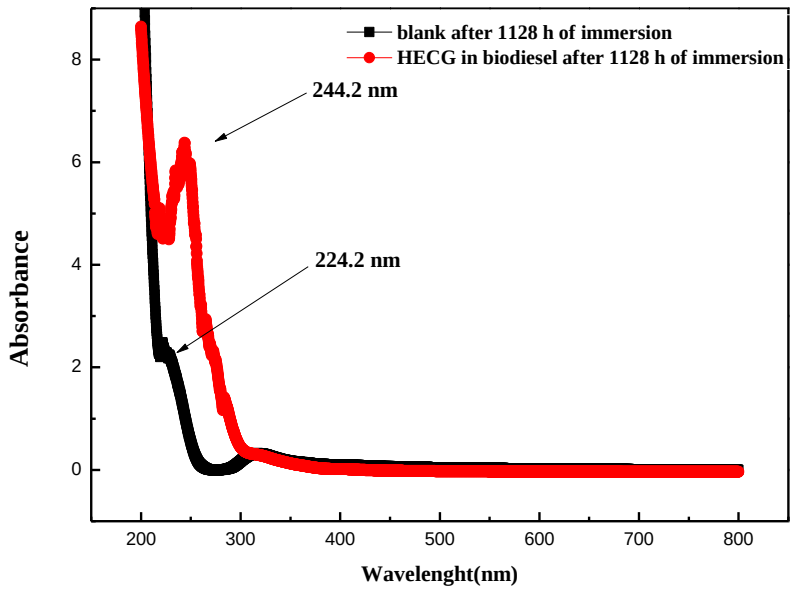

Figure III . 54: UV-Vis absorption spectrum of a stainless-steel immersion for 1128H at 37°C in SWCO biodiesel (white) and optimal HECG inhibitor concentration (1500 ppm).

From the illustration in ***Figure III . 54*** we can see that the increase in the absorption band is due to a hypochromic effect with a shift in the wavelength band from 224.2 nm to 244.2 nm (bathochromic effect). The oxidation of polyunsaturated fatty acids causes this modification, which is associated with the passage of isolated double bonds into conjugated double bonds. This might be attributed to the oxidation-induced conjugation of linoleic acid's two double bonds. [238]. Furthermore, after the addition of HECG at a concentration of 1500 ppm, we noticed that the formulation (SWCO biodiesel/inhibitor) became more stable than that free of the inhibitor. This finding suggests that the inhibitor's influence was effective in slowing the metal dissolution process. As a result, it was determined that HECG has a high inhibitory efficiency.

III.4.7 Surface Characterization

III.4.7.1 SEM/EDX study

The surface morphology of the S-steel investigated for polished, uninhibited, and exposed surfaces inhibited in biodiesel after 1128 hours of immersion was characterized using SEM/EDX.

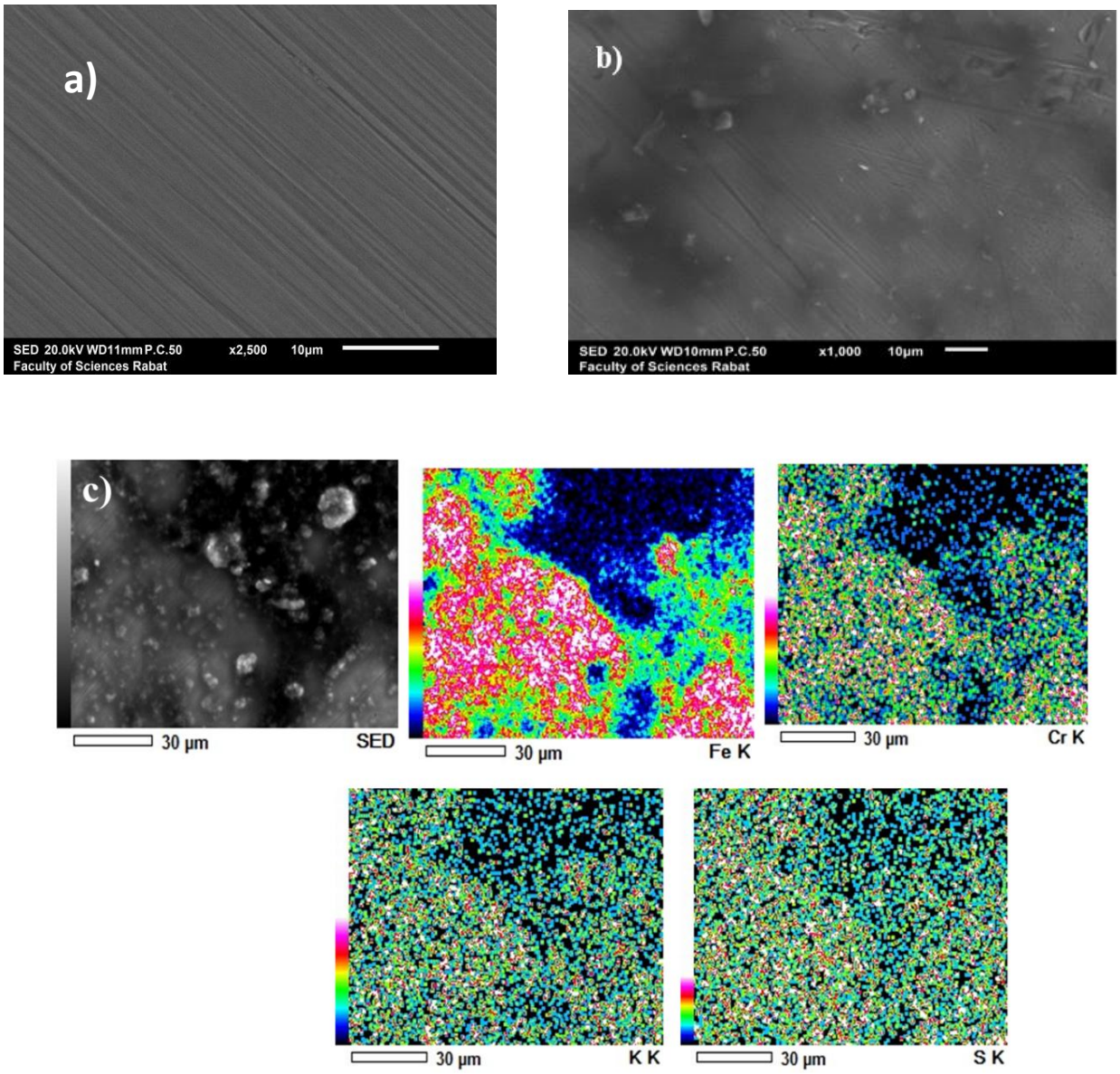

Figure III . 55: Stainless steel SEM images for polished (a), uninhibited (b), and inhibited (c) mapping exposed to SWCO biodiesel.

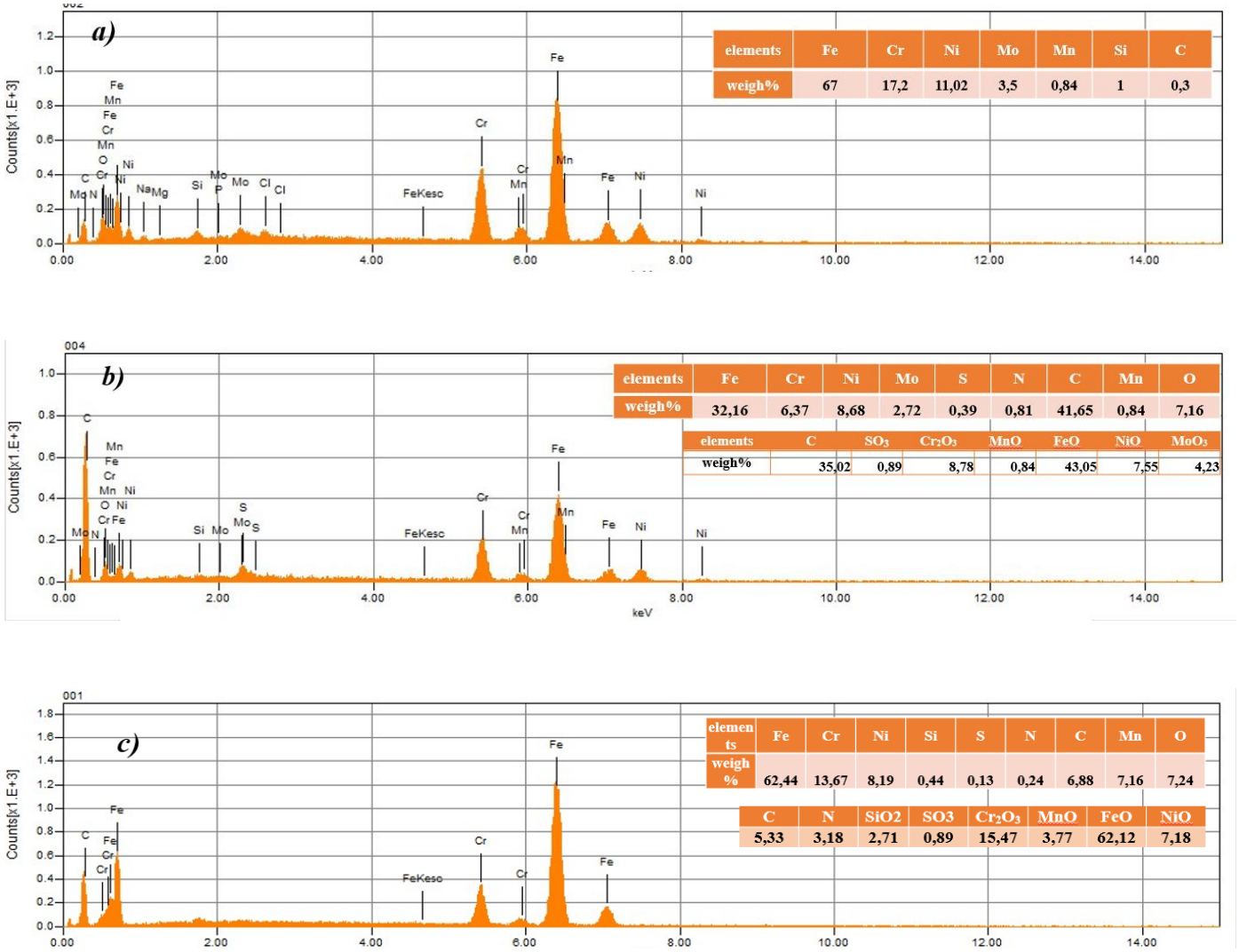

Figure III . 56: EDX spectra of S steel in the following states: (a) polished, (b) exposed to SWCO biodiesel without inhibitor, and (c) exposed to SWCO biodiesel with an inhibitor solution containing 1500ppm HECG

The morphology of the polished specimen is shown in the first image ***Figure III . 55(a)*** which also amply demonstrates the scratches left behind by manual polishing. The second image ***Figure III . 55*** *(b)* demonstrates the corrosion caused on the stainless steel by the acid molecules present in the SWCO biodiesel. This aggressive attack caused a slight change in the exposed surface and the presence of some deep pits (dark spots), indicating severe surface damage. The addition of HECG in the third image ***Figure III . 55(c)***) changed the surface morphology.

To represent the distribution of passive layers formed on the surface of S steel, EDX spectra were used in ***Figure III . 55(b)***) Adhesive metal oxides composed of carbon and oxygen, including those of NiO, MoO_3, Fe_2O_3, and Cr_2O_3, can be seen on the corroded surface of S steel. Additionally, stainless steel that has

been immersed in SWCO biodiesel has several organic deposits visible on its surface. Partial corrosion products adsorb and adhere as the metal oxide reacts with numerous unsaturated fatty acids, adding more carbon and oxygen to the SWCO biodiesel.

Moreover, the EDX spectra of ***Figure III . 56****(C)* demonstrates how the nitrogen peak, a component of the inhibitor molecule, appears in place of the carbon and oxygen peaks, disappearing altogether; The formation of a passive layer on the stainless-steel surface was used to confirm the adsorption of the inhibitor molecules[239].

The steel's peaks were also intensified due to the corrosive solution's restriction of metal dissolution, whereas the active surface of the stainless steel was significantly reduced with the appearance of flat areas due to the formation of a protective coating. It was confirmed that the adsorption of HECG on the surface-enhanced this protection[240].

III.4.7.2 Analysis by X-ray diffraction.

X-ray diffraction is a highly effective technique for identifying compounds and elements with atomic-scale crystal structure or periodicity. Due to the possibility of interaction between stainless steel and the corrosive environment under various circumstances, it also enables the study of the constituent species of natural corrosion.

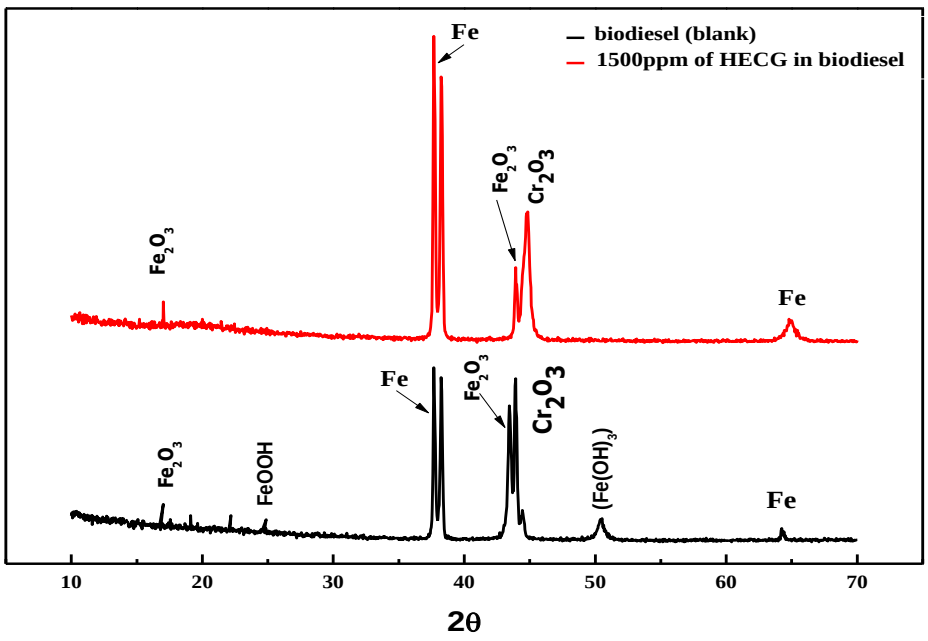

Figure III. 57: The XRD patterns of the formed corrosion products on the S-steel surface after 1128 hours of immersion in the optimal inhibitor concentration and blank SWCO biodiesel.

As illustrated in ***Figure III. 57,*** *t*he components that protect the steel against corrosion are found on the surface of the metal: Fe_2O_3, which is the iron oxide, and Cr_2O_3, which is the dominant oxide responsible for its high corrosion resistance in the absence and presence of HECG, with intensities increasing after the addition of the inhibitor[241]. Similarly, the appearance of peaks corresponding to non-protective corrosion compounds Fe $(OH)_3$, and FeOOH in the blank solution was observed. The oxygenation of biodiesel can enhance the S-steel corrosion additionally[242]. It has been mentioned that biodiesel's resistance towards oxygenation is related to its fatty constituents, which disappear after the addition of the optimum concentration of 1500ppm of HECG, which proves its effectiveness in blocking the dissolution of the metal by retread the corrosion rate[243].

Conclusion

According to the findings of the study, HCGE is a highly effective corrosion inhibitor for stainless steel in biodiesel solutions at temperatures ranging from 298 to 350 K. Furthermore, weight loss measurements, electrochemical measurements, and surface analysis techniques have all confirmed the preceding suggestion. According to potentiodynamic polarization studies, by inhibiting its active sites, the HCGE inhibitor limits absorption corrosion. The efficiency of this HCGE inhibitor at room temperature increased to 91.97% at 1500 ppm. Additionally, because stainless steel dissolves at high temperatures, its effectiveness reduces with increasing temperature, approaching 62,4 % in our case. Based on the EIS data, a sharp decrease in CPE_f values is observed, along with an increase in polarization resistance, which could be attributed to the thickening of the film formed by the HCGE molecules on the stainless-steel surface. In addition, the study of temperature effect on the corrosion inhibiting power of HECG by a thermodynamic approach using polarization curves allowed us, firstly, to quantify several thermodynamic parameters, namely, the activation energies $\boldsymbol{E_a}$, the activation enthalpies $\Delta \boldsymbol{H_a^\circ}$ and the activation entropies $\Delta \boldsymbol{S_a^\circ}$ .These findings indicate that HECG adsorption on the steel surface is primarily caused by electrostatic bonding and that the adsorption isotherm is used, implying that HECG adsorption follows the Langmuir isotherm mode. The SEM and XRD analysis also revealed that the metal surface was effectively protected in the presence of the HCGE inhibitor by the formation of a protective layer in the metal surface.

General conclusion

The entire study reported in this thesis is structured in three main areas:

The first section aims to apply monitoring techniques such as open circuit potential (OCP) and electrochemical impedance spectroscopy (EIS) followed by potentiodynamic plolarization (tafel); SEM/EDS, X-ray diffraction, and spectroscopy analyses to evaluate the corrosion behavior of copper, aluminum, and stainless steel in biodiesel during manufacture at room temperature while assessing its effect on overall fuel characteristic degradation. For a deep understanding, quantum chemical computations (DFT) and molecular dynamics simulations (MDS) were performed to improve our knowledge of the adsorption phenomena.

According to these findings, copper and stainless steel are less durable during the biodiesel synthesis process than aluminum, which is also chemically compatible. Additionally, the results of the electrochemical technique showed that the corrosion rate was higher for every metal during the earliest stages of biodiesel generation than it diminished for aluminum and stainless steel, which showed a slightly lower corrosion rate.

Based on the SEM/EDS assessment, the methyl esters had a negligible effect on the metal's degradation, resulting in a slow corrosion rate and the development of small localized pitting on the metal's surface. Similar results were obtained by FAAS analysis, which confirmed the electrochemical methods' findings of the presence of a low concentration of metal ions released into the solution. On the other hand, the experimental results are corroborated by DFT and MD simulation data; Based on the estimated percentage of FFV which was 13.06%. The small FFV obtained shows that the ML molecules behave as a protective barrier and reduces the corrosive ions to reach the surface of the studied metals. Furthermore, the correlation approach (DFT and molecular dynamics (MD) simulations) was applied to support the experimental results that favor aluminum as the base metal for biodiesel synthesis due to its low corrosion rate during the production process.

The second section of our investigation consists of studying in more detail the link between biodiesel degradation and the corrosion behavior of the 307L stainless steel used for storage. In addition, waste soybean cooking oil (SWCO) was converted into biodiesel using a transesterification method based on heterogeneous catalysts and methanol; Furthermore, the corrosion behavior of 307L during 264 hours of storage was investigated using electrochemical techniques;

The results reveal a weak influence of methyl ester on metal degradation, indicating a low corrosion rate with a localized micro pitting on its surface. Moreover, flame atomic absorption spectroscopy (FAAS) showed the existence of a diminutive number of metal ions, and the electrochemical assays such as electrochemical impedance spectroscopy (EIS) and the polarization curves (PC) exhibited a great corrosion resistance of the 307 L stainless steel by the formation of a passive film of oxide de chrome (Cr2O3) in the steel surface this means that the corrosion rate is the smallest. It is manifested as localized corrosion, especially pitting, mainly due to the oxidation of biodiesel, which can enhance the corrosive compounds. According to the spectroscopic techniques (UV-Vis and FAAS), the Fe content is high compared to Ni and Cr in the solution, which means that the corrosion products are formed on the stainless-steel surface. Furthermore, these results were confirmed by DRX and SEM/EDS techniques.

In the third section of this thesis, many different approaches, including gravimetry with 1128 H of immersion and electrochemical techniques (OCP, EIS, polarization curves), have been employed to assess the efficiency of coffee grounds as a green inhibitor of the corrosion of 307 L stainless steel in SWCO biodiesel. We coupled various surface characterization methods (SEM/EDS, XRD, and UV-Vis-NIR) with these basic techniques to further comprehend the inhibitory mechanism. Furthermore, the temperature effect on HECG inhibition efficiency was examined using a thermodynamic approach, which allowed us, initially determine several thermodynamic parameters, such as activation energies Ea, activation enthalpies (**ΔHa**), and activation entropies **ΔSa**.

The results of this investigation reveal that HCGE is a very good inhibitor of corrosion of stainless steel in biodiesel solutions at temperatures ranging from 298 to 350 K. Likewise, weight loss studies, electrochemical measurements, and surface analysis techniques all confirmed the previous state. According to potentiodynamic polarization experiments, the efficiency of this HCGE inhibitor at room temperature improved to 91.97% at 1500 ppm. Additionally, while stainless steel dissolves at high temperatures, its effectiveness declines with rising temperatures, nearing 71%. Depending on the EIS data, a sharp drop in CPE_f values is noticed, as well as an increase in polarization resistance, which could be due to the thickening of the film produced by the HCGE molecules on the stainless-steel surface.

According to the thermodynamic parameter data, HECG adsorption on the steel surface occurs primarily through electrostatic bonding. This demonstrates the process's spontaneity and the durability of the adsorbed double layer, verifying the inhibitor's adsorption on the steel surface via electrostatic bonding. The adsorption process can be described as exothermic.

Furthermore, the adsorption of the HECG obeys the Langmuir isotherm model. The SEM and XRD analyses also revealed that the metal surface was effectively protected in the presence of the HCGE inhibitor by the formation of a protective layer on the metal surface.

The perspectives

This research could lead to the development of more sustainable and durable biodiesel fuels. This could benefit the biodiesel industry, as well as consumers and the environment.

Here are some specific research directions that could be pursued:

- Develop new heterogeneous catalysts that are effective at both producing biodiesel and preventing corrosion.
- Optimize the production of biodiesel from waste feedstocks using heterogeneous catalysts.
- Evaluate the performance and durability of biodiesel produced from waste feedstocks using heterogeneous catalysts in real-world applications.
- Optimization of the photocatalytic degradation of biodiesel using nanocomposites

.

References

[1] The White House, Report on the Impact of climate change on Migration, 2021.

[2] H. Esmaeili, E. Nourafkan, M. Nakisa, W. Ahmed, Application of nanotechnology for biofuel production, Emerg. Nanotechnologies Renew. Energy. (2021) 149–172. https://doi.org/10.1016/B978-0-12-821346-9.00005-5.

[3] K. Hanaki, J. Portugal-Pereira, The Effect of Biofuel Production on Greenhouse Gas Emission Reductions, 2018. https://doi.org/10.1007/978-4-431-54895-9_6.

[4] A.T. Hoang, M. Tabatabaei, M. Aghbashlo, A review of the effect of biodiesel on the corrosion behavior of metals/alloys in diesel engines, Energy Sources, Part A Recover. Util. Environ. Eff. 42 (2020) 2923–2943. https://doi.org/10.1080/15567036.2019.1623346.

[5] A.S.M.A. Haseeb, H.H. Masjuki, L.J. Ann, M.A. Fazal, Corrosion characteristics of copper and leaded bronze in palm biodiesel, Fuel Process. Technol. 91 (2010) 329–334. https://doi.org/10.1016/j.fuproc.2009.11.004.

[6] Y. Zhang, Y. Zhong, J. Wang, D. Tan, Z. Zhang, D. Yang, Effects of different biodiesel-diesel blend fuel on combustion and emission characteristics of a diesel engine, Processes. 9 (2021). https://doi.org/10.3390/pr9111984.

[7] M.S. Ahmmad, M. Bin Haji Hassan, M.A. Kalam, Comparative corrosion characteristics of automotive materials in Jatropha biodiesel, Int. J. Green Energy. 15 (2018) 393–399. https://doi.org/10.1080/15435075.2018.1464925.

[8] M. Ateeq, L. Li, M. Abdullah, A. Ahmed, G.A. Gohar, M. Rafiq, S. Rauf, A. Ali, H. Saleem, Evaluating corrosion effect of biodiesel produced from neem oil on automotive materials, Mater. Today Sustain. 18 (2022) 100130. https://doi.org/https://doi.org/10.1016/j.mtsust.2022.100130.

[9] A. Saydut, A.B. Kafadar, Y. Tonbul, C. Kaya, Comparison of the biodiesel quality produced from refined sunflower (Helianthus annuus L) oil and waste cooking oil Author (s): Abdurrahman Saydut , Aylin Beycar Kafadar , Yalcin Tonbul , Canan Kaya , Firat Aydin and Candan Hamamci Source : Energy Exp, 28 (2010).

[10] U. Rashid, F. Anwar, Production of biodiesel through base-catalyzed transesterification of safflower oil using an optimized protocol, Energy and Fuels. 22 (2008) 1306–1312. https://doi.org/10.1021/ef700548s.

[11] S. Deng, X. Li, Inhibition by Ginkgo leaves extract of the corrosion of steel in HCl and H2SO4 solutions, Corros. Sci. 55 (2012) 407–415.

https://doi.org/https://doi.org/10.1016/j.corsci.2011.11.005.

[12] E.D. Larson, U.B. Initiative, Biofuel production technologies : status, prospects and implications for trade and development, The United Nations, 2008. https://policycommons.net/artifacts/128135/biofuel-production-technologies/.

[13] N. Khan, K. Sudhakar, R. Mamat, Role of biofuels in energy transition, green economy and carbon neutrality, Sustain. 13 (2021). https://doi.org/10.3390/su132212374.

[14] R. Amirta, E. Herawati, W. Suwinarti, T. Watanabe, Two-steps utilization of Shorea wood waste biomass for the production of oyster mushroom and biogas - a zero waste approach., Agric. Agric. Sci. Procedia. 9 (2016) 202–208.

[15] M.A. Bassi, M.A. Lopez, L. Confalone, R.M. Gaudio, L. Lombardo, D. Lauritano, Enhanced Reader.pdf, Nature. 388 (2020) 539–547.

[16] T.J. Tse, D.J. Wiens, M.J.T. Reaney, Production of bioethanol—a review of factors affecting ethanol yield, Fermentation. 7 (2021). https://doi.org/10.3390/fermentation7040268.

[17] S. Chincholkar, Biodiesel as an Alternative Fuel for Pollution Control in Diesel Engine Biodiesel as an Alternative Fuel for Pollution Control in Diesel Engine Introduction : With increasing power consumption and an increase in number of, Mech. Engneering Dep. Appl. Chem. Dep. 19 (2005) 13–22.

[18] scholar, (n.d.).

[19] N. Eloutassi, B. Louaste, L. Boudine, A. Remmal, Valorisation de la biomasse lignocellulosique pour la production de bioéthanol de deuxième génération, Rev. Des Energies Renouvelables. 17 (2014) 600–609.

[20] J.C. Ogier, D. Ballerini, J.P. Leygue, L. Rigal, J. Pourquié, Production d'éthanol à partir de biomasse lignocellulosique, Oil Gas Sci. Technol. 54 (1999) 67–94. https://doi.org/10.2516/ogst:1999004.

[21] C. Debnath, T.K. Bandyopadhyay, B. Bhunia, U. Mishra, S. Narayanasamy, M. Muthuraj, Microalgae: Sustainable resource of carbohydrates in third-generation biofuel production, Renew. Sustain. Energy Rev. 150 (2021) 111464. https://doi.org/10.1016/j.rser.2021.111464.

[22] W. Klinthong, Y.H. Yang, C.H. Huang, C.S. Tan, A Review: Microalgae and their applications in CO2 capture and renewable energy, Aerosol Air Qual. Res. 15 (2015) 712–742. https://doi.org/10.4209/aaqr.2014.11.0299.

[23] K. Atsonios, M.A. Kougioumtzis, K.D. Panopoulos, E. Kakaras, Alternative thermochemical routes for aviation biofuels via alcohols synthesis: Process modeling, techno-economic assessment and comparison, Appl. Energy. 138 (2015) 346–366.

https://doi.org/10.1016/j.apenergy.2014.10.056.

[24] B. Sen, Concluding remarks, Lect. Notes Energy. 27 (2014) 265–267. https://doi.org/10.1007/978-1-4471-6482-1.

[25] E.S. Shuba, D. Kifle, Microalgae to biofuels: 'Promising' alternative and renewable energy, review, Renew. Sustain. Energy Rev. 81 (2018) 743–755. https://doi.org/10.1016/j.rser.2017.08.042.

[26] R.M. Jingura, R. Kamusoko, Temporal and spatial analysis of electricity generation from biomass sources in sub-Saharan Africa, Cogent Eng. 4 (2017). https://doi.org/10.1080/23311916.2017.1296757.

[27] H. El Arroussi, R. Benhima, N. El Mernissi, R. Bouhfid, C. Tilsaghani, I. Bennis, I. Wahby, Screening of marine microalgae strains from Moroccan coasts for biodiesel production, Renew. Energy. 113 (2017) 1515–1522. https://doi.org/10.1016/j.renene.2017.07.035.

[28] B. Amigun, R. Sigamoney, H. von Blottnitz, Commercialisation of biofuel industry in Africa: A review, Renew. Sustain. Energy Rev. 12 (2008) 690–711. https://doi.org/https://doi.org/10.1016/j.rser.2006.10.019.

[29] B. Ghobadian, H. Rahimi, A.M. Nikbakht, G. Najafi, T.F. Yusaf, Diesel engine performance and exhaust emission analysis using waste cooking biodiesel fuel with an artificial neural network, Renew. Energy. 34 (2009) 976–982. https://doi.org/10.1016/j.renene.2008.08.008.

[30] M.H. Hassan, M.A. Kalam, An overview of biofuel as a renewable energy source: Development and challenges, Procedia Eng. 56 (2013) 39–53. https://doi.org/10.1016/j.proeng.2013.03.087.

[31] S. Mekhilef, S. Siga, R. Saidur, A review on palm oil biodiesel as a source of renewable fuel, Renew. Sustain. Energy Rev. 15 (2011) 1937–1949. https://doi.org/https://doi.org/10.1016/j.rser.2010.12.012.

[32] L. Wei, C.S. Cheung, Z. Ning, Influence of waste cooking oil biodiesel on combustion, unregulated gaseous emissions and particulate emissions of a direct-injection diesel engine, Energy. 127 (2017) 175–185. https://doi.org/https://doi.org/10.1016/j.energy.2017.03.117.

[33] A.W. Schwab, M.O. Bagby, B. Freedman, Preparation and properties of diesel fuels from vegetable oils, Fuel. 66 (1987) 1372–1378. https://doi.org/https://doi.org/10.1016/0016-2361(87)90184-0.

[34] H. Fukuda, A. Kondo, H. Noda, Biodiesel fuel production by transesterification of oils, J. Biosci. Bioeng. 92 (2001) 405–416. https://doi.org/https://doi.org/10.1016/S1389-1723(01)80288-7.

[35] D. Mohan, C.U. Pittman, S. Philip, Pyrolysis of Wood/Biomass for Bio-oil: A Critical Review Dinesh, Prog. Energy Combust. Sci. 62 (2017) 848–889.

http://dx.doi.org/10.1016/j.pecs.2017.05.004.

[36] F. Ma, M.A. Hanna, Biodiesel production: a review1Journal Series #12109, Agricultural Research Division, Institute of Agriculture and Natural Resources, University of Nebraska–Lincoln.1, Bioresour. Technol. 70 (1999) 1–15. https://doi.org/https://doi.org/10.1016/S0960-8524(99)00025-5.

[37] K.D. Maher, D.C. Bressler, Pyrolysis of triglyceride materials for the production of renewable fuels and chemicals, Bioresour. Technol. 98 (2007) 2351–2368. https://doi.org/https://doi.org/10.1016/j.biortech.2006.10.025.

[38] J.M. Marchetti, V.U. Miguel, A.F. Errazu, Possible methods for biodiesel production, Renew. Sustain. Energy Rev. 11 (2007) 1300–1311. https://doi.org/https://doi.org/10.1016/j.rser.2005.08.006.

[39] A. Bajaj, P. Lohan, P.N. Jha, R. Mehrotra, Biodiesel production through lipase catalyzed transesterification: An overview, J. Mol. Catal. B Enzym. 62 (2010) 9–14. https://doi.org/https://doi.org/10.1016/j.molcatb.2009.09.018.

[40] E. Alptekin, M. Canakci, H. Sanli, Biodiesel production from vegetable oil and waste animal fats in a pilot plant, Waste Manag. 34 (2014) 2146–2154. https://doi.org/10.1016/j.wasman.2014.07.019.

[41] J.N. Reddy, A.Ã. Ramesh, Parametric studies for improving the performance of a Jatropha oil-fuelled compression ignition engine, 31 (2016) 1994–2016. https://doi.org/10.1016/j.renene.2005.10.006.

[42] L.H.D.E. Pourghere, Universite de sherbrooke, n.d.

[43] A. Macario, G. Giordano, B. Onida, D. Cocina, A. Tagarelli, A.M. Giuffrè, Biodiesel production process by homogeneous/heterogeneous catalytic system using an acid–base catalyst, Appl. Catal. A Gen. 378 (2010) 160–168. https://doi.org/https://doi.org/10.1016/j.apcata.2010.02.016.

[44] K. Bunyakiat, S. Makmee, R. Sawangkeaw, S. Ngamprasertsith, Continuous Production of Biodiesel via Transesterification from Vegetable Oils in Supercritical Methanol, Energy & Fuels. 20 (2006) 812–817. https://doi.org/10.1021/ef050329b.

[45] S. Benjapornkulaphong, C. Ngamcharussrivichai, K. Bunyakiat, Al2O3-supported alkali and alkali earth metal oxides for transesterification of palm kernel oil and coconut oil, Chem. Eng. J. 145 (2009) 468–474. https://doi.org/https://doi.org/10.1016/j.cej.2008.04.036.

[46] H.-J. Kim, B.-S. Kang, M.-J. Kim, Y.M. Park, D.-K. Kim, J.-S. Lee, K.-Y. Lee, Transesterification of vegetable oil to biodiesel using heterogeneous base catalyst, Catal. Today. 93–95 (2004) 315–320. https://doi.org/https://doi.org/10.1016/j.cattod.2004.06.007.

References

[47] A. Casas, Applied Catalysis A : General Transesterification of sunflower oil over zeolites using different metal loading : A case of leaching and agglomeration studies ´ a Jesu, 346 (2008) 79–85. https://doi.org/10.1016/j.apcata.2008.05.008.

[48] I.M. Atadashi, M.K. Aroua, A.R. Abdul Aziz, N.M.N. Sulaiman, The effects of catalysts in biodiesel production: A review, J. Ind. Eng. Chem. 19 (2013) 14–26. https://doi.org/10.1016/j.jiec.2012.07.009.

[49] S.N. Gebremariam, J.M. Marchetti, Biodiesel production through sulfuric acid catalyzed transesterification of acidic oil: Techno economic feasibility of different process alternatives, Energy Convers. Manag. 174 (2018) 639–648. https://doi.org/https://doi.org/10.1016/j.enconman.2018.08.078.

[50] M.G. Kulkarni, A.K. Dalai, Waste cooking oil - An economical source for biodiesel: A review, Ind. Eng. Chem. Res. 45 (2006) 2901–2913. https://doi.org/10.1021/ie0510526.

[51] A. Demirbas, Comparison of transesterification methods for production of biodiesel from vegetable oils and fats, Energy Convers. Manag. 49 (2008) 125–130. https://doi.org/10.1016/j.enconman.2007.05.002.

[52] J.K. Raman, V. Foo, W. Ting, R. Pogaku, Life cycle assessment of biodiesel production using alkali , soluble and immobilized enzyme catalyst processes, Biomass and Bioenergy. 35 (2011) 4221–4229. https://doi.org/10.1016/j.biombioe.2011.07.010.

[53] A. Abbaszaadeh, B. Ghobadian, M.R. Omidkhah, G. Najafi, Current biodiesel production technologies : A comparative review, 63 (2012) 138–148.

[54] A.E. Atabani, A.S. Silitonga, I.A. Badruddin, T.M.I. Mahlia, H.H. Masjuki, S. Mekhilef, A comprehensive review on biodiesel as an alternative energy resource and its characteristics, Renew. Sustain. Energy Rev. 16 (2012) 2070–2093. https://doi.org/https://doi.org/10.1016/j.rser.2012.01.003.

[55] J. Ali, A. Semwal, Biodiesel as an alternative fuel for diesel engine - An overview, Int. J. Appl. Eng. Res. 9 (2014) 1159–1168.

[56] M. Balat, Potential alternatives to edible oils for biodiesel production – A review of current work, Energy Convers. Manag. 52 (2011) 1479–1492. https://doi.org/https://doi.org/10.1016/j.enconman.2010.10.011.

[57] A. Ulusik, Advantages and disadvantages of biodiesels, Energy Educ. Sci. Technol. Part A Energy Sci. Res. 28 (2011) 221–226.

[58] O.D. Sylvester, F. V Adams, L.N. Okoro, Impact of Biodiesel on the Corrosion of Zinc and Copper Strips, 6 (2015) 546–549.

[59] S. Kaul, R.C. Saxena, A. Kumar, M.S. Negi, A.K. Bhatnagar, H.B. Goyal, A.K. Gupta, Corrosion behavior of biodiesel from seed oils of Indian origin on diesel engine parts, Fuel Process. Technol. 88 (2007) 303–307. https://doi.org/10.1016/j.fuproc.2006.10.011.

[60] J. Van Gerpen, B. Shanks, R. Pruszko, D. Clements, G. Knothe, Biodiesel Analytical Methods August 2002 - January 2004, Nrel/Sr-510-36240. (2004) 100.

[61] 884960.pdf, (n.d.).

[62] J. Bénard, A. Michel, J.J. Philibert, T. Préf, M. Chevreton, Métallurgie générale, par J. Bénard, A. Michel, J. Philibert et J. Talbot. Préf. du Prof. G. Chaudron, 1970, 93 (2019) 409–410.

[63] G. Gunasekaran, S. Chongdar, S.N. Gaonkar, P. Kumar, Influence of bacteria on film formation inhibiting corrosion, Corros. Sci. 46 (2004) 1953–1967. https://doi.org/https://doi.org/10.1016/j.corsci.2003.10.023.

[64] D.U.D. De, TFilSE, 1979.

[65] G.S. Frankel, N. Sridhar, Understanding localized corrosion, Mater. Today. 11 (2008) 38–44. https://doi.org/https://doi.org/10.1016/S1369-7021(08)70206-2.

[66] S.N.A. G, A. Cell, NACE International Glossary of, (2010).

[67] A.C. Balaskas, I.A. Kartsonakis, D. Snihirova, M.F. Montemor, G. Kordas, Improving the corrosion protection properties of organically modified silicate–epoxy coatings by incorporation of organic and inorganic inhibitors, Prog. Org. Coatings. 72 (2011) 653–662. https://doi.org/https://doi.org/10.1016/j.porgcoat.2011.07.008.

[68] M.S.A. Kamel, A. Al-jumaili, M. Oelgemöller, M. V Jacob, Inorganic nanoparticles to overcome efficiency inhibitors of organic photovoltaics: An in-depth review, Renew. Sustain. Energy Rev. 166 (2022) 112661. https://doi.org/https://doi.org/10.1016/j.rser.2022.112661.

[69] c3gc42540a 3349..3357 ++ _ Enhanced Reader.pdf, (n.d.).

[70] CHILTON JP, Corrosion of metals, Met. Finish J. 17 (1971) 140–142. https://doi.org/10.1016/s0016-0032(10)90887-9.

[71] O. Access, We are IntechOpen , the world ’ s leading publisher of Open Access books Built by scientists , for scientists TOP 1 % Investigation of Corrosion Inhibitors Adsorption on Metals Using Density Functional Theory, (n.d.).

[72] F. Chiter, D. Costa, V. Maurice, P. Marcus, Corrosion inhibition of locally de-passivated surfaces by DFT study of 2-mercaptobenzothiazole on copper, Npj Mater. Degrad. 5 (2021). https://doi.org/10.1038/s41529-021-00198-x.

[73] N. Zaouri, Adsorption of Different Fractions of Organic Matter on the Surface of Metal Oxide, (2013).

[74] L.W. Bruch, Theory of physisorption interactions, Surf. Sci. 125 (1983) 194–217. https://doi.org/10.1016/0039-6028(83)90453-3.

[75] G. Ehrlich, The mechanism of chemisorption on metals, J. Phys. Chem. Solids. 1 (1956) 3–13. https://doi.org/https://doi.org/10.1016/0022-3697(56)90003-8.

[76] B. Hatzold, Julia; Conradt, untitled _ Enhanced Reader.pdf, (2008) 6.

[77] M.D. Engelhart, H. Moughamian, Book Reviews : Book Reviews, Educ. Psychol. Meas. 31 (1971) 297–297. https://doi.org/10.1177/001316447103100132.

[78] M.D.E. Master, Etude de l ' efficacité de l ' inhibiteur organique (extrait d ' oignon) sur la corrosion de l ' acier C45 en milieu acide, (2021).

[79] K.A. Sorate, P. V. Bhale, Biodiesel properties and automotive system compatibility issues, Renew. Sustain. Energy Rev. 41 (2015). https://doi.org/10.1016/j.rser.2014.08.079.

[80] P. V. Bhale, K.A. Sorate, Impact of biodiesel on fuel system materials durability, J. Sci. Ind. Res. (India). 72 (2013) 48–57.

[81] X.P. Nguyen, H.N. Vu, Corrosion of the metal parts of diesel engines in biodiesel-based fuels, Int. J. Renew. Energy Dev. 8 (2019) 119–132. https://doi.org/10.14710/ijred.8.2.119-132.

[82] C.I. Rocabruno-Valdés, J.A. Hernández, A.U. Juantorena, E.G. Arenas, R. Lopez-Sesenes, V.M. Salinas-Bravo, J.G. González-Rodriguez, An electrochemical study of the corrosion behaviour of metals in canola biodiesel, Corros. Eng. Sci. Technol. 53 (2018) 153–162. https://doi.org/10.1080/1478422X.2018.1443621.

[83] D.M. Fernandes, A.L. Squissato, A.F. Lima, E.M. Richter, R.A.A. Munoz, Corrosive character of Moringa oleifera Lam biodiesel exposed to carbon steel under simulated storage conditions, Renew. Energy. 139 (2019) 1263–1271. https://doi.org/10.1016/j.renene.2019.03.034.

[84] S. Banga, P.K. Varshney, Effect of impurities on performance of biodiesel: A review, J. Sci. \& Ind. Res. 69 (2010) 575–579.

[85] H.M. Yang, Role of organic and eco-friendly inhibitors on the corrosion mitigation of steel in acidic environments—a state-of-art review, Molecules. 26 (2021). https://doi.org/10.3390/molecules26113473.

[86] R.T. Loto, C.A. Loto, O. Joseph, G. Olanrewaju, Adsorption and corrosion inhibition properties of thiocarbanilide on the electrochemical behavior of high carbon steel in dilute acid solutions, Results Phys. 6 (2016) 305–314. https://doi.org/10.1016/j.rinp.2016.05.013.

[87] R. Haldhar, D. Prasad, D. Kamboj, S. Kaya, O. Dagdag, L. Guo, Corrosion inhibition, surface adsorption and computational studies of Momordica charantia extract: a sustainable and green approach, SN Appl. Sci. 3 (2021) 1–13. https://doi.org/10.1007/s42452-020-04079-x.

[88] J. Lazrak, E. Ech-chihbi, B. El Ibrahimi, F. El Hajjaji, Z. Rais, M. Tachihante, M. Taleb, Detailed DFT/MD simulation, surface analysis and electrochemical computer explorations of aldehyde derivatives for mild steel in 1.0 M HCl, Colloids Surfaces A Physicochem. Eng. Asp. 632 (2022). https://doi.org/10.1016/j.colsurfa.2021.127822.

[89] D. Dill, Schrödinger ' s master equation of quantum mechanics Notes on Quantum Mechanics, Quantum. (2004).

[90] T. Born-, XII . The Born-Oppenheimer Approximation, (n.d.).

[91] L.H. Thomas, E. Fermi, Thomas-Fermi method, 542 (1991) 1–7. www.home.uni-osnabrueck.de/apostnik/Lectures/DFT-1.pdf.

[92] W. Koch, M.C. Holthausen, The Hohenberg-Kohn Theorems The First Hohenberg-Kohn Theorem : Proof of Existence, A Chem. Guid. to Density Funct. Theory. 3 (2001) 33–40.

[93] P. Geerlings, F. De Proft, W. Langenaeker, Conceptual density functional theory, Chem. Rev. 103 (2003) 1793–1873. https://doi.org/10.1021/cr990029p.

[94] V. Polo, J. Gräfenstein, E. Kraka, D. Cremer, Long-range and short-range Coulomb correlation effects as simulated by Hartree-Fock, local density approximation, and generalized gradient approximation exchange functionals, Theor. Chem. Acc. 109 (2003) 22–35. https://doi.org/10.1007/s00214-002-0398-y.

[95] X. Ren, P. Rinke, V. Blum, J. Wieferink, A. Tkatchenko, A. Sanfilippo, K. Reuter, M. Scheffler, Resolution-of-identity approach to Hartree-Fock, hybrid density functionals, RPA, MP2 and GW with numeric atom-centered orbital basis functions, New J. Phys. 14 (2012). https://doi.org/10.1088/1367-2630/14/5/053020.

[96] A. Albavera-Mata, K. Botello-Mancilla, S.B. Trickey, J.L. Gázquez, A. Vela, Generalized gradient approximations with local parameters, Phys. Rev. B. 102 (2020). https://doi.org/10.1103/PhysRevB.102.035129.

[97] M. Yu, S. Yang, C. Wu, N. Marom, Machine learning the Hubbard U parameter in DFT+U using Bayesian optimization, Npj Comput. Mater. 6 (2020). https://doi.org/10.1038/s41524-020-00446-9.

[98] R. Haunschild, A. Barth, B. French, A comprehensive analysis of the history of DFT based on the bibliometric method RPYS, J. Cheminform. 11 (2019) 1–15. https://doi.org/10.1186/s13321-019-0395-y.

[99] A.D. Boese, N.C. Handy, New exchange-correlation density functionals: The role of the kinetic-energy density, J. Chem. Phys. 116 (2002) 9559–9569. https://doi.org/10.1063/1.1476309.

[100] J.C. Slater, A simplification of the Hartree-Fock method, Phys. Rev. 81 (1951) 385–390.

https://doi.org/10.1103/PhysRev.81.385.

[101] J.P. Perdew, Density-functional approximation for the correlation energy of the inhomogeneous electron gas, Phys. Rev. B. 33 (1986) 8822–8824. https://doi.org/10.1103/PhysRevB.33.8822.

[102] A.D. Becke, Density-functional exchange-energy approximation with correct asymptotic behavior, Phys. Rev. A. 38 (1988) 3098–3100. https://doi.org/10.1103/PhysRevA.38.3098.

[103] C. Lee, W. Yang, R.G. Parr, Development of the Colle-Salvetti correlation-energy formula into a functional of the electron density, Phys. Rev. B. 37 (1988) 785–789. https://doi.org/10.1103/PhysRevB.37.785.

[104] F. Bechstedt, Exchange-Correlation Functionals, Springer Ser. Solid-State Sci. 181 (2015) 105–127. https://doi.org/10.1007/978-3-662-44593-8_7.

[105] A.D. Boese, J.M.L. Martin, N.C. Handy, The role of the basis set: Assessing density functional theory, J. Chem. Phys. 119 (2003) 3005–3014. https://doi.org/10.1063/1.1589004.

[106] D.A. Dixon, Density functional theory, Encycl. Earth Sci. Ser. (2018) 347–352. https://doi.org/10.1201/b15281-8.

[107] S. Wilson, Basis Sets, Adv. Chem. Phys. 67 (2007) 439–500. https://doi.org/10.1002/9780470142936.ch8.

[108] B.S. Used, M.O. Calculations, Basis Sets Used in Molecular Orbital Calculations 1., (n.d.) 1–19.

[109] A. V. Mitin, J. Baker, P. Pulay, An improved 6-31G* basis set for first-row transition metals, J. Chem. Phys. 118 (2003) 7775–7783. https://doi.org/10.1063/1.1563619.

[110] R.G. Parr, R.G. Pearson, Absolute Hardness: Companion Parameter to Absolute Electronegativity, J. Am. Chem. Soc. 105 (1983) 7512–7516. https://doi.org/10.1021/ja00364a005.

[111] R.G. Pearson, Chemical hardness and the electronic chemical potential, Inorganica Chim. Acta. 198–200 (1992) 781–786. https://doi.org/10.1016/S0020-1693(00)92423-X.

[112] R.G. Parr, L. V. Szentpály, S. Liu, Electrophilicity index, J. Am. Chem. Soc. 121 (1999) 1922–1924. https://doi.org/10.1021/ja983494x.

[113] E. Chamorro, P. Ṕrez, Condensed-to-atoms electronic Fukui functions within the framework of spin-polarized density-functional theory, J. Chem. Phys. 123 (2005). https://doi.org/10.1063/1.2033689.

[114] A.D. Isravel, J.K. Jeyaraj, S. Thangasamy, W.J. John, DFT, NBO, HOMO-LUMO, NCI, stability, Fukui function and hole – Electron analyses of tolcapone, Comput. Theor. Chem. 1202 (2021) 113296. https://doi.org/10.1016/j.comptc.2021.113296.

[115] P.C. Rathi, R.F. Ludlow, M.L. Verdonk, Practical High-Quality Electrostatic Potential Surfaces

for Drug Discovery Using a Graph-Convolutional Deep Neural Network, J. Med. Chem. 63 (2020) 8778–8790. https://doi.org/10.1021/acs.jmedchem.9b01129.

[116] Hardness , Softness , and the Fukui Function in the Electronic Theory of Metals and Catalysis Author (s): Weitao Yang and Robert G . Parr Source : Proceedings of the National Academy of Sciences of the United States of America , Published by : National , 82 (2022) 6723–6726.

[117] R.G. Pearson, Hard and Soft Acids and Bases, J. Am. Chem. Soc. 85 (1963) 3533–3539. https://doi.org/10.1021/ja00905a001.

[118] H.A.L. Filipe, L.M.S. Loura, Molecular Dynamics Simulations: Advances and Applications, Molecules. 27 (2022) 37–47. https://doi.org/10.3390/molecules27072105.

[119] I. V. Likhachev, N.K. Balabaev, O. V. Galzitskaya, Available Instruments for Analyzing Molecular Dynamics Trajectories, Open Biochem. J. 10 (2016) 1–11. https://doi.org/10.2174/1874091x01610010001.

[120] A. Kokalj, Molecular modeling of organic corrosion inhibitors: Calculations, pitfalls, and conceptualization of molecule–surface bonding, Elsevier Ltd., 2021. https://doi.org/10.1016/j.corsci.2021.109650.

[121] M.S. 2017, Materials Studio, Revision 8.0, Accelrys Inc., San Diego, USA, Thesis. (2017).

[122] S. Supplementary, Design , molecular modeling and synthesis of metal- free sensitizers of thieno pyridine dyes as light- harvesting materials with efficiency improvement by plasmonic nanoparticles, (n.d.).

[123] J. Yang, Y. Ren, A. Tian, No Title, (2000) 4951–4957.

[124] W. Qian, X. Xue, J. Liu, Molecular Forcefield Methods for Describing Energetic Molecular Crystals : A Review, (2022).

[125] X. Li, J.D. Henderson, F.P. Filice, D. Zagidulin, M.C. Biesinger, F. Sun, B. Qian, D.W. Shoesmith, J.J. Noël, K. Ogle, The contribution of Cr and Mo to the passivation of Ni22Cr and Ni22Cr10Mo alloys in sulfuric acid, Corros. Sci. 176 (2020). https://doi.org/10.1016/j.corsci.2020.109015.

[126] S. Zhang, C. Sun, J. Di, Y. Tan, Corrosion behavior and morphology of passive films modified with zinc–aluminum simultaneous treatment on different metals, Metals (Basel). 10 (2020) 1–20. https://doi.org/10.3390/met10080986.

[127] A.L.G. Stern, M., Electrochemical Polarization: I . A Theoretical Analysis of the Shape of Polarization Curves, J. Electrochem. Soc. 104 (1957) 56.

[128] K. Krukiewicz, Electrochemical impedance spectroscopy as a versatile tool for the characterization of neural tissue: A mini review, Electrochem. Commun. 116 (2020) 106742.

https://doi.org/10.1016/j.elecom.2020.106742.

[129] R.G. Kelly, J.R. Scully, D. Shoesmith, R.G. Buchheit, Electrochemical Techniques in Corrosion Science and Engineering, 2002. https://doi.org/10.1201/9780203909133.

[130] C.T. Pham, D. Månsson, On the physical system modelling of energy storages as equivalent circuits with parameter description for variable load demand (Part I), J. Energy Storage. 13 (2017) 73–84. https://doi.org/10.1016/j.est.2017.05.015.

[131] Y. He, Y. Yang, S. Nie, R. Liu, Q. Wan, Electric-double-layer transistors for synaptic devices and neuromorphic systems, J. Mater. Chem. C. 6 (2018) 5336–5352. https://doi.org/10.1039/c8tc00530c.

[132] J.L. Burguera, M. Burguera, Analytical applications of emulsions and microemulsions, Talanta. 96 (2012) 11–20. https://doi.org/10.1016/j.talanta.2012.01.030.

[133] C. Costa, B. Medronho, A. Filipe, I. Mira, B. Lindman, H. Edlund, M. Norgren, Emulsion formation and stabilization by biomolecules: The leading role of cellulose, Polymers (Basel). 11 (2019). https://doi.org/10.3390/polym11101570.

[134] R.S. Amais, E.E. Garcia, M.R. Monteiro, J.A. Nóbrega, Determination of Ca, Mg, and Zn in biodiesel microemulsions by FAAS using discrete nebulization, Fuel. 93 (2012) 167–171. https://doi.org/10.1016/j.fuel.2011.10.042.

[135] M.B. Galuch, A.F.B. Piccioli, E.S. Neto, N. Fier, N.C. Saldan, E.E. Garcia, Microemulsion as sample preparation for direct flame atomic absorption spectrometry (FAAS) determination of total iron in crude and refined vegetable oils, J. Braz. Chem. Soc. 29 (2018) 748–756. https://doi.org/10.21577/0103-5053.20170197.

[136] J.T.G. Overbeek, G.J. Verhoeckx, P.L. de Bruyn, H.N.W. Lekkerkerker, On understanding microemulsions. II. Thermodynamics of droplet-type microemulsions, J. Colloid Interface Sci. 119 (1987) 422–441. https://doi.org/10.1016/0021-9797(87)90288-8.

[137] Z. Szalai, K. Kiss, G. Jakab, P. Sipos, B. Belucz, T. Németh, The use of UV-VIS-NIR reflectance spectroscopy to identify iron minerals, Astron. Nachrichten. 334 (2013) 940–943. https://doi.org/10.1002/asna.201211965.

[138] T. Meaning, F. Derivative, S. Derivative, The First and Second Derivatives, Writing. 2 (n.d.) 2–4.

[139] N. Leone, M. Mercurio, E. Grilli, A.P. Leone, A. Langella, A. Buondonno, Potential of vis-NIR reflectance spectroscopy for the mineralogical characterization of synthetic gleys: a preliminary investigation, Period. Di Mineral. 80 (2011) 433–453.

[140] G.W. Stachowiak, A.W. Batchelor, G.B. Stachowiak, 6 - Characterization of Test Specimens, in:

G.W. Stachowiak, A.W. Batchelor, G.B. Stachowiak (Eds.), Exp. Methods Tribol., Elsevier, 2004: pp. 115–150. https://doi.org/https://doi.org/10.1016/S0167-8922(04)80022-1.

[141] L.R.B. Elton, D.F. Jackson, X-Ray Diffraction and the Bragg Law, Am. J. Phys. 34 (1966) 1036–1038. https://doi.org/10.1119/1.1972439.

[142] B. Delley, From molecules to solids with the DMol3 approach, J. Chem. Phys. 113 (2000) 7756–7764. https://doi.org/10.1063/1.1316015.

[143] Materials Studio 20th anniversary _ Enhanced Reader.pdf, (n.d.).

[144] F. Poshtiban, G. Bahlakeh, B. Ramezanzadeh, A detailed computational exploration and experimental surface/electrochemical analyses of mild steel functionalized by zinc-aminotris methylene phosphonic acid complex film, Appl. Surf. Sci. 495 (2019) 143582. https://doi.org/10.1016/j.apsusc.2019.143582.

[145] I.B. Obot, D.D. Macdonald, Z.M. Gasem, Density functional theory (DFT) as a powerful tool for designing new organic corrosion inhibitors: Part 1: An overview, Corros. Sci. 99 (2015) 1–30. https://doi.org/10.1016/j.corsci.2015.01.037.

[146] BIOVIA, Adsorption Locator Guide, (2016) 1–39.

[147] M.M. Marinho, F.W.Q. Almeida-Neto, E.M. Marinho, L.P. da Silva, R.R.P.P.B. Menezes, R.P. dos Santos, E.S. Marinho, P. de Lima-Neto, A.M.C. Martins, Quantum computational investigations and molecular docking studies on amentoflavone, Heliyon. 7 (2021). https://doi.org/10.1016/j.heliyon.2021.e06079.

[148] H. Jabbari, Production of methyl ester biofuel from sunflower oil via transesterification reaction, Asian J. Nanosci. Mater. 1 (2018) 52–55. http://www.ajnanomat.com/article_58261.html%0Ahttp://www.ajnanomat.com/pdf_58261_a57bf035e3613b8f50d961b5e1fdb434.html.

[149] W.N.N. Wan Omar, N.A. Saidina Amin, Optimization of heterogeneous biodiesel production from waste cooking palm oil via response surface methodology, Biomass and Bioenergy. 35 (2011) 1329–1338. https://doi.org/10.1016/j.biombioe.2010.12.049.

[150] Liquid Petroleum Products—Fatty Acid Methyl Esters (FAME) for Use in Diesel Engines and Heating Applications—Requirements and Test Methods; EN 14214; BSI Group; London, United Kingdom, 2012.

[151] T. Tsoutsos, S. Tournaki, Z. Gkouskos, O. Paraíba, F. Giglio, P.Q. García, J. Braga, H. Adrianos, M. Filice, Quality characteristics of biodiesel produced from used cooking oil in Southern Europe, ChemEngineering. 3 (2019) 1–13. https://doi.org/10.3390/chemengineering3010019.

[152] L. de Fátima Bezerra de Lira, F.V.C. de Vasconcelos, C.F. Pereira, A.P.S. Paim, L. Stragevitch,

M.F. Pimentel, Prediction of properties of diesel/biodiesel blends by infrared spectroscopy and multivariate calibration, Fuel. 89 (2010) 405–409. https://doi.org/10.1016/j.fuel.2009.05.028.

[153] M. Tariq, S. Ali, F. Ahmad, M. Ahmad, M. Zafar, N. Khalid, M.A. Khan, Identification, FT-IR, NMR (1H and 13C) and GC/MS studies of fatty acid methyl esters in biodiesel from rocket seed oil, Fuel Process. Technol. 92 (2011) 336–341. https://doi.org/10.1016/j.fuproc.2010.09.025.

[154] E. Hu, Y. Xu, X. Hu, L. Pan, S. Jiang, Corrosion behaviors of metals in biodiesel from rapeseed oil and methanol, Renew. Energy. 37 (2012) 371–378. https://doi.org/10.1016/j.renene.2011.07.010.

[155] M.A. Fazal, A.S.M.A. Haseeb, H.H. Masjuki, Corrosion mechanism of copper in palm biodiesel, Corros. Sci. 67 (2013) 50–59. https://doi.org/10.1016/j.corsci.2012.10.006.

[156] R. Chen, J. Hu, Y. Ma, W. Guo, H. Huang, J. Wei, S. Yin, Q. Yu, Characterization of the passive film formed on the reinforcement surface in alkali activated fly ash: Surface analysis and electrochemical evaluation, Corros. Sci. 165 (2020) 108393. https://doi.org/10.1016/j.corsci.2019.108393.

[157] K. Oh, S. Ahn, K. Eom, K. Jung, H. Kwon, Observation of passive films on Fe–20Cr–xNi (x=0, 10, 20wt.%) alloys using TEM and Cs-corrected STEM–EELS, Corros. Sci. 79 (2014) 34–40. https://doi.org/https://doi.org/10.1016/j.corsci.2013.10.023.

[158] L. Xu, P. Wu, X. Zhu, G. Zhao, X. Ren, Q. Wei, L. Xie, Structural characteristics and chloride intrusion mechanism of passive film, Corros. Sci. 207 (2022). https://doi.org/10.1016/j.corsci.2022.110563.

[159] S.M. Gateman, O. Gharbi, H. Gomes de Melo, K. Ngo, M. Turmine, V. Vivier, On the use of a constant phase element (CPE) in electrochemistry, Curr. Opin. Electrochem. 36 (2022) 101133. https://doi.org/10.1016/j.coelec.2022.101133.

[160] W. Xu, H. Yu, F. Yang, F. Yang, D. Liu, K. Lu, H. Gao, Y. Song, Second derivative UV–visible spectroscopy characterizing structural components of dissolved and particulate organic matter in an urbanized river, Environ. Sci. Eur. 34 (2022). https://doi.org/10.1186/s12302-022-00609-z.

[161] A.J. Owen, Uses of Derivative Spectroscopy, Spectroscopy. (1995) 8.

[162] R. Guillamet, M. Lenglet, F. Adam, Reflectance spectroscopy of oxides films α-Cr2O3 and α-Fe2O3 on iron, Solid State Commun. 81 (1992) 633–637. https://doi.org/10.1016/0038-1098(92)90609-D.

[163] S.R. de Sanchez, L.E.A. Berlouis, D.J. Schiffrin, Difference reflectance spectroscopy of anodic films on copper and copper base alloys, J. Electroanal. Chem. Interfacial Electrochem. 307 (1991) 73–86. https://doi.org/https://doi.org/10.1016/0022-0728(91)85540-6.

[164] R.E. Hummel, Differential reflectometry and its application to the study of alloys, ordering, corrosion, and surface properties, Phys. Status Solidi. 76 (1983) 11–44. https://doi.org/10.1002/pssa.2210760102.

[165] T. Holland, A.M. Abdul-Munaim, C. Mandrell, R. Karunanithy, D.G. Watson, P. Sivakumar, Uv-visible spectrophotometer for distinguishing oxidation time of engine oil, Lubricants. 9 (2021) 1–13. https://doi.org/10.3390/lubricants9040037.

[166] O.D. Samuel, M. Gulum, Mechanical and corrosion properties of brass exposed to waste sunflower oil biodiesel-diesel fuel blends, Chem. Eng. Commun. 206 (2019) 682–694. https://doi.org/10.1080/00986445.2018.1519508.

[167] F.D. Avila Orozco, A.C. Sousa, C.E. Domini, M.C. Ugulino Araujo, B.S. Fernández Band, An ultrasonic-accelerated oxidation method for determining the oxidative stability of biodiesel, Ultrason. Sonochem. 20 (2013) 820–825. https://doi.org/10.1016/j.ultsonch.2012.10.012.

[168] E.N. Frankel, S.W. Huang, R. Aeschbach, Antioxidant activity of green teas in different lipid systems, JAOCS, J. Am. Oil Chem. Soc. 74 (1997) 1309–1315. https://doi.org/10.1007/s11746-997-0062-8.

[169] C.L. Kugelmeier, M.R. Monteiro, R. da Silva, S.E. Kuri, V.L. Sordi, C.A. Della Rovere, Corrosion behavior of carbon steel, stainless steel, aluminum and copper upon exposure to biodiesel blended with petrodiesel, Energy. 226 (2021). https://doi.org/10.1016/j.energy.2021.120344.

[170] M.A. Deyab, Corrosion inhibition of aluminum in biodiesel by ethanol extracts of Rosemary leaves, J. Taiwan Inst. Chem. Eng. 58 (2016) 536–541. https://doi.org/10.1016/j.jtice.2015.06.021.

[171] T. SUGA, H. MIYAKAWA, Y. MURASHIMA, T. YAOSAKA, K. KOITO, K. NATSUI, T. SATO, M. WATANABE, Y. OIKAWA, T. NAGAKAWA, A. NOBUTA, Peroral Micro-Pancreatoscopy (PMPS) for the Diagnosis of Pancreatic Diseases, Dig. Endosc. 2 (1990) 345–350. https://doi.org/10.1111/j.1443-1661.1990.tb00061.x.

[172] M.A. Fazal, A.S.M.A. Haseeb, H.H. Masjuki, Effect of different corrosion inhibitors on the corrosion of cast iron in palm biodiesel, Fuel Process. Technol. 92 (2011) 2154–2159. https://doi.org/10.1016/j.fuproc.2011.06.012.

[173] S. Norouzi, F. Eslami, M.L. Wyszynski, A. Tsolakis, Corrosion effects of RME in blends with ULSD on aluminium and copper, Fuel Process. Technol. 104 (2012) 204–210. https://doi.org/10.1016/j.fuproc.2012.05.016.

[174] C.E. Akhabue, F.A. Aisien, C.O. Ojo, The effect of Jatropha oil biodiesel on the corrosion rates

of aluminium and mild carbon steel, Biofuels. 5 (2014) 545–550. https://doi.org/10.1080/17597269.2014.1002995.

[175] K. Draou, N. Bellakhal, B.G. Chéron, J.L. Brisset, Heat transfer to metals in low pressure oxygen plasma: application to oxidation of the 90Cu-10Zn alloy, Mater. Chem. Phys. 58 (1999) 212–220. https://doi.org/10.1016/S0254-0584(98)00268-5.

[176] R. Hsissou, S. Abbout, Z. Safi, F. Benhiba, N. Wazzan, L. Guo, K. Nouneh, S. Briche, H. Erramli, M. Ebn Touhami, M. Assouag, A. Elharfi, Synthesis and anticorrosive properties of epoxy polymer for CS in [1 M] HCl solution: Electrochemical, AFM, DFT and MD simulations, Constr. Build. Mater. 270 (2021) 121454. https://doi.org/10.1016/j.conbuildmat.2020.121454.

[177] I. Lukovits, E. K, F. Zucchi, Corrosion Inhibitors — Correlation Between Electronic Structure and Efficiency, 57 (2001) 3–8.

[178] J. Saranya, F. Benhiba, N. Anusuya, R. Subbiah, A. Zarrouk, S. Chitra, Experimental and computational approaches on the pyran derivatives for acid corrosion, Colloids Surfaces A Physicochem. Eng. Asp. 603 (2020) 125231. https://doi.org/10.1016/j.colsurfa.2020.125231.

[179] W. Yang, R.G. Parr, Hardness , softness , and the fukui function in the electronic theory of metals and catalysis, 82 (1985) 6723–6726.

[180] C. Morell, A. Grand, A. Toro-Labbé, Theoretical support for using the Δf(r) descriptor, Chem. Phys. Lett. 425 (2006) 342–346. https://doi.org/10.1016/j.cplett.2006.05.003.

[181] S.A. Hollingsworth, R.O. Dror, Molecular Dynamics Simulation for All, Neuron. 99 (2018) 1129–1143. https://doi.org/10.1016/j.neuron.2018.08.011.

[182] Z. Rouifi, M. Rbaa, A.S. Abousalem, F. Benhiba, T. Laabaissi, H. Oudda, B. Lakhrissi, A. Guenbour, I. Warad, A. Zarrouk, Synthesis, characterization and corrosion inhibition potential of newly benzimidazole derivatives: Combining theoretical and experimental study, Surfaces and Interfaces. 18 (2020). https://doi.org/10.1016/j.surfin.2020.100442.

[183] D.Q. Huong, N.T.L. Huong, T.T.A. Nguyet, T. Duong, D. Tuan, N.M. Thong, P.C. Nam, Pivotal role of heteroatoms in improving the corrosion inhibition ability of thiourea derivatives, ACS Omega. 5 (2020) 27655–27666. https://doi.org/10.1021/acsomega.0c04241.

[184] A. Dutta, S.K. Saha, P. Banerjee, D. Sukul, Correlating electronic structure with corrosion inhibition potentiality of some bis-benzimidazole derivatives for mild steel in hydrochloric acid: Combined experimental and theoretical studies, Corros. Sci. 98 (2015) 541–550. https://doi.org/10.1016/j.corsci.2015.05.065.

[185] Z. Rouifi, M. Rbaa, F. Benhiba, T. Laabaissi, H. Oudda, B. Lakhrissi, A. Guenbour, I. Warad, A. Zarrouk, Preparation and anti-corrosion activity of novel 8-hydroxyquinoline derivative for

carbon steel corrosion in HCl molar: Computational and experimental analyses, J. Mol. Liq. 307 (2020). https://doi.org/10.1016/j.molliq.2020.112923.

[186] I.I. Fairushin, A. V. Mokshin, Calculation of Thermodynamic Characteristics and Sound Velocity for Two-Dimensional Yukawa Fluids Based on a Two-Step Approximation for the Radial Distribution Function, Fluids. 8 (2023) 1–8. https://doi.org/10.3390/fluids8020072.

[187] V. Mehmeti, F.I. Podvorica, Experimental and theoretical studies on corrosion inhibition of niobium and tantalum surfaces by carboxylated graphene oxide, Materials (Basel). 11 (2018). https://doi.org/10.3390/ma11060893.

[188] S.G. Charati, S.A. Stern, Diffusion of gases in silicone polymers: Molecular dynamics simulations, Macromolecules. 31 (1998) 5529–5535. https://doi.org/10.1021/ma980387e.

[189] X. Zhang, J. Zhang, J. Wang, M. Liu, Y. Xu, R. Li, Y. Chen, X. Li, W.Y. Lai, W. Huang, Efficient non-doped blue phosphorescent organic light-emitting devices by incorporating Ag-island nanostructures, Org. Electron. 58 (2018) 25–32. https://doi.org/10.1016/j.orgel.2018.03.049.

[190] A. Guo, G. Duan, K. He, B. Sun, C. Fan, S. Hu, Synergistic effect between 2-oleyl-1-oleylamidoethyl imidazoline ammonium methylsulfate and halide ion by molecular dynamics simulation, Comput. Theor. Chem. 1015 (2013) 21–26. https://doi.org/10.1016/j.comptc.2013.04.001.

[191] F. Benhiba, N.K. Sebbar, H. Bourazmi, M.E. Belghiti, R. Hsissou, T. Hökelek, A. Bellaouchou, A. Guenbour, I. Warad, H. Oudda, A. Zarrouk, E.M. Essassi, Corrosion inhibition performance of 4-(prop-2-ynyl)- [1,4]-benzothiazin-3-one against mild steel in 1 M HCl solution: Experimental and theoretical studies, Int. J. Hydrogen Energy. 46 (2021) 25800–25818. https://doi.org/10.1016/j.ijhydene.2021.05.091.

[192] S.-Q. Hu, A.-L. Guo, Y.-G. Yan, X.-L. Jia, Y.-F. Geng, W.-Y. Guo, Computer simulation of diffusion of corrosive particle in corrosion inhibitor membrane, Comput. Theor. Chem. 964 (2011) 176–181. https://doi.org/https://doi.org/10.1016/j.comptc.2010.12.019.

[193] V. Winoto, A. Charoenphol, N. Tuangtee, N. Yoswathana, Optimization Study in Rubber Seed Biodiesel Production Using Nano-Magnetic Catalyst and Subcritical Methanol, (2018) 155–163.

[194] Y. Wang, S.O. Pengzhan Liu, Z. Zhang, Preparation of biodiesel from waste cooking oil via two-step catalyzed process, Energy Convers. Manag. 48 (2007) 184–188. https://doi.org/10.1016/j.enconman.2006.04.016.

[195] M. Rosset, O.W. Perez-Lopez, FTIR spectroscopy analysis for monitoring biodiesel production by heterogeneous catalyst, Vib. Spectrosc. 105 (2019) 102990. https://doi.org/10.1016/j.vibspec.2019.102990.

[196] S.K. Thangavelu, A.S. Ahmed, F.N. Ani, Impact of metals on corrosive behavior of biodiesel–diesel–ethanol (BDE) alternative fuel, Renew. Energy. 94 (2016) 1–9. https://doi.org/https://doi.org/10.1016/j.renene.2016.03.015.

[197] B.S. Sazzad, M.A. Fazal, A.S.M.A. Haseeb, H.H. Masjuki, Retardation of oxidation and material degradation in biodiesel: A review, RSC Adv. 6 (2016) 60244–60263. https://doi.org/10.1039/c6ra10016c.

[198] M.A. Deyab, S.T. Keera, On corrosion and corrosion inhibition of carbon steel in stored biodiesel: electrochemical (AC and DC) studies, J. Taiwan Inst. Chem. Eng. 68 (2016) 187–191. https://doi.org/10.1016/j.jtice.2016.08.035.

[199] P. Shukla, 7 - Thermodynamics of corrosion and potentiometric methods for measuring localized corrosion, in: L. Yang (Ed.), Tech. Corros. Monit., Woodhead Publishing, 2008: pp. 156–186. https://doi.org/https://doi.org/10.1533/9781845694050.1.156.

[200] K. V. Akpanyung, R.T. Loto, Pitting corrosion evaluation: A review, J. Phys. Conf. Ser. 1378 (2019). https://doi.org/10.1088/1742-6596/1378/2/022088.

[201] V. Maurice, W.P. Yang, P. Marcus, X-Ray Photoelectron Spectroscopy and Scanning Tunneling Microscopy Study of Passive Films Formed on (100) Fe-18Cr-13Ni Single-Crystal Surfaces, J. Electrochem. Soc. 145 (1998) 909–920. https://doi.org/10.1149/1.1838366.

[202] K. Jüttner, Electrochemical impedance spectroscopy (EIS) of corrosion processes on inhomogeneous surfaces, Electrochim. Acta. 35 (1990) 1501–1508. https://doi.org/https://doi.org/10.1016/0013-4686(90)80004-8.

[203] M. Luo, R.Y. Zhang, Z. Zheng, J.L. Wang, J.B. Ji, Impact of some natural derivatives on the oxidative stability of soybean oil based biodiesel, J. Braz. Chem. Soc. 23 (2012) 241–246. https://doi.org/10.1590/S0103-50532012000200008.

[204] C.O.A. Olsson, D. Landolt, Passive films on stainless steels - Chemistry, structure and growth, Electrochim. Acta. 48 (2003) 1093–1104. https://doi.org/10.1016/S0013-4686(02)00841-1.

[205] S. Rashid, N. Islami, A.K. Ariffin, M. Ridha, S. Fauna, The effect of immersion time on the corrosion behavior of SUS304 in brine using half-cell potential measurement, J. Teknol. 78 (2016) 91–99. https://doi.org/10.11113/jt.v78.9152.

[206] A.C. Scheinost, A. Chavernas, V. Barrón, J. Torrent, Use and limitations of second-derivative diffuse reflectance spectroscopy in the visible to near-infrared range to identify and quantify Fe oxide minerals in soils, Clays Clay Miner. 46 (1998) 528–536. https://doi.org/10.1346/CCMN.1998.0460506.

[207] N. Leone, M. Mercurio, E. Grilli, A.P. Leone, A. Langella, A. Buondonno, Potential of vis-NIR

reflectance spectroscopy for the mineralogical characterization of synthetic gleys: A preliminary investigation, Period. Di Mineral. 80 (2011) 433–453. https://doi.org/10.2451/2011PM0029.

[208] M. Le Calvar, M. Lenglet, UV-Vis-NIR and FTIR Reflectance Studies of the Initial Stage of Oxidation of 80 Ni-20 Cr Alloy, Stud. Surf. Sci. Catal. 48 (1989) 575–580. https://doi.org/10.1016/S0167-2991(08)60718-1.

[209] C. Schneider, N.A. Porter, A.R. Brash, Routes to 4-hydroxynonenal: Fundamental issues in the mechanisms of lipid peroxidation, J. Biol. Chem. 283 (2008) 15539–15543. https://doi.org/10.1074/jbc.R800001200.

[210] E.N. Frankel, S.W. Huang, J. Kanner, J.B. German, Interfacial Phenomena in the Evaluation of Antioxidants: Bulk Oils vs Emulsions, J. Agric. Food Chem. 42 (1994) 1054–1059. https://doi.org/10.1021/jf00041a001.

[211] F. Shahidi, S.P.J.N. Senanayake, Fatty Acids, in: H.K. (Kris) Heggenhougen (Ed.), Int. Encycl. Public Heal., Academic Press, Oxford, 2008: pp. 594–603. https://doi.org/https://doi.org/10.1016/B978-012373960-5.00433-0.

[212] M.B. Dantas, A.R. Albuquerque, A.K. Barros, M.G. Rodrigues Filho, N.R. Antoniosi Filho, F.S.M. Sinfrônio, R. Rosenhaim, L.E.B. Soledade, I.M.G. Santos, A.G. Souza, Evaluation of the oxidative stability of corn biodiesel, Fuel. 90 (2011) 773–778. https://doi.org/https://doi.org/10.1016/j.fuel.2010.09.014.

[213] B. Prandi, M. Ferri, S. Monari, C. Zurlini, I. Cigognini, S. Verstringe, D. Schaller, M. Walter, L. Navarini, A. Tassoni, S. Sforza, T. Tedeschi, Extraction and chemical characterization of functional phenols and proteins from coffee (Coffea arabica) by-products, Biomolecules. 11 (2021) 1–17. https://doi.org/10.3390/biom11111571.

[214] S.I. Mussatto, E.M.S. Machado, S. Martins, J.A. Teixeira, Production, Composition, and Application of Coffee and Its Industrial Residues, Food Bioprocess Technol. 4 (2011) 661–672. https://doi.org/10.1007/s11947-011-0565-z.

[215] A. Tipler, Coffee Characterization Using Clarus SQ 8 GC / MS , TurboMatrix HS Trap and GC SNFR Olfactory Port, (2013).

[216] P.T.K. Le, Q.T.H. Vu, Q.T.V. Nguyen, K.A. Tran, K.A. Le, Extraction and evaluation the biological activities of oil from spent coffee grounds, Chem. Eng. Trans. 56 (2017) 1729–1734. https://doi.org/10.3303/CET1756289.

[217] A. Panusa, A. Zuorro, R. Lavecchia, G. Marrosu, R. Petrucci, Recovery of natural antioxidants from spent coffee grounds., J. Agric. Food Chem. 61 (2013) 4162–4168. https://doi.org/10.1021/jf4005719.

[218] A. Duangjai, N. Suphrom, J. Wungrath, A. Ontawong, N. Nuengchamnong, A. Yosboonruang, Comparison of antioxidant, antimicrobial activities and chemical profiles of three coffee (Coffea arabica L.) pulp aqueous extracts., Integr. Med. Res. 5 (2016) 324–331. https://doi.org/10.1016/j.imr.2016.09.001.

[219] J.P. Silva, G.L. Mendez, J. Lombana, D.G. Marrugo, R. Correa-Turizo, Physicochemical Characterization of Spent Coffee Ground (Coffea Arabica L) and its Antioxidant Evaluation, Adv. J. Food Sci. Technol. 16 (2018) 220–225. https://doi.org/10.19026/ajfst.16.5958.

[220] J. Simões, É. Maricato, F.M. Nunes, M.R. Domingues, M.A. Coimbra, Thermal stability of spent coffee ground polysaccharides: Galactomannans and arabinogalactans, Carbohydr. Polym. 101 (2014) 256–264. https://doi.org/https://doi.org/10.1016/j.carbpol.2013.09.042.

[221] O. Sanni, O. Sunday Isaac Fayomi, A. Patricia Idowu Popoola, Eco-friendly Inhibitors for Corrosion Protection of Stainless steel: An Overview, J. Phys. Conf. Ser. 1378 (2019). https://doi.org/10.1088/1742-6596/1378/4/042047.

[222] N. Soltani, N. Tavakkoli, M. Khayatkashani, M.R. Jalali, A. Mosavizade, Green approach to corrosion inhibition of 304 stainless steel in hydrochloric acid solution by the extract of Salvia officinalis leaves, Corros. Sci. 62 (2012) 122–135. https://doi.org/https://doi.org/10.1016/j.corsci.2012.05.003.

[223] M. Scendo, J. Trela, Adenine as an effective corrosion inhibitor for stainless steel in chloride solution, Int. J. Electrochem. Sci. 8 (2013) 9201–9221.

[224] X. Wang, H. Yang, F. Wang, An investigation of benzimidazole derivative as corrosion inhibitor for mild steel in different concentration HCl solutions, Corros. Sci. 53 (2011) 113–121. https://doi.org/10.1016/j.corsci.2010.09.029.

[225] M.P. Kamil, T. Suhartono, Y.G. Ko, Corrosion behavior of plasma electrolysis layer cross-linked with a conductive polymer coating, J. Mater. Res. Technol. 15 (2021) 4672–4682. https://doi.org/https://doi.org/10.1016/j.jmrt.2021.10.090.

[226] R.T. Loto, Corrosion inhibition of mild steel in acidic medium by butyl alcohol, (2013). https://doi.org/10.1007/s11164-013-1088-1.

[227] A.S. Fouda, M.A. Migahed, A.A. Atia, I.M. Mousa, Corrosion Inhibition and Adsorption Behavior of Some Cationic Surfactants on Carbon Steel in Hydrochloric Acid Solution, J. Bio-Tribo-Corrosion. 2 (2016) 22. https://doi.org/10.1007/s40735-016-0052-1.

[228] S. Kadapparambil, K. Yadav, M. Ramachandran, N. Victoria Selvam, Electrochemical investigation of the corrosion inhibition mechanism of Tectona grandis leaf extract for SS304

stainless steel in hydrochloric acid, Corros. Rev. 35 (2017) 111–121. https://doi.org/10.1515/corrrev-2016-0074.

[229] R. Naderi, A. Bautista, F. Velasco, M. Soleimani, M. Pourfath, Use of licorice plant extract for controlling corrosion of steel rebar in chloride-polluted concrete pore solution, J. Mol. Liq. 346 (2022) 117856. https://doi.org/10.1016/j.molliq.2021.117856.

[230] A. Popova, Temperature effect on mild steel corrosion in acid media in presence of azoles, Corros. Sci. 49 (2007) 2144–2158. https://doi.org/https://doi.org/10.1016/j.corsci.2006.10.020.

[231] A. Hamdy, N.S. El-Gendy, Thermodynamic, adsorption and electrochemical studies for corrosion inhibition of carbon steel by henna extract in acid medium, Egypt. J. Pet. 22 (2013) 17–25. https://doi.org/https://doi.org/10.1016/j.ejpe.2012.06.002.

[232] A.A. Khadom, A.S. Yaro, A.S. Altaie, A.A.H. Kadum, Electrochemical, activations and adsorption studies for the corrosion inhibition of low carbon steel in acidic media, Port. Electrochim. Acta. 27 (2009) 699–712. https://doi.org/10.4152/pea.200906699.

[233] M. Behpour, S.M. Ghoreishi, M. Khayatkashani, N. Soltani, The effect of two oleo-gum resin exudate from Ferula assa-foetida and Dorema ammoniacum on mild steel corrosion in acidic media, Corros. Sci. 53 (2011) 2489–2501. https://doi.org/10.1016/j.corsci.2011.04.005.

[234] E.E. Oguzie, Y. Li, F.H. Wang, Corrosion inhibition and adsorption behavior of methionine on mild steel in sulfuric acid and synergistic effect of iodide ion, J. Colloid Interface Sci. 310 (2007) 90–98. https://doi.org/10.1016/j.jcis.2007.01.038.

[235] C.A. Loto, R.T. Loto, Corrosion inhibition effect of Allium Cepa extracts on mild steel in H 2 SO 4, Der Pharma Chem. 8 (2016) 272–281.

[236] M. BenarioBenarioua, M. et al. (2019) 'Mild steel corrosion inhibition by Parsley (Petroselium Sativum) extract in acidic media', Egyptian Journal of Petroleum, 28(2), pp. 155–159. doi:https://doi.org/10.1016/j.ejpe.2019.01.001.ua, A. Mihi, N. Bouzeghaia, M. Naoun, Mild steel corrosion inhibition by Parsley (Petroselium Sativum) extract in acidic media, Egypt. J. Pet. 28 (2019) 155–159. https://doi.org/https://doi.org/10.1016/j.ejpe.2019.01.001.

[237] Y. Kerroum, A. Guenbour, A. Bellaouchou, H. Idrissi, J. Garcia-Anton, A. Zarrouk, The Corrosion of White Cast Iron in Polluted Phosphoric Acid Medium Contains Fluoride Ions, Anal. Bioanal. Electrochem. 11 (2019) 497–509.

[238] F.H.N. Souza, L.R. De Almeida, F.S.C.L. Batista, M.A.D.S. Rios, UV-Visible Spectroscopy Study of Oxidative Degradation of Sunflower Biodiesel, 2 (2011) 56–61. https://doi.org/http://dx.doi.org/10.3968/j.est.1923847920110202.112.

[239] C.-O.. Olsson, D. Landolt, Passive films on stainless steels—chemistry, structure and growth,

Electrochim. Acta. 48 (2003) 1093–1104. https://doi.org/https://doi.org/10.1016/S0013-4686(02)00841-1.

[240] H. Wei, B. Heidarshenas, L. Zhou, G. Hussain, Q. Li, K. (Ken) Ostrikov, Green inhibitors for steel corrosion in acidic environment: state of art, Mater. Today Sustain. 10 (2020) 100044. https://doi.org/https://doi.org/10.1016/j.mtsust.2020.100044.

[241] D.L. Cursaru, G. Brănoiu, I. Ramadan, F. Miculescu, Degradation of automotive materials upon exposure to sunflower biodiesel, Ind. Crops Prod. 54 (2014) 149–158. https://doi.org/10.1016/j.indcrop.2014.01.032.

[242] M.S. Graboski, R.L. McCormick, Combustion of fat and vegetable oil derived fuels in diesel engines, Prog. Energy Combust. Sci. 24 (1998) 125–164. https://doi.org/https://doi.org/10.1016/S0360-1285(97)00034-8.

[243] B.R. Moser, F.J. Eller, B.H. Tisserat, A. Gravett, Preparation of fatty acid methyl esters from osage orange (Maclura pomifera) oil and evaluation as biodiesel, Energy and Fuels. 25 (2011) 1869–1877. https://doi.org/10.1021/ef200195v.

Publications list

EL Hawary, M.., Khachani, M., Benhiba, F., Kaichouh, G., Warad, I., Guenbour, A., Zarrouk, A., & Bellaouchou, A. (2022***). "Investigation of the corrosion of stainless steel, copper and aluminum in sunflower biodiesel solution: Experimental and theoretical approaches"***. Chemical Data Collections, 40, 100870**.**

https://doi.org/10.1016/j.cdc.2022.100870

El Hawary, M., Khachani, M., Kaichouh, G , Warad, I., Guenbour, A., Zarrouk, A., & Bellaouchou, A(2021).“ ***Evolution of 307 L Stainless Steel Corrosion on the Oxidative Stability of Biodiesel During Storage***.” J Bio Tribo Corros 7, 143 (2021).

https://doi.org/10.1007/s40735-021-00586-5

A. Belafhaili**, M. El Hawary, A**.Bellaouchou. A.Guenbour ,I. Ward, A., Zarrouk. ***"Omeprazole's Inhibitive Activity on the Corrosion of the Al Alloy in 0.5 M H2SO4 Solution"*** **(**2023) Analytical and Bioanalytical Electrochemistry. 15issue

https://doi.org/10.22034/ABEC.2023.702330

ROYAUME DU MAROC
Université Mohammed V - RABAT -
جامعة محمد الخامس – الرباط –
Faculté des sciences
كلية العلوم

CENTRE D'ETUDES DOCTORALES - SCIENCES ET TECHNOLOGIES

Résumé

Ces dernières années ont vu une augmentation significative de l'utilisation du biodiesel comme alternative aux carburants fossiles conventionnels. Cependant, l'impact du biodiesel sur la corrosion des métaux suscite de vives inquiétudes. Ceci est dû à la présence d'impuretés, en particulier l'eau, qui peut créer des conditions acides dans les réservoirs de carburant et finalement conduire à la corrosion des métaux utilisés pour le stockage et le transport des carburants.

Cette thèse vise à évaluer le comportement à la corrosion des métaux dans le biodiesel provenant de différentes matières premières en utilisant des catalyseurs homogènes et hétérogènes. L'étude examinera le comportement des métaux par des méthodes électrochimiques (OCP, EIS, et courbes de polarisation) à température ambiante pendant deux heures de production et pendant le stockage ; en outre, des techniques spectroscopiques (FTIR, GS-MS, absorption UV et FAAS) ont été appliquées pour examiner les changements dans la composition du biodiesel avant et après les tests. Ensuite, la surface métallique a été évaluée par (SEM/EDX), (XRD) et absorption UV-Vis-NIR. En outre, l'effet inhibiteur du marc de café (HECG) sur le biodiesel SWCO a été étudié en utilisant des mesures de poids pendant 1128 h et diverses techniques électrochimiques précédemment appliquées à la surface métallique.

Mots- clés : corrosion-biodiesel ; L'acier inoxydable 307L -Alumimim -Cuivre ; DFT&MDS ; UV-Vis-NIR ; SEM/EDX, DRX ; corrosion inibition ' HECG' ; FAAS ; FTIR, GS-MS.

Abstract

Recent years have seen a significant increase in the use of biodiesel as an alternative to conventional fossil fuels. However, there are serious concerns about the impact of biodiesel on metal corrosion. This is due to the presence of impurities, particularly water, which can create acidic conditions in fuel tanks and ultimately lead to corrosion of metals used for fuel storage and transportation.

This thesis aims to evaluate the corrosion behavior of metals in biodiesel from different feedstocks using homogeneous and heterogeneous catalysts. The study will examine the behavior of metals by electrochemical methods (OCP, EIS, and polarization curves) at room temperature during two hours of production and storage; in addition, spectroscopic techniques (FTIR, GS-MS, UV absorption, and FAAS) were applied to examine changes in the composition of the biodiesel before and after the tests. Subsequently, the metal surface was evaluated by (SEM/EDX), (XRD) and UV-Vis-NIR absorption. In addition, the inhibitory effect of coffee grounds (HECG) on SWCO biodiesel was investigated using weight measurements for 1128 h and various electrochemical techniques previously applied to the metal surface.

Keywords ; corrosion-biodiesel ; 307L stainless steel- Alumimim -Copper ; DFT&MDS ; UV-Vis-NIR ; SEM/EDX, DRX ; corrosion inibition ' HECG' ; FAAS ; FTIR, GS-MS.